DEVELOPMENT OF AUTOMATIC MICROMANIPULATION MEASUREMENT SYSTEM TO ANALYSE THE MECHANICAL STRENGTH OF MICRO-SIZED MATERIALS

by

ZHIHUA ZHANG

A thesis submitted to the University of Birmingham for the degree of

DOCTOR OF PHILOSOPHY

School of Chemical Engineering
College of Engineering and Physical Sciences
University of Birmingham
September 2022

Abstract

Biological and nonbiological micro-sized materials are widely used in many industry sectors. Measuring their mechanical strength is essential to optimise their performance from manufacturing, to further processing, storage and end-use applications. Among all available techniques to experimentally determine the mechanical strength of micro-sized materials, the micromanipulation technique originally developed in the University of Birmingham UK, based on diametrical compression of single microparticles between two parallel flats, is very powerful, and has evolved with several different versions of the apparatus and several analytical and numerical mathematical models to determine the intrinsic mechanical properties of the tested materials from the experimental data. The mechanical properties of the tested micro-sized materials determined by the micromanipulation technique, include their rupture strength, elasticity, plasticity and viscoelasticity. However, it is time-consuming, laborious and technically demanding as the micromanipulation and data analysis were mainly undertaken manually. Therefore, it is pivotal to improve the micromanipulation technique to achieve automatic measurement and automatic data analysis, which is the main objective of this PhD project. Moreover, some new micro-sized materials were tested using the enhanced micromanipulation technique with mathematical models to determine their intrinsic mechanical properties for a range of new applications.

In this study, a new control system has been developed based on the existing micromanipulation technique to automatically test single microparticles by modifying the existing hardware system and developing new software to enable autofocusing, auto image processing, and auto micromanipulation. The manually-operated micromanipulator to support the sample stage has been replaced by DC servo linear actuators with motion controllers to achieve automatic motion control. A passive autofocus algorithm based on the sharpness of images and only the sideview camera has been developed to autofocus single microparticles by moving the sample stage from side to side and end to end. An object detection algorithm based on Otsu thresholding, Canny edge detection, and blob detection algorithms has been developed to automatically locate single microparticles from the autofocused images to determine their size and position. Two other essential algorithms have also been developed to automatically determine the magnification of the optical system and to automatically detect possible debris adhered to the force transducer output probe.

In order to achieve automatic data analysis, three algorithms based on the “three-sigma rule”, a moving window and the Hertz model to identify the starting point where the onset of compression begins and an algorithm based on the maximum deceleration to locate the rupture point have been developed, and a software package has been developed incorporated with these algorithms to determine the rupture strength parameters and force-displacement data of single microparticles from the raw voltage-sampling sequence data obtained from micromanipulation experiments.

Some elastic and plastic models used for analysing the data from micromanipulation, indentation, and uniaxial compression and tensile tests have been summarised and general forms of equations for the force versus displacement have been developed, based on which general approaches to extend the elastic and plastic analysis to viscoelastic and viscoplastic analysis, and general principles and strategies to incorporate these models into software have been developed, which can also be used in other related applications. Another software package has been developed incorporated with some mathematical models, including the Hertz model, the plastic model, the viscoelastic model and the core/shell model based on the finite element model (FEM) simulation results, to determine the intrinsic mechanical properties of microparticles from the force-displacement (or force-time) data of micromanipulation.

Some new micro-sized materials, including the self-sensing microcapsules to fabricate smart composites, the fragrance oil microcapsules with low content of formaldehyde, and the porous polystyrene (PS) microspheres and the poly (lactic acid) (PLA) microspheres, which can be potentially used in a variety of applications, have been tested using the conventional micromanipulation technique and their data have been analysed using the developed data analysis software packages to determine their mechanical property parameters as well as to validate the developed data analysis software packages.

Three mathematical models have been developed to determine the mechanical strength parameters corresponding to maximum stress, and the elastic and viscoelastic properties of microneedles from the experimental data of micromanipulation. Six microneedle samples based on hyaluronic acid (HA) have been tested using the micromanipulation technique and their data were analysed using the three developed mathematical models to obtain their intrinsic mechanical property parameters which can be used to predict their penetration efficiency comprehensively and more reliably.

The fragrance oil microcapsules with low content of formaldehyde, and the porous PS microspheres have also been tested using both the developed automatic and conventional micromanipulation systems to validate the former and the results show that the experimental results of the mechanical strength of the tested samples generated from both systems have no significant difference. The developed data analysis software packages can be used both together with the automatic micromanipulation system and alone to analyse the experimental data from either the developed automatic or conventional micromanipulation systems. The data analysis time has been shortened from around 3 hours manually to within 20 minutes automatically using the developed data analysis software package. Moreover, the newly developed micromanipulation system can auto focus, detect and test microparticles with size of 3-1000 μm currently and is much easier to use, needs much less time and labour work to complete the same task. It is believed that the achievements from this project represent a step change in enhancing the capabilities of the micromanipulation technique, which has now been commercialised for being used by more and more users in academic and industry.

Acknowledgement

I would like to express my sincere thanks and gratitude to my lead supervisor Professor Zhibing Zhang for his patient guidance and enormous support on my PhD project. He also has spent a lot of time in improving my writing and presentation skills which really has benefitted me a lot. I also would like to thank my co-supervisor Dr Zhenyu Zhang and my home institute supervisor Professor Jianghai Zhao for their guidance and support.

I would like to thank the MCAP group members in School of Chemical engineering, University of Birmingham, for their great help, friendship, advice and feedback to the developed data analysis software packages. Many thanks go to Dr Dan Baiocco and Dr Iryna Mikheenko for the training and discussion on the micromanipulation rig.

Sincere thanks also go to Mr. Huafeng Li for his great work on the development of the conventional version of the single sideview-based micromanipulation rig which the automatic micromanipulation system developed in this PhD project is based on. The layout of the UI of the developed software package for automatic micromanipulation system is also partially inspired by that of the manual version he developed.

I also would like to thank Dr Zhenxue Zhang, in School of Metallurgy and Materials, University of Birmingham UK for providing the sample of self-sensing microcapsules. Thank Dr Yanping He, in School of Chemical Engineering, Kunming University of Science and Technology China, for providing the samples of porous PS microspheres, PLA microspheres and MF microcapsules with lily oil. Thank Dr Guangsheng Du in West China School of Pharmacy, Sichuan University China, for providing microneedle samples and discussing their formulation details.

Many thanks go to the financial support from the University of Birmingham UK, Jiangsu Industrial Technology Research Institute (JITRI) China, and Changzhou Institute of Advanced Manufacturing Technology (Institute of Robotics and Intelligent Equipment, JITRI) China.

Last but not least, I would like to express my deepest gratitude to my dear parents, my dear parents-in-law and my dear sisters for their support and love. Thank my dear wife Juan and my two lovely kids Han and Jun for their love, great support and motivation.

Contents

Figure captions

Table titles

Nomenclature

$A,\ A(\delta)$	contact area
A_1	area of the microneedle bottom (m^2)
B_0	relaxed force (Equation (4-26)) (N)
$B_i, i = 1, 2, \cdots$	proportional constants (Equation (4-26)) (N)
c	compliance of the force transducer (m/N)
C_0	is related to B_0
$C_i, i = 1,2, \cdots$	proportional constants (Equations (4-25), (4-38)) (N)
CoD	coefficient of determination
d_1	autofocus starting point threshold
d_2	autofocus end point threshold
d_A	diameter of the lens (aperture) (m)
d_i	diameter of image circle in Equation (6-11) (m)
D	diameter of a single particle (m)
$e_t,\ e(t)$	random noise
E	Young's modulus (Pa)
E^*	reduced Young's modulus (Pa)
E_0	instantaneous Young's modulus (Pa)
E_∞	long-term Young's modulus (Pa)
E_H	apparent Young's modulus of microcapsules calculated

	using Hertz model by treating it as a homogeneous sphere (Pa)
E_S	Young's modulus of shell obtained from FEM core/shell model (Pa)
f	focal length of a lens (m)
F	force on particle (N)
F'	estimated force in the "3σ + window + Hertz" algorithm (N)
$\hat{F}$	predicted force from models (N)
F/ERh	dimensionless force
F_i	the ith force (N)
F_{MS}	force at maximum stress of microneedles (N)
F_r	rupture force (N)
F_s	smoothed force by Equation (4-50) (N)
$F(t)$	time-dependent force (N)
G	shear modulus (Pa)
G_0	instantaneous shear modulus (Pa)
G_∞	long-term shear modulus (Pa)
$G(t)$	time-dependent shear modulus (Pa)
h	shell thickness of a microcapsule (m)

h_0	height of the microneedle (m)
h'	height of the missing tip assuming the microneedle is perfectly sharp (m)
H	hardness (Pa)
I_B	intensity of background pixels in an image
I_F	intensity of foreground pixels in an image
I_H	intensity of in-focus particles in an image
I_0	intensity threshold in Equation (6-23)
$k,\ k'$	$k = 1/(k')^{2/3}$, used in the "3σ + window + Hertz" algorithm
k_e	coefficient in Equation (4-46)
le	elastic limit index
l_i	distance from the lens to the image sensor plane (m)
Δl_i	distance from the image plane to the image sensor plane (m)
l_o	work distance of a lens (m)
Δl_o	distance from an object to the work plane of a lens (m)
L	the range within which single particle appears in the field of view (m)
ΔL	difference of the length of one-dimensional material

	before and after deformation (m)
L_0	initial length of one-dimensional material before deformation (m)
LoR	limit of resolution (m)
m	starting point index
m_1	starting point index found by the "3σ" algorithm
m_2	starting point index found by the "3σ + window" algorithm
m_3	starting point index found by the "3σ + window + Hertz" algorithm
m'	estimated starting point index in the "3σ + window + Hertz" algorithm
Δm	values to compensate starting point index in the "3σ + window + Hertz" algorithm
ms	index of maximum stress
M	magnification of optical system (pixels/m)
n	index number in viscoelastic and viscoplastic analysis
n_1	related to the morphology of the tested microparticles but independent of the displacement in Equations (4-8) (4-9)
n_2	a real number standing for the power of displacement in

	Equations (4-8) (4-9)
Δn	probe position difference in pixel numbers (Equation (6-34))
N	number of data points
NA	numerical aperture of the lens
N_0	an integer set by the autofocus algorithm
$p_1,\ p_2,\ p_3$	coefficients in Equation (4-10)
Δp	moving distance of sample stage in Equation (6-34) (m)
ΔP_1	autofocus searching moving step (m)
ΔP_2	autofocus focusing moving step (m)
ΔP_3	autofocus fine-tuning moving step (m)
r	rupture point index
$r_1,\ r_2$	half side length of a quadrangular microneedle base and tip (m)
R	radius of a single particle (m)
s	sensitivity of the force transducer (N/V)
S_B	standard deviation of voltages in baseline
t	time (s)
t_R	time taken to compress a particle (Equation (17)) (s)
t_c	control loop time (s)

t_s	acquisition time (sampling time) (s)
T_c	toughness (Pa)
T_{MS}	toughness of microneedles determined by maximum stress (Pa)
T_r	nominal rupture tension (N/m)
v_1	autofocus searching (high) speed (m/s)
v_2	autofocus focusing (low) speed (m/s)
v_3	autofocus fine-tuning speed (m/s)
$v_c,\ v$	compression speed (m/s)
V_{MB}	volume of the microneedle body (m^3)
V_B	average voltage of baseline (V)
V_r	voltage at the rupture point (V)
$V(t)$	time-varying voltage (V)
$V(i),\ V_i$	the i^{th} sampled voltage (V)
w	width of moving window in data analysis

Greek Symbol

γ	the depth of field (m)
δ	displacement (m)
δ_b	displacement of the microneedle base (m)
δ_i	the i^{th} displacement (m)

δ_n	displacement of the microneedle body (m)
δ'	estimated displacement in the "3σ + window + Hertz" algorithm (m)
$\Delta\delta$	difference between the true displacement and the one obtained from the "3σ + window" algorithm (m)
δ_0	maximum displacement before relaxation (m)
δ_{MS}	displacement at maximum stress (m)
δ_r	displacement at rupture (m)
ε	fractional (nominal) deformation (ratio of the displacement δ to the initial diameter D of a microparticle, or ratio of the displacement to the initial height h_0 of a microneedle)
ε_{LE}	fractional deformation at elastic limit
ε_{MS}	fractional deformation at maximum stress
ε_r	fractional deformation at rupture
ε_Y	fractional deformation at pseudo-yield point
η	height of the microneedle from the top until sectional area $A(\eta)$ (m)
$d\eta$	element height at η (m)
λ	light wavelength (m)

ξ	strain
π	the ratio of the circumference of a circle to its diameter
σ	(nominal) stress (Pa)
σ_B	failure stress (Pa)
σ_{LE}	stress at elastic limit (Pa)
σ_Y	yield stress (Pa)
σ_{MS}	maximum stress of microneedles (Pa)
σ_r	nominal rupture stress (Pa)
$\tau_i, i = 1, 2, \cdots$	relaxation times (s)
$\Phi_i, i = 1, 2, \cdots$	ramp correction factors (Equation (4-28))
ψ	Poisson's ratio

Abbreviations

AC	acrylic copolymer
AF	autofocus
AFM	atomic force microscopy
BC	bacterial nanocellulose
CCD	charge-coupled device
CHT	circular Hough transform
CLSM	confocal laser scanning microscopy

CP	contact point
DC	direct current voltage
DCM	dichloromethane
DCPD	dicyclopentadiene
ESEM	environmental scanning electron microscope
FEA	finite element analysis
FEM	finite element model
FL	change of focus value over its moving average
FLP	focus lens position
FMF	focus measure function
FOV	field of view
FV	focus value
FVW	moving average of focus value in a time window
HA	hyaluronic acid
HSI	hue, saturation, intensity
HT	Hough transform
MBA	methylenebisacrylamide
MCS	mountain-climbing search
MeHA	methacrylated hyaluronic acid
MF	melamine-formaldehyde

MGF	melamine-glutaraldehyde-formaldehyde
MN	microneedle
MS	maximum stress
PDMS	polydimethylsiloxane
PEGDA	poly(ethylene glycol) diacrylate
PLA	poly (lactic acid)
PLGA	poly (lactide-co-glycolide)
PS	polystyrene
PS-DVB	polystyrene-co-divinylbenzene
PU	polyurethane
PUF	urea formaldehyde
RGB	red, green, blue
SC	stratum corneum
SE	standard error
SEM	scanning electron microscopy
TEM	transmission electron microscopy
UI	user interface
UoB	University of Birmingham
UTS	ultimate tensile strength

CHAPTER 1: INTRODUCTION

1.1 Background

Microparticles are usually referred to as particles with size in the range of 1μm to 1000 μm. They can be divided into biological and non-biological particles (Zhang et al., 2009). Animal cells, yeasts, pollen grains are instances of biological microparticles, while microcapsules, microspheres, granules are members of non-biological microparticles. They are widely used in many industrial fields like printing and imaging, chemical, agrochemical, food and feed, pharmaceutical and medical, cosmetic, and household care products (Zhang, 2016; Zhang et al., 2009). For example, microcapsules, which are made by coating the active ingredient(s) with wall (shell) materials, have been widely used to encapsulate perfumes (Fernandez-Gonzalez, 2011; Liu, 2010), inks (Kim et al., 2006), and drugs (Li et al., 2015) to protect, change form of, or control the release of the core component.

Among many fundamental properties of microparticles, the mechanical strength is considered to be essential as it links the other properties like physicochemical and structural properties (Gray et al., 2016). Understanding the mechanical strength of microparticles can provide crucial data for new particulate product development and production as well as help to optimize their efficiency and performance in end-use applications. For example, perfume microcapsules are usually added into detergents to give long-lasting nice smell on the cloths after washing (Fernandez-Gonzalez, 2011; Liu, 2010). The microcapsules should survive during various engineering processing steps from manufacture to washing machine, including

mixing with detergent, pumping and washing, but break via friction and rubbing between human body and the fabrics to release the perfume after drying to keep the cloths fragrant as long as possible (Fernandez-Gonzalez, 2011; Liu, 2010). Testing the mechanical strength of perfume microcapsules is one of the key requirements to make sure that the perfume is properly encapsulated for such scenarios. Furthermore, characterising the mechanical strength of other micro-sized materials, e.g., calcium alginate microspheres for tissue engineering (Nguyen et al., 2009) and dissolvable microneedles for drug delivery (Du et al., 2021a; Du et al., 2021b), is also essential to ensure their functionality and performance both in product development and end-use applications. Moreover, when new processes are introduced to fabricate microparticles, their mechanical properties also need to be determined and compared with their conventional counterparts to ensure their performance. For example, Fernandez-Gonzalez (2011) explored the mechanical strength of perfume microcapsules made by interfacial polymerisation to ensure their desired performances similar to those with a melamine-formaldehyde (MF) shell which were widely used before (Liu, 2010).

With the rapid development of particle technology all over the world, eco-friendliness has become one of the most important issues. More and more microparticles that are made from biodegradable, sustainable materials will be developed to replace their conventional counterparts. More and more functional materials will be produced in the form of microparticles to optimise their performance (Zhang, 2016). Techniques to determine the mechanical strength of microparticles, especially those of single microparticles, have played

an important role in the process of microparticle development and production, and are expected to become more and more popular in the future.

This project is based on an existing micromanipulation technique developed in the University of Birmingham (UoB), which was firstly designed by Zhang et al. (1991) to test the mechanical strength of single mammalian cells. Thereafter it has been widely used to test the mechanical strength of a range of single micro-particles or micro-sized materials, including rupture strength, elasticity, plasticity, viscoelasticity of chondrocytes (Nguyen et al., 2010), pollens (Liu & Zhang, 2004), microspheres (Wang et al., 2005; Yap et al., 2008), microcapsules (Sun & Zhang, 2001; Sun & Zhang, 2002), and microneedles (Du et al., 2021a; Du et al., 2021b). The technique has also been modified to quantify adhesion of fouling deposits (biofilm and food) to substrate and their cohesion under various processing conditions (Garrett et al., 2008; Liu et al., 2006a; Liu et al., 2006b).

Although the micromanipulation technique is powerful, it is quite time consuming and technically demanding in undertaking the measurement and data analysis. Therefore, an automatic measurement system including an automatic data analysis function needs to be developed to enhance its capability (Zhang et al., 2009).

1.2 Aim and objectives

This PhD project aims to improve the capability of the existing micromanipulation technique and also to characterise the mechanical properties of different kinds of micro-sized materials, including microcapsules, microspheres and microneedles using the improved

micromanipulation technique. It mainly has four objectives:

1) to develop a software package to analyse the rupture strength of micro-particles automatically from experimental data;
2) to incorporate mathematical models into the software package to determine intrinsic material properties of microparticles;
3) to develop a new control system to test microparticles automatically by combining an autofocus system, an image analysis system and micromanipulators; and
4) to investigate the mechanical properties of different micro-sized materials, including microcapsules, microspheres and microneedles.

1.3 Outline of the thesis

Chapter 2 Literature review. The existing micromanipulation technique is reviewed including evolution of the setup, types of tests and mathematical models for the data analysis. Previously available techniques relating to the automatic data analysis and automatic micromanipulation are summarised, and some typical micro-sized materials with functionalities are presented.

Chapter 3 Development of software for automatic analysis of microparticle rupture strength. A software package to determine the rupture strength parameters of microparticles from the experimental data obtained using the micromanipulation technique has been developed, including three algorithms to locate the starting point and one algorithm to locate the rupture point. The rupture strength results of two microparticle samples obtained from the

software package automatically are compared with those obtained manually to validate the capability of the software package developed.

Chapter 4 Development of a computer software package to determine the intrinsic material properties of microparticles. Some relevant mathematical models are summarised and the general forms of equations for the force versus displacement related to the intrinsic mechanical property parameters have been developed, based on which general approaches to extend the elastic and plastic analysis to viscoelastic and viscoplastic analysis, and general principles and strategies to incorporate these models into software have been developed. Several mathematical models have been incorporated into the developed software package to determine the intrinsic material properties including elasticity, plasticity, yield property and viscoelasticity.

Chapter 5 Mechanical characterisation of microneedles. Several batches of hyaluronic acid-based microneedles for drug delivery have been tested using the micromanipulation technique. Some mathematical models are developed to obtain the mechanical strength parameters from the experimental data, including mechanical strength at maximum stress, elastic parameters and viscoelastic parameters.

Chapter 6 Development of an automatic micromanipulation system. An automatic control system has been developed to autofocus, detect, test microparticles to determine their mechanical strength automatically. Algorithms for autofocus, particle detection from image processing are proposed. Experiments have been carried out to validate the developed system

by comparing its results with the existing micromanipulation system.

Chapter 7 Overall conclusions and future work. An overall summary of the PhD project is presented and conclusions are drawn. Possible approaches to further exploit the achievements of this project and improve the capability of the automatic micromanipulation system are proposed.

CHAPTER 2: LITURATURE REVIEW

2.1 Introduction

There are many properties of microparticles which need to be characterised, including physicochemical, structural and mechanical properties, which may be related to each other (Gray et al., 2016). Understanding the mechanical strength of microparticles plays an important role in ensuring their desirable performances during manufacturing, further processing and end-use applications (Mercadé-Prieto & Zhang, 2012).

To test the mechanical strength of microparticles, a number of techniques have been devised, which can be classified as ensemble and single-particle test methods (Gray et al., 2016; Zhang et al., 2009). Ensemble test methods are usually used to measure the mechanical strength of a population of particles and characterise their strength as whole, thus only average values can be obtained. In contrast, the single-particle test methods measure single particles one by one, thus the variation and distribution of their strength can be identified, which is essential to optimize their performance in many applications.

Several techniques have been developed to experimentally determine the mechanical properties of single particles, including pressure probe (Boyer & Kramer, 1995; Hüsken et al., 1978), micropipette aspiration (Heinrich & Rawicz, 2005; Shojaei-Baghini et al., 2013), optical/magnetic tweezers (Neuman & Nagy, 2008), atomic force microscopy (AFM) (Baykara & Schwarz, 2017; Bennig, 1988), and micromanipulation based on diametrical compression (Zhang et al., 1991; Zhang et al., 2009). The main difference among these

techniques lies in the magnitude of typical force which can be applied and the corresponding deformations that can be generated. The typical force generated by micromanipulation is from micro-Newtons to Newtons, while the others, e.g., AFM, are from pico-Newtons to micro-Newtons as illustrated in Figure 2-1 (Gray et al., 2016; Mercadé-Prieto & Zhang, 2012; Zhang et al., 2022).

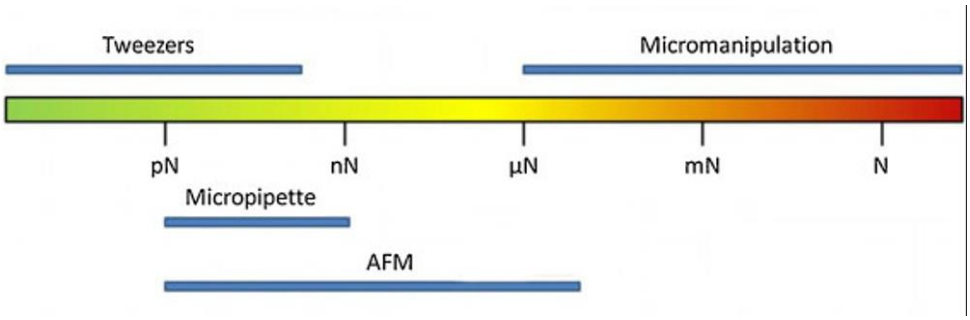

Figure 2-1 Typical available force ranges of single-particle measurement techniques (adapted from Gray et al., 2016)

The micromanipulation technique was firstly developed by Zhang et al. (1991) to test the bursting strength of single mammalian cells. It is based on diametrical compression of single microparticles between two parallel flat ends and can compress them into different deformations including rupture and therefore has been modified to test the mechanical properties including strength of a variety of biological and non-biological materials in the form of microparticles (Zhang, 2016). However, this technique relied on manual operations, which is time-consuming, laborious and technically-demanding. Ideally, automatic measurement that is more user-friendly and more powerful should be achieved (Zhang, 2016), which is the main objective of this PhD project.

A review of the micromanipulation technique is carried out in Section 2.2. The techniques involved in automatic data analysis and automatic micromanipulation are reviewed in Section 2.3 and 2.4 respectively. Some relevant micro-sized materials with desirable functionalities, which need to be mechanically characterised in this project, are reviewed in Section 2.5.

2.2 Micromanipulation technique

2.2.1. Evolution of the apparatus

2.2.1.1. Birth of the technique

The first version of the micromanipulation apparatus was developed by Zhang et al. (1991) to test the bursting strength of single mammalian cells as illustrated in Figure 2-2 (Zhang et al., 1992a; Zhang et al., 1991; Zhang et al., 1992b). Single cells from a culture medium were captured and compressed horizontally between two probes, one of which was fixed to a three-dimensional/axis micromanipulator, and the other was fixed to the output tube of a force transducer mounted to another three-dimensional/axis micromanipulator, to measure the force on the cell simultaneously during the compression. The compression process can be seen under the help of a microscope.

2.2.1.2. Modification to test adhesion and cohesion

Then the micromanipulation apparatus was modified by introducing a T-shaped probe to directly test the adhesive force of *Pseudomonas fluorescens* biofilms by pulling them horizontally as shown in Figure 2-3 (Chen et al., 1998; Chen et al., 2005). It was then used to measure the cohesive and adhesive strengths of food fouling deposits on their substrates (Liu

et al., 2002; Liu et al., 2006a; Liu et al., 2006b; Liu et al., 2006c), which provided vital information for cleaning processing equipment in food plants.

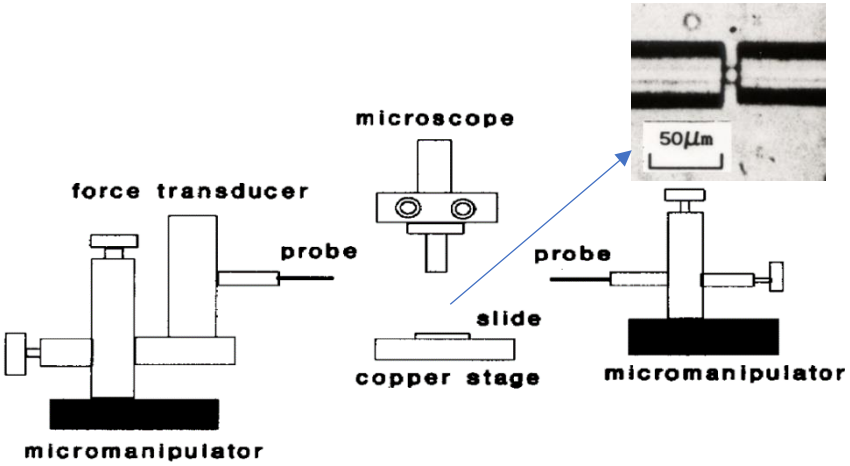

Figure 2-2 Schematic diagram of the first version of micromanipulation rig (Zhang et al., 1991; Zhang et al., 1992b)

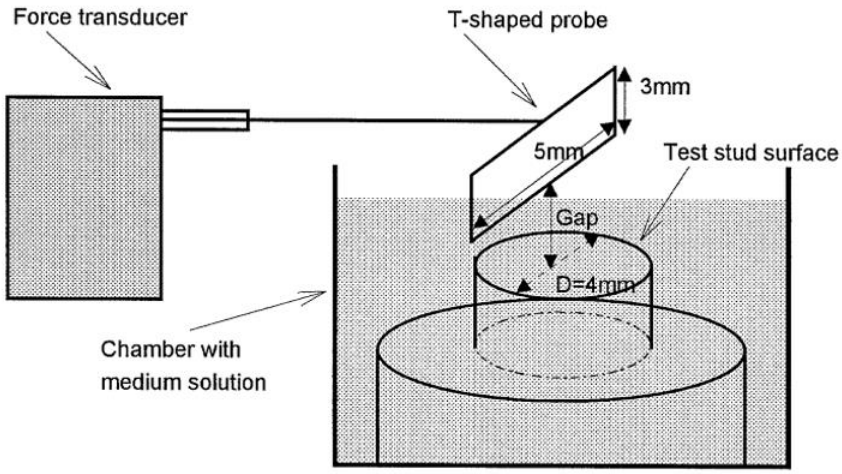

Figure 2-3 Schematic diagram of the T-shaped probe and the test stud surface (Chen et al., 1998)

2.2.1.3. Vertical compression version

A novel vertical compression version of the micromanipulation apparatus was developed to measure the rupture strength of individual yeast cells as shown in Figure 2-4 (Mashmoushy et al., 1998). There were two cameras for visulising single particle deformation under

compresison. The main difference between the versions described in last two sections and this new version is that the latter is vertical and the cells can be squeezed without the need to capture them from the slide, which simplifies the experimental procedures. Besides, both dry and wet single microparticles can be compressed, on the top surface of a slide and in a chamber filled with liquid respectively. (In contrast, the horizontal-compression versions cannot be used to test samples in a chamber whose vertical walls will prevent the probe from touching single particles inside it.) This setup has been widely used to test different kinds of microparticles, including microcapsules (Long et al., 2009; O'Sullivan et al., 2009; Pan et al., 2012; Sun & Zhang, 2001; Sun & Zhang, 2002; Zhang et al., 1999), microspheres (Müller et al., 2005; Nguyen et al., 2009; Olderøy et al., 2012; Yan et al., 2009; Yap et al., 2008), pollen grains (Liu & Zhang, 2004), yeast cells (Mashmoushy et al., 1998; Smith et al., 2000), and chondrocytes and chondrons (Nguyen et al., 2010; Wang et al., 2009).

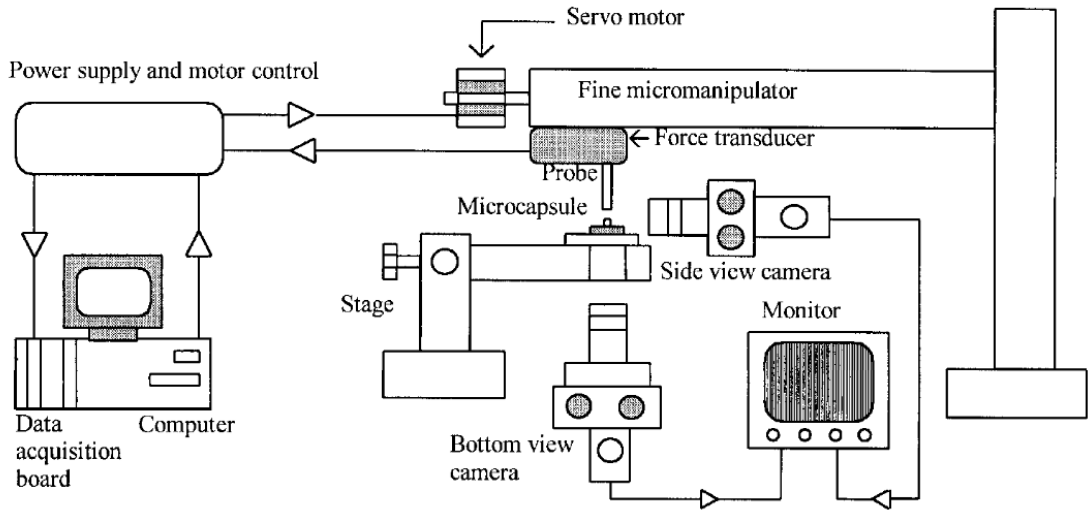

Figure 2-4 Schematic diagram of the vertical compression version of the micromanipulation apparatus (Mashmoushy et al., 1998; Sun & Zhang, 2001)

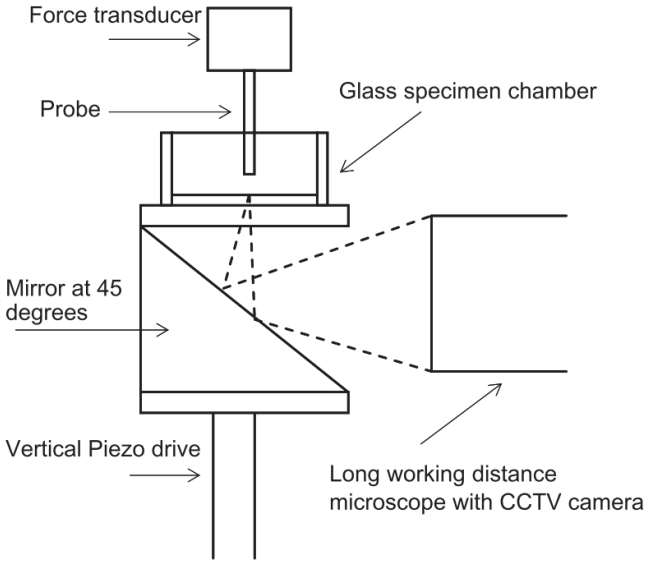

Figure 2-5 Schematic diagram of high-strain rate micromanipulation apparatus (Wang et al., 2005)

2.2.1.4. High-strain rate version

A high-strain rate version of the micromanipulation rig was developed that was very suitable to investigate the time-dependent behaviour of single microparticles using a piezo-stack drive that could move with high speeds potentially up to 10 mm/s as illustrated in Figure 2-5 (Wang et al., 2006a; Wang et al., 2005). Loading-holding and loading-unloading experiments can be carried out at different speeds to determine the time-dependent mechanical behaviours of single microparticles.

2.2.1.5. Novel single sideview-based version

A novel single sideview-based micromanipulation rig, which is a simpler and cheaper version of the one as illustrated in Figure 2-4, has recently been developed that can test the mechanical strength of single particles (Zhang et al., 2022) and this PhD project is mainly based on this version that will be described in detail in Chapter 6.

2.2.2. Type of experiments using micromanipulation technique

Usually, three types of tests can be carried out to characterise a microparticle sample thoroughly, including loading (compress), loading-holding (compress and hold) and loading-unloading (compress and release) tests (Fernandez-Gonzalez, 2011; Liu, 2010; Sun & Zhang, 2001).

2.2.2.1. Loading tests

In loading tests, single microparticles are usually compressed up to burst/fracture/rupture, during which the corresponding force versus displacement data are obtained. The typical force-displacement curve of a single particle during the loading tests is illustrated in Figure 2-6 (Yap et al., 2006). The force kept increasing from A where the onset of compression began, dropped at B where the particle was ruptured, and increased from C as the probe compressed the debris of the particle till D where the compression was completed.

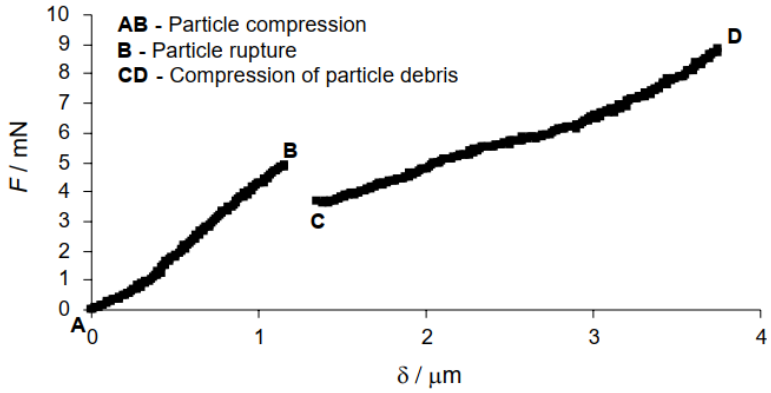

Figure 2-6 Typical force-displacement curve of an Eudragit® L100-55 particle (diameter: 20.0 µm) under loading tests (Yap et al., 2006)

From the force-displacement data obtained in the loading tests, the relationship between rupture strength parameters (rupture force, nominal rupture stress, etc.) versus diameter can be

determined and used to mechanically characterise the tested samples (Zhang et al., 1991; Zhang et al., 1999). Further analysis can also lead to determination of the intrinsic mechanical properties, e.g., Young's modulus by fitting the force-displacement data into theoretical models, e.g., the Hertz model, if applicable.

2.2.2.2. Loading-holding tests

In loading-holding tests, individual particles are usually compressed one by one to different deformations at different speeds and then held at constant deformation to let them relax, during which the force versus time data is recorded. A typical force-time curve of a single calcium alginate particle corresponding to the loading-holding tests is shown in Figure 2-7 (Zhao & Zhang, 2004). The force started to increase from A where the onset of compression began and kept increasing to B where the compression was stopped, from which the force relaxed to a certain value when the particle was held.

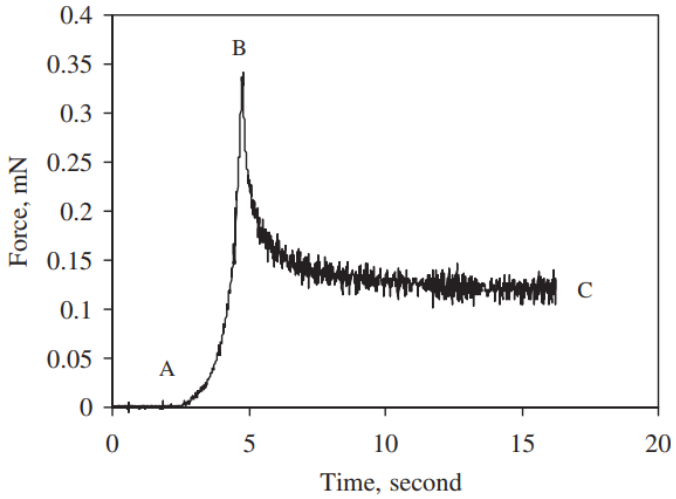

Figure 2-7 Typical curve of force and time during loading-holding tests of a calcium alginate particle (compression speed: 8μm/s, diameter: 28μm) (Zhao & Zhang, 2004)

The force relaxation during the holding of the microparticles indicates their viscoelastic

behaviour, and the corresponding force-holding time data can be fitted into viscoelastic models to obtain the intrinsic viscoelastic parameters of the tested microparticles (Wang et al., 2005; Wang et al., 2006b; Yan et al., 2009).

2.2.2.3. Loading-unloading tests

In loading-unloading tests, single particles are usually compressed to different deformations and the loads are released, from which the force versus displacement data is recorded. A typical curve of force and displacement data of a single melamine-formaldehyde (MF) microcapsule corresponding to the loading-unloading test is shown in Figure 2-8 (Sun & Zhang, 2001). The force increased during the compression and decreased when the compression was released. When compressed to small deformation (12%) within elastic range, only a marginal hysteresis was found and the force dropped to zero when the probe returned to the original position (Figure 2-8a). In contrast, when compressed to relatively large deformation (39%), significant hysteresis was found and the force dropped to zero before the probe returned to its original place because of the plastic deformation (Figure 2-8b).

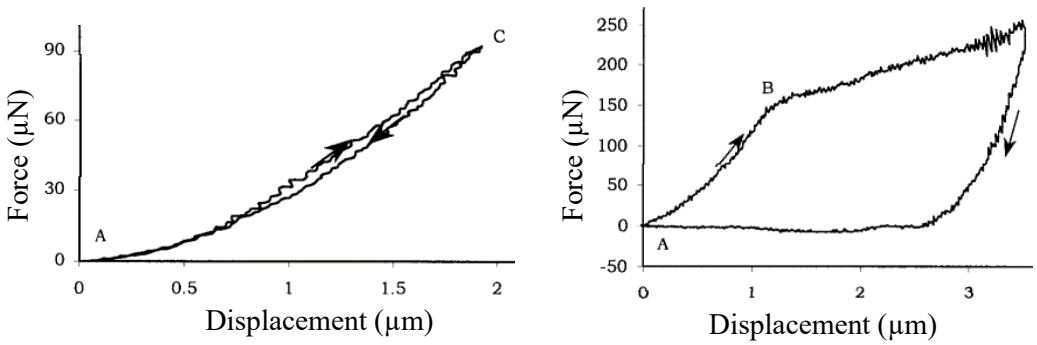

(a) Compressed to 12% fractional deformation (diameter 16.0 μm)

(b) Compressed to 39% fractional deformation (diameter 9.6 μm)

Figure 2-8 Force-displacement curves of single MF microcapsules generated from loading-unloading tests (Sun & Zhang, 2001)

The elastoplastic properties like the elastic limit (B in Figure 2-8b) can be determined by fitting the force-displacement data into elastic models (Mercadé-Prieto et al., 2011a; Mercadé-Prieto et al., 2011b) or by increasing the largest deformation gradually for each cycle until the plastic behaviour (i.e., permanent deformation) was observed (Liu, 2010).

2.2.3. Analyses of the experimental data from micromanipulation

With the data obtained from tests described in last section, different kinds of analysis can be carried out to characterise the mechanical property parameters of the tested microparticles.

2.2.3.1. Rupture strength analysis

In the rupture strength analysis, the points where the onset of compression and rupture occurred are determined first from the force versus displacement data and the rupture strength parameters including displacement at rupture, rupture force, fractional deformation at rupture, nominal rupture stress, nominal rupture tension and toughness can be determined from the force versus displacement data obtained from compression up to burst/fracture/rupture in loading tests (Zhang et al., 2022). The relationship between rupture strength versus diameter of single particles can be established, which provides important data to compare the mechanical strength of microparticles from different samples prepared under different formulation and processing conditions. For example, the mechanical strengths of two microcapsule samples were compared using burst force (rupture force) versus diameter by Zhang et al. (1999).

However, the aforementioned rupture strength property parameters are not intrinsic. They can

depend on the diameter (Zhang et al., 2009). Therefore, some useful mathematical models, including analytical and numerical, are introduced to determine the intrinsic mechanical property parameters of microparticles using the data from the micromanipulation tests.

2.2.3.2. Hertz analysis

Hertz theory provides a model for single spherical particles compressed between two rigid flat surfaces, which can be used to determine their Young's modulus by fitting the force-displacement data corresponding to small deformations in elastic range to the model (Zhang et al., 2009).

When using the Hertz model, the particle should be spherical, linear elastic, has a Young's modulus value far less than that of the two flat surface materials, and has negligible friction with the end surfaces. Although it was found that the Hertz model is in good agreement with experimental results using nominal strain up to 30% in some microparticles like calcium alginate spheres (Liu et al., 1998; Wang et al., 2005; Yan et al., 2009), it is usually applied to describe force versus displacement data corresponding to small deformations with a nominal strain less than 10% (Zhang et al., 2009).

2.2.3.3. Tatara analysis

To determine the elastic modulus of microparticles in the range of large deformation (nominal strain up to 60%), the Tatara model can be used (Zhang et al., 2009) by fitting the force-displacement data in the elastic range into it. When using the Tatara model, the tested particle should be homogenous and spherical.

The Tatara model can be considered as an extension from the Hertz model by removing the limitations on small strain and linear elasticity. However, for a given force, the displacement calculated using the Tatara model is always smaller than that of using the Hertz model (Zhang et al., 2009). It was also found that the Young's modulus value obtained with the Tatara analysis is strain dependent for nonlinear elastic materials, i.e., its value can vary with the strain (Liu et al., 1998).

2.2.3.4. Viscoelastic Analysis

Some particles show a time-dependent behaviour, i.e., in loading-holding test the force decreases notably with the time during holding, which may be due to viscoelasticity or loss of liquid. For viscoelastic materials when water loss is negligible, a viscoelastic model can be used to determine their material properties, including the relaxation times, the instantaneous and long-term shear moduli (related to the instantaneous and long-term Young's moduli) by fitting the force-time data during the relaxation (holding) to the model (Yan et al., 2009; Zhang et al., 2009).

Yan et al. (2009) studied the viscoelastic properties of agarose microparticles with a narrow size distribution and found that the average Young's modulus value (E) for a given microparticle from the Hertz model was between the values of the instantaneous Young's modulus (E_0) and long-term Young's modulus (E_∞) but more comparable with the latter. This is reasonable as for viscoelastic materials the instantaneous Young's modulus corresponds to the response of the extremely fast loading during which no stress relaxation occurs, whilst the

long-term Young's modulus corresponds to the response of the infinitely slow loading so that there is a sufficient period of time for the force to relax during compression. That the Young's modulus value from the Hertz model was more comparable with the long-term value suggested that the compression speeds were relatively slow so that considerable viscous force relaxation occurred.

2.2.3.5. Finite element model (FEM) to determine the elastic properties of microcapsules

Mercadé-Prieto et al. (2011b) developed a model based on FEM simulation that can be widely used to determine the intrinsic mechanical properties of microcapsules with a core/shell structure, compressed between two parallel flat plates. In this model, the microspheres were modelled as unswollen impermeable spheres full of liquids without any elasticity and the shell was modelled as linear elastic. The Young's modulus of the shell material and the shell thickness can be determined by fitting the experimental force profile to the simulation results from the FEM. However, the fitting is not easy to be carried out automatically. A method was introduced by Zhang (2019) to determine the Young's modulus of the shell material and shell thickness using Microsoft™ Excel Solver, which will be presented in Chapter 4.

This core/shell model based on FEM simulation results by Mercadé-Prieto et al. (2011b) is basically extended from the Hertz model and should usually be used for the elastic deformation where the fractional deformation is less than 0.1 as plastic behaviour usually happens in the range of 0.11 to 0.19, e.g., for microcapsules with a shell of MF (Sun & Zhang, 2001; Sun & Zhang, 2002).

2.2.3.6. Finite element model to determine the yield stress of microcapsules

To understand the whole behaviour of microspheres with a core/shell structure before rupture, a FEM based elastic-perfectly plastic model was proposed by Mercadé-Prieto et al. (2011a). The core/shell wall was modelled as a linear elastic material followed by a perfectly plastic regime. The dimensionless force versus fractional deformation profiles from the elastic-perfectly plastic model and fully elastic model are illustrated in Figure 2-9a. Three methods were introduced to estimate the yield stress of the shell from the slope of the dimensionless force (F/ERh) varying with yield stress ratio (σ_E/E) at a given fractional deformation (0.3-0.45) corresponding to plastic deformation for MF microcapsules since their relationship is linear based on the FEM simulation results (Figure 2-9b), the pseudo-yield point ε_Y (where the force-displacement curve changes from concave to convex), and the elastic limit ε_{LE} (where the predicted force from elastic model starts to deviate from the experimental force data continuously) respectively as illustrated in Figure 2-9a.

A method was proposed by Zhang (2019) to calculate the yield stress from Young's modulus and the elastic limit based on the FEM simulation results by Mercadé-Prieto et al. (2011a). Briefly, the force-displacement data up to 10% fractional deformation was firstly fitted into the FEM simulation results for core/shell structured microcapsules and the elastic parameters including the Young's modulus of the shell material, and the shell thickness are obtained, from which the theoretical force data are predicted. Then, the elastic limit is determined where the predicted force deviates from the experimental force continuously and the yield stress can be

obtained using the stress corresponding to the elastic limit.

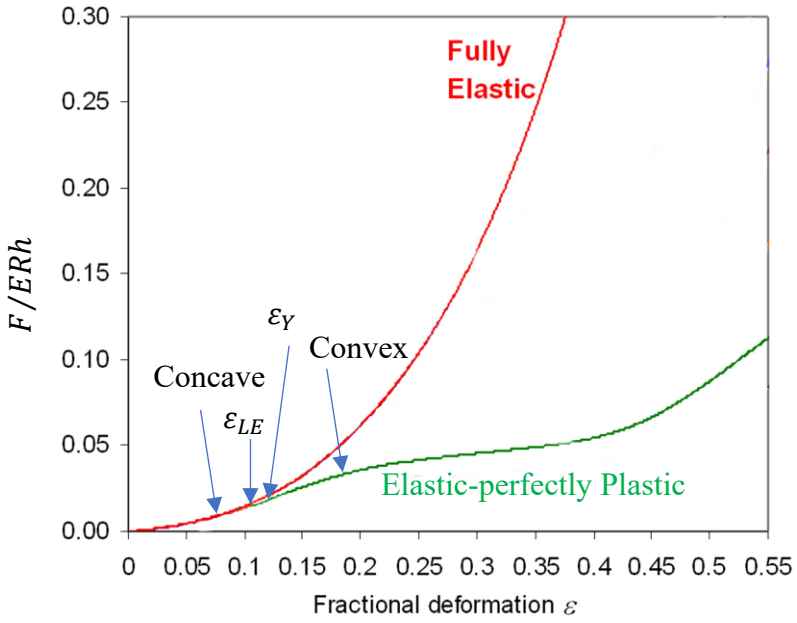

(a) Dimensionless force F/ERh versus fractional deformation ε profiles from fully elastic model and elastic-perfectly plastic model and pseudo-yield point ε_Y and elastic limit ε_{LE}

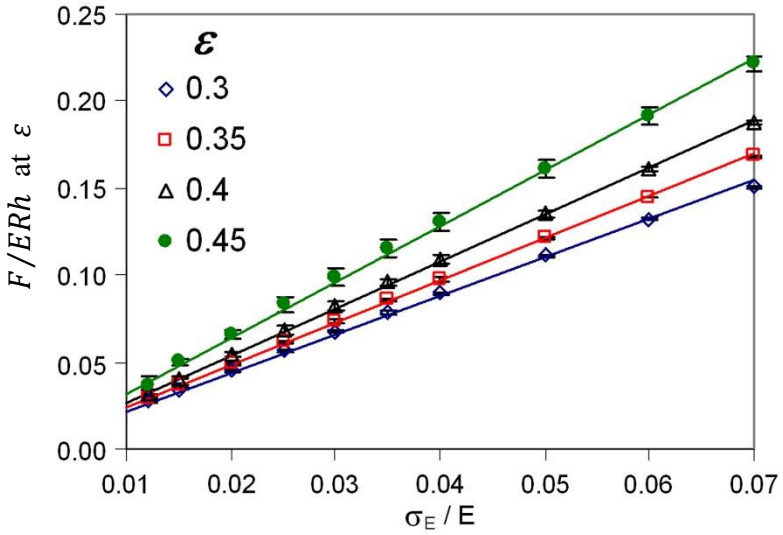

(b) Dimensionless force F/ERh at different fractional deformations ε from simulations with different yield stress ratios σ_E/E. Points are the average of values of 7 h/R ratios between 0.6% and 9.1%, error bars represent the standard deviation

Figure 2-9 Different methods to determine yield stress of microcapsules (Mercadé-Prieto et al., 2011a)

2.2.3.7. Abbott & Firestone model for plastic analysis of microspheres

Abbott & Firestone (1933) model can be used to determine the hardness of a homogenous spherical microparticle normally compressed between two flat ends from the slope of the linear region of force-displacement data corresponding to plastic deformation (Yap et al., 2008). The contact area in this model is simply estimated from the intersection of the flat surface with the original undeformed microsphere which overestimates the contact area (Paul et al., 2014) and continuously underestimates the hardness especially in the range of large strains (the maximum contact radius is bigger than $0.2\,R$) (Yap et al., 2008).

2.3 Techniques involved in automatic analysis of experimental data from micromanipulation

2.3.1.1. Introduction

The raw data from the micromanipulation technique is a series of voltage versus sampling time and the force can be calculated using the voltage and sensitivity of the force transducer (Mashmoushy et al., 1998). A typical raw experimental data of the voltage and force versus sampling time of a single yeast cell in the suspension during the loading test is illustrated in Figure 2-10 (Mashmoushy et al., 1998). The force remained stable from A' as the probe moved in the suspension and increased from A where the onset of compression started, then kept increasing till B and dropped significantly to C as the cell ruptured. Then the force increased from D when the probe compressed the debris of the cell and decreased from E to F as the probe withdrew to its original position.

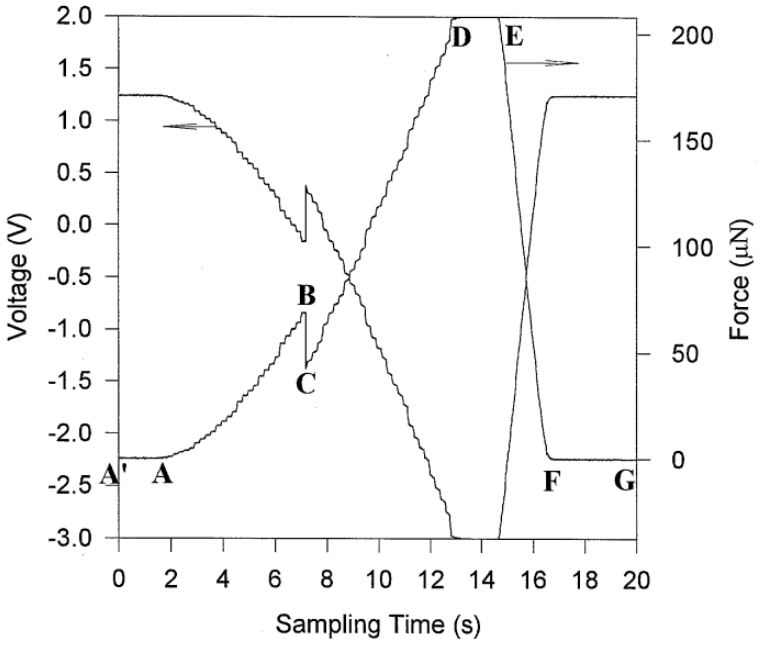

Figure 2-10 A typical curve of the raw voltage and force versus sampling time during compressing a yeast cell (Mashmoushy et al., 1998)

The displacement data can be calculated from the voltage data and the compression speed, acquisition frequency, sensitivity and compliance of the transducer (Mashmoushy et al., 1998). Thus, the data of force versus displacement can be obtained and used for post analysis to determine the intrinsic mechanical property parameters from different mathematical models as reviewed in Section 2.2.3.

Before calculation, some key points need to be identified, such as the starting point at which the probe starts to touch the surface of the microparticle (A in Figure 2-7 and Figure 2-10), rupture point at which the microparticle is ruptured or fractured (B in Figure 2-10) in loading tests, and peak force point at which the holding begins (B in Figure 2-7) in loading-holding tests. In the past, they were selected by manually inspecting the raw data followed by interacting with spreadsheet templates to obtain the force-displacement data and rupture

strength parameters, which was quite laborious and time-consuming. Algorithms need to be developed to identify these key points automatically. The rupture point can be determined where the voltage dropped most significantly and the peak force point in loading-holding test can be identified as the maximum value of the voltage series. In contrast, determination of the starting point is relatively difficult because of the relatively low signal-noise ratio around it. Thus, the following review of this section will focus on techniques involved to locate the starting point.

*2.3.1.2. Algorithms to identify contact point of experimental data from AFM***

Automatic analysis of experimental data from other techniques also involves the determination of key points, e.g., the contact point (CP) in force data from AFM tests. Several algorithms have been developed to locate the CP of AFM data, which can be inspiring in the new algorithm development for micromanipulation data analysis. They can mainly be summarised as thresholding-, linear regression-, and model fitting- based methods, etc. Monclus et al. (2010) introduced an algorithm based on a predefined threshold level (typically 0.1%) above the constant voltage in pre-contact region to locate the CP from the approach curve. But the threshold needed adjusting manually according to the baseline and noise, thus it is not proper to be used for automatic analysis. (BenÍtez et al., 2013) proposed an algorithm based on local linear regression and used the slope changes to detect the CP. To make it work, three parameters needed to be properly tuned, including the data length for regression and two thresholds to distinguish slope changes caused by true signal from the noise. Chang et al. (2014)

developed an algorithm to estimate CP by fitting the data in a linear elastic region into a Hertz like model. Based on the well-adjusted parameters for the nano indentation data of the tested linear elastic materials, the algorithm worked well but can require new sets of parameters for other materials.

Moreover, in AFM force data analysis, usually a force map, e.g., 64×64 force curves are obtained for a single particle to yield spatial distribution of mechanical property parameters. These algorithms above are aimed to locate the CPs for the force curves from testing single particles so that the parameters set for the algorithms may not need to be adjusted frequently for every force curve. In contrast, in micromanipulation, a single voltage (force) curve is obtained for a single particle and usually the particles in a sample have different sizes and mechanical strength values so that the parameters set may need to be modified frequently for each dataset to ensure the algorithms (mentioned in last paragraph) work properly for every single particle from a sample. Therefore, the algorithms for AFM are not suitable for automatic analysis of the force versus displacement data obtained by the micromanipulation technique directly.

(** **N.B.** This section is adapted from our published paper (Zhang et al., 2022) whose primary author was the author of this PhD thesis.)

2.3.1.3. The three-sigma rule

Substantially, detection of the starting point where the onset of compression begins (the same as CP) requires identification of the change from one state to another state in the voltage series.

The three-sigma rule has been used. Let X be a real random variable with mean X_{mean} and variance X_{SD}^2. If the distribution of X is unimodal, i.e., the distribution of X permits a Lebesgue density that is non-decreasing up to a mode and non-increasing thereafter, then the probability (Pr) for X falling away from its mean by more than three times of standard deviation is at most 5% (Pukelsheim, 1994),

$$\Pr\left(|X - X_{mean}| \geq 3X_{SD}\right) \leq 0.05 \qquad (2\text{-}1)$$

In the case of a normal distribution for random noise, the probability is at most 0.27% (Ha, 2005),

$$\Pr\left(|X - X_{mean}| \geq 3X_{SD}\right) \leq 0.0027 \qquad (2\text{-}2)$$

Following the three-sigma rule, the point from which the voltage starts to differ from the mean value of the baseline by three times of standard deviation may be selected as the starting point.

2.4 Techniques involved in automatic micromanipulation

As was pointed out by Zhang et al. (2009), "although it is powerful, micromanipulation is very technically demanding, time consuming and not easy to use. Semi- or full automation of micromanipulation equipment should enhance its popularity." In order to achieve automatic micromanipulation, some essential functions need to be developed, e.g., auto focusing on specimen, specimen auto detection and motion control. The related techniques are reviewed in the following sections.

2.4.1. Autofocus (AF)

2.4.1.1. Active or passive

Autofocus is an important technique in modern image and video systems, like digital camera and electric microscopy, which can automatically tune the sharpness of the object to ensure in-focus images. There are three kinds of autofocus techniques: active, passive and the hybrid of the two (Zhang et al., 2018b).

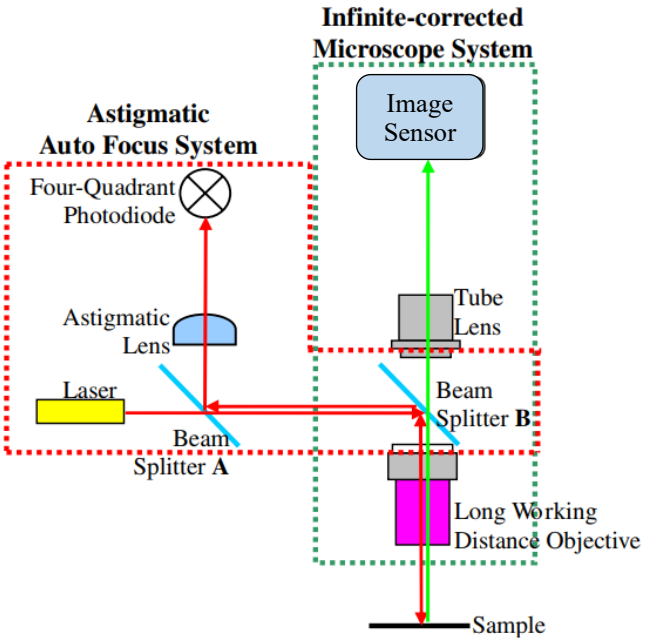

Figure 2-11 The optical layout of the astigmatic auto-focus microscope system (Hsu et al., 2009)

In active autofocus, a beam of ultrasonic waves or infrared light, etc. is used to detect the distance of the object before adjusting the lens to let the object fall into the focal plan (Hsu et al., 2009; Zhang et al., 2019). Figure 2-11 illustrates a fast active autofocus microscopy system based on astigmatic approach (Hsu et al., 2009). A subsystem including an infrared laser beam, an astigmatic lens, two beam splitters and a four-quadrant photodiode were used to detect the

defocus distance of the sample and a stepping motor was used to adjust the microscope system to focus the sample automatically. However, the focus error signal detected by the four-quadrant photodiode was not linear with the defocus distance and the working range was ±50μm for a 20× objective.

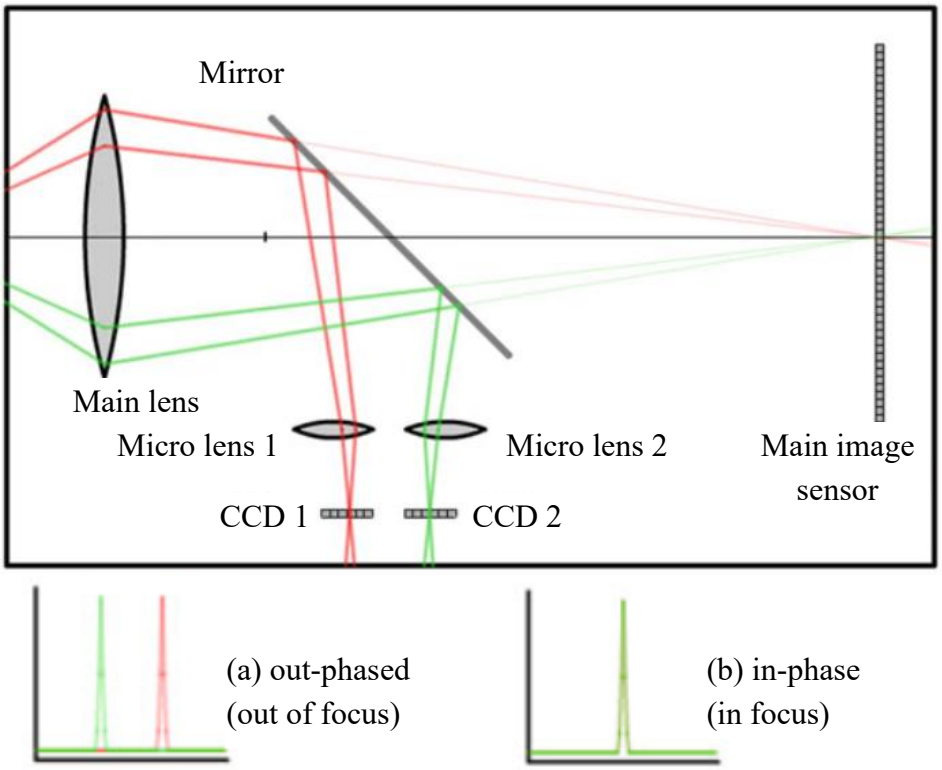

Figure 2-12 Schematic diagram of a phase detection-based autofocus system (Israni et al., 2016)

Unlike active autofocus that sends out light or sound beams to estimate the distance of the subjects, passive autofocus only utilizes the information that enters into the system to adjust focus states. Passive autofocus can be divided into phase detection-based method and contrast detection-based method. The focus state is determined by detecting the deviation between two incident images in the former method (Sasakura, 1999) while by comparing the sharpness among each frame in the latter (Chen et al., 2010; Xu et al., 2014). Figure 2-12 illustrates one

autofocus system schematically based on phase detection (Israni et al., 2016). The focus state was estimated from the correlation between the two images formed from a pair of small sensors (CCD 1 and CCD 2) which are usually one-dimensional looking at one part of the FOV of the main image sensor as illustrated in (a) and (b) in Figure 2-12.

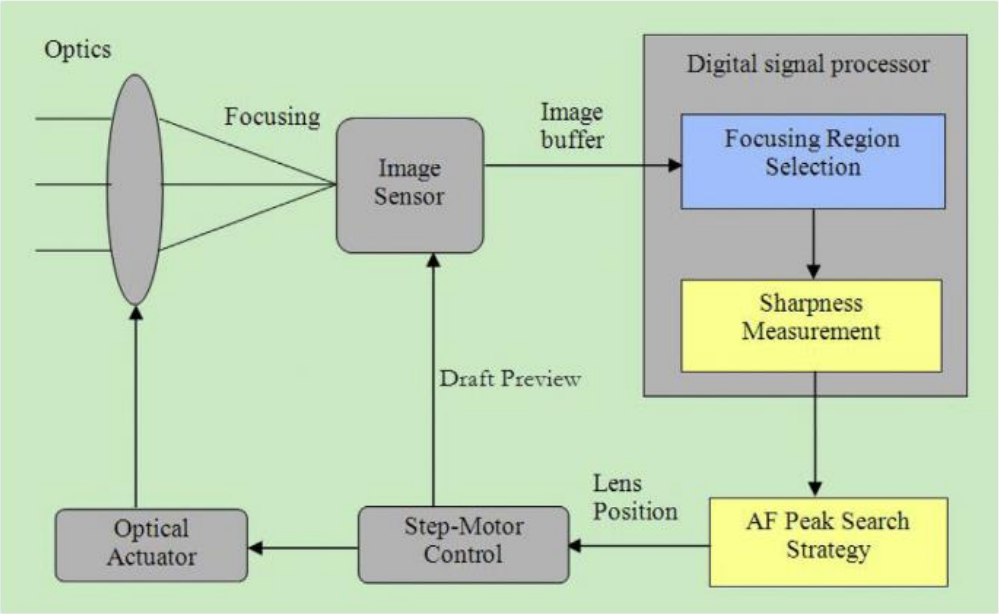

Figure 2-13 Typical diagram of contrast-based autofocus system (Xu et al., 2014)

A typical diagram of contrast detection-based autofocus system is illustrated in Figure 2-13 (Xu et al., 2014). Unlike phase detection-based autofocus system, it only contains the main image sensor system without other small sensor systems and uses the images obtained from the main sensor system to focus. After a frame (image) is obtained, a value of sharpness measurement is calculated from the selected region and a peak search algorithm is used to search the in-focus position by driving the step motor to move the optical actuator.

Under the help of an extra subsystem to measure the distance between the lens and the object, active autofocus can work under low illumination conditions, but cannot focus through

windows of glass, because ultrasonic sound and infrared light can be reflected by the glass which will result in misfocusing (Kehtarnavaz & Oh, 2003). Passive autofocus does not have such problems but needs enough illumination. As to the two passive methods, phase detection is usually faster as it can determine the precise de-focus distance from the phase detection system. However, if the phase detection system is out of alignment with the main image sensor system, it will end up with consistent misfocusing (Dflux & Kedves, 2022). The contrast detection is generally more accurate because the images used for focusing are obtained just from the main image sensor system (Zhang et al., 2018b) and needs no extra hardware.

2.4.1.2. Focus measure function

In contrast detection-based autofocus system, a focus measure function (FMF) is used to measure the sharpness of each frame, from which the focus state can be determined. Mir et al. (2014) carried out a thorough comparison among many different kinds of FMFs and found that Brenner FMF and squared gradient FMF performed quite well in digital images. The Brenner FMF will be used in this project.

2.4.1.3. Search algorithms

In autofocus, a search algorithm is used to search the best in-focus position based on the focus value (FV) of each frame. It can be divided into mountain-climbing search (MCS), Fibonacci search, global search, and machine learning based search, etc. (Zhang et al., 2018b).

The basic MCS algorithm determines the direction of moving by comparing FVs between two sequential frames and keeps climbing until the current FV value is smaller than the last one,

which suggests the mountain top is crossed as illustrated in Figure 2-14 (Fu et al., 2015). It is mainly used to focus on static objects and may result in misfocusing when the object is moving or under vibration. Ooi et al. (1990) introduced an adaptive MCS algorithm based on quasi condition reasoning by comparing the real time FV with its moving average together with the change of the latter, which acted well in the presence of disturbance. But MCS is usually slow to get high accurate focusing. Fu et al. (2015) proposed a three-step MCS that increased both the efficiency and accuracy of autofocus based on the variance and Brenner function of the images. The parameters to obtain the step lengths may need to be changed with the objects to be focused.

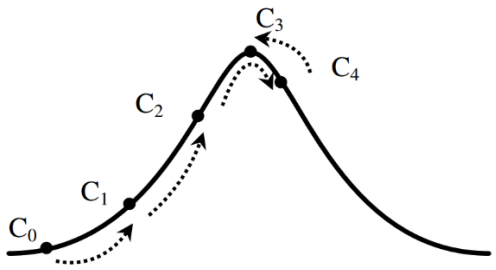

Figure 2-14 Basic MCS search algorithm (Fu et al., 2015)

The Fibonacci search algorithm is based on the unimodal assumption of focus profile and continuously narrowing the search region by subdividing it according to the Fibonacci sequence (Marrugo et al., 2014; Xiong & Shafer, 1993). The search is easily trapped in local maximum.

The global search goes through every lens step to get the optimal focus position so that it is quite time consuming, but it guarantees good focus (Marrugo et al., 2014).

Machine learning based search methods (Mir et al., 2015; Pinkard et al., 2019) can locate the

best focus position if they are well trained, therefore can be very fast and accurate. But one essential problem of machine learning is that it needs a large training set that should be representative and thorough to get an optimum model that can be generalised into any concrete application scenario.

2.4.2. Image processing

When an image of microparticles is focused, the subsequent work is to process it to automatically detect and locate the in-focus single particle(s). Once the location and size of a single in-focus particle is determined, it will be moved to under the force probe by the sample stage. Then the compression will begin automatically. To detect and locate the in-focus particle as well as estimate its size, several important image processing operations need to be carried out, including pre-processing, segmentation, and object detection.

2.4.2.1. Image pre-processing

Image pre-processing usually includes format converting and image filtering. Format converting is to convert the image from colour to grayscale or convert between different colour formats, like RGB (red, green, blue) and HSI (hue, saturation, intensity) (Davies, 2017). Image filtering involves the application of useful functions, e.g., Gaussian Smoothing, to suppress noise or other artefacts or to enhance the image (Davies, 2017). As most subsequent operations like Canny edge detection operator in segmentation include the function of smoothing, the details of filtering will not be studied in depth here.

2.4.2.2. Image segmentation

Image segmentation is to divide the image into several non-overlapped sub-regions within which the pixels are similar according to some criteria, like intensity, colour, and texture. Segmentation is essential since many subsequent operations, like object detection and feature extraction depend on its quality (Mohanta & Sethi, 2012). Image segmentation algorithms can be divided into several categories, like thresholding, edge detection and clustering.

Thresholding an image at a suitable intensity level is one of the simplest ways to carry out segmentation. However, it turns out to be quite difficult to implement as finding a suitable threshold is not easy in practice. Fortunately, there are many rigorous mathematical-based methods that can select the threshold more thoroughly and automatically, such as histogram-based thresholding (Otsu, 1979), variance-based thresholding and entropy-based thresholding (Davies, 2017).

Edge detection divides an image by observing the changes in intensity or pixels of the image (Gurusamy et al., 2014). Edge detection uses a moving window to convolute with the pixels all over the image to estimate local intensity gradients. The moving window is termed as a convolutional mask for an edge operator. There are a variety of edge detection operators, such as Prewitt operator, Robinson operator, Sobel operator, and Canny operator (Davies, 2017). Sobel operator and Canny operator are two of the most popular ones. Canny operator is entirely principled, fully integrated and reliable (Davies, 2017) and thus will be used in the thesis.

Clustering is the process of finding similarities in data sets so that they can be grouped (Zheng

et al., 2018). Clustering-based segmentation divides an image into subareas using clustering algorithms into the pixels. K-means is one of the widely used clustering algorithms in image segmentation. It iteratively gathers the pixels into different clusters according to the selected measurement distance until the cluster centres no longer change or reach the set number of iterations (Yuheng & Hao, 2017). K-means can be implemented without knowledge of the image but the number of clusters needs to be assigned before segmentation.

2.4.2.3. Object detection

Object detection involves finding instances of objects like humans, cars, dogs in the images. Objects in real world are usually projected into some shapes of the image that can be characterised by lines, circles, blobs etc. For example, microspheres are projected into circles by the sideview camera.

Circular Hough transform (CHT) is the specialised HT (Davies, 2017) used to detect circles based on voting schemes. It was used to detect sizes of nanoparticles in transmission electron microscopy (TEM) images reliably (Meng et al., 2018; Mirzaei & Rafsanjani, 2017). However, HTs are so time-consuming in computation that it is not proper to be used in real-time applications like the automatic micromanipulation system to detect microparticles while the sample stage is moving.

Wei et al. (2019) proposed a machine vision-based approach to detect nanoparticles in microscopy images by using a minimum external rectangular boundary box to locate the nanoparticles. It was claimed to be fast and of high precision. But the size of the minimum

external rectangular boundary box needs to be optimised based on the knowledge of the sample. Besides, it seemed not able to deal with overlapped particles.

Blob detection has been widely used to detect objects of interest, including in medical image processing (Han & Uyyanonvara, 2016; Xu et al., 2019) and intelligent visual surveillance (Nguyen & Chung, 2009). Blobs are connected areas in a binary image, which are different from its surroundings (Han & Uyyanonvara, 2016). They are very likely to contain the real objects of interest, i.e., objects can be extracted from the blobs based on some features, such as its area and perimeter (Kulpa, 1977). Blobs can be detected from the binary image using the connected component labelling algorithm (He et al., 2017). A blob can provide a lot of information, such as area, centre of gravity, edge points and boundary rectangle, which can be used to extract useful objects from the image.

2.5 Mechanical characterisation of some typical micro-sized materials using micromanipulation technique

2.5.1. Microcapsules

2.5.1.1. Different types of microcapsules and their properties

Microcapsules are capsules in the size of 1-1000μm made by coating the active ingredient(s) with wall (shell) materials to protect, change form of, or control the release of the core component (Whelehan & Marison, 2011; Zhang et al., 2009). They can be classified as simple (single-core and single-shell), multicore, multi-shell, and irregular microcapsules as shown in Figure 2-15 based on their structure forms (Bakry et al., 2016; Whelehan & Marison, 2011)

and they can be fabricated using several techniques including interfacial polymerisation, in-situ polymerisation, coacervation, solvent evaporation, fluidized bed coating, extrusion, spray drying, and spray cooling (Jyothi et al., 2010; Whelehan & Marison, 2011).

Microcapsules have found ever increasing applications in many industrial fields, including printing and imaging, chemical and agrichemical, food and feed, pharmaceutical and medical, cosmetic and household (Zhang et al., 2009) and smart functional materials (e.g., self-healing and self-sensing microcapsules for smart structure composites) (Althaqafi et al., 2020; Mishra et al., 2018).

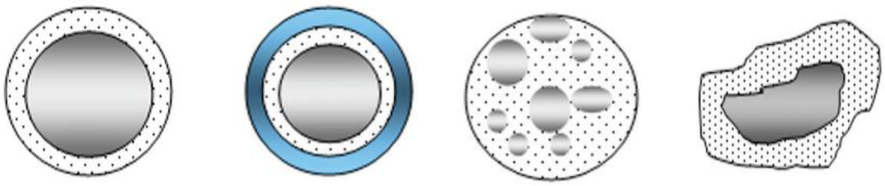

(a) simple (b) multi-shell (c) multi-core (d) irregular

Figure 2-15 Different types of microcapsules (Whelehan & Marison, 2011)

Microcapsules should have desirable fundamental properties, including physicochemical, structural, mechanical and thermal properties to optimise their performance from the manufacturing, to further processing, storage and end-use applications (Choudhury et al., 2021; Gray et al., 2016) and these properties usually relate to each other. Physicochemical properties, including size and size distribution, surface roughness and morphology, chemical composition, and surface charge and zeta potential usually determine their flow properties, payload, adhesion, and aggregation. Structural properties including shell thickness, pore size, crystallinity of microcapsules can affect the flowability, dispersibility, permeability and

mechanical strength. The mechanical strength of microcapsules is usually determined by the chemical composition, the structure of wall materials, the size and shell thickness of the capsules. Thermal properties (glass transition temperature and melting point) can determine the storage stability and the release rates of microcapsules as well as affect their mechanical strength under different temperature conditions (Choudhury et al., 2021). The crystallinity is also intrinsically linked to thermal properties. Although all the properties are important, some of them are dominant in given applications, e.g., optimised mechanical strength is essential for fragrant microcapsules in detergents and desirable shell porosity is most important for microcapsules for controlled-release drug delivery (Gray et al., 2016). There are some other properties of microcapsules including solubility, hygroscopicity, surface hydrophobicity and hydrophilicity, and stability under heat and light, which are also very important, especially for special products with added functionalities (Choudhury et al., 2021; Mendanha et al., 2009). They can determine the processing and storage conditions as well as the release behaviour of the microcapsules.

Fully understanding these properties is essential to produce microcapsules with required quality and there are many techniques to fulfil this task, which were summarised by Gray et al. (2016) and Choudhury et al. (2021). For example, optical microscopy can be used to characterise the size and size distribution of microcapsules, and scanning electron microscopy (SEM) can be used to determine the size, the surface roughness and morphology, and shell thickness of microcapsules. TEM can be used to determine the shell thickness more precisely

than SEM. AFM can be used to characterise the surface roughness and mechanical properties of microcapsules and their adhesion on surface. As to characterisation of their mechanical strength, bulk methods including loading a population of microcapsules with shear force, compression force or osmotic pressures are used but only average parameters can be obtained (Gray et al., 2016; Zhang et al., 2009). To obtain the variations among individual microcapsules, optical tweezers, shear flow, micropipette aspiration, AFM and micromanipulation based on diametrical compression are widely used to determine the mechanical properties of single microcapsules (Gray et al., 2016; Zhang et al., 2009). As aforementioned in Section 2.1, micromanipulation can provide relatively strong load to compress single microcapsules to any deformation (including to rupture), whereas the other techniques can generate only small deformations of microcapsules, as their loading scales are significantly smaller (Neuman & Nagy, 2008).

2.5.1.2. Microcapsules for self-sensing

Microcapsules for self-sensing (Aniskevich et al., 2020; Maia et al., 2014; Zheng et al., 2020) are usually incorporated into functional structural materials to form smart composites that can automatically detect microcracks without additional detection equipment/sensors, e.g., piezoelectric sensors (Rana et al., 2016). Therefore, the initial damage can be identified and repaired before deteriorating catastrophically.

Microcapsules for self-sensing should have high thermal resistance, adequate chemical and mechanical stability, and long shelf life, to optimise their performance. Among them, similar

to microcapsules for self-healing (Hu et al., 2009), optimised mechanical strength is essential for the self-sensing microcapsules. They should be mechanically strong enough to survive different engineering processing steps leading to incorporation into composites but weak enough to break as soon as microcracks are occurring to indicate the need for repair. Thus, precise determination of their mechanical strength is crucial to optimise their functionalities. Several approaches have been used for this purpose. One is testing the neat shell material of the microcapsules rather than directly testing the microcapsules themselves (Aniskevich et al., 2020; Zeleniakienė et al., 2016). However, the mechanical properties, e.g., rupture force, of the microcapsules depend not only on the mechanical properties of the shell materials, but also on the diameter, shell thickness and core materials of the microcapsules, i.e., shell materials which are mechanically strong enough cannot guarantee microcapsules with an encapsulated liquid core to be sufficiently strong (Zhang et al., 1999). Another way is directly testing the self-sensing microcapsules by nanoindentation with AFM. The maximal force to rupture the microcapsules and the elastic modulus of the shell were determined by nanoindentation experiments (Aniskevich et al., 2020). However, the maximal force value obtained here depended on the size of the indenter and was a local value of the microcapsule shell where the indentation was applied, which may not reflect the true property of the whole microcapsule.

The rupture strength of MF-shelled microcapsules with dicyclopentadiene (DCPD) as core material for self-healing was determined using the micromanipulation technique and it was found that the rupture strength parameters including the rupture force and nominal rupture

stress depended on the size of the capsules, which can be used to produce self-healing microcapsules with desirable mechanical strength (Hu et al., 2009). However, little work was found in literature to test the mechanical strength of single self-sensing microcapsules using the diametrical compression techniques, including micromanipulation and more research needs to be carried out on it.

2.5.1.3. Fragrance oil microcapsules with low content of formaldehyde

Fragrance oils are widely used in household and personal care products, including detergents, disinfectants, soaps, perfume and shampoos to give a pleasant scent and bring delight to consumers (Bone et al., 2011; He et al., 2014). However, most fragrance oils are very volatile and their performance will lose quickly if used directly. Therefore, they are widely encapsulated to optimise their performance from manufacturing to further processing, storage and end-use applications (Bone et al., 2011; He et al., 2014; Lee et al., 2002; Tekin et al., 2013). Formaldehyde-contained resins, including MF and urea-formaldehyde (UF), are less expensive, moisture and surfactant resistant, mechanically stronger and less permeable in comparison with other materials such as gelatine (Hu et al., 2009; Liu, 2010; Sun & Zhang, 2002) and thus are widely used to encapsulate fragrance oils. However, formaldehyde is very toxic to living organisms including human (Yuan et al., 2015).

Great efforts have been made to produce microcapsules with less or no formaldehyde, including reducing formaldehyde to melamine ratio by adjusting the pH of reaction medium (Lee et al., 2002), replacing formaldehyde with other low-toxic aldehydes (Deng et al., 2014;

Long et al., 2009), and adding scavengers to reduce the residual formaldehyde (Duan et al., 2015; Šumiga et al., 2011). However, when the formulation and preparation conditions are changed, the fundamental properties, including physical, structural, mechanical and thermal properties, need to be characterised to ensure that the fabricated microcapsules show similar or superior performance to their conventional counterparts. A lot of work has been carried out to determine the morphology, size and size distribution, shell permeability, thermostability, residual concentration of formaldehyde and encapsulation efficiency of the fragrance microcapsules (Deng et al., 2014; Frank, 2001; Lee et al., 2002; Long et al., 2009; Šumiga et al., 2011), whereas little work was available in literature on their mechanical characterisation, especially direct measurement of the mechanical strength of single microcapsules, with no or low content of formaldehyde. However, the mechanical strength is pivotal to them such as the microcapsules with fragrance added into detergents, which should remain intact during various engineering processing steps from manufacture to washing machine, including mixing with detergent, pumping and washing, but break via friction and rubbing between human body and the fabrics to release the fragrance after drying to keep the cloths fragrant as long as possible (Gray et al., 2016). Frank (2001) measured the Vickers hardness of the MF polycondensate used to prepare MF microcapsules and found that MF polycondensate became more brittle as the formaldehyde/melamine (F/M) molar ratio decreased. However, the mechanical strength of the MF microcapsules is not only determined by the polycondensate but also by the structure, the size and shell thickness of the capsules (Gray et al., 2016). Long et al. (2009) studied the

mechanical strength of single MF microcapsules with a typical perfume blend as liquid core made under different F/M molar ratios and found that the shell thickness and mechanical strength of single microcapsules decreased significantly with the decrease of F/M molar ratio. Therefore, simply reducing the F/M ratio may not produce mechanically optimised microcapsules with fragrance oils. Deng et al. (2014) substituted formaldehyde with non-toxic glyoxal to form urea-glyoxal (UG) resin for wood adhesive and found that the UG bonded plywood could provide enough shear strength that met China national standard GB/T 9846.3-2004. Therefore, replacing formaldehyde with other aldehyde may be a good solution to produce fragrance oil microcapsules with low content of formaldehyde by maintaining their performances, which need to be characterised and optimised, especially their mechanical strength which is crucial (Luo et al., 2022).

2.5.2. Microspheres

2.5.2.1. Different types of microspheres and their properties

Microspheres usually refer to spherical microparticles in size range of 1-1000 μm that have a homogenous solid or porous structure in which active agent (if used) is evenly spread at the molecular level (Arefin et al., 2021; Campos et al., 2013). However, sometimes, microcapsules, cells and microbeads are also classified as microspheres (Mercadé-Prieto & Zhang, 2012; Xue & Zhang, 2009). They are used in a variety of applications ranging from construction industry to cosmetic and personal care, medicine, and life science (Microspheres-Online, 2022). Similar to microcapsules, there are several essential properties, including chemical composition,

particle size and size distribution, melting point, solvent resistance, surface properties, thermo and mechanical strength, which should be considered and characterised for their applications (Microspheres-Online, 2022).

2.5.2.2. Porous microspheres

Porous microspheres have interconnective pores inside and on their surface and can be classified as microporous, mesoporous and macroporous, according to the pore size of < 2nm, 2-50 nm and > 50 nm respectively (Gokmen & Du Prez, 2012). Several techniques, including solvent evaporation, polymerisation, seed swelling, sintering, phase separation and spray drying can be used to produce porous microspheres. Formulation and processing conditions including type and concentration of porogen, polymer and its concentration, temperature, pH, stirring speed for emulsification can affect the size, shape and pore structure of the porous microspheres. Figure 2-16 illustrates porous polystyrene (PS) microspheres prepared under different concentrations of added ethanol (Li et al., 2021b). It appears that the concentration of ethanol affected the porosity of the PS microspheres significantly.

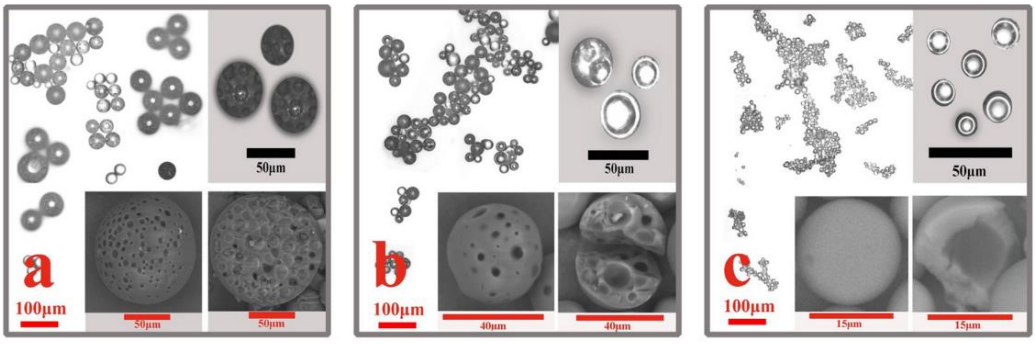

Figure 2-16 Optical microscopy images and SEM images of porous PS microspheres prepared under different concentrations of ethanol (EtOH): (a) 0 wt%, (b) 10.0 wt%, and (c) 20.0 wt% (Li et al., 2021b)

Porous microspheres have excellent absorption and desorption capacities because of their unique properties including low density and enormous specific area and thus are (potentially) used in many applications, including tissue regeneration scaffolds, chromatography, and drug carriers (Cai et al., 2013; Ghosh Dastidar et al., 2018; Gokmen & Du Prez, 2012). There are several properties of the porous microspheres, including particle size and size distribution, porosity, surface charge, swelling/solvent uptake and mechanical strength, which need to be characterised (Gokmen & Du Prez, 2012). Porosity, including pore structure, pore size and size distribution, is related to the absorption capacity, kinetics as well as mechanical stability of the porous microspheres (Cai et al., 2013; Garcia-Diego & Cuellar, 2005). For example, when used for tissue regeneration scaffolds, interconnective internal and external pores work as vessels for nutrients, growth factors and oxygen to be transported easily and thus the porosity and pore interconnectivity are crucial in such applications (Cai et al., 2013; Ghosh Dastidar et al., 2018). Porosity can be measured using TEM and SEM combined with digital image analysis (Ghosh Dastidar et al., 2018).

The mechanical strength is crucial for porous microspheres. For example, when used for tissue regeneration and controlled-release drug delivery, they may be “exposed to mechanical forces generated at the site where they are applied to including compression in cartilage and bone, tension in muscle and tendon, and shear force in blood vessels” (Lee et al., 2001; Zhao & Zhang, 2004). The force can also act as a trigger for the drug release. Understanding the mechanical strength of porous microspheres in such applications is crucial to optimising their

performance. Moreover, when porous microparticles are used as stationary phase in chromatography, narrow particle size, good mechanical strength and chemical stability in a wide range of pH are the basic requirements (Ghosh Dastidar et al., 2018). Characterising the mechanical strength of the porous microspheres for chromatography can help to understand and predict their stability in chromatographic columns and help in design and operation of related equipment (Müller et al., 2005). However, most studies of porous microspheres are concentrated on synthesising porous microparticles with varying porosity, pore size, shape and structure (Ghosh Dastidar et al., 2018). Few studies were related with characterisation of the mechanical strength of porous microspheres, especially of single ones. Although the porous microspheres are relatively mechanically weak compared to nonporous ones, most techniques that can be used to determine the mechanical strength of single particles, including micro- or nano-indentation, and micropipette aspiration, may not be suitable to test their mechanical strength because of the external pores that are not suitable for indentation probes to apply to and cannot hold the pressure of aspiration. The micromanipulation technique based on diametrical compression provides a powerful solution to determine the mechanical strength of microspheres, including the porous ones. Single alginate microspheres widely used as carriers for entrapment of drugs and cells, and single chromatographic particles made of different formulations and with different surface modifications were tested using the micromanipulation technique to determine their mechanical strength (Müller et al., 2005; Zhao & Zhang, 2004). It was found that alginate microspheres showed viscoelastic behaviours, i.e., with the increase

of compression speed, the average rupture force increased but the deformation at rupture remained unchanged (Zhao & Zhang, 2004). For the chromatographic microparticles, their mechanical stiffness decreased significantly in wet state in comparison with dry state because the water absorbed by the pores softened the polymer porous microspheres. Therefore, the initial water content and the speed of water release could affect the mechanical stability of polymer resins significantly (Müller et al., 2005).

2.5.2.3. PLA and PLGA microspheres

Poly (lactic acid) (PLA) and poly (lactic-co-glycolic acid) (PLGA) are biocompatible, biodegradable, environmentally friendly, non-toxic material usually made from annually renewable resources (Li et al., 2021a; Qi et al., 2019). They have been widely used in many fields, including biomedical and pharmaceutical, domestic, engineering and agricultural, to replace their petrochemical-based counterparts (Farah et al., 2016; Liu et al., 2019). They are usually used in the form of micro-sized materials, including microcapsules (Ma, 2014), microspheres (Qi et al., 2019) and microneedles (Park et al., 2006) for different applications, e.g., PLA microcapsules and porous PLA microspheres are used to encapsulate a variety of drugs to control their release in a sustainable/controlled or targeted way (Ma, 2014), and blank PLA/PLGA microspheres have been used as fillers to treat nasolabial fold contour deficiencies and other facial wrinkles because of their biocompatibility and controllable degradation (Qi et al., 2019; Reszko et al., 2009). PLA microspheres can be fabricated using several techniques, including solvent evaporation, solvent extraction, spray drying, hot-melt extrusion, membrane

emulsification and precision particle fabrication (PPF) and the last three have been applied in pilot or production scale (Ma, 2014; Qi et al., 2019).

Similar to the microcapsules, several fundamental properties of PLA/PLGA microspheres, including physicochemical, structural, mechanical and thermal properties, also need to be fully understood to optimise their performance. Many studies have focused on their size and size distribution, surface morphology (Wang et al., 2017; Zhang et al., 2018a; Zhang et al., 2014a), drug-loading capacity and encapsulation efficiency (Liu et al., 2005; Wang et al., 2017), drug distribution inside microspheres, drug stability, and drug release (Qi et al., 2014; Wang et al., 2017), and PLA degradation (Wang et al., 2017; Yang et al., 2009). However, similar to the porous microspheres in last section, information about the mechanical strength of the PLA microspheres is also essential. Moreover, it was found that the mechanical stability of PLA can be used to tune the release of the encapsulated drugs (Farah et al., 2016). Therefore, understanding the mechanical strength of the PLA microspheres plays an important role in optimising their functionalities. Most studies on characterising the mechanical strength of PLA have been carried out on the macro-sized PLA materials, including PLA cuboids (thickness: around 3mm) (Teymoorzadeh & Rodrigue, 2015), 3D printed PLA specimen (thickness: around 3mm) (Vian & Denton, 2018), PLA film (MW155,000g/mol) (Gong et al., 2017), and PLA fibres (Fambri et al., 1997) to determine their mechanical strength parameters, including tensile modulus, tensile strength, flexural modulus, flexural strength, and hardness. Few studies were on the determination of the mechanical strength of PLA microspheres especially

the single ones and more research needs to be undertaken on it.

2.5.3. Microneedles

2.5.3.1. Different types of microneedles and their functionalities

Microneedles are needle-like structures with a length shorter than 1000 μm and tip width of several tens of microns and usually an array of microneedles (e.g., 10×10) are fabricated in a patch to use. They can effectively overcome stratum corneum (the up-most layer of skin) without touching the blood vessels or nerves, thus generate no pain and low infection risk in contrast with traditional hypodermic needle sticks (Yang et al., 2019). They can be used for transdermal drug delivery (Prausnitz, 2004), disease diagnose (sampling) (Chang et al., 2017) and skin care (McCrudden et al., 2015), etc. Microneedles can be classified into several types based on different criteria, e.g., from pyramid-shaped, truncated cone-shaped and other complicated shaped microneedles based on their shapes (Prausnitz, 2004), to glass, metal and polymer microneedles based on the materials they are made from (Faraji Rad et al., 2021). Based on their structure and solubility in body liquid, microneedles can be classified as solid, coated, dissolvable (dissolving) and hollow microneedles (MN) as shown in Figure 2-17 (Kim et al., 2012).

Solid microneedles are inserted into the skin and removed to make micro-scale holes on the skin, followed by administration of drugs for slow diffusion into the body (a). Drugs are coated onto the surface of the (coated) microneedles and dissolved into the skin after penetration, after which the microneedles are removed (b). Drugs are encapsulated with the matrix of dissolving

microneedles made of biocompatible and biodegradable polymers which will dissolve into the skin together with the drugs after insertion (c). Drugs (liquid) run through the hole of hollow microneedles into the skin for administration (d). The hollow microneedles can also be used for sampling of body liquid through the skin. Microneedles can be fabricated by several methods including micro-moulding, etching, 3D-printing, and photolithography (Faraji Rad et al., 2021; Yang et al., 2019).

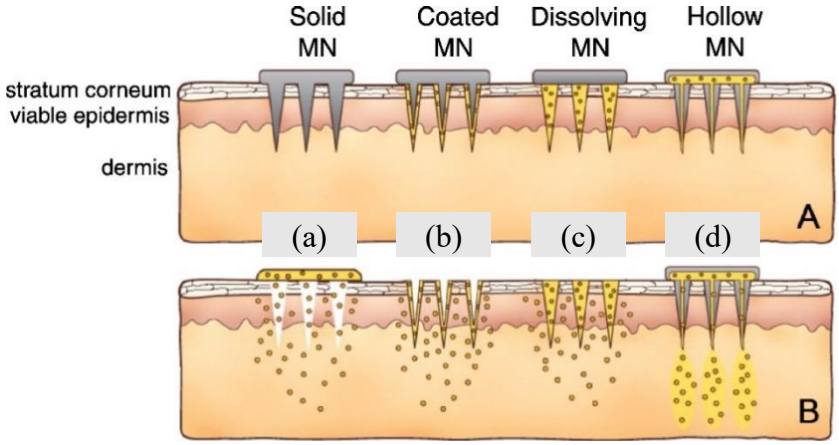

Figure 2-17 Different types of microneedles (MN) based on their structure and solubility in body liquid. A: Microneedles penetrate the skin. B: Drug delivery (Kim et al., 2012)

Similar to microparticles, microneedles should have desirable fundamental properties, including chemical, structural, geometrical, thermal and mechanical, to function properly in end-use applications. Their chemical compositions usually determine solubility, stability, and drug loading capacity, etc. (Huang et al., 2022). Thermal properties (glass transition temperature and melting point) can affect the storage stability and mechanical strength under different temperature conditions. The mechanical strengths are usually affected by the chemical composition, structure and geometry of the microneedles (Jung-Hwan et al., 2004).

Many techniques used to measure various properties of microparticles can also be used for characterising microneedles, e.g., SEM and confocal microscopy have been used to characterise the morphological and geometrical properties of microneedles in many studies (Dardano et al., 2015; Du et al., 2021a; Du et al., 2021b; Gittard et al., 2013). The surface roughness (~1 μm) and curvature radius (~3 μm) of the tip of microneedles made from poly (ethylene glycol) diacrylate (PEGDA) were estimated using SEM and the microneedle lengths were also obtained from image analysis of the microneedle images from SEM (Dardano et al., 2015). The surface morphology of several hyaluronic acid (HA) based microneedle samples was visualised using SEM and confocal laser scanning microscopy (CLSM) (Du et al., 2021a; Du et al., 2021b).

2.5.3.2. Dissolvable microneedles made from biocompatible and biodegradable polymers

The dissolvable microneedles made from biocompatible and biodegradable polymers can be adsorbed by the body and do not produce harmful waste after administration in comparison to microneedles made from other materials such as metals and glass (Du et al., 2021b). Therefore, they have been widely investigated for many potential biomedical applications (Du et al., 2021a; Fonseca et al., 2021; Kim et al., 2018). However, they are mechanically weak compared to those made of metal or glass materials. One of the ultimate requirements of microneedles is that they should be mechanically strong enough to penetrate the skin sufficiently. Therefore, precisely characterising their mechanical strength to guarantee they are strong enough to penetrate the stratum corneum without failure is essential to ensure their functions in end-use

applications.

2.5.3.3. Techniques for measuring the mechanical strength of microneedles

Several techniques have been used to test the mechanical strength of microneedles indirectly or directly. The indirect methods characterise the mechanical strength of microneedles by penetration efficiency which is the percent of microneedles over the whole patch that can successfully penetrate the skin sample indicated by dyes (van der Maaden et al., 2014). However, the results can vary with the applied force (to the microneedle patches) and time as well as the skin sample penetrated into (van der Maaden et al., 2014). Moreover, the mechanical strength of microneedles was also estimated by that of macro samples prepared using the same material to produce the microneedles (Loizidou et al., 2015). However, the obtained results can have great uncertainty, because the fabrication mechanism of the microneedles was not the same as that of the macro samples used in tensile tests, which can result in different mechanical property results.

The direct methods measure the mechanical strength of microneedles by axial compression which can be classified as ensemble and single microneedle test techniques. In ensemble tests, an array of microneedles (on a patch) were compressed together (Figure 2-18a), during which the overall loading force was recorded and the average force of single microneedles was obtained by dividing the whole loading force by the number of microneedles on the patch (Davis et al., 2004; Fonseca et al., 2021; Gittard et al., 2013; Kim et al., 2018; Park et al., 2005; Park et al., 2006; Wang et al., 2018).

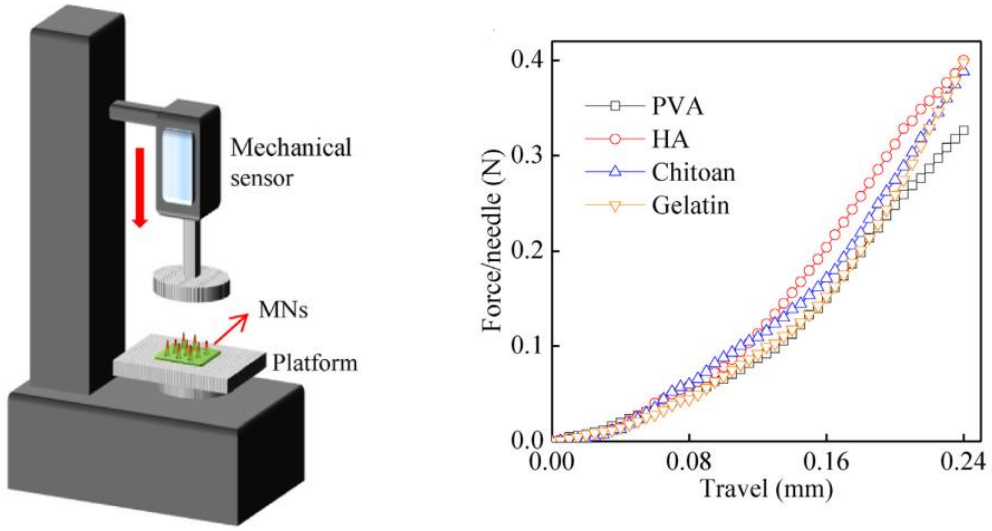

(a) (b)

Figure 2-18 Ensemble compression tests of microneedle array (Wang et al., 2018)

A micro-mechanical test station with a mechanical sensor was used to test the mechanical strength of four microneedle samples in different humidity environments (Wang et al., 2018). In the tests, 5×5 microneedles on one patch were compressed together as illustrated in Figure 2-18a but the force value was converted into single microneedle case in the force-travel curves shown in Figure 2-18b. The force values at the travel distance of 0.25 mm of the four microneedle samples were determined and it was found that PVA microneedles were softest as the force value at 0.25 mm was 0.34 N while that of the other three were nearly 0.40 N. Fonseca et al. (2021) evaluated the failure force of four samples of HA and bacterial nanocellulose (BC) microneedles using a texture analyser. All 225 microneedles on a single patch were compressed together and their average mechanical strength parameters were obtained. However, the parameters of individual microneedles and their variation over the patch could not be obtained, which was crucial to ensure a high percent of the needles can penetrate the

skin successfully. Moreover, in most of such studies (Choi et al., 2018; Davis et al., 2004; Fonseca et al., 2021; García et al., 2016; Gittard et al., 2013; Park et al., 2006; Prausnitz, 2004), the average failure force was used to characterise the mechanical strength of microneedles and to predict their penetration efficiency by comparing it with the insertion force required to pierce the skin using microneedles with the same geometric parameters, especially the tip size as the required insertion force was mainly determined by interfacial area at needle tip and the corresponding pressure (Davis et al., 2004; Park et al., 2006). Therefore, in order to carry out the comparison, the required insertion force of microneedles with the same or similar geometry needs to be determined first. Otherwise, it is not sufficient to draw conclusions simply using the failure force without knowing the geometrical and structural parameters of the tested microneedles as the force is not an intrinsic mechanical property parameter, and depends on the geometry and structure of the microneedles for a given intrinsic mechanical strength (Du et al., 2021b).

In single microneedle tests, microneedles are tested one by one and thus the variations among the needle patch can be obtained. Dardano et al. (2015) tested the mechanical strength of single microneedles by indenting the centre point of a single tip using AFM in the force/displacement spectroscopy mode. The relative indentation hardness was compared with that of an artificial skin by comparison of their slope values of the force-displacement curves during the indentation. It was found that the force-displacement curves of microneedles had a greater slope than that of the artificial skin, which indicates the microneedles were sufficiently strong

for penetration. However, the obtained hardness was local value corresponding to where the nanoindentation had been applied, and rupture parameters cannot be obtained because of the limit of the applied force that AFM can generate. Similar problems remain in many other techniques for characterising the mechanical strength of single microparticles, including pressure probe (Boyer & Kramer, 1995), micropipette aspiration (Heinrich & Rawicz, 2005), and optical/magnetic tweezers (Neuman & Nagy, 2008) and thus are not proper for determination of the mechanical strength of microneedles, whose failure forces are usually in the range of milli-Newtons (Du et al., 2021b).

2.6 Conclusion

In this chapter, the micromanipulation technique which this PhD project is based on was firstly reviewed, including different versions of the equipment, types of experiments that can be done and mathematical models that can be used to determine the mechanical properties of single particles from the experimental data. Briefly, three kinds of tests can be carried out including loading, loading-holding and loading-unloading. Several mathematical models can be used to analyse the mechanical property parameters from the experimental data, including the Hertz, Tatara, FEM, viscoelastic and plastic models. The Hertz model and Tatara model have been used for analysis of elastic homogenous microspheres in small and large deformation respectively. The FEM can extend the Hertz model and be used for analysis of microcapsules with core/shell structure, which are deformed elastically and then plastically until rupture. The viscoelastic model has been used for microspheres which showed viscoelastic behaviours. The

plastic model has been developed for microspheres deformed in the plastic range. It can be seen that the existing micromanipulation technique with different versions of well-built apparatus, three types of experiments that can be carried out, and several mathematical models that can be used to analyse the experimental data, is very powerful and has been used to determine the mechanical properties of a wide range of biological and nonbiological micro-sized materials. However, it is quite time-consuming, laborious and technically demanding because it was mainly based on manual operation and manual data analysis. Therefore, an automatic micromanipulation system needs to be developed to undertake the operation and data analysis automatically to enhance the capability of the existing micromanipulation technique.

Then, the techniques that can be used in the automatic data analysis were reviewed, including the algorithms to locate the contact point (CP) in AFM tests and the three-sigma rule. However, it has been found that the reviewed algorithms for CP detection in AFM tests cannot be directly used for automatic analysis of the experimental data obtained from micromanipulation as the parameters set for the algorithms need to be adjusted manually. New algorithms need to be developed to automatically determine the mechanical strength of microparticles from the manipulation tests.

After that, the techniques that can be used for automatic operation of the micromanipulation system were reviewed, including those to achieve autofocus, image segmentation, and object detection. The passive autofocus technique based on the sharpness of the images looks

desirable and will be further developed in our project as it is low-cost and pretty accurate among the autofocus technique family and may be suitable for the micromanipulation system. However, it has been identified that the reviewed algorithms cannot be used directly in the development of the automatic micromanipulation system because of the different application scenarios. For example, all the reviewed search algorithms in Section 2.4.1.3 are under the assumption that objects are already in the field of view (FOV) of the camera, which is not the case in the automatic micromanipulation system based on the sideview camera, as there may be no microparticles in the FOV of the sideview camera during the movement of the sample stage and thus the algorithms cannot be used directly in this work. New algorithms need to been developed to fulfil the autofocus task based on only the sideview camera in the micromanipulation system.

Finally, some typical microparticles, including self-sensing microcapsules, fragrance oil microcapsules with low content of formaldehyde, porous PS microspheres and PLA microspheres, including their applications, fundamental properties, as well as techniques to experimentally determine their properties were reviewed. It has been identified that determination of the mechanical strength of these micro-sized materials is extremely important, but such studies were limited, especially on mechanical characterisation of single micro-particles. Although a significant amount of work has been undertaken on the determination of the mechanical strength of microneedle arrays, but few studies were carried out to determine that of single microneedles so that the variations among them can be obtained, which is crucial

to predict their penetration efficiency reliably. Moreover, the approach to characterise the mechanical strength of microneedles simply by the failure force in many studies seems not sufficient because the force is not an intrinsic mechanical strength parameter, and it depends on the geometry and structure of the microneedles. Therefore, mathematical models need to be developed to determine the intrinsic mechanical properties of microneedles.

CHAPTER 3: DEVELOPMENT OF SOFTWARE FOR AUTOMATIC ANALYSIS OF MICROPARTICLE RUPTURE STRENGTH**

3.1 Introduction

The rupture strength of various microparticles was characterised previously using the micromanipulation technique, which has provided essential technical data for new microparticle product development (Gray et al., 2016; Sun & Zhang, 2002; Yap et al., 2006). The technique also has played a very important role in academic research to develop new applications of various microparticles.

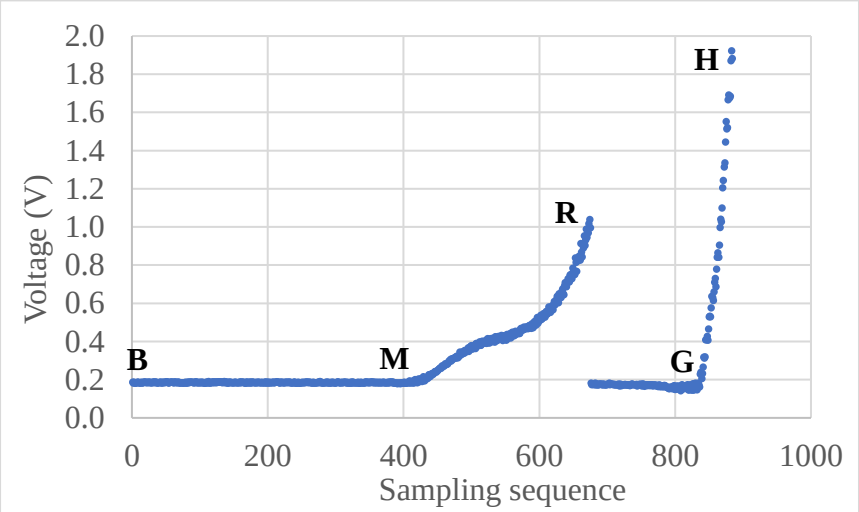

Figure 3-1 Typical curve of voltage versus sampling sequence from compression of single particles

The raw data from a micromanipulation test are a series of voltage data versus sampling sequence corresponding to a given sampling frequency as shown in Figure 3-1. The main task of the data analysis is to identify the starting point M, where the onset of loading occurs, and

rupture point R, where the tested particle is ruptured, from which the rupture strength parameters and force-displacement data can be obtained (Mashmoushy et al., 1998; Smith et al., 2000). Unlike using some commercial or open-source software packages to analyse the force-displacement data from AFM experiments (Charles et al., 2012; Dinarelli et al., 2018), the data of the micromanipulation experiments were analysed manually by interacting with the raw data and template spreadsheets to obtain the required results, which is quite laborious and time-consuming.

The software packages for AFM are not easy to be adapted to process the data from the micromanipulation technique because of the differences in data formats, mechanical property parameters to be obtained, and specific mathematical model formulas required to be used. However, similar to the starting point M in the micromanipulation tests, the contact point (CP) is also crucial to analysing the force-displacement data from AFM experiments. Several algorithms have been developed to locate the CP from the force-displacement data obtained from AFM experiments, which have been reviewed in Section 2.3.1.2, where it was found that they are not suitable for automatic analysis of the experimental data from micromanipulation. The aim of research presented in this chapter is to develop a software package to analyse the experimental data from using the micromanipulation technique to automatically obtain the rupture strength parameters of microparticles to simplify the procedure, save time and labour, and enhance the capability of the micromanipulation technique. Three algorithms are proposed to identify the starting point M, and an algorithm is introduced to locate the rupture point R

from the raw voltage versus sampling sequency data of micromanipulation. Two samples of microparticles, i.e., the microcapsules for self-sensing and the porous PS microspheres with various potential applications, have been tested using the micromanipulation technique, and the experimental data analysed using the new software package are compared with the manual results to validate the algorithms developed.

3.2 Materials and methods

3.2.1. Microparticles for micromanipulation

3.2.1.1. Microcapsules for self-sensing

The microcapsules for self-sensing were a very robust type of double-walled microcapsules made by interfacial polymerization, provided by Dr Zhenxu Zhang in School of Metallurgy and Materials of University of Birmingham UK. The detailed fabrication methods are described in Roche et al. (2022). The outer and inner shells were made from poly urea formaldehyde (PUF) and polyurethane (PU), respectively. The core was oil with a fluorophore substance.

3.2.1.2. Porous polystyrene microspheres

The porous polystyrene (PS) microspheres with various potential applications were fabricated via a novel solvent evaporation methodology based on foaming transfer as shown in Figure 3-2. It is based on a traditional solvent evaporation method but utilizes a higher temperature (40 °C) so that the solvent evaporates more quickly. Bulk foams are formed, accumulated and flow out to the receiving vessel during which oil droplets are entrained and delivered to the

receiving vessel. Porous PS microspheres are obtained after defoaming, washing, filtration and drying. The detailed fabrication process is reported in Li et al. (2021b). Specifically, the formed porous PS microspheres were obtained by introducing 20 wt% ethanol concentration to the continuous phrase, provided by Dr. Yanping He in the School of Chemical Engineering of University of Science and Technology, China.

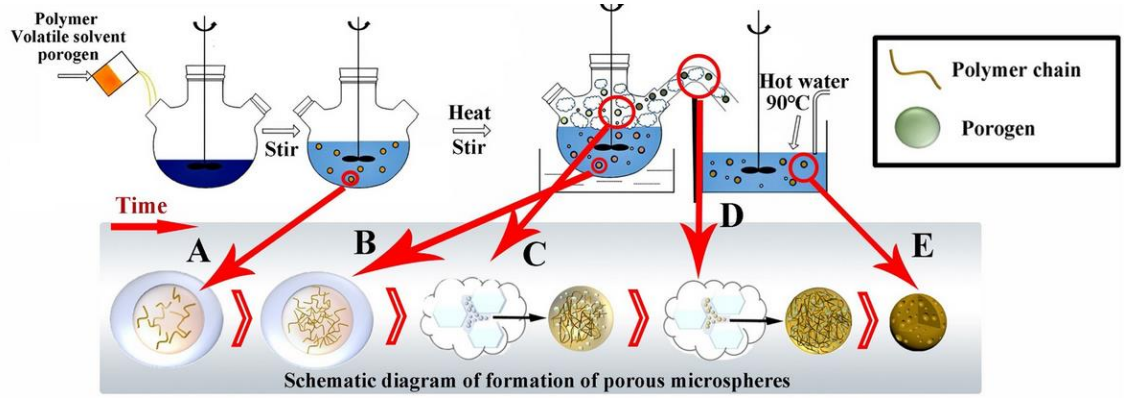

A: the oil and water phase are just mixed; B: dichloromethane (DCM) in the oil droplets begins to evaporate; C: DCM evaporates to induce phase separation between the porogen and the polymer solution; D: the further phase separation between the porogen and the polymer solution in the oil droplets; E: the oil droplets are solidified into microspheres.

Figure 3-2 Improved solvent evaporation method to produce the porous PS microspheres (Li et al., 2021b).

3.2.2. Micromanipulation of the microparticles

3.2.2.1. Micromanipulation of the microcapsules for self-sensing

Dry microcapsules were placed onto a glass slide, and single microcapsules were compressed to rupture using the conventional micromanipulation rig at a compression speed of 2.0 μm/s. The sampling frequency was 53 Hz and the total sampling time for each single microcapsule was 30-50 s. The force transducer model was GS0-10 (Transducer Techniques, LLC, Temecula,

CA, USA) with a pre-calibrated sensitivity of 8.67 mN/V. In total, 50 microcapsules were tested at ambient temperature of 26 ± 2 °C. Figure 3-3 shows a typical single microcapsule for self-sensing to be compressed.

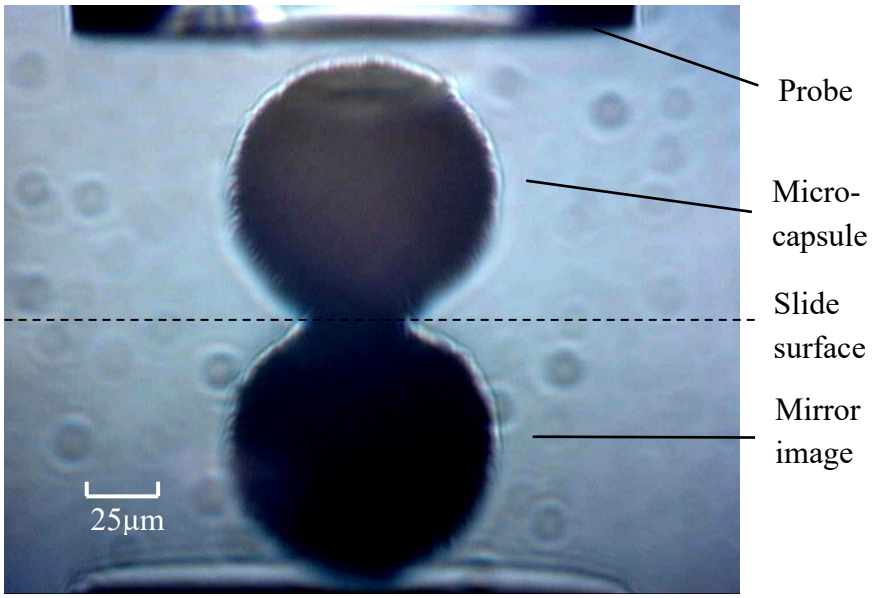

Figure 3-3 Microscopy image of a single self-sensing microcapsule to be compressed (diameter: 78.9 μm)

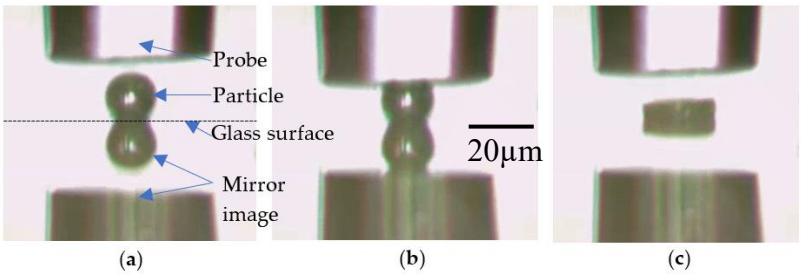

Figure 3-4 A porous PS microsphere (diameter: 16.3 μm) before (a), during (b), and after (c) compression

3.2.2.2. Micromanipulation of the porous PS microspheres

The micromanipulation procedure of the porous PS microspheres was the same as the measurement of the self-sensing microcapsules. The force transducer used was GS0-10 (Transducer Techniques, LLC, Temecula, CA, USA) with a pre-calibrated sensitivity of 7.42

mN/V. In total, 50 PS microspheres were tested under ambient temperature of 16 ± 2 °C. Figure 3-4 illustrates the procedure to compress a porous PS microsphere between the two parallel surfaces, i.e., the probe end and the glass surface.

3.2.3. Rupture Strength Parameters of Microparticles

The raw data from a micromanipulation test is a series of voltage versus sampling sequence data $(V_1, V_2, \dots, V_N)$, where N is the number of the voltage data points. A typical curve is shown in Figure 3-1. At the beginning, the voltage remains stable along the baseline as the probe moves in the air due to the initial gap between the probe and the microparticle. Then, it starts to increase at M when the probe begins to touch the particle. The voltage keeps rising until R and drops suddenly when the particle is ruptured. After that, the voltage rises again from G as the probe compresses the debris of the particle on the hard bottom surface and stops at H when the voltage limit is reached, or the movement is stopped manually. Point M is named as the starting point and R as the rupture point. The line segment BM is termed as "baseline". The main task of the data analysis is to identify the starting point M and rupture point R from which the rupture strength parameters, including rupture force F_r, displacement at rupture δ_r, nominal deformation at rupture ε_r, nominal rupture stress σ_r, nominal rupture tension T_r, and toughness T_C, can be calculated using the following equations

$$F_r = s(V_r - V_B) \tag{3-1}$$

$$\delta_r = vt_s(r - m) - cF_r \tag{3-2}$$

$$\varepsilon_r = \frac{\delta_r}{D} \tag{3-3}$$

$$\sigma_r = \frac{4F_r}{\pi D^2} \tag{3-4}$$

$$T_r = \frac{F_r}{D} \tag{3-5}$$

and

$$T_C = \int_0^{\varepsilon_r} \sigma d\varepsilon \tag{3-6}$$

where m is the starting point index, r is the rupture point index, V_r is the voltage corresponding to rupture, V_B is the average voltage of the baseline, v is the compression speed, t_s is the sampling time, s is the sensitivity of the force transducer, c is the compliance of the force transducer, D is the initial diameter of the single microparticle, σ is the nominal stress, and ε is the fractional deformation. The force-displacement data can be obtained using the following two equations:

$$F_i = s(V_{i+m} - V_B) \tag{3-7}$$

and

$$\delta_i = ivt_s - cF \tag{3-8}$$

where i ($1 \le i \le N - m$) is the index, F is the compression force, and δ is the displacement. Then, the nominal stress and fractional deformation can be calculated using

$$\sigma_i = \frac{4F_i}{\pi D^2} \tag{3-9}$$

and

$$\varepsilon_i = \frac{\delta_i}{D} \tag{3-10}$$

In practice, the microparticle toughness in Equation (3-6) can be determined using the trapezoidal numerical integration as follows

$$T_C = \frac{1}{2}\sum_{i=1}^{r}(\sigma_i + \sigma_{i+1})(\varepsilon_{i+1} - \varepsilon_i) \quad (3\text{-}11)$$

3.2.4. Algorithms to Locate the Starting Point

3.2.4.1. "3σ" Algorithm

During the micromanipulation test, the voltage $V(t)$ at a given time *t* can be expressed as follows

$$V(t) = \frac{1}{s}F(t) + e(t) \quad (3\text{-}12)$$

where $F(t)$ is the true value of the compression force, and $e(t)$ is a random noise. Before the onset of compression, $F(t)$ is constant (zero), thus $V(t)$ and $e(t)$ have the same distribution during this period. Assuming the distribution is Gaussian (the most common distribution (Smith, 1997) for noise), according to the three-sigma rule (Pukelsheim, 1994) in Equation (2-2), if the voltage value at a point starts to deviate from the baseline mean value by three standard deviations, it has a high possibility (99.73%) that the onset of compression begins, i.e., the first point when the voltage deviates from the baseline by three standard deviations can be located as the starting point. In practice, the X_{mean} and X_{SD}(Equation (2-2)) can be estimated by the average (V_B) and standard deviation (S_B) of the voltage data of the baseline. Then, a criterion is obtained to determine the starting point.

$$|V_m - V_B| > 3S_B \quad (3\text{-}13)$$

where m is the index of the starting point.

The flowchart of the "3σ" algorithm is illustrated in Figure 3-5. After initialization, the first z

points of voltage $(V_1, V_2, \dots, V_z)$ are taken from the raw voltage data series $(V_1, V_2, \dots, V_N)$ as the baseline, from which the average V_B and standard deviation S_B are calculated using Equation (3-14).

$$V_B = \frac{1}{z}\sum_{i=1}^{z} V_i,$$
$$S_B = \sqrt{\frac{\sum_{i=1}^{z}(V_i - V_B)^2}{z-1}} \tag{3-14}$$

Then, the voltage data after z, $(V_{z+1}, V_{z+2}, \dots, V_n)$, are looked through for the first point when Inequality (3-13) is satisfied, whereafter the algorithm is stopped. The value of z can be estimated by the compression speed, sampling time, and the initial gap between the probe and the particle. Usually, $z = 20$ is used, which is sufficiently accurate to determine V_B and S_B.

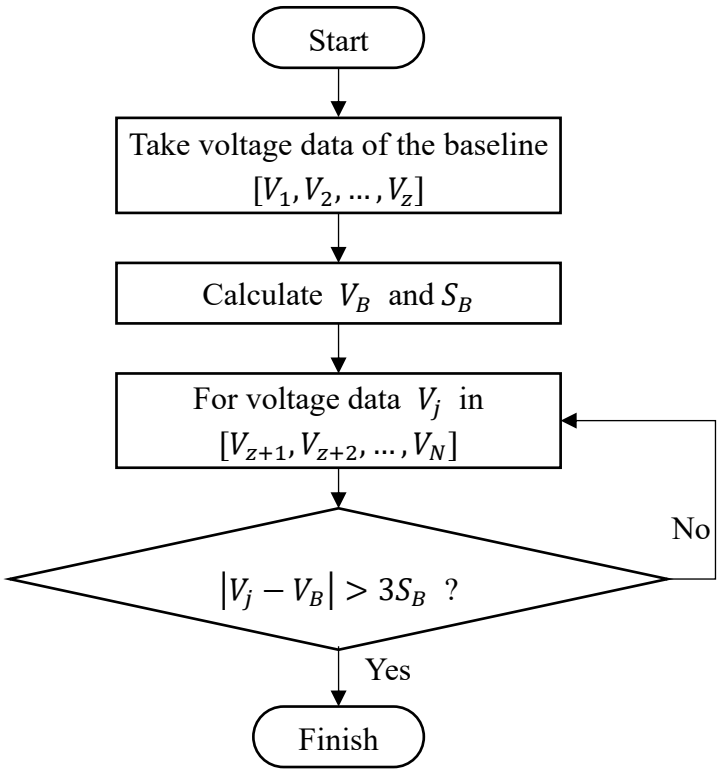

Figure 3-5 Flowchart of the "3σ" algorithm

3.2.4.2. "3σ + Window" Algorithm

Normally, the "3σ" algorithm can locate the starting point successfully. However, if a pulse noise exists, the starting point may be determined incorrectly as illustrated in Figure 3-6, where the point m_1 rather than m_2 will be misidentified as the starting point because of the impulse noise around m_1. Although smoothing the raw data by filtering can deal with the impulse noise, other key points such as the rupture value will likely be evened (i.e., the magnitude of the rupture force will be reduced).

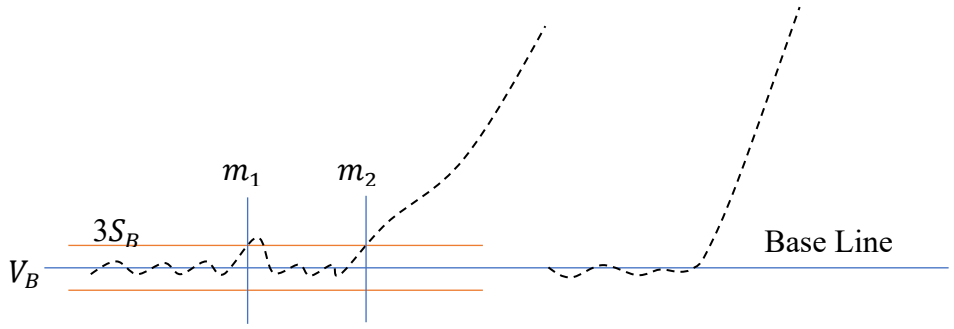

Figure 3-6 Problem of the "3σ" algorithm when impulse noise exists

To tackle this problem, the "3σ" algorithm was modified by introducing a moving window with width w. A point m can be identified as the starting point only if all the points from it in the moving window fall away from V_B by $3S_B$, which leads to the following criterion

$$\bigwedge_{i=0}^{w-1}(|V_{m+i} - V_B| > 3S_B) == true \qquad (3\text{-}15)$$

where ∧ is the logical "and" Boolean operator. The width of the moving window w can be estimated as an integer corresponding to a percent of the diameter of the microparticle. As some brittle capsules and biological cells may rupture at a fractional deformation as small as 0.06 (Mercadé-Prieto et al., 2012), a percent of 5% can ensure w less than the rupture

deformation of most microparticles. Thus, w can be estimated using the following equation

$$w = \frac{0.05D}{vt_s} \tag{3-16}$$

3.2.4.3. "3σ + Window + Hertz" Algorithm

The "3σ + window" algorithm can deal with most cases including those with random noise and impulse noise. However, it may underestimate the displacement when the voltage corresponding to three standard deviations of the baseline is just chosen as the starting point. This can result in a bigger value of the starting point index (m) so that the displacement will be underestimated, as it is related to the starting point by Equations (3-2), (3-7) and (3-8). The underestimation will be even worse when the signal to noise ratio is low. Following the same strategy described by Chang et al. (2014), a mathematical model such as the Hertz model can be used to estimate the starting point (m) from the force-displacement data calculated using the "3σ + window" algorithm.

For diametrical compression of purely linear elastic microspheres, the Hertz model (Zhang et al., 2009) relates the force to the displacement by the following equation

$$F = \frac{E\sqrt{D}}{3(1-v^2)}\delta^{\frac{3}{2}} \tag{3-17}$$

where E is the Young's modulus, and ψ is the Poisson's ratio. Assume the force and displacement obtained from the "3σ + window" is F' and δ', respectively, and the difference between the true displacement and the one obtained from the "3σ + window" is $\Delta\delta$; then, Equation (3-17) can be written as

$$F' = k'(\delta' + \Delta\delta)^{\frac{3}{2}} \tag{3-18}$$

Equation (3-18) can be transformed to

$$\delta' = k(F')^{\frac{2}{3}} - \Delta\delta \tag{3-19}$$

where $k = 1/(k')^{2/3}$. Although the Hertz model is for purely linear elastic microspheres, it can be used to evaluate the true starting point by fitting into the initial compression data, such as within 5% deformation of the force-displacement data (Yan et al., 2009) obtained using the "3σ + window" algorithms. The flowchart of the algorithm can be illustrated by Figure 3-7.

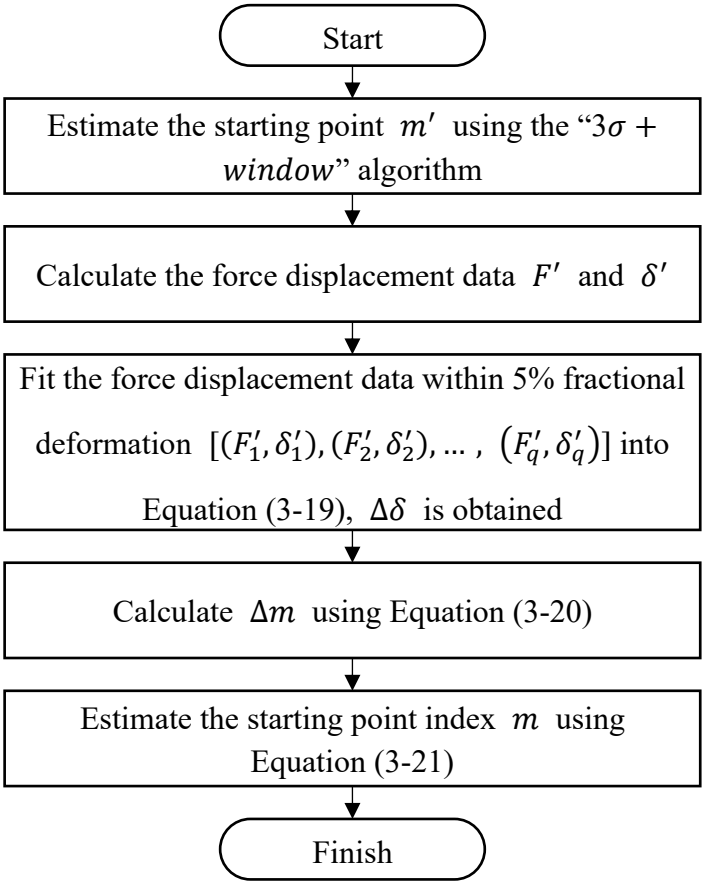

Figure 3-7 Flowchart of the "3σ + window + Hertz" algorithm

Firstly, a starting point index m' is estimated using the "3σ + window" algorithm, and the force-displacement data series $[(F_1', \delta_1'), (F_2', \delta_2'), \dots, (F_N', \delta_N')]$ are calculated using Equations (3-7) and (3-8). Then, the force-displacement data within 5% deformation

$[(F_1', \delta_1'), (F_2', \delta_2'), \dots, (F_q', \delta_q')]$ are fitted into Equation (3-19), and thus, $\Delta\delta$ is obtained, from which the different number Δm is estimated by Equation (3-20) to compensate the starting point.

$$\Delta m = \frac{(CoD) \cdot \Delta\delta}{vt_s} \tag{3-20}$$

where CoD is the coefficient of determination, often explained as the proportion of the variance in the dependent variable that is predictable from the independent variable (Montgomery et al., 2012). It also indicates the extent to which the dependent variable is predictable by the fitting model. In this case, the CoD represents how well the Hertz model can be used to represent the relationship between the force-displacement data up to 5% fractional deformation. A value of 1.0 indicates a perfect fit, whilst a value of 0.0 implies that the Hertz model fails to model the data. Multiplying $\Delta\delta$ by CoD is expected only to use the predictable percent of $\Delta\delta$ to compensate the starting point. In other words, the compensated number Δm is not only calculated from the $\Delta\delta$ value estimated by the Hertz model but also from the "goodness" of the fit, i.e., how well the Hertz model can fit the data. In this way, Equation (3-20) adjusts the compensation extent automatically according to the goodness of fit (CoD), which makes the compensation algorithm intelligent.

Finally, the index of the starting point can be obtained by Equation (3-21).

$$m = m' - \Delta m \tag{3-21}$$

3.2.5. Algorithms to Locate the Rupture Point

3.2.5.1. Maximum-Deceleration Algorithm

Normally, the voltage drops most dramatically just after the rupture point so that it can be identified by looking for the maximum deceleration through the voltage series. Practically, the deceleration is calculated from the following equation:

$$\Delta V_i = \frac{V_{i+1} + V_{i+2}}{2} - V_i, \quad i = 1,2,\cdots,N-2 \tag{3-22}$$

where $(V_{i+1} + V_{i+2})/2$ rather than V_{i+1} is used to filter the data slightly to reduce the possible impact of random noise.

The flowchart of the algorithm is illustrated in Figure 3-8. Initially, the drop (deceleration) series is calculated from the voltage series. Then, the point with the maximum drop (point p) is found, and the rupture point (r) is located as the peak point before p.

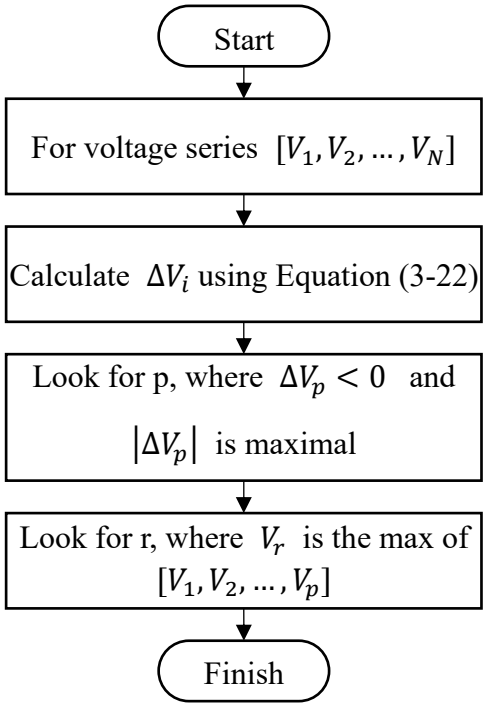

Figure 3-8 Flowchart of the maximum-deceleration algorithm

3.2.6. Development of the microparticle rupture strength analysis software package

3.2.6.1. Functions and structure of the software package

In order to analyse the test results automatically, the software needs to read the raw data and convert it to the format that is easy to analyse. Then it will use the above algorithms to identify the key points, from which the software can extract the interesting data, calculate the rupture strength parameters and present them to the users through the user interface and excel reports.

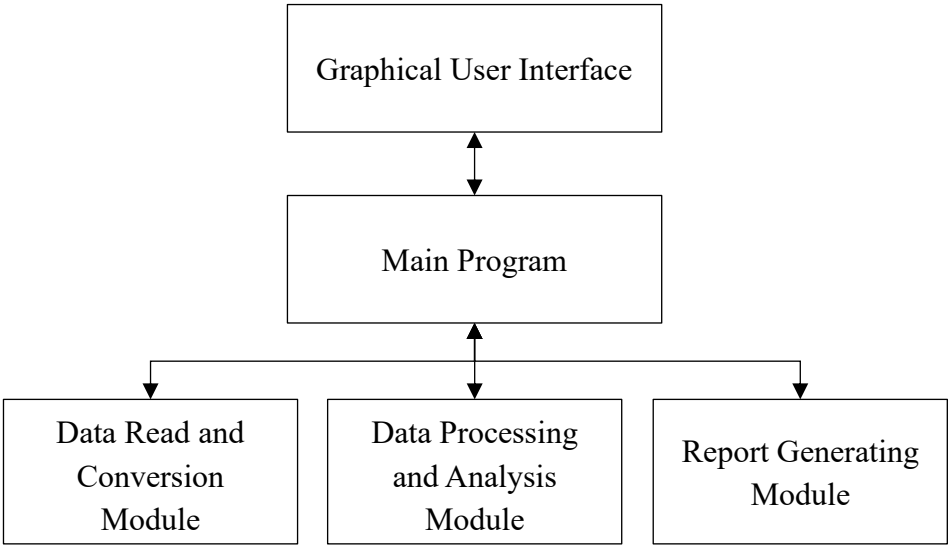

Figure 3-9 Function and structure of the software package

The developed rupture strength data analysis software package is mainly composed of five modules, i.e., the data read and conversion module, the data processing and analysis module, the report generating module, the graphical user interface (GUI) module, and the main program as shown in Figure 3-9.

The data read and conversion module is used to read experimental raw data and convert it into a unified data set for further processing. There are several file formats of experimental data, including XML, CSV, XLS, and XLSX, because of different versions of micromanipulation

compression rigs which are routinely used. Besides, different rigs may store the data in different ways. This module reads the raw data with several data providers according to their file formats and transfer them into a unified voltage-time sequence to facilitate the following data processing and analysis.

The data processing and analysis module is mainly aimed at identifying the key points, including the starting point and the rupture point from the voltage-time data and to use the data between them to calculate the force-displacement data corresponding to the compression, from which the rupture strength characteristics of the microparticles are determined. The algorithms described in Sections 3.2.4 and 3.2.5 are incorporated into this module.

The report generating module is used to organise the rupture strength results obtained from the data processing and analysis module, estimate their statistical parameters, including the mean, standard deviation and standard error, arrange them altogether into the required format and output them through the spreadsheet report files.

The graphical user interface (GUI) module is used for human-computer interaction and communication. It includes a series of command elements, such as buttons, checkboxes and textboxes, from which the user can input parameters, and control the data analysis software to get the correct results. It also has some presentation elements, such as data grid views and charts, which can display the results of the analysis. A screenshot of the developed GUI is illustrated in Figure 3-10. After selecting one record of a tested microparticle, its raw voltage-time data as well as the starting point and rupture point obtained automatically will display in

the voltage-time chart (bottom left). The obtained force-displacement data will be shown in the force-displacement chart (bottom right).

The main program mainly aims to organize the other modules, coordinate the mutual calls of them, handle exceptions and so on, to ensure the smooth running of the data analysis software package.

3.2.6.2. Platform and open-source libraries used

Visual Studio 2017 Community and .NET from Microsoft were chosen as the main development platform to develop the automatic data analysis software package. The user interface (UI) module, report-generating module, and main program module are mainly developed with the C# language, and the data read and conversion module, data processing and analysis module are mainly developed with the F# language. Besides, some open-source software libraries, such as Math.Net and EEPlus, are used to facilitate the software development. The libraries used are listed in Table 3-1.

Table 3-1 Open-source libraries used in the development of the software package

Library	Version	License
DarkUI	2.0.2	MIT
EEPlus	4.5.3.2	LGPL-3.0-or-later
ExcelDataReader	3.6.0	MIT
ExcelDataReader.DataSet	3.6.0	MIT
Math.NET Numerics	4.8.0	https://numerics.mathdotnet.com/License.html (accessed on 8 May 2022).
Accord.NET	3.8.0	http://accord-framework.net/license.txt (accessed on 8 May 2022).

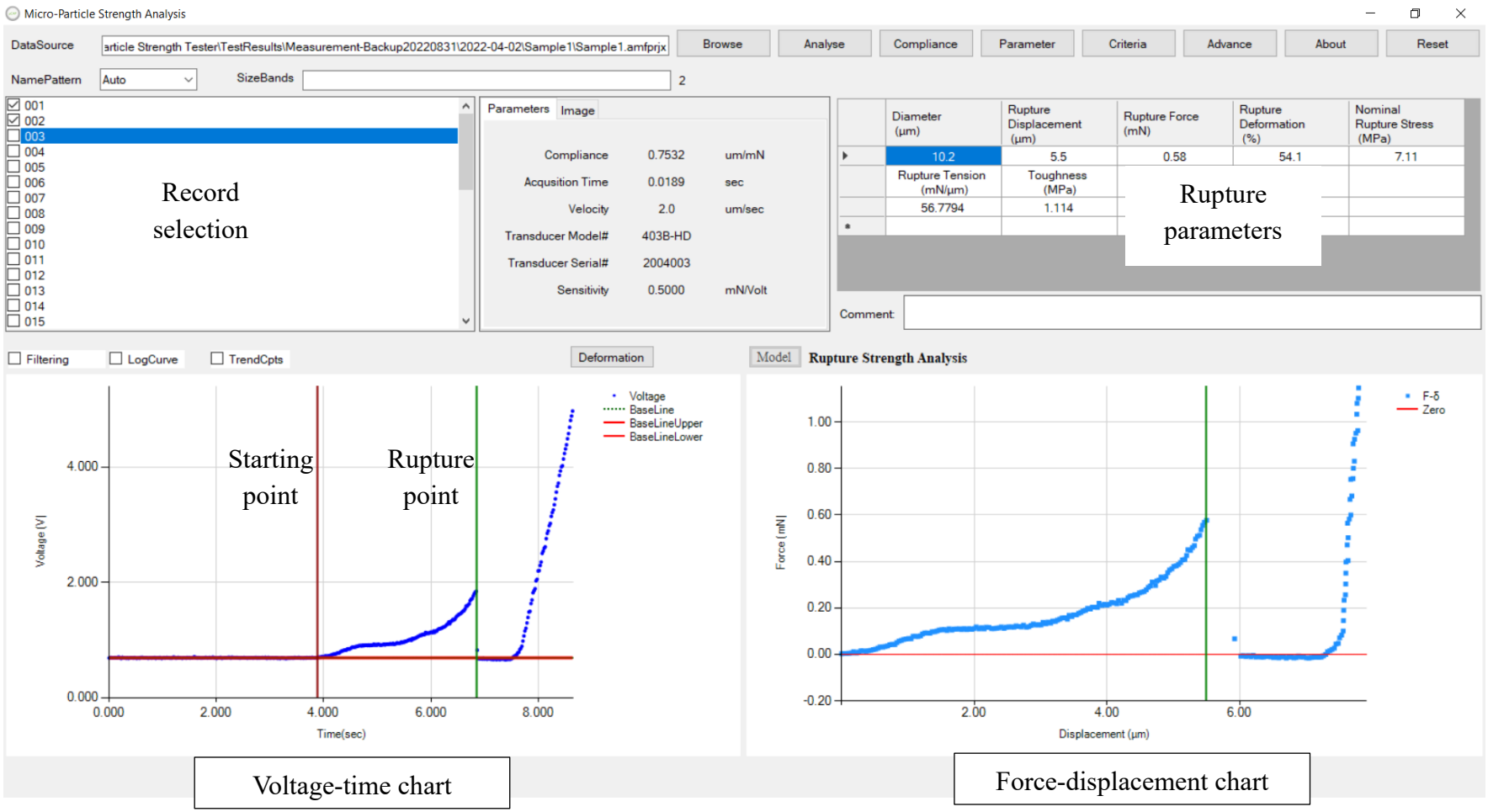

Figure 3-10 Screenshot of developed GUI

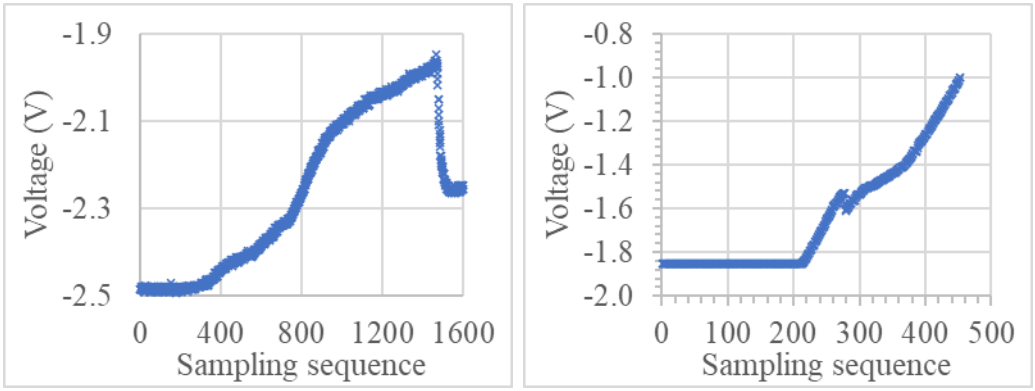

(a) (b)

Figure 3-11 Experimental voltage-sampling sequence curves of a self-sensing microcapsule (a) and a porous PS microsphere (b).

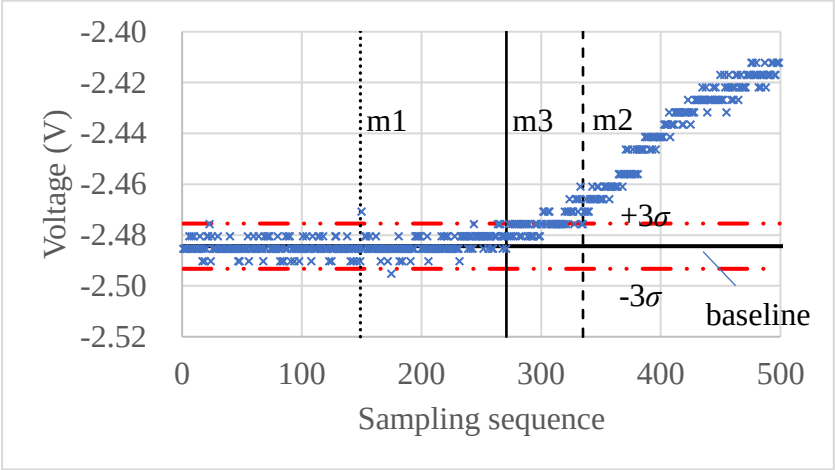

(a)

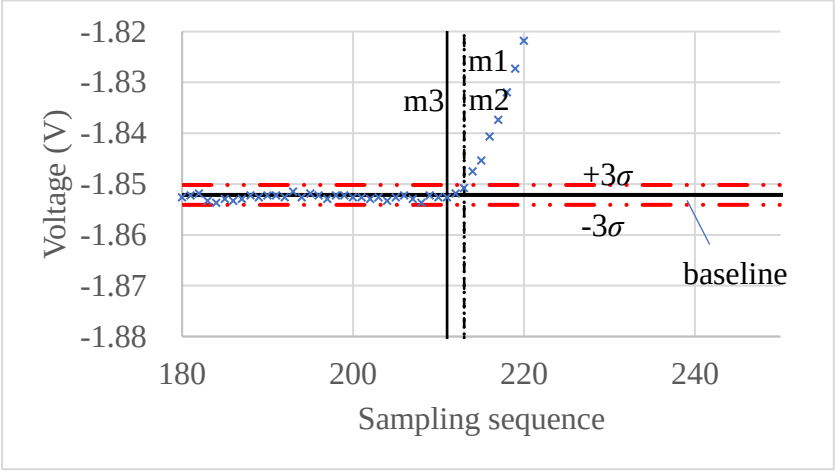

(b)

Figure 3-12 Starting point values found by the three algorithms. (a) Results for a self-sensing microcapsule and (b) results for a porous PS microsphere.

3.3 Results and Discussion

3.3.1. Performance of the algorithms

For the experimental raw voltage data of a microcapsule for self-sensing shown in Figure 3-11a , the starting point m1, m2, and m3 found by the "3σ", "3σ + window", and "3σ + window + Hertz" algorithms, respectively, are presented in Figure 3-12a. The diameter of the microcapsule was 87.6 μm. It can be seen that for this set of experimental data, the result of the "3σ" algorithm seems to underestimate the starting point because of the impulse noise, whilst the result of the "3σ + window" appears to overestimate the starting point. The starting point found by the "3σ + window + Hertz" algorithm looks more reasonable as the voltage starts to increase around this point. However, when no impulse noise exists, the starting point values obtained from the "3σ" (m1) and "3σ + window" (m2) algorithms are the same. For instance, for the raw voltage data of a porous PS microsphere in Figure 3-11b, the starting point is m1 = m2 = 213 as shown in Figure 3-12b. In both cases, the rupture points are successfully identified by the maximum-deceleration algorithm.

In the following analysis, ***the staring point (m3) found by the "3σ + window + Hertz" algorithm was used***, as it is more reasonable as discussed above. The force-displacement data of the microcapsule in Figure 3-11a and microsphere in Figure 3-11b were calculated using Equations (3-7) and (3-8), and their curves are shown in Figure 3-13a and b, respectively. It can be seen from Figure 3-13a that the force-displacement curve of the self-sensing microcapsule is not very smooth, with some local peaks before rupture that might be due to

the roughness of the outer-layer PUF as shown in Figure 3-14a (Roche et al., 2022; Song et al., 2019). The outer layer could crack several times before the rupture point shown in Figure 3-13a, where the inner shell was ruptured, and the force dropped sharply. In contrast, the force-displacement curve of the PS microsphere is quite smooth before rupture, as its shell was smooth Figure 3-14b (Li et al., 2021b). However, the force at the rupture point did not drop as dramatically as the self-sensing microcapsule since there was no release of any material from the PS microsphere at the rupture point.

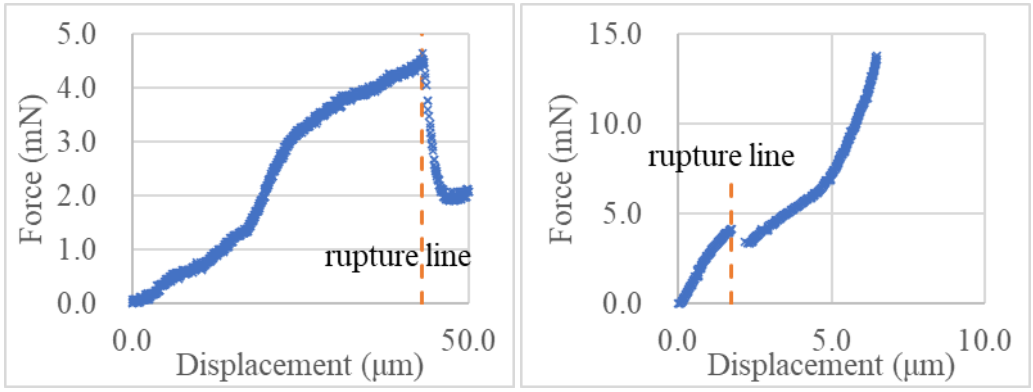

(a) (b)

Figure 3-13 The force-displacement curves obtained for the experimental data of the self-sensing microcapsule (a) and the PS microsphere (b) in Figure 3-11a and b.

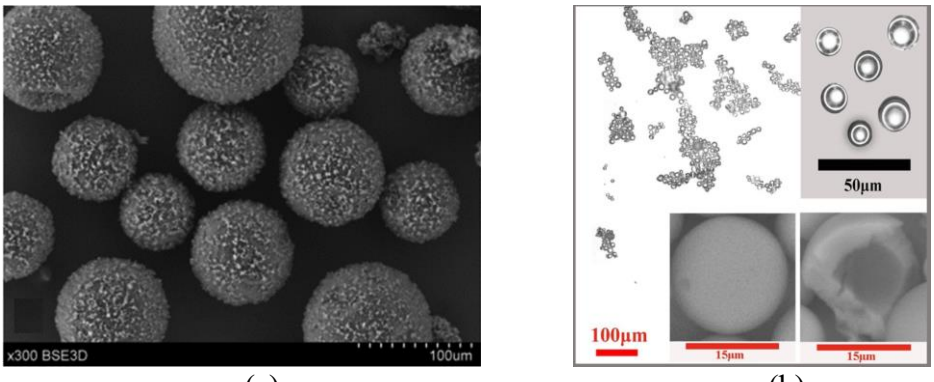

(a) (b)

Figure 3-14 SEM images of the self-sensing microcapsules (a) and the porous PS microspheres (b) (Roche et al., 2022; Li et al., 2021b).

(a)

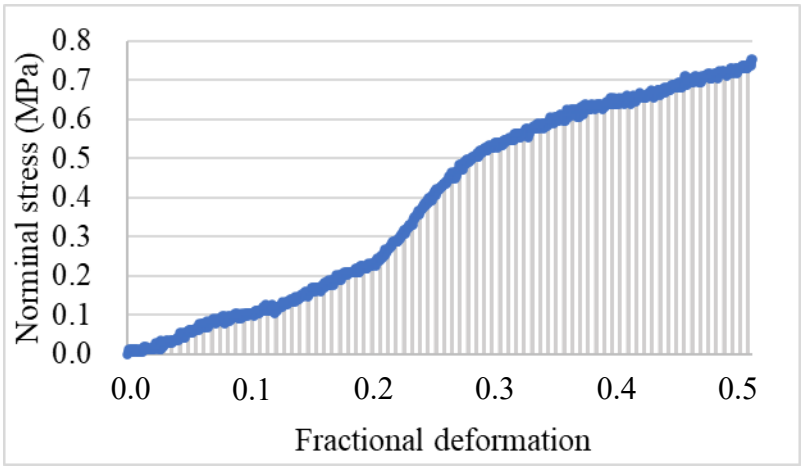

(b)

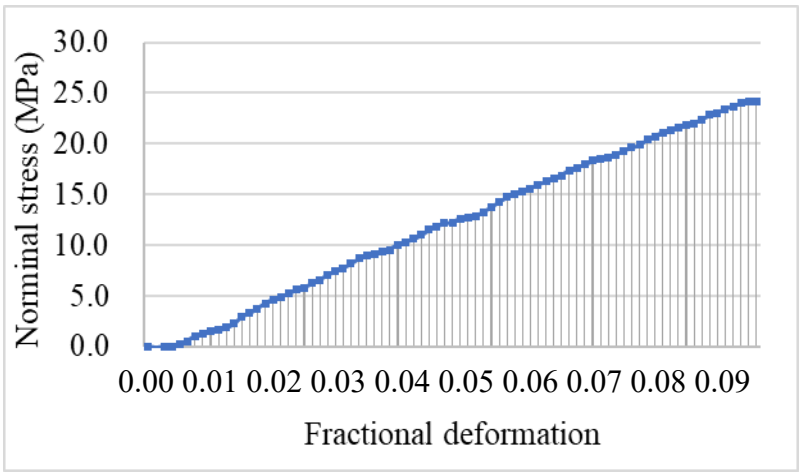

Figure 3-15 Nominal stress versus fractional deformation up to rupture of the self-sensing microcapsule (a) and the PS microsphere (b) in Figure 3-11a and b

The nominal stress-fractional deformation data up to rupture of the self-sensing microcapsule and PS microsphere in Figure 3-11a and b was calculated using Equation (3-9) and (3-10), and their curves are shown in Figure 3-15a and b respectively. The starting points used were m3 in Figure 3-12a and b, found using the "3σ + window + Hertz" algorithm. The toughness of them were 0.19MPa and 1.15 MPa respectively, calculated using the trapezoidal numerical integration in Equation (3-11), corresponding to the area under the curves up to rupture.

The experimental data of 50 self-sensing microcapsules and 50 PS microspheres were analysed

using the developed software package, and a manual analysis was also carried out for comparison. The average and standard error of the calculated rupture strength parameters for the two samples are shown in Table 3-2 and Table 3-3. It appears that for the two samples, the average rupture force values from the automatic data analyses are all the same as those from the manual analysis, which shows that the "maximum-deceleration" algorithm is very robust to locate the rupture point. So are the average values of nominal rupture stress, nominal rupture tension and the toughness as the former two parameters are calculated from the rupture force and the diameter of the microparticles. Although the toughness is related to the fractional deformation, which depends on the starting point, the force values are very small around the starting point so that the effect on the integration of the nominal stress over the fractional deformation (i.e., the toughness value) is negligible. Thus, the average values of the toughness from the four analyses show no significant difference. The values of the displacement at rupture from "3σ + window" and "3σ + window + Hertz" overlap with the results from the manual analysis. Because of the appearance of impulse noises, the values of displacement at rupture and deformation at rupture from "3σ" algorithm appear to be different significantly from the manual analysis results. It was found that the starting points for nearly half (24/50) of the tested self-sensing microcapsules and 17/50 of the porous PS microspheres were not correctly identified using the "3σ" algorithm.

Based on the data of these two samples, the results obtained from using "3σ + window" and "3σ + window + Hertz" algorithms have no significant difference from the manual results so

that they both can be used in the automatic analysis of the rupture strength of microparticles.

Table 3-2 Rupture strength of the self-sensing microcapsules obtained from different algorithms

Algorithm	$\boldsymbol{D}$ **(μm)**	δ_r **(μm)**	F_r **(mN)**	$\boldsymbol{\varepsilon_r}$ **(%)**	$\boldsymbol{\sigma_r}$ **(MPa)**	$\boldsymbol{T_r}$ **(μN/μm)**	$\boldsymbol{T_c}$ **(MPa)**
Manual	86.2±3.1	40.5±1.4	4.61±0.22	47.7±1.1	0.85±0.05	53.8±2.2	0.19±0.01
3σ	86.2±3.1	44.7±1.7	4.61±0.22	52.6±1.5	0.85±0.05	53.8±2.2	0.19±0.01
3σ + Window	86.2±3.1	39.0±1.4	4.61±0.22	45.7±1.1	0.85±0.05	53.8±2.2	0.19±0.01
3σ + Window + Hertz	86.2±3.1	41.0±1.4	4.61±0.22	48.2±1.1	0.85±0.05	53.8±2.2	0.19±0.01

Table 3-3 Rupture strength of the porous PS microspheres obtained from different algorithms

Algorithm	$\boldsymbol{D}$ **(μm)**	δ_r **(μm)**	F_r **(mN)**	$\boldsymbol{\varepsilon_r}$ **(%)**	$\boldsymbol{\sigma_r}$ **(MPa)**	$\boldsymbol{T_r}$ **(μN/μm)**	$\boldsymbol{T_c}$ **(MPa)**
Manual	11.1±0.4	1.3±0.1	2.53±0.15	12.0±0.4	26.4±1.2	223.0±9.9	1.73±0.11
3σ	11.1±0.4	2.5±0.3	2.53±0.15	21.9±2.3	26.4±1.2	223.0±9.9	1.73±0.11
3σ + Window	11.1±0.4	1.3±0.1	2.53±0.15	11.9±0.4	26.4±1.2	223.0±9.9	1.73±0.11
3σ + Window + Hertz	11.1±0.4	1.4±0.1	2.53±0.15	12.7±0.4	26.4±1.2	223.0±9.9	1.73±0.11

3.3.2. Further Discussion

From the data presented in Table 3-2 and Table 3-3, it appears that the fractional deformation at rupture of the self-sensing microcapsules is quite big (nearly 50%) in comparison with that of the porous PS microspheres (just around 12%). This indicates that the self-sensing

microcapsules with double PUF-PU shells showed a ductile failure behaviour, while the porous PS microspheres showed a brittle failure behaviour (Mercadé-Prieto et al., 2012). However, the nominal rupture stress of the former (0.85 MPa) is much smaller than the latter (26.4 MPa). This might result from the large difference in the particle sizes between the two samples since the nominal rupture stress normally decreases with the increasing particle diameter (Hu et al., 2009). The values of the diameter for the self-sensing microcapsules and PS microspheres are 86.2 ± 3.1 μm and 11.1 ± 0.4 μm, respectively. Moreover, the nominal rupture tension of the self-sensing microcapsules (53.9 μN/μm) is also much smaller than that of the porous PS microspheres (227.9 μN/μm). This is reasonable, as the former had a liquid core surrounded by a solid shell with thickness between 200 and 500 nm (Roche et al., 2022), whilst the latter were solid with a few pores on the surface (Li et al., 2021b). The mean toughness value of the porous microspheres was also greater, as it is related to the nominal stress versus fractional deformation up to rupture.

The nominal rupture tension and the toughness versus diameter of the two samples of individual microspheres are illustrated in Figure 3-16. Statistical analysis of the data shows that the nominal rupture tension does not change with diameter for each sample significantly (Figure 3-16a, b), which can be used to compare the mechanical strength between samples with particles of different sizes. In contrast, the toughness decreases with the diameter, which indicates bigger particles were weaker than smaller ones (Figure 3-16c, d), similar to the nominal rupture stress (Hu et al., 2009).

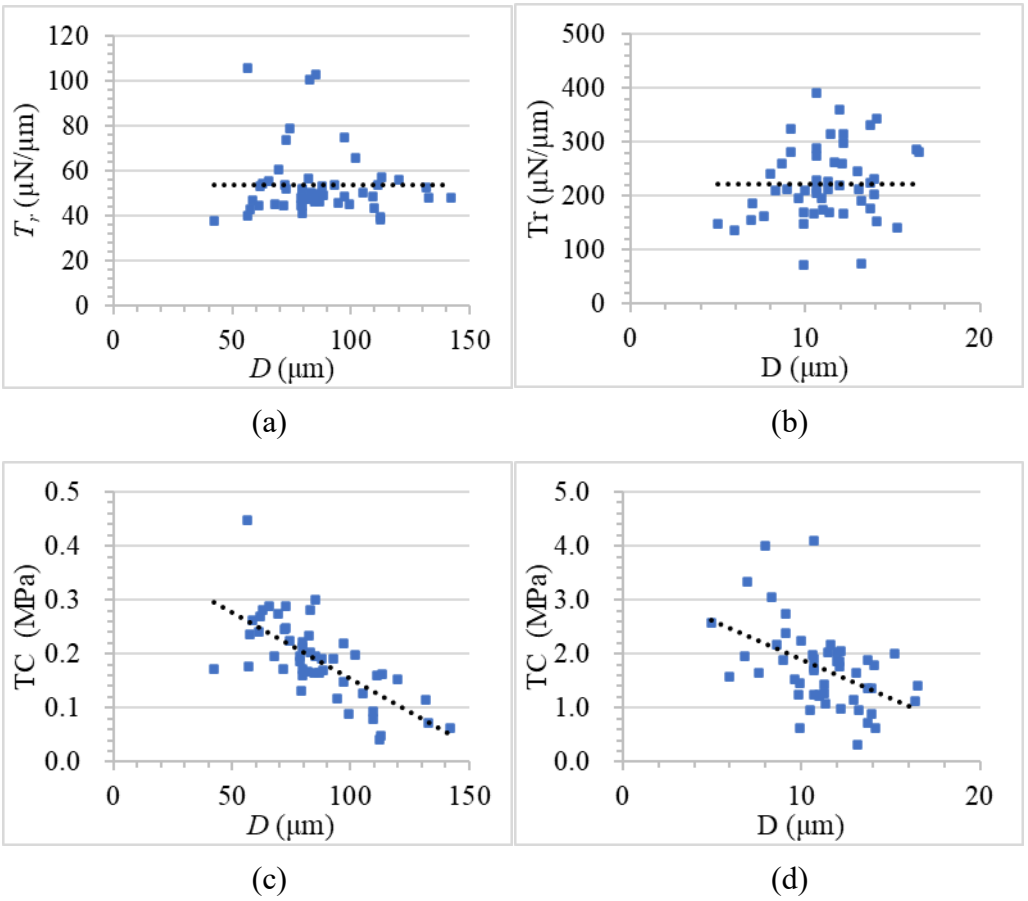

Figure 3-16 Data of the nominal rupture tension and toughness versus diameter of the two samples. (a): nominal rupture tension of the self-sensing microcapsules; (b): nominal rupture tension of the porous PS microspheres; (c): toughness of the self-sensing microcapsules and (d): toughness of the porous PS microspheres. Each fitted line (dotted) only indicates the trend.

3.3.3. Comparison with Other Algorithms

The standard deviation was used in several algorithms to evaluate the noise level of the raw data and to help estimate the parameters of the algorithms to identify CP for AFM force data (BenÍtez et al., 2013; Chang et al., 2014; Charles et al., 2012; Gergely et al., 2001). A moving window was also introduced to help the identification of the CP (BenÍtez et al., 2013; Chang et al., 2014). However, it was only used for local regression rather than dealing with the

impulse noise as addressed by the "3σ+ window" algorithm. Besides, the width of the moving window needs to be set manually in the reported algorithms, whilst it is estimated automatically by Equation (3-16) in the "3σ + window" and "3σ + window + Hertz" algorithms developed in this work. Furthermore, the algorithm in Chang et al. (2014) pre-estimates a CP* with a threshold of five standard deviations of the baseline values and then determines the CP by fitting force-displacement data into a Hertz-like model from CP* to an indentation depth empirically determined by the stiffness of the force curve. The "3σ + window + Hertz" algorithm also pre-estimates a prone starting point m' followed by the regression of the force-displacement data within 5% fractional deformation to the Hertz model to determine the real starting point m in this work. However, these two algorithms have two main differences. One is that the "3σ + window" algorithm is used to estimate the prone starting point, which can well deal with the impulse noises in the "3σ + window + Hertz" algorithm, whereas CP* is just estimated with a threshold of five standard deviations of the baseline values (Chang et al., 2014), which may result in a wrong value when the impulse noise greater than the threshold exists before the real CP. The other difference is that after the Hertz regression, the CoD is used in Equation (3-20) to adjust the degree of the compensation automatically so that when the tested material is not linear ealstic, fewer points will be compensated to m'. (The CoD values for the self-sensing microcapsules and the porous PS microspheres were 0.83 ± 0.02 and 0.97 ± 0.01 respectively.) In contrast, the algorithm reported in (Chang et al., 2014) was designed for linear elastic materials and cannot adjust automatically for other mechanical

behaviours of the tested materials. Besides, using the "maximum-deceleration" algorithm for the detection of rupture point in this work requires no parameter to be adjusted and is fully automatic, which is advantageous.

3.4 Conclusions

In this study, a data analysis software package was developed to analyse the rupture strength of microparticles automatically from the experimental data of micromanipulation measurements. Three algorithms were developed to find the starting point of the compression data, i.e., the "3σ", "3σ + window" and "3σ + window + Hertz". The "3σ" algorithm determines the starting point where the voltage of a point deviates from the mean of baseline (V_B) by three standard deviations ($3S_B$), whilst in the "3σ + window" algorithm, a point is determined as the starting point only if the following w points (including this point) all deviate from V_B by $3S_B$. In the "3σ + window + Hertz" algorithm, the starting point is further adjusted by fitting the force-displacement data corresponding to very small deformations (up to 5% fractional deformation) into the Hertz model to compensate the underestimation of the displacement corresponding to the three standard deviations. One algorithm based on the maximum deceleration of the voltage series was developed to determine the rupture point. The results show that the combination of the "3σ + window" or "3σ + window + Hertz" algorithm with the "maximum-deceleration" algorithm can produce results that are in excellent agreement with those obtained manually, and there is no significant difference between them. Moreover, all the developed algorithms work fully automatically without any parameter modification.

For analysing 50 microparticles in a typical sample, the time spent on analysing the rupture strength parameters manually was from 2 to 3 h. In contrast, it took less than 20 min to analyse the same data automatically using the software package developed in this work. It is believed that this software package can also be used to analyse the force-displacement data obtained using conventional mechanical testing machines for macro-scale materials, which can have a wide range of applications.

****N.B.** This Chapter is based on and adapted from our published paper (Zhang et al., 2022) whose **primary author is the author** of this PhD thesis.

CHAPTER 4: DEVELOPMENT OF A COMPUTER SOFTWARE PACKAGE TO DETERMINE THE INTRINSIC MECHANICAL PROPERTIES OF MICROPARTICLES

4.1 Introduction

With the utilisation of the software package developed as described in Chapter 3, the rupture strength parameters can be obtained and the relationship between each rupture strength parameter versus diameter of single particles can be established automatically, which can provide important technical data to compare the mechanical strength of microparticles from different samples prepared under different formulations and/or processing conditions.

However, as aforementioned in Section 2.2.3.1 the rupture strength parameters of microparticles are not their intrinsic mechanical property parameters, since they might depend on the size of microparticles and particular method of measurement (Zhang et al., 2009). Several mathematical models, including the Hertz model, Tatara model (Zhang et al., 2009), viscoelastic model (Mattice et al., 2006; Yan et al., 2009), core/shell model based on FEM simulation results (Mercadé-Prieto et al., 2011b), and Abbott & Firestone plastic model (Paul et al., 2014), have been developed that can be used to determine the intrinsic mechanical properties of microparticles from the data obtained using the micromanipulation technique. Undertaking the analysis with these models manually is quite time-consuming. Therefore, it is important to develop a software package which can be used to fulfil the task automatically.

Moreover, various force versus displacement data (or force versus time data) from other material tests, both in macroscale and microscale, including the tension and compression tests, micro indentation and nanoindentation tests, can be obtained, which also require similar analysis to that from micromanipulation. Ideally, a software package should be developed, which can be widely used to analyse the force-displacement (or force-time) data from various material tests. Besides, the apparent Young's modulus value of a microcapsule determined using the Hertz model by treating it as a homogeneous sphere is always smaller than that of its shell material, which can be calculated using analytical or numerical analysis (Lulevich et al., 2004; Mercadé-Prieto et al., 2011b; Zhang et al., 2020), and their relationship remains to be established.

The research presented in this chapter is not only aimed to develop a software package incorporated with some typical mathematical models to determine the intrinsic mechanical properties more easily and faster, but also aimed to develop some general principles that can be followed by researchers to deal with related problems in other applications. Some typical mathematical models for elastic and plastic analysis, are summarised and general equations of the relationship between force and displacement have been derived, based on which, general approaches to extend the elastic and plastic analysis to viscoelastic and viscoplastic analysis have been developed following the method of Yan et al. (2009). An algorithm to automatically determine the yield stress of microcapsules from the elastic limit, has been developed based on the method of Mercadé-Prieto et al. (2011a) and Zhang (2019). The principles to incorporate

different mathematical models into the software package have been devised and several typical models have been built into the software package. The relationship between the apparent Young's modulus of a microcapsule determined using the Hertz model and that of its shell material determined by the FEM simulation results (Mercadé-Prieto et al., 2011b) have been studied and established. Two samples of microparticles, i.e., the PLA microspheres and the MF microcapsules with lily oil as core material, have been tested using the micromanipulation technique and their data have been analysed using the developed software package incorporated with mathematical models to determine their intrinsic mechanical properties and to validate the developed software package as well as the mathematical models built in.

4.2 Mathematical models to obtain intrinsic mechanical properties from uniaxial tests

4.2.1. Elastic analysis

4.2.1.1. Hook's law

When a body is deformed within the elastic range, the normal stress σ and the strain ξ can be modelled with the following equation according to Hook's law (Müller et al., 2005):

$$\sigma = E \cdot \xi \tag{4-1}$$

where E is the Young's modulus. The aim of elastic analysis is to determine the value of the Young's modulus of the tested material to quantify its ability to resist elastic deformation. The equivalent loading force F can be calculated by

$$F = \int_A \sigma \, dA = E \int_A \xi \, dA \tag{4-2}$$

For one-dimensional materials under uniaxial loading, the strain ξ can be represented by

$$\xi = \frac{\Delta L}{L_0} = \frac{\delta}{L_0} \tag{4-3}$$

where δ is the displacement caused by the applied force F, L_0 is the initial length before deformation, and ΔL is the difference of the length before and after deformation. The contact area is determined by the morphology of the tested material and the displacement δ and thus can be expressed as a function of δ

$$A = f_1(\delta) \tag{4-4}$$

Combining Equation (4-2) to (4-4) results in the following Equation

$$F = E \int_{f_1(\delta)} \frac{\delta}{L_0} \, df_1(\delta) \tag{4-5}$$

Let $f(\delta) = \int_{f_2(\delta)} \frac{\delta}{L_0} \, df_1(\delta)$ and the relationship between the loading force and the displacement can be expressed as follows

$$F = E \cdot f(\delta) \tag{4-6}$$

The form of the function $f(\delta)$ can vary with the morphology of the tested materials and the model used.

Specifically, some models can be expressed in the form of the following equation (Briscoe et al., 1994)

$$F = n_1 \cdot E \cdot \delta^{n_2} \tag{4-7}$$

and

$$f(\delta) = n_1 \delta^{n_2} \tag{4-8}$$

where n_1 is related to the morphology of the tested microparticles but independent of the

displacement δ and n_2 is a real number.

4.2.1.2. Hertz analysis

For diametrical compression of a linear elastic homogenous microsphere, the Hertz model (Zhang et al., 2009) can be used to relate the loading force (F) and the corresponding displacement (δ) as the following equation

$$F = \frac{E\sqrt{2R}}{3(1-\psi^2)}\delta^{\frac{3}{2}} \tag{4-9}$$

where R is the radius and ψ is the Poisson's ratio of the microparticle. The constraints for using the Hertz model are summarised in Section 2.2.3.2.

4.2.1.3. FEM analysis for core/shell-structured microparticles

Mercadé-Prieto et al. (2011b) proposed a model based on finite element modelling (FEM) that can be used to determine the intrinsic mechanical properties of microcapsules with a core/shell structure tested using the micromanipulation technique. In this model, the compression force F can be expressed as

$$\frac{F}{ERh} = p_1\varepsilon^2 + p_2\varepsilon + p_3, \qquad 0.03 < \varepsilon < 0.1 \tag{4-10}$$

where $\frac{F}{ERh}$ is termed as dimensionless force, h is the shell thickness, ε is the fractional deformation obtained from Equation (3-10) and the three coefficients p_1, p_2, p_3 are correlated with h/R (denoted by x = 0.004 – 0.14) by Equations (4-11) to (4-13)

$$p_1 = 95071.891x^5 - 28426.030x^4 + 2411.056x^3 - 7.476x^2 - 10.829x + 1.52882 \tag{4-11}$$

$$p_2 = -318.702x^4 + 120.784x^3 - 11.380x^2 + 2.518x - 0.05792 \quad (4\text{-}12)$$

$$p_3 = -0.004242x + 0.00107 \quad (4\text{-}13)$$

Substituting Equations (4-11) to (4-13) into Equation (4-10) and re-arranging it leads to the following equation

$$\begin{aligned} F = ExR^2[&(95071.891x^5 - 28426.030x^4 + 2411.056x^3 \\ &- 7.476x^2 - 10.829x + 1.52882)\varepsilon^2 \\ &+ (-318.702x^4 + 120.784x^3 - 11.380x^2 \\ &+ 2.518x - 0.05792)\varepsilon + (-0.004242x \\ &+ 0.00107)] \end{aligned} \quad (4\text{-}14)$$

For given F-ε data and radius R, the Young's modulus E and ratio of shell thickness to radius h/R can be determined by comparing the experimental force profile with FEM simulation results, theoretically speaking. However, this is not easy to implement. To overcome the issue, Zhang (2019) devised an approach to determine the Young's modulus and shell thickness using Microsoft™ Excel Solver based on the least squares method, which will be incorporated into the developed software package (see Section 4.3.2.3).

It is worth pointing out that this FEM model (including the coefficients) is **purely geometric** except that the shell material is assumed to be linearly elastic and therefore it can be used for core-shelled microcapsules made from a large range of materials

4.2.1.4. Relationship between the Hertz and core/shell models for core/shell structured materials

For a core/shell structured microparticle, let apparent Young's modulus calculated using Hertz analysis be E_H and Young's modulus of the shell obtained from the FEM be E_S. As the force in both models is equal for a given fractional deformation, combination of Equations (4-9) and (4-10) leads to

$$\frac{4}{3}\frac{\sqrt{R}}{2^{1.5}}\frac{E_H}{1-\psi^2}\delta^{\frac{3}{2}} = E_S R h(p_1\varepsilon^2 + p_2\varepsilon + p_3) \tag{4-15}$$

The displacement δ and fractional deformation ε are connected by the following equation:

$$\varepsilon = \frac{\delta}{2R} \tag{4-16}$$

Thus

$$\frac{E_H}{E_S} = \frac{3}{4}\cdot(1-\psi^2)\cdot\frac{h}{R}\cdot(p_1\varepsilon^{0.5} + p_2\varepsilon^{-0.5} + p_3\varepsilon^{-1.5}) \tag{4-17}$$

With Equation (4-17), if the shell thickness of single microcapsules is known, the Young's modulus of the shell material can be calculated from the apparent Young's modulus determined using the Hertz model, which is much easier to be carried out than using the approach proposed by (Mercadé-Prieto et al., 2011b).

4.2.2. Plastic analysis

4.2.2.1. Determination of the yield stress of microcapsules based on elastic limit and FEM analysis

For deformations just beyond the elastic limit, Mercadé-Prieto et al. (2011a) modelled the shell

material of core/shell microparticles (i.e. microcapsules) as a perfectly plastic material using FEM and presented three methods to estimate the yield stress σ_Y, respectively from the slope of the dimensionless force (F/ERh) varying with yield stress ratio (σ_E/E) at a given fractional deformation (0.3-0.45) corresponding to plastic deformation for MF microcapsules since their relationship is linear based on the FEM simulation results, the pseudo-yield point where the force profile changes from concave to convex (Sun & Zhang, 2001; Sun & Zhang, 2002), and the elastic limit where the experimental force starts to deviate from the predicted force based on the pure elastic model (Section 2.2.3.6). Among them, the method based on the elastic limit is easy to be implemented and the procedure is listed as follows (Zhang, 2019):

1) fit the force-displacement data within the elastic range (e.g. up to 10% fractional deformation, which is appropriate for melamine formaldehyde shell (Sun & Zhang, 2001)) to obtain the parameters of the elastic model,

2) use the obtained elastic model to predict the force $\hat{F}$ up to high deformation, e.g., 20% fractional deformation, as the fractional deformation at elastic limit (ε_{LE}) for melamine formaldehyde shell is usually less than 0.2 (Mercadé-Prieto et al., 2011a),

3) look through the predicted elastic force corresponding to $0.1 < \varepsilon < 0.2$ and locate ε_{LE} where the experimental force significantly deviates from the predicted elastic force,

4) calculate the yield stress σ_Y at the elastic limit using the following equation (Mercadé-Prieto et al., 2011a),

$$\sigma_Y = \sigma_{LE} = E \cdot \frac{\varepsilon_{LE} + 3.833(h/R)^2 - 0.93\, h/R + 0.011}{1.95\ (h/R)^{-0.126}} \qquad (4\text{-}18)$$

4.2.2.2. Plastic models for uniaxial loading

When the uniaxial loading is beyond the elastic regime, irreversible or permanent deformation will happen (Kelly, 2013). If the permanent deformation is time independent, then a plastic model can be used to characterise the plastic loading process. The relationship between the force (F) and contact area (A) during plastic compression can be expressed as follows (Kelly, 2013; Paul et al., 2014):

$$F = HA \tag{4-19}$$

where H is the hardness, a parameter to characterise how strong the material can resist the plastic deformation. The contact area A can be seen as a function of the displacement δ, denoted by $A(\delta)$, and Equation (4-19) can be expressed as

$$F = HA(\delta) \tag{4-20}$$

The form of $A(\delta)$ is determined by δ and the morphology of the tested material. For instance, in the Abbott & Firestone model, within the range of small strains (the maximum contact radius $a < 0.2\,R$) of microspheres normally compressed between two flat surfaces, it can be evaluated as follows (Paul et al., 2014; Yap et al., 2008)

$$\begin{aligned} A(\delta) &= \pi R\delta \\ F &= \pi RH\delta \end{aligned} \tag{4-21}$$

where the δ here is the total displacement rather than half of it as in Yap et al. (2008).

4.2.3. Viscoelastic analysis

4.2.3.1. A general approach to extend elastic analysis to viscoelastic analysis

The mathematical relationship between the Young's modulus E and the shear modulus G is

$$G = \frac{E}{2(1+\psi)} \tag{4-22}$$

Combining Equation (4-6) with (4-22) leading to the following equation

$$F = (1+\psi) \cdot 2G \cdot f(\delta) \tag{4-23}$$

Following the approach of Yan et al. (2009), replacing the constant term $2G$ by the time-varying shear modulus $G(t)$ leading to

$$F(t) = (1+\psi) \cdot G(t) \cdot f(\delta) \tag{4-24}$$

During the relaxation,

$$G(t) = C_0 + \sum_{i=1}^{n} C_i e^{-\frac{t}{\tau_i}} \tag{4-25}$$

and

$$F(t) = B_0 + \sum_{i=1}^{n} B_i e^{-\frac{t}{\tau_i}} \tag{4-26}$$

where τ_i is the relaxation time. The relationship between C_0, C_i and B_0, B_i are

$$B_0 = (1+\psi) \cdot f(\delta_0) \cdot C_0 \tag{4-27}$$

and

$$B_i = (1+\psi) \cdot f(\delta_0) \cdot \Phi_i \cdot C_i \tag{4-28}$$

where Φ_i is the ramp correction factor given by

$$\Phi_{\mathrm{i}} = \frac{\tau_i}{t_R}(e^{t_R/\tau_i} - 1) \tag{4-29}$$

where t_R is the rising time from the onset of loading to the onset of relaxation.

Then from the coefficients C_0, C_1, C_2, …, C_n, the instantaneous shear modulus G_0 and long-term shear modulus G_∞ can be estimated by

$$G_0 = \frac{\sum_{i=0}^{n} C_i}{2} \tag{4-30}$$

and

$$G_\infty = \frac{C_0}{2} \tag{4-31}$$

The corresponding instantaneous Young's modulus E_0 and long-term Young's modulus E_∞ can be calculated by

$$E_0 = 2(1+\psi)G_0 \tag{4-32}$$

and

$$E_\infty = 2(1+\psi)G_\infty \tag{4-33}$$

Then the following equation can be used to predict the loading force data with the parameters obtained during the relaxation

$$F(t) = (1+\psi)\cdot\int_0^t G(t-u)\cdot\left\{\frac{d}{du}f[\delta(u)]\right\}du \tag{4-34}$$

Especially, for the elastic model in Equation (4-7), if the compliance of the force transducer is negligible,

$$\delta(t) = vt \tag{4-35}$$

where v is the loading speed. Substituting Equations (4-8) and (4-35) into Equation (4-34) leads to the following equation

$$F(t) = (1+\psi)n_1 v^{n_2}(C_0 t^{n_2} + n_2 \sum_{i=1}^{n} C_i {\tau_i}^{n_2} e^{-\frac{t}{\tau_i}} \cdot \int_0^{\frac{t}{\tau_i}} u^{n_2-1} e^u \, du) \quad (4\text{-}36)$$

The integral part $\int_0^{\frac{t}{\tau_i}} u^{n_2-1} e^u \, du$ can be solved by numerical integration if it cannot be solved analytically.

4.2.4. Viscoplastic analysis

4.2.4.1. A general approach to extend plastic analysis to viscoplastic analysis

For rate-dependent plastic materials, the hardness H is rate-dependent, and viscoplastic analysis can be used to characterise their intrinsic mechanical properties. Following the approach of Yan et al. (2009), during relaxation, replacing the time-invariant hardness H in Equation (4-20) with the time-dependent value $\frac{1}{2}H(t)$ leads to

$$F(t) = \frac{1}{2}H(t) \cdot A(\delta) \quad (4\text{-}37)$$

where $F(t)$ is expressed in Equation (4-26) and

$$H(t) = C_0 + \sum_{i=1}^{n} C_i e^{-t/\tau_i} \quad (4\text{-}38)$$

The relationship between C_0, C_i and B_0, B_i are

$$B_0 = \frac{1}{2}A(\delta_0) \cdot C_0 \quad (4\text{-}39)$$

and

$$B_i = \frac{1}{2}A(\delta_0) \cdot \Phi_i \cdot C_i \quad (4\text{-}40)$$

where Φ_i is the ramp correction factor given by Equation (4-29). Then the instantaneous hardness H_0 and long-term hardness H_∞ can be estimated by

$$H_0 = \frac{\sum_{i=1}^{n} C_i}{2} \tag{4-41}$$

and

$$H_\infty = \frac{C_0}{2} \tag{4-42}$$

Then the following equation can be used to predict the loading force with the parameters obtained using the relaxation data

$$F(t) = \int_0^t H(t-u) \cdot \left\{ \frac{d}{du} A[\delta(u)] \right\} du \tag{4-43}$$

Specifically, for microspheres of viscoplasticity tested by the micromanipulation technique, if the compliance of the force transducer is negligible, the displacement $\delta(t)$ can also be expressed as Equation (4-35). Substituting Equation (4-21) and (4-35) into Equation (4-43) results in the following Equation

$$F(t) = \pi R v [C_0 t + \sum_{i=1}^{n} C_i \tau_i (1 - e^{-\frac{t}{\tau_i}})] \tag{4-44}$$

4.3 Incorporation of mathematical models into the software package

4.3.1. Different strategies to incorporate the models

Ideally, the mathematical models as many as possible should be built into the software package to ensure its flexibility and extensive utilisation. But this will be unrealistic because of the time and resource limits. To enhance its flexibility and utilisation within limited resources, the following strategies are used:

Strategy 1: Models that can be solved analytically will be fully incorporated into the software package without the interaction with other applications., e.g., the Hertz model in Equation (4-

9) and the Abbott & Firestone plastic model in Equation (4-21).

Strategy 2: Models that cannot be solved analytically will be partially incorporated into the software package and function by interacting with other professional data analysis applications such as Microsoft™ Excel Solver. The core/shell model based on the FEM simulation results (Section 4.2.1.3) and the viscoelastic model (Section 4.2.3.1) will be built in this way.

4.3.2. Incorporation of the elastic models

4.3.2.1. General approach

For the elastic model in Equation (4-6), the procedure to obtain the Young's modulus from the experimental data can be illustrated in Figure 4-1.

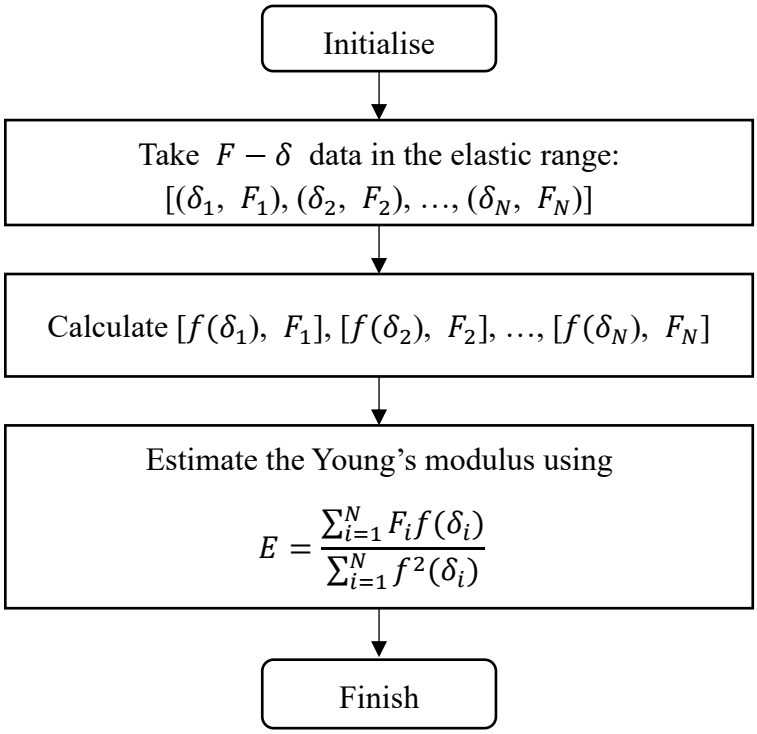

Figure 4-1 Basic flowchart of the elastic analysis

For force-displacement data in the elastic range, usually up to 10% fractional deformation, (δ_1,

F_1), (δ_2, F_2), …, (δ_N, F_N), calculating [$f(\delta_1)$, F_1], [$f(\delta_2)$, F_2], …, [$f(\delta_N)$, F_N], and fitting them into a line through origin, the Young's modulus E can be estimated with the least-squares estimator as follows

$$E = \frac{\sum_{i=1}^{N} F_i f(\delta_i)}{\sum_{i=1}^{N} f^2(\delta_i)} \tag{4-45}$$

Alternatively, the elastic model in Equation (4-7) can be incorporated into the software package by first calculating δ^{n_2} in Equation (4-7) rather than $f(\delta)$ in Equation (4-6). For force-displacement data in the elastic range (the range can be changed through the software), (δ_1, F_1), (δ_2, F_2), …, (δ_n, F_N), let $x_i = \delta_i^{n_2}$, $y_i = F_i$, $i = 1,2,\dots,n$, calculating (x_1, y_1), (x_2, y_2), …, (x_N, y_N) and fitting them into a line through origin: $y(x) = k_e x$, the coefficient k_e can be obtained with the least-squares estimator as follows

$$k_e = \frac{\sum_{i=1}^{N} y_i x_i}{\sum_{i=1}^{N} x_i^2} \tag{4-46}$$

Then the Young's modulus E can be calculated from the coefficient k_e as follows:

$$E = \frac{k_e}{n_1} \tag{4-47}$$

4.3.2.2. Incorporation of the Hertz model

For the Hertz model in Equation (4-9), it has been built using the approach described in last section, by just letting

$$n_1 = \frac{\sqrt{2R}}{3(1-\psi^2)} \tag{4-48}$$

and

$$n_2 = 1.5 \tag{4-49}$$

Before using this method, make sure the assumptions of the model are satisfied, i.e., the particle should be spherical, linear elastic, homogenous with a Young's modulus far less than that of the force transducer probe and the glass substrate, and the friction with the ends of the probe and the substrate is negligible.

4.3.2.3. Incorporation of the FEM simulation results for microcapsules

The FEM simulation results for microcapsules in Equation (4-14) cannot be used analytically to determine the values of Young's modulus and the ratio of shell thickness to radius from the experimental data. The procedure proposed by Mercadé-Prieto et al. (2011b) involves the comparison of the experimental force profile with the FEM simulation results, which is not easy to be carried out automatically. A method was introduced by Zhang (2019) to determine the Young's modulus and shell thickness using Microsoft™ Excel Solver based on the least squares method using optimisation algorithms, which has inspired to develop Strategy 2 mentioned in Section 4.3.1. Briefly, the raw experimental data is preprocessed by the developed software package and written to an excel template to solve by optimisation, after which the obtained Young's modulus E and the ratio of shell thickness to radius (h/R) are read back to the software package for postprocessing. The specifical procedure is as follows:

1) Selecting the force-displacement data up to 10% fractional deformation, calculating the fractional deformation ε for every point, and fitting the force and fractional deformation data into a quadratic equation (Equation (4-50)), which tends to fit the experimental data very well, then the coefficients q_1 and q_2 can be obtained.

$$F_s = q_1\varepsilon^2 + q_2\varepsilon \tag{4-50}$$

2) Using q_1, q_2 and ε to calculate the smoothed force F_s in $\varepsilon = 0.03, 0.04, \ldots, 0.10$. Then the smoothed force F_s and the fractional deformation ε corresponding to $\varepsilon = 0.03, 0.04, \ldots, 0.10$ are written into the excel template which will be opened and forwarded to the user automatically. The predicted force $\hat{F}$ is estimated from Equation (4-14) and the aim is to minimize the squared differences between $\hat{F}$ and the smoothed force F_s by adjusting the values of E and h/R as in Equation (4-51).

$$\min_{E,\ h/R} \sum_{\varepsilon=0.03}^{0.10} (\hat{F} - F_s)^2 \tag{4-51}$$

After optimisation, the Young's modulus of shell E and shell thickness to radius ratio h/R are determined in Excel Solver (Zhang, 2019), and their results will be read back to the software for post processing.

4.3.3. Incorporation of the Plastic models

4.3.3.1. General approach

The general approach to incorporate the plastic analysis model in Equation (4-20) is quite similar to that in Section 4.3.2.1. Its basic flowchart is illustrated in Figure 4-2. Briefly, for the force-displacement data in the linear plastic range $(\delta_1,\ F_1)$, $(\delta_2,\ F_2)$, …, $(\delta_N,\ F_N)$, calculating $[A(\delta_1),\ F_1]$, $[A(\delta_2),\ F_2]$, …, $[A(\delta_N),\ F_N]$, and fitting them into a line through origin, the hardness H can be estimated with the least-squares estimator as follows

$$H = \frac{\sum_{i=1}^{N} F_i A(\delta_i)}{\sum_{i=1}^{N} A^2(\delta_i)} \tag{4-52}$$

Currently, the Abbott & Firestone plastic model for diametrical compression in Equation (4-21) is built into the software package.

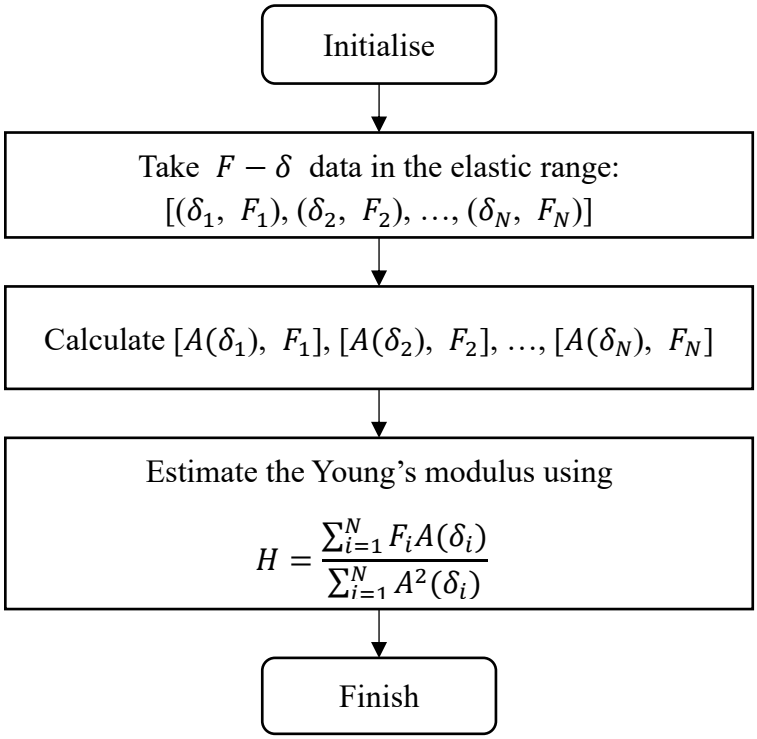

Figure 4-2 Basic flowchart of the plastic analysis

4.3.3.2. Determination of the yield stress of microcapsules based on elastic limit

Based on the method described in Section 4.2.2.1, for a compressed microparticle satisfying the conditions of the core/shell elastic model based on the FEM simulation results, the force-displacement data in the initial part (e.g., up to 10% factional deformation) is first fitted into the elastic model, i.e., Equation (4-14). Thus, the elastic parameters are obtained. Then the elastic parameters are used to predict the loading force $\hat{F}$ and using a window with a width of w to identify the elastic limit when all the predicted force in the window deviates significantly from the experimental data, i.e., the elastic limit index le is located when the

following equation is satisfied

$$\bigwedge_{i=le}^{w+le} (\hat{F}_i - F_i > 0) == true \tag{4-53}$$

Then the yield stress can be calculated using Equation (4-18). The value of w can be estimated using Equation (3-16).

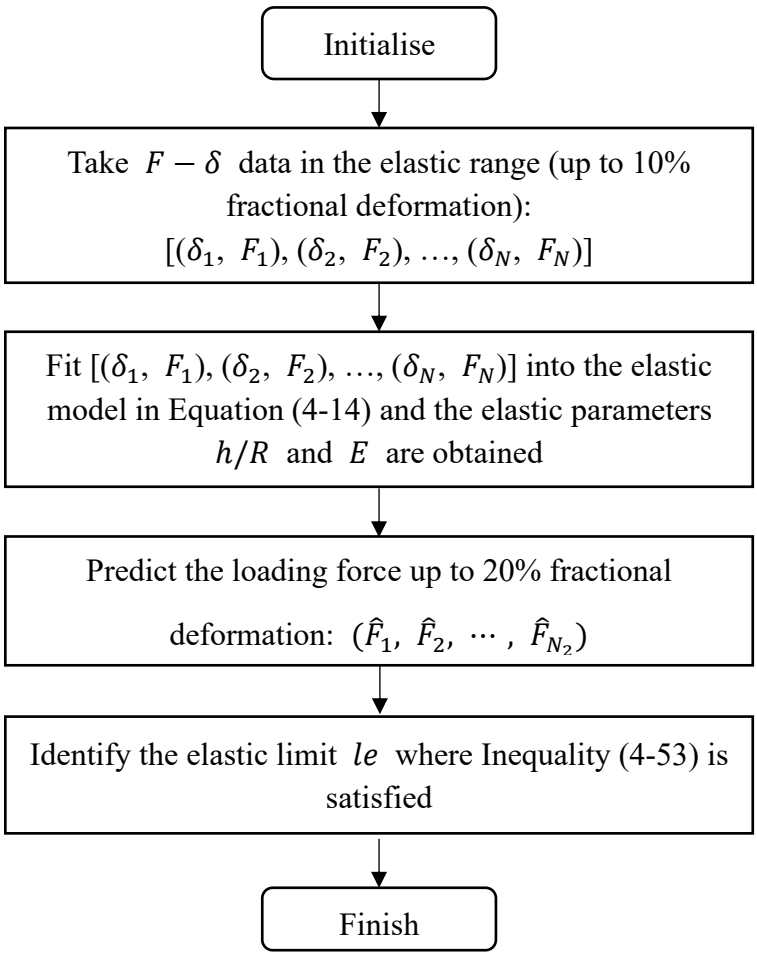

Figure 4-3 Flowchart to determine the yield stress of microcapsules from elastic limit

4.3.4. Incorporation of the viscoelastic model

The viscoelastic model with index $n \geq 2$ as shown in Equation (4-26) cannot be used analytically to determine the model parameters from experimental data. Therefore, it is incorporated by interacting with the Microsoft™ Excel Solver. Briefly, the force-time data

during holding is firstly extracted from the loading-holding experimental data and written into an excel template for viscoelastic analysis. The excel template will be popped up to the users to determine the viscoelastic parameters in Excel Solver by numerical optimisation to minimise the sum of squared difference between the predicted force $\hat{F}_i$ and the experimental force F_i based on the following equation

$$\min_{B_0,B_1,\cdots B_n,\tau_1,\cdots,\tau_n} \sum_{i=1}^{N} (\hat{F}_i - F_i)^2 \qquad (4\text{-}54)$$

where the predicted force $\hat{F}_i$ is calculated using Equation (4-26), N is the number of data points during the holding experiment. When a solution is reached, the obtained parameters including B_0, B_1, …, B_n, τ_1, τ_2, …, τ_n will be read back to the software package and the coefficients C_0, C_1, …, C_n will be obtained using Equation (4-27) and (4-28). Then the instantaneous and long-term shear and Young's moduli can be obtained using Equation (4-30) to (4-33). The force during compression will be predicted using Equation (4-36).

The default value of n is 2, which is sufficiently precise to represent the force varying with time data from typical holding experiments (Yan et al., 2009).

4.3.5. Development of the software package with the mathematical models

The software package with the mathematical models to obtain the intrinsic mechanical properties of microparticles were incorporated into the rupture strength analysis software package by adding the developed functions into the data read and conversion module, the data processing and analysis module, and the report generating module in Figure 3-9.

A function was added into the data read and conversion module to read the force-displacement data generated in the rupture strength analysis to be used by the data processing and analysis module to process. Functions were also added to allow the raw experimental data of voltage versus time that is used by the rupture strength analysis software package can still be used for the analysis of the mathematical models in this chapter.

Functions were added into the data processing and analysis module to obtain the force displacement data up to 10% fractional deformation (the specific percent value can be changed from the GUI) and to fit the data into the Hertz model and the core-shell model based on the FEM simulation results as described above automatically to obtain the values of the elastic parameters. Functions were added to locate the peak point (just by finding the maximum of force values) of the force-time data from the loading-holding experiments and to split the experimental data into loading and holding. Then the viscoelastic analysis can be undertaken using the incorporated functions as presented in Section 4.2.3.1. Functions were also added to analyse the plasticity of microspheres from the force-displacement data but the plastic segment needs selecting manually by the users currently.

Functions were added to the report generating module to output reports of the intrinsic mechanical properties of microparticles from using the incorporated mathematical models.

Currently, the Hertz model, the viscoelastic model, the core-shell model based on FEM simulation results and the Abbott & Firestone plastic model described in Section 4.2 have been incorporated into the developed software package.

Extra open-source libraries used in the development of this software package are listed in Table 4-1 (only libraries not listed in Table 3-1 are listed here).

Table 4-1 Open-source libraries used in the development of the software package

Library	Version	License
Microsoft.Office.Interop.Excel	15.0.4795.1000	https://www.nuget.org/packages/Microsoft.Office.Interop.Excel (accessed on 24 July 2022)

4.4 Mechanical characterisation of PLA microspheres with data analysis using the developed software package with incorporated models

4.4.1. Micromanipulation of PLA microspheres

The tested PLA microspheres were fabricated and provided by Dr Yanping He and her students in School of Chemical Engineering, Kunming University of Science and Technology, China, prepared using an improved solvent evaporation method via a foam-transfer methodology similar to that of preparing the PS microspheres as shown in Figure 3-2. The detailed procedure is reported by (Li et al., 2021a). Specifically, Sample A5 (oil/water ratio = 30:100) were tested in this work. The micromanipulation procedure of the PLA microspheres was the same as the measurement of the self-sensing microspheres as described in Section 3.2.2.1.

Totally, 30 PLA microspheres were tested under ambient temperature of 26 ± 2 ℃. The force transducer model used was GS0-10 (Transducer Techniques, LLC, Temecula, CA, USA) with a sensitivity of 7.42 mN/V, and the compression speed was 2 μm/s. The sampling frequency was 53 Hz and the total sampling time for each single particle was 15-60 s. Figure 4-4

illustrates a typical PLA microsphere to be compressed.

Figure 4-4 A PLA microsphere to be compressed (diameter: 28.3 µm)

4.4.2. Plastic analysis results of PLA microspheres

A typical force-displacement data from compression of the PLA microspheres is shown in Figure 4-5. The force increases linearly with the displacement from the very beginning which can be described by the Abbott & Firestone plastic model in Section 4.2.2.2. Fitting the force-displacement data in the initial linear section into Equation (4-21), the obtained hardness was 100.1 MPa and the *CoD* was 0.99 that indicates good fitting. The experimental and predicted (straight line) force data from the plastic model are shown in Figure 4-6.

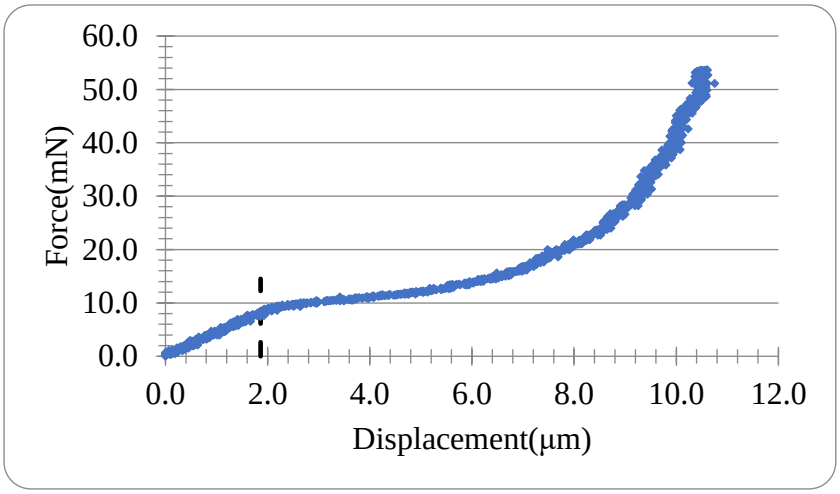

Figure 4-5 Force-displacement curve of the tested PLA microsphere as shown in Figure 4-4

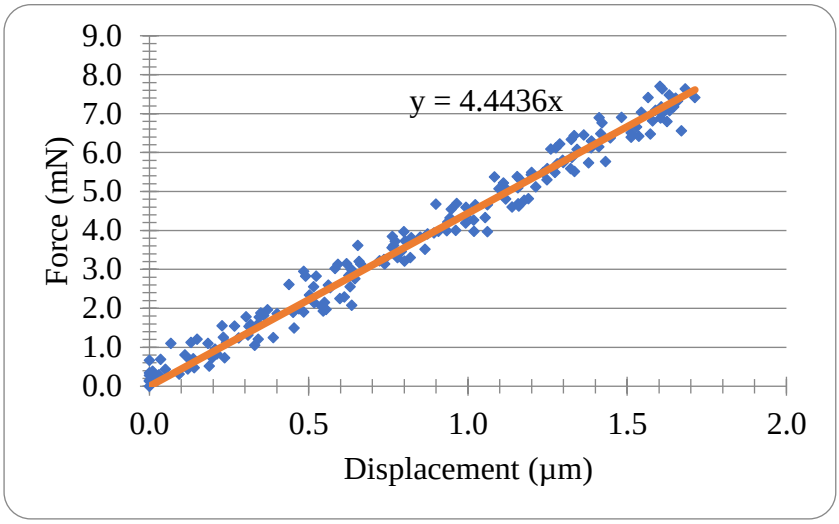

Figure 4-6 Fitting of the force versus displacement data from compression of the PLA microsphere in Figure 4-4 using the plastic model (Equation (4-21))

The experimental data of 30 tested PLA microspheres were analysed using the developed software package. The mean values of the diameter and the hardness of the 30 PLA microspheres are 45.5 ± 3.9 µm and 90.1 ± 8.2 MPa respectively, which is quite consistent with the reported values of around 80MPa (Shore Hardness) of PLA cuboids (thickness: ~3mm) (Teymoorzadeh & Rodrigue, 2015), 80-100 MPa (Shore Hardness) of 3D printed PLA specimen (thickness: around 3mm) (Vian & Denton, 2018), and around 95 MPa (Shore Hardness) of PLA film (Gong et al., 2017). It should be noted that the hardness value can be affected by the molecular weight, crystallinity and stereochemical makeup of the backbone of the PLA samples (Garlotta, 2001).

The hardness versus the diameter of the 30 PLA microspheres is illustrated in Figure 4-7. It can be seen that among the tested microspheres, several (6/30) PLA microspheres had very small hardness values (<40MPa) in comparison with the others, which suggests that microparticles in the same batch can show different properties. Similar results were observed

for those MF microcapsules tested by Mercadé-Prieto et al. (2011b).

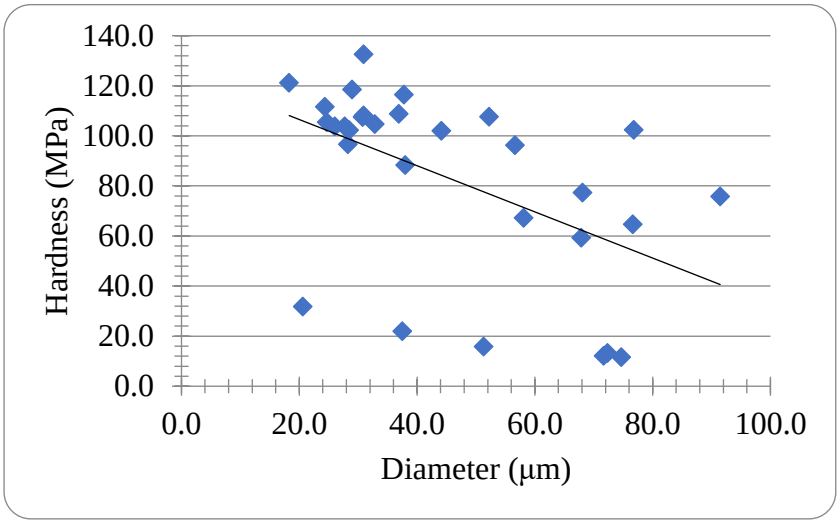

Figure 4-7 Hardness versus diameter of the tested PLA microspheres.

It appears that the hardness decreases with the increase of the diameter (the slope is from -1.5 to -0.34 MPa/μm with 95% confidence), which is usually referred to as size effect on mechanical properties (He et al., 2009; He et al., 2008; Mordehai et al., 2011).

The stress-strain curves of several polymer microparticles, including acrylic copolymer (AC) (size: 3.0-4.8 μm), and polystyrene-co-divinylbenzene (PS-DVB) microparticles (size: 2.6-25.1 μm), obtained from compression between a diamond flat probe and a silicon substrate were also found to be size dependent (He et al., 2009; He et al., 2008). It was found that the size effect was mainly due to the inhomogeneity of crosslink distribution, which resulted in a stronger surface shell and relatively weaker core. (However, unlike microcapsules, there is no sharp interface between the so-called shell and core.) As the shell was relatively thicker in small particles, small particles are relatively stronger than big ones (He et al., 2009; He et al., 2008). Similarly, in our tests, the size effect on hardness of the PLA microspheres may result

from the different compactness and/or porosity of the microspheres.

4.5 Mechanical characterisation of MF microcapsules with a core of lily oil -micromanipulation measurements and data analysis using the developed software package with incorporated models

4.5.1. Micromanipulation of the MF microcapsules

The MF microcapsules were also fabricated and provided by Dr Yanping He and her students in School of Chemical Engineering, Kunming University of Science and Technology, China, preparing via in-situ polymerization. The detailed fabrication procedure is presented in Luo et al. (2022). Specifically, the Sample MGF1-1 was used. The shell material was MF and the core was lily oil. The MF microcapsules slurry were resuspended in distilled water (~100 μL/ 50 mL), and about 50 μL of obtained diluted suspension was deposited onto a glass slide and dried at a room temperature to expose the single microcapsules, which were compressed to rupture in the micromanipulation tests.

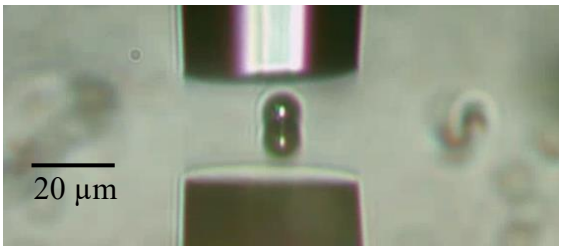

Figure 4-8 A MF microcapsule with lily oil to be compressed (diameter 9.4 μm)

Totally, 36 MF microcapsules with lily oil as liquid core were tested under ambient temperature of 17 ± 2 ℃. The transducer model used was 403B-HD (Aurora Scientific Inc., Canada) with a sensitivity of 0.50 mN/V. The sampling frequency was 53Hz and the total

acquisition time for each capsule was 5-10 s. The compression speed was 2 μm/s. Figure 4-8 illustrates an MF microcapsule to be compressed.

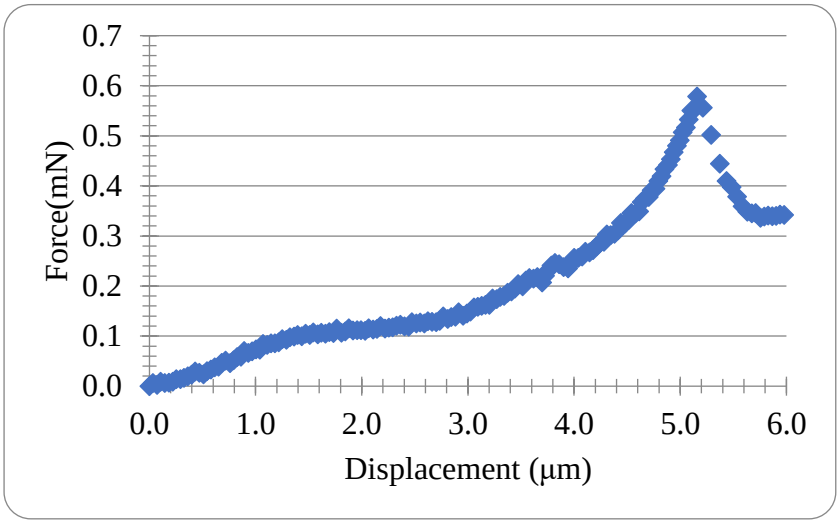

Figure 4-9 Force-displacement data of a tested MF microcapsule (Diameter = 9.4μm)

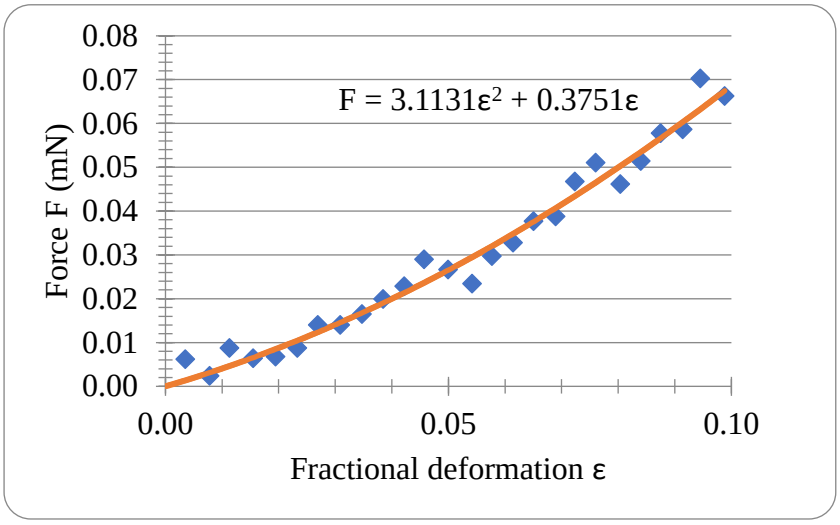

Figure 4-10 Fitting of the force versus fractional deformation data with the quadratic Equation (4-50) (line in orange, $CoD = 0.98$)

4.5.2. Determination of the shell Young's modulus and thickness of MF microcapsules

A typical force-displacement curve of the tested single MF microcapsules is illustrated in Figure 4-9. The force-displacement data was calculated from the raw voltage-sampling sequence data using the software package developed in Chapter 3 with the "3σ + window +

Hertz" algorithm (Section 3.2.4.3). By calculating the fractional deformation up to 10% and fitting the force-fractional deformation data to Equation (4-50), the results are as follows (Figure 4-10)

$$F_s = 3.1131\varepsilon^2 + 0.3751\varepsilon \quad (4\text{-}55)$$

The CoD is 0.98, which indicates good fitting.

The smoothed force values corresponding to fractional deformations at 0.03, 0.04, 0.05, 0.06, 0.07, 0.08, 0.09 and 0.10 calculated using Equation (4-55) are listed in Table 4-2.

Table 4-2 Smoothed force versus fractional deformation

ε	0.03	0.04	0.05	0.06	0.07	0.08	0.09	0.10
F_s (mN)	0.014	0.020	0.027	0.034	0.042	0.050	0.059	0.069

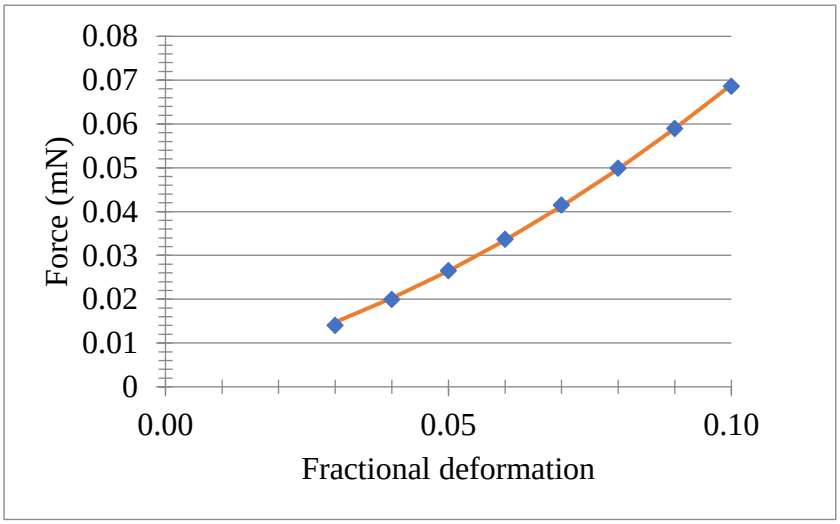

Figure 4-11 Force data obtained by optimisation. The line represents the predictions.

Then, the smoothed force-fractional deformation data in Table 4-2 was fitted into Equation (4-14) using Solver in Excel based on the least-squares method to minimise the deviation between the predicted force value and the corresponding experimental data, see Equation (4-51), and

the outcomes are shown in Figure 4-11. The CoD between the predicted force and the experimental force within 10% fractional deformation was 0.98, which indicates good optimisation. The search algorithm used was GRG nonlinear (Lasdon et al., 1978) in Excel. The Young's modulus (E) and the ratio of shell thickness to radius (h/R) obtained were 2.53 GPa and 0.063 respectively. The shell thickness (h) was 0.30 μm.

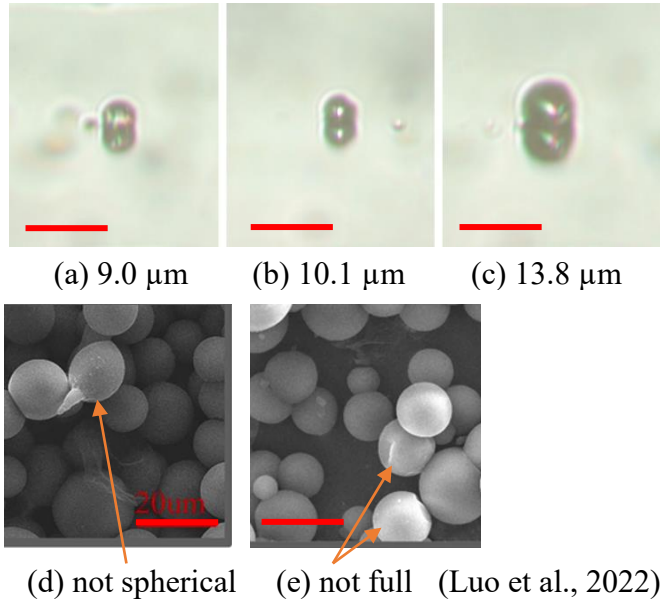

Figure 4-12 Tested MF microparticles not spherical or not full (scale bar: 20 μm)

Among the tested 36 microcapsules, some of them were not spherical or not full with lily oil as shown in Figure 4-12. When such single microcapsules were compressed, their force-displacement data profile (Figure 4-13), especially within the small fractional deformations, differed significantly from that of compression of single spherical MF microcapsules full of liquid (Figure 4-9). For example, the force-displacement curve up to 10% fractional deformation of a tested MF microcapsule is even convex rather than concave (for normal microcapsules) as illustrated in Figure 4-13. If such data was fitted into the FEM simulation

results (Equations (4-14) and (4-50)), the obtained parameters are not valid. Thus, such microcapsules that were not spherical or not full with lily oil have not been included when analysing the data of the MF microcapsules using the FEM simulation results. The exclusion of such capsules was undertaken following a strict procedure that includes inspecting images of tested microcapsules, regression results of force versus fractional deformation profiles, and CoD values. The microcapsules that were apparently irregular or not full, with abnormal force profiles and/or CoD less than 0.8 were excluded.

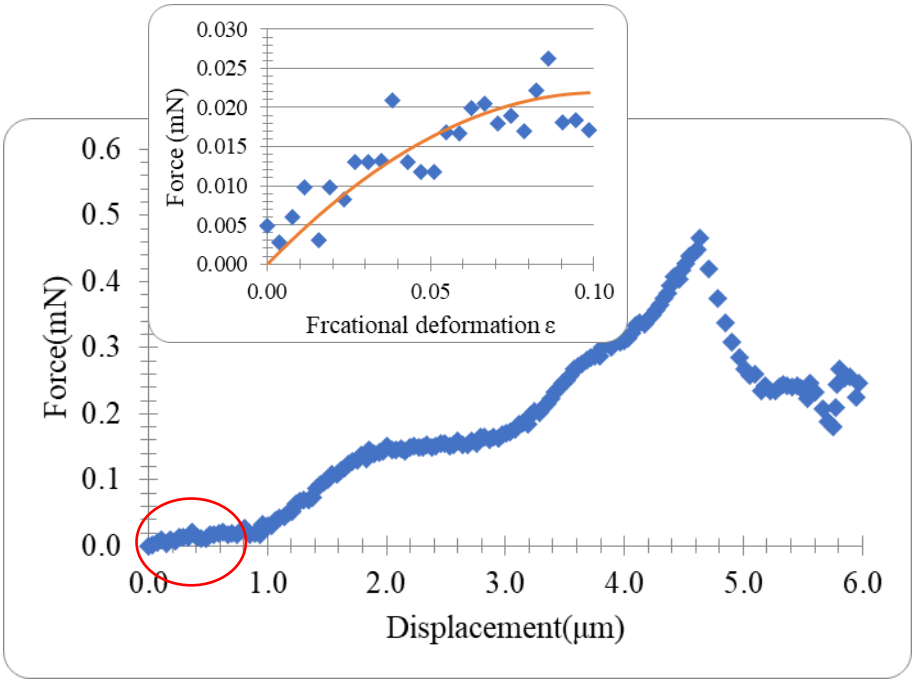

Figure 4-13 Force-displacement profile of a MF microcapsule not full with lily oil (diameter 9.0 μm)

Finally, experimental data of 29/36 tested MF microcapsules were analysed using the core/shell model based on the FEM simulation results using the developed software package in this Chapter. The average and standard error (SE) values of the calculated parameters are listed in Table 4-3. It appears that the shell thickness value 0.28 ± 0.03 μm (SE) is significantly

greater than the reported value 0.20 ± 0.01 μm of the MF microcapsules with hexyl salicylate oil as the liquid core tested in wet condition (Mercadé-Prieto et al., 2011b) and 0.19 ± 0.01 tested in dry condition (Mercadé-Prieto et al., 2011a). This is reasonable as the shell thickness depends on the formaldehyde /melamine (F/M) molar ratio, and it was found that, under the same processing conditions, the wall thickness increased by 14 ± 0.8% when the F/M molar ratio increased from 0.49 to 2.3 (Long et al., 2009). The molar ratio of the total formaldehyde content to melamine was 3.0 for MF microcapsules tested in this project but 0.49 for the MF microcapsules tested by Mercadé-Prieto et al. (2011a; 2011b).

The Young's modulus value 2.9 ± 0.3 GPa is significantly greater than the reported value 1.6 ± 0.3 GPa of MF microcapsules tested in wet condition which is reasonable as the MF microcapsules with lily oil were tested in dry condition in this study and the Young's modulus of MF microcapsules can be significantly increased by drying (Mercadé-Prieto et al., 2011a). However, the Young's modulus value (2.9 ± 0.3 GPa) is significantly smaller than the reported value 4.8 ± 0.4 GPa also tested in dry condition (Mercadé-Prieto et al., 2011a). This might result from different formulations and processing conditions used to prepare these microcapsules. For example, the emulsion was formed under 1000 rpm, 40 ℃ for around 40 minutes for the capsules tested in this project but under 1500 rpm, 15 ℃ for about 30 minutes for those tested by Mercadé-Prieto et al. (2011a; 2011b). The reaction time was only 2h for the capsules tested in this work but 4h for those tested by Mercadé-Prieto et al. (2011a; 2011b) and different reaction time can affect the compactness of the MF shell depositing on the surface

of the core oil. Moreover, the encapsulated liquid core was lily oil for the capsules studied here but hexyl salicylate for those studied by Mercadé-Prieto et al. (2011a; 2011b). It was found that the encapsulated liquid oil can affect the mechanical strength of the microcapsules significantly because of different hydrophobicity and viscosity of fragrance oil (Luo et al., 2022).

Table 4-3 FEM analysis results of the MF microcapsules (average ± SE)

***D* (μm)**	***h/r* (%)**	***E* (GPa)**	***h* (μm)**
10.0 ± 0.8	6.7 ± 0.7	2.9 ± 0.3	0.28 ± 0.03

Moreover, although the FEM simulation results is reported only suitable to process microcapsules whose h/R values are in the range of 0.004 to 0.12 (Mercadé-Prieto et al., 2011b), experimental data of some (4/29) MF microcapsules with h/R ratio values of 0.12-0.15 are successfully processed with the developed software package incorporated with the FEM simulation results followed by the optimisation approach in Section 4.3.2.3. The overall values of CoD between the predicted force value from the model and the experimental force are all greater than 0.95. This suggests that the FEM simulation results for MF microcapsules with core/shell structure are very powerful.

One limit of the original approach by comparing the profile of the experimental force with that of FEM simulation results (Mercadé-Prieto et al., 2011b) is that profiles of compression force normalised with that at 0.1 fractional deformation ($F/F_{0.1}$) at large h/R ratio (e.g. >12%) are increasingly linear as illustrated in Figure 4-14 so that it is not easy to distinguish them by manual inspection. However, slight difference still exists among them that can be identified

by the optimisation algorithm incorporated into the developed software package which enhances the capability of the FEM simulation results significantly.

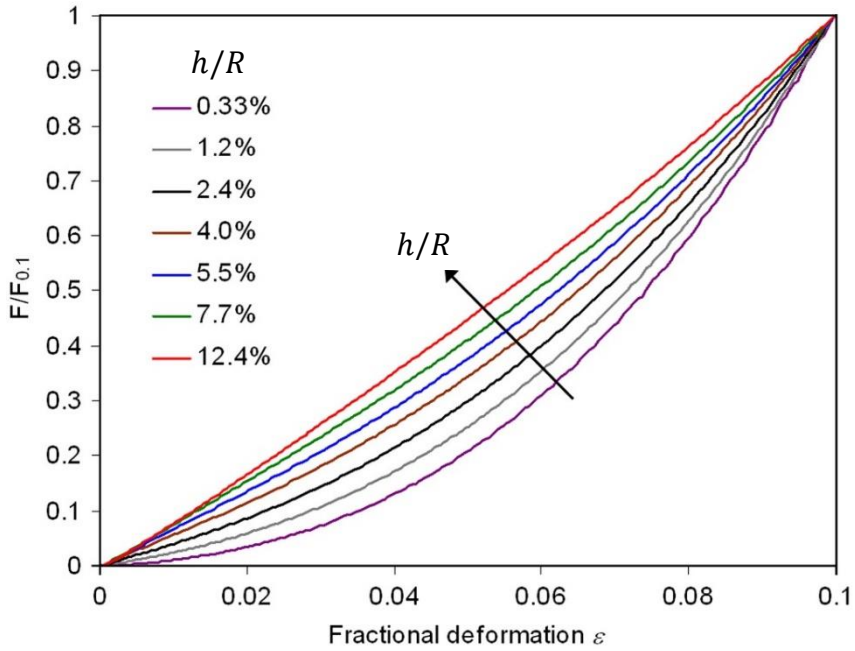

Figure 4-14 Curves of compression force normalised with that at 0.1 fractional deformation versus fractional deformation of MF microcapsules with different h/R generated by FEM (Mercadé-Prieto et al., 2011b)

4.5.3. Hertz analysis of the MF microcapsules

The force-displacement data up to 10% fractional deformation of the microcapsule shown in Figure 4-9 was also fitted into the Hertz model (Equation (4-9)) as illustrated in Figure 4-15 and the CoD was 0.97 indicating good fitting. The apparent Young's modulus value obtained was 0.056 GPa. It is much smaller than the Young's modulus value of 2.53 GPa obtained from the core/shell analysis. This difference is expected, because the apparent Young's modulus obtained from the Hertz analysis represents the overall stiffness of the core liquid and the shell material, whilst the value obtained from the core/shell analysis only indicates the latter.

The Young's modulus (E_S) value of the FM shell was also predicted from E_H (0.056 GPa) using Equation (4-17) to be 2.57 GPa, which is very consistent with the value obtained from the core/shell analysis directly (2.56 GPa).

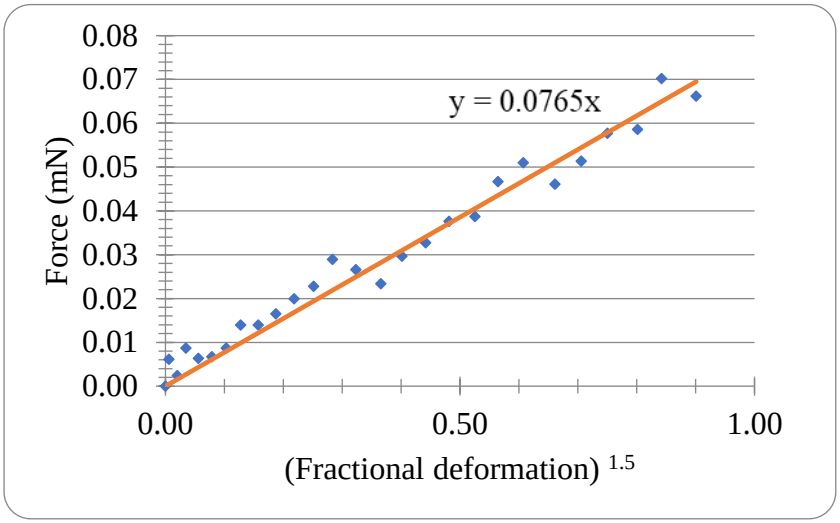

Figure 4-15 The force versus fractional deformation data of the MF microcapsule in Figure 4-9 (diameter 9.4 µm) fitted by the Hertz model (straight line). The CoD value is 0.97.

The average apparent Young's modulus value of the 29 MF microcapsules (analysed in last section) obtained from using the Hertz analysis was 61.4 ± 7.5 MPa. Using them and Equation (4-17), the Young's modulus values (E_S) of the MF shell has been predicted to be 2.90 ± 0.27 GPa, which is perfectly consistent with the value obtained directly from the core/shell analysis (2.92 ± 0.29 GPa). This validated the relationship established between the Hertz model and the core/shell model based on FEM simulation results for the same microcapsules (Equation (4-17)). Moreover, the relationship validates the FEM simulation results as well as providing another method to estimate the Young's modulus of the shell material of microcapsules from the Hertz analysis that is easier to be carried out if the shell thickness is known.

4.5.4. Yield stress of the MF microcapsules

Substituting the values of Young's modulus E, shell thickness to radius ratio h/R (x) of the MF microcapsule in Figure 4-9 into Equation (4-14), the force up to 20% fractional deformation can be predicted from the FEM analysis for microcapsules. The elastic limit (LE) can be determined where the predicted force (F-Pred) deviates from the experimental data (F) continuously as illustrated in Figure 4-16.

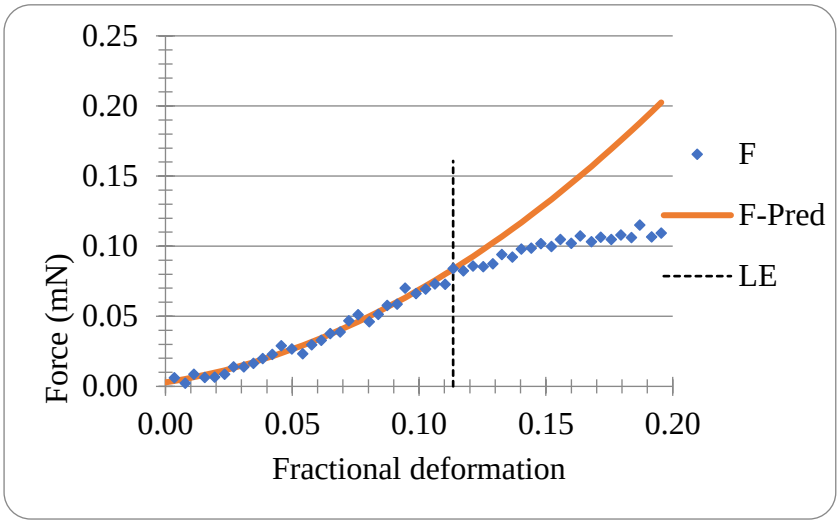

Figure 4-16 Determination of the elastic limit from the experimental force versus fractional deformation data and FEM simulation results for the MF microcapsule.

The elastic limit $\varepsilon_{LE} = 0.113$, and the yield stress $\sigma_Y = 88.8$ MPa, which was calculated from Equation (4-18). Using the same approach, the elastic limit and yield stress of the other MF microcapsules can be determined and their average values are 0.118 ± 0.002 and 97.8 ± 12.5 MPa respectively. The average of σ_Y/E is 0.032 ± 0.001, which is significantly greater than the reported value 0.024 ± 0.001 for MF microcapsules determined using the same approach (Mercadé-Prieto et al., 2011a). This is reasonable as the MF microcapsules here had relatively thicker shell (0.28 ± 0.03 μm) than the reported value (0.19 ± 0.1 μm) (Mercadé-

Prieto et al., 2011a) and because of the effects of bending and transverse shear, the thicker shell elements are subject to higher stresses at equal fractional deformation than thinner shell elements (Mercadé-Prieto et al., 2011a).

4.6 Conclusions

In this chapter, the models for elastic analysis and plastic analysis of micro-sized materials tested using micromanipulation, micro- and nano-indentation, and uniaxial tensile and compression techniques were summarised and the general equations of force versus displacement related to the intrinsic mechanical property parameters were developed. General approaches to extend elastic and plastic analysis to the viscoelastic and viscoplastic analysis were developed based on the well-established equations (Equations (4-6), (4-7) and (4-20)) following the method of Yan et al. (2009). An algorithm (Equation (4-53)) to determine the yield point of microcapsules from the elastic limit was introduced by comparing the force data predicted from the core/shell elastic model based on FEM simulation results and the experimental force data based on the method of Mercadé-Prieto et al. (2011a) and Zhang (2019).

A software package was developed to determine the intrinsic mechanical properties of micro-sized materials. The strategies and approaches to incorporate the different mathematical models, including the Hertz model, the core/shell model (Mercadé-Prieto et al., 2011b), the viscoelastic model (Yan et al., 2009) and the Abbott & Firestone plastic model (Paul et al., 2014), into the software package were developed and implemented based on the equations

(Equations (4-6), (4-7) and (4-21)).

The relationship between the Hertz model and the core/shell model (based on the FEM simulation results) was studied and an equation (Equation (4-16)) was derived relating the apparent Young's modulus E_H obtained from the Hertz model considering single microcapsules as homogenous spheres and the Young's modulus of the shell material E_S determined using the core/shell model. Therefore, if the shell thickness is known, the equation can be used to calculate the Young's modulus of the shell material from the apparent Young's modulus obtained using the Hertz model, which is easier to carry out.

Two typical micro-sized particle samples, the PLA microspheres and the MF microcapsules, were tested using the micromanipulation technique and their data were analysed using the newly developed software package incorporated with different mathematical models to determine their intrinsic mechanical properties.

The developed software package has been demonstrated to simplify the procedures of using the models and enhance the capabilities of the micromanipulation technique tremendously. It is believed that it can also be used to determine the intrinsic mechanical properties from using other techniques, e.g., using texter analyser to do mechanical characterisation of biological and non-biological materials, which can have a wide range of applications.

Moreover, the developed general equations and the incorporation strategies and approaches in this chapter can also be used by researchers or programmers for other relevant applications.

CHAPTER 5: MECHANICAL CHARACTERISATION OF MICRONEEDLES

5.1 Introduction

Among several types of microneedles developed in the past few decades, dissolvable microneedles made from biocompatible and biodegradable materials can potentially have a wide range of applications including sustained and controlled drug and vaccine delivery, and skin care because of their advantages including no sharp waste will remain after administration (Yang et al., 2019). Sustained release of loaded drug is easy to achieve by modifying the dissolvable microneedles with cross-linkable groups (Du et al., 2021a). Being mechanically strong enough to pierce the skin barrier is one of the most fundamental and crucial requirements for microneedles. However, dissolvable microneedles are mechanically weaker in comparison with those made of metals and glass (Faraji Rad et al., 2021). Therefore, precisely characterising their mechanical strength is essential to ensure their penetration capacity in academic research and new product development based on microneedles.

Several techniques have been used to test the mechanical strength of microneedles indirectly or directly. In indirect measurement, the mechanical strength of microneedles is estimated by that of macro samples prepared using the same material rather than from directly testing of the microneedles (Loizidou et al., 2015). However, the results obtained using this method can have great uncertainty, because the fabrication mechanism of the microneedles was not the same as that of the macro samples used in tensile tests which can result in different mechanical property

results.

To directly determine their mechanical strength, microneedles on a patch were usually tested together (Figure 2-18) and the average force of single microneedles was calculated by dividing the whole loading force by the number of microneedles on the patch (Davis et al., 2004; Fonseca et al., 2021; Gittard et al., 2013; Kim et al., 2018; Park et al., 2006; Wang et al., 2018). However, the possible variations of mechanical properties among single microneedles across the patch, which is very important to ensure their penetration efficiency, cannot be identified. Moreover, in most of such studies, the average failure force was used to characterise the mechanical strength of microneedles and to predict their penetration efficiency by comparing it with the insertion force required to pierce the skin with microneedles with the same geometric parameters, especially the tip size as the required insertion force was mainly determined by interfacial area at needle tip and the corresponding pressure (Davis et al., 2004; Park et al., 2006). Therefore, in order to carry out the comparison, the required insertion force of microneedles with the same or similar geometry needs to be determined first. Otherwise, it is not sufficient to draw conclusions simply using the failure force without knowing the geometrical and structural parameters of the tested microneedles as the failure force is not an intrinsic mechanical property for a given intrinsic mechanical strength (Du et al., 2021b).

AFM was used to determine the (relative) indentation hardness of single microneedles by indentation of their tips, and their penetration capacity was predicted by comparing the slope of the force-displacement curves of the microneedles with that of an artificial skin tested using

the same indentation probe (Dardano et al., 2015). However, the obtained hardness was local value corresponding to where the nanoindentation had been applied, and rupture parameters cannot be obtained because of the limit applied force that AFM can generate. Similar problems remain in other techniques for characterising the mechanical strength of single particles, including pressure probe (Boyer & Kramer, 1995), micropipette aspiration (Heinrich & Rawicz, 2005), and optical/magnetic tweezers (Neuman & Nagy, 2008) and they thus are not proper for determination of the mechanical strength of microneedles whose failure forces are usually in the range of milli-Newtons (Du et al., 2021b).

The micromanipulation technique widely used to determine the mechanical strength of single microparticles can generate loading force in the range of micro-Newtons to Newtons and thus is very suitable to measure the mechanical strength of singe microneedles. However, because of the different structures between microneedles and microparticles, the mathematical models used for microparticles cannot be used directly to analyse the experimental data of microneedles. Therefore, new mathematical models need to be developed to obtain their intrinsic mechanical property parameters, which can be used to compare the mechanical strength and predict the penetration efficiency of microneedles made of different formulations and processing conditions even without the knowledge of their geometrical or structural parameters.

In the work presented in a co-authored paper (Du et al., 2021b), the micromanipulation technique was used to test the HA-300kDa, Lido-HA300kDa and HA-10kDa microneedle

samples. Two mathematical models, including one to determine the mechanical strength at rupture (failure) and an elastic model to determine the Young's modulus of single microneedles from the micromanipulation experimental data. The data of the three microneedle samples were analysed using the two developed models and the obtained mechanical strength parameters including the rupture force, displacement at rupture, deformation at rupture, rupture stress and the Young's modulus were compared thoroughly and two major results were found, i.e., the loading of drug significantly decreased the mechanical strength of microneedles and higher molecular weight of HA resulted in higher Young's modulus. However, as illustrated in Section 5.3.1, the mechanical strength at rupture for microneedles may be not as relevant as that corresponding to maximum stress in characterising microneedles as the loading profile at failure might change because of significant bending. Moreover, it was found that the penetration efficiency of microneedles by impact insertion (high speed) was much higher than by manual insertion (low speed) (van der Maaden et al., 2014), which implies that the mechanical strength of microneedles can vary with the insertion procedure, including the insertion speed, i.e., the microneedles show some speed-dependent (viscoelastic) behaviour. Therefore, research needs to be carried out on their viscoelastic and/or viscoplastic behaviour. The research presented in this chapter is focused on the development of different mathematical models to comprehensively determine the mechanical strength of single microneedles and demonstration of their applications in predicting the penetration efficiency of microneedles using new batches of microneedle samples. Three mathematical models have been developed

to determine the mechanical strength parameters including those corresponding to maximum stress (MS), elastic parameters and viscoelastic parameters of single microneedles from the experimental data of the micromanipulation tests. Six samples of HA based microneedles with or without loading drug have been tested using the micromanipulation technique and their data have been analysed using the developed mathematical models to obtain intrinsic mechanical property parameters. Part of the results were published in two co-authored papers (Du et al., 2021a; Du et al., 2021b). Besides, the influence of drug loading and molecular weight of dissolvable microneedles on their mechanical strength based on using Lido-HA300kDa and HA-300kDa, and HA-10kDa and HA-300kDa microneedles had been systematically studied and published in the co-authored paper (Du et al., 2021b), which will not be repeated in this chapter.

5.2 Materials and methods

5.2.1. Fabrication of the dissolvable microneedles

In this study, the tested dissolvable microneedles were fabricated by micro moulding, and the detailed preparation procedure is reported elsewhere (Du et al., 2021a; Du et al., 2021b). The samples were made and provided by Dr. Guangsheng Du and his colleagues, in West China School of Pharmacy, Sichuan University, China. Briefly, polydimethylsiloxane (PDMS) moulds were firstly duplicated from the stainless-steel mould and the microneedle body parts were formed by compressing the solution of polymers (with or without drugs and other agents) into PDMS mould by pressured air. After being dried in controlled environment for a given

time, the microneedle base plate was prepared by adding pure hyaluronic acid (HA) to the PDMS mould. Finally, the microneedle patches were peeled off from the PDMS mould after drying for the required time.

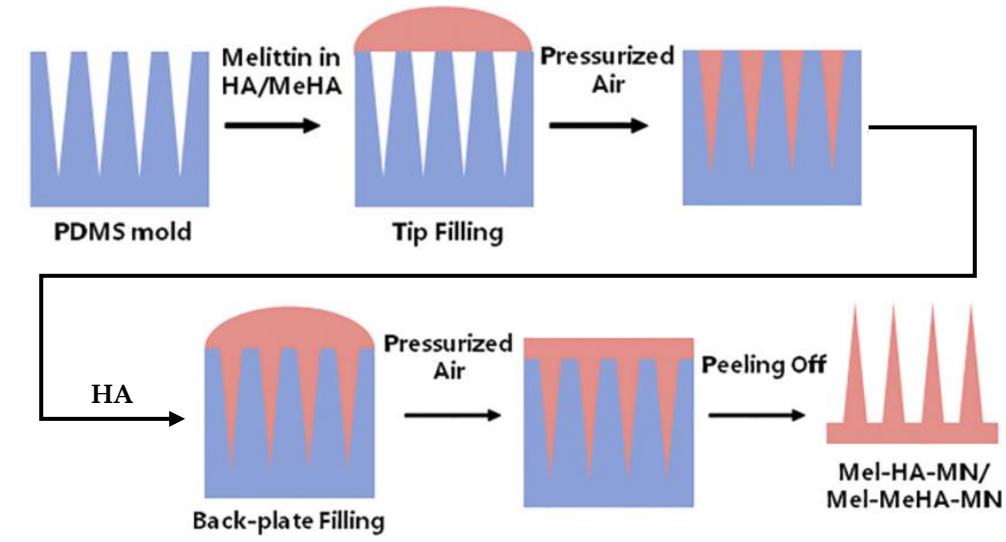

a)

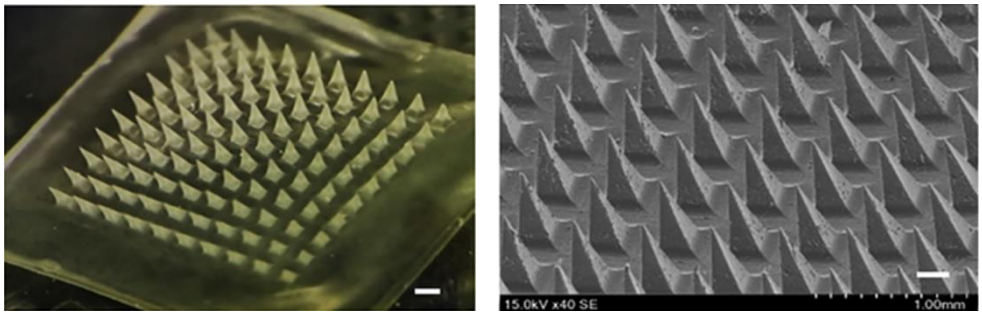

b) c)

Figure 5-1 Fabrication scheme (a) and representative bright field (b) and SEM (c) images for Mel-HA and Mel-MeHA microneedles tested. Scale bar: 200 µm (adapted from Du et al., 2021a)

Figure 5-1 illustrates a schematic diagram of the procedure to fabricate the Mel-HA and Mel-MeHA microneedles (Table 5-1) and their images from light microscopy and SEM (Du et al., 2021a). The single microneedles were pyramid shaped and 10 × 10 microneedles with a needle

length of 700 μm and base to base length of 300 μm were arrayed in one patch.

5.2.2. Microneedle samples tested

Six samples of microneedle based on hyaluronic acid (HA) with or without loading drug tested are listed in Table 5-1. Their detailed fabrication procedure and some of the mechanical strength data are reported elsewhere (Du et al., 2021a; Du et al., 2021b).

Table 5-1 Microneedle samples tested

Sample Number	Abbreviation name	Matrix
1	HA-300kDa	Hyaluronic acid (HA), MW: 300,000 Da
2	Lido-HA300kDa	Lidocaine + Hyaluronic acid (MW: 300,000 Da) Lidocaine to HA weight ratio 4:5
3	HA-10kDa	Hyaluronic acid (MW: 10,000 Da)
4	Mel-HA	Melittin loaded hyaluronic acid (MW: 10,000 Da) Melittin to HA weight ratio 1:9
5	MeHA	Methacrylate groups modified hyaluronic acid MeHA + N′-methylenebisacrylamide (MBA) + Irgacure 2959 (MW of HA: 10,000 Da) (MeHA to MBA to Irgacure weight ratio 80:40:1)
6	Mel-MeHA	Melittin loaded MeHA + MBA + Irgacure) (MW of HA: 10,000 Da) (Melittin to (MeHA + MBA + Irgacure) weight ratio 1:9, MeHA to MBA to Irgacure weight ratio 80:40:1)

5.2.3. Axial compression of single microneedles

In the micromanipulation tests, the bottom of a patch of microneedles was fixed to the surface of a glass slide using double-sided tape. The glass slide was fixed onto the sample stage of the

micromanipulation rig. Single microneedles were then compressed axially against the force transducer probe as illustrated in Figure 5-2. Loading and loading-holding tests were carried out. During the tests, the tip width ($2r_2$ in Figure 5-3 and Figure 5-5) was measured and **the other geometry parameters were calculated in the analysis.**

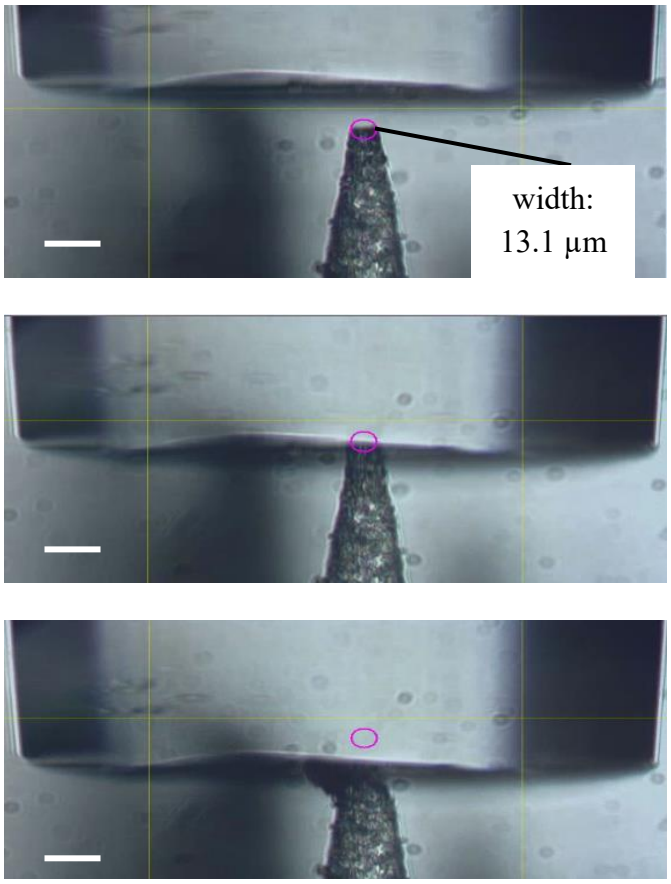

Figure 5-2 A microneedle from Sample HA-300kDa before (a), under (b) and after compression (scale bar: 20µm).

5.3 Mathematical models to determine the microneedle strength from experimental data of micromanipulation

5.3.1. Mechanical strength corresponding to maximum stress (MS analysis)

The scheme of a single microneedle under compression is illustrated in Figure 5-3, where F is the compression force, h_0 is the initial microneedle height, r_1 and r_2 are half side length of a quadrangular microneedle base and tip respectively, and A is the contact area between the force transducer probe and the microneedle tip.

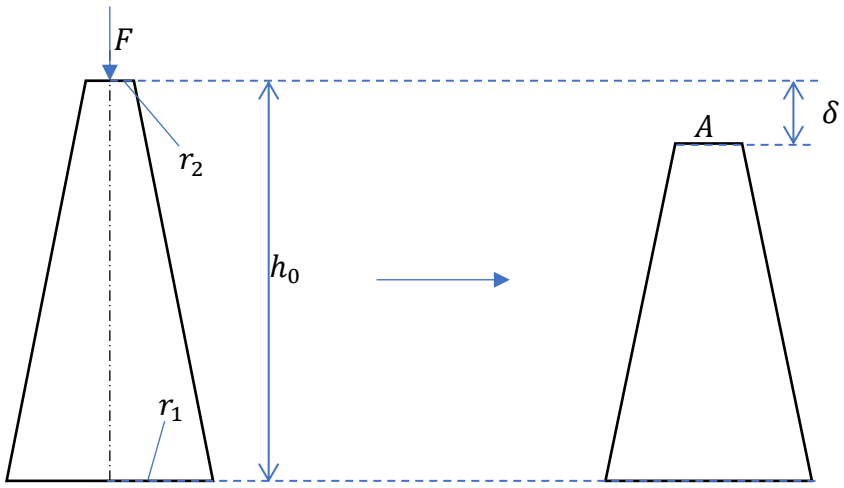

Figure 5-3 Scheme of a single microneedle under compression

The force versus displacement data can be obtained from the raw data of voltage versus sampling sequence using Equations (3-7) and (3-8). Then the fractional deformation ε, and normal stress σ can be calculated using the following two equations respectively (Du et al., 2021b),

$$\varepsilon = \frac{\delta}{h_0} \tag{5-1}$$

$$\sigma = \frac{F}{A} \tag{5-2}$$

The contact surface area A can be calculated from Equation (5-3) assuming the volume of the microneedle body during the compression is unchanged and ignoring the deformation of the microneedle base (Section 5.3.2) (Du et al., 2021b),

$$r_\delta = \frac{1}{2}\left\{-r_1 + \sqrt{r_1^2 - 4\left[r_1^2 - \frac{V_{MB}}{\pi/3 \cdot (h_0 - \delta)}\right]}\right\} \qquad (5\text{-}3)$$

$$A = 4r_\delta^2$$

where r_δ is the contact radius (contact half side length for pyramid shaped microneedles) and V_{MB} is the volume of the microneedle body given by

$$V_{MB} = \frac{4}{3}h_0(r_1^2 + r_1 r_2 + r_2^2) \qquad (5\text{-}4)$$

It is worth noting that unlike the nominal stress of the microparticles calculated by dividing the force by the initial cross-sectional area at the diameter using Equation (3-9), the stress obtained using Equation (5-2) can be seen as the true normal stress which uses the real contact area.

Figure 5-4 illustrates the process of compressing a typical microneedle of the HA-300kDa sample and the corresponding curves of force-displacement data and stress-displacement data. The force and the corresponding stress increase from the onset of compression A (2) to B where the stress reaches the maximum value (3). Then the force keeps increasing till C where a small part of the needle tip (around 20 μm in height) was bent significantly (4) and the force dropped notably. The force and the stress both decrease after C as the microneedle was bent further or ruptured (5). After compression, permanent bending or break was found (6).

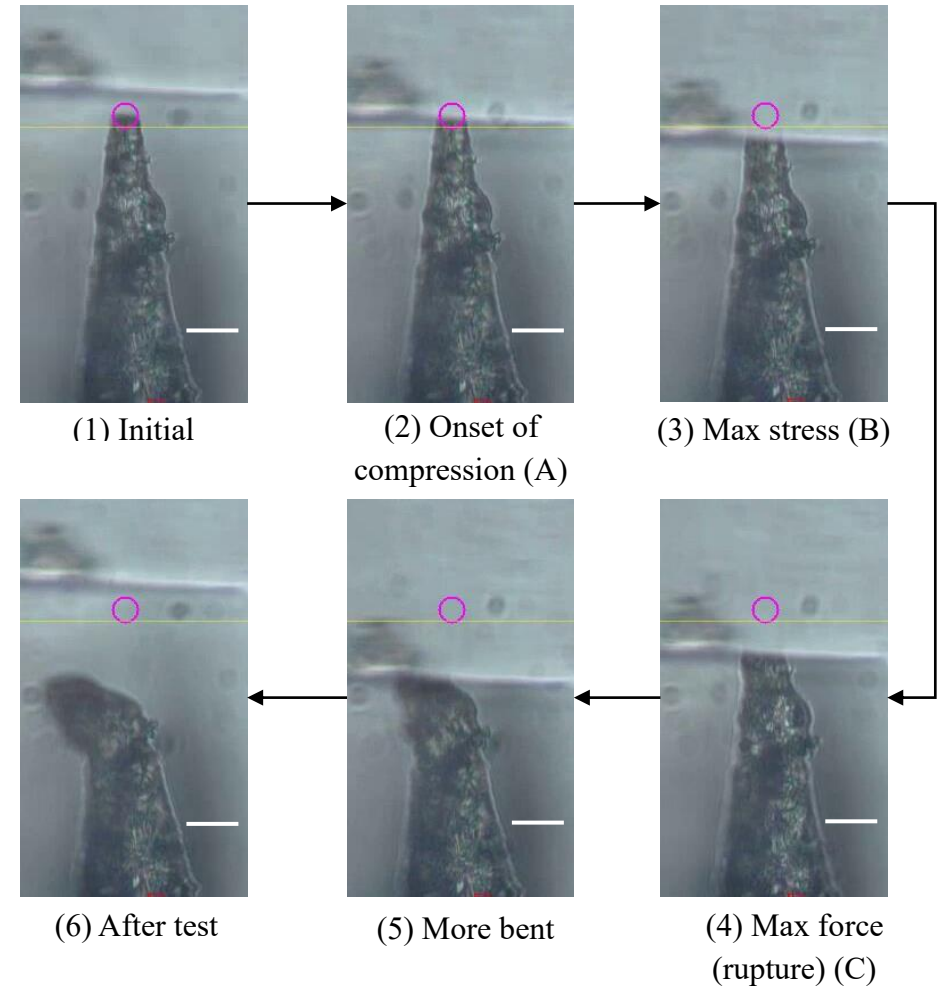

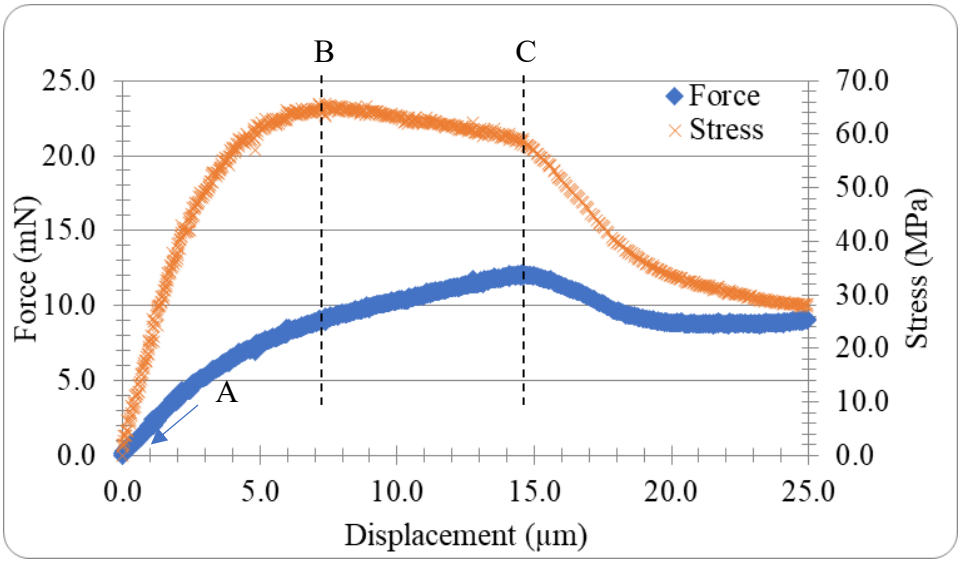

(7)

Figure 5-4 Microscopy image showing compression of a typical HA-300kDa microneedle (initial tip width: 9.3µm, scale bar: 20 µm) and the corresponding curves of force versus displacement data and stress versus displacement data

Although the loading topology changed after B from compression-dominant to bending-dominant at C, no notable bending was found at B corresponding to the maximum stress. Thus, if the microneedle cannot overcome the skin resistance at the maximum stress point B, it can hardly penetrate it anymore as a significantly bent microneedle tip tends to bend further or slide away from the skin surface resulting in unsuccessful penetration. Therefore, the mechanical property parameters at the maximum stress (MS) point (B) are more important than those at the rupture point (C) where significant bending happened and the former can be used to characterise the mechanical strength of microneedles. Moreover, Equation (5-2) for the calculation of stress still holds for the calculation of the maximum stress where no significant bending was found. However, Equation (5-2) cannot be used to calculate the stress at the rupture point where the vertical compression assumption for the equation is not satisfied if the failure is caused by bending. In this study, the mechanical strength parameters corresponding to MS, including the force at MS F_{MS}, displacement at MS δ_{MS}, fractional deformation at MS ε_{MS}, maximum stress σ_{MS} and toughness T_{MS} are used to determine the mechanical strength of microneedles. F_{MS} and δ_{MS} can simply be obtained from the force-displacement data at MS, and ε_{MS} and σ_{MS} can be calculated by substituting F_{MS} and δ_{MS} into Equations (5-1) to (5-4). T_{MS} can be determined using Equation (5-5) based on the trapezoidal integration (Zhang et al., 2022)

$$T_{MS} = \frac{1}{2}\sum_{i=1}^{ms}(\sigma_i + \sigma_{i+1})(\varepsilon_{i+1} - \varepsilon_i) \tag{5-5}$$

where ms is the index of maximum stress.

5.3.2. Elastic analysis of microneedles

The scheme of elastic deformation of a single microneedle under compression is illustrated in Figure 5-5. A_1 is the area of the microneedle bottom, h' is height of the missing tip assuming the microneedle is perfectly sharp, η is height of the microneedle from the top until sectional area $A(\eta)$, and $d\eta$ is element height at η. Suppose the microneedle body and the patch base can both deform under the compression load, then

$$\delta = \delta_n + \delta_b \tag{5-6}$$

where δ_n and δ_b are the displacement of the microneedle body and base respectively and δ is the overall displacement.

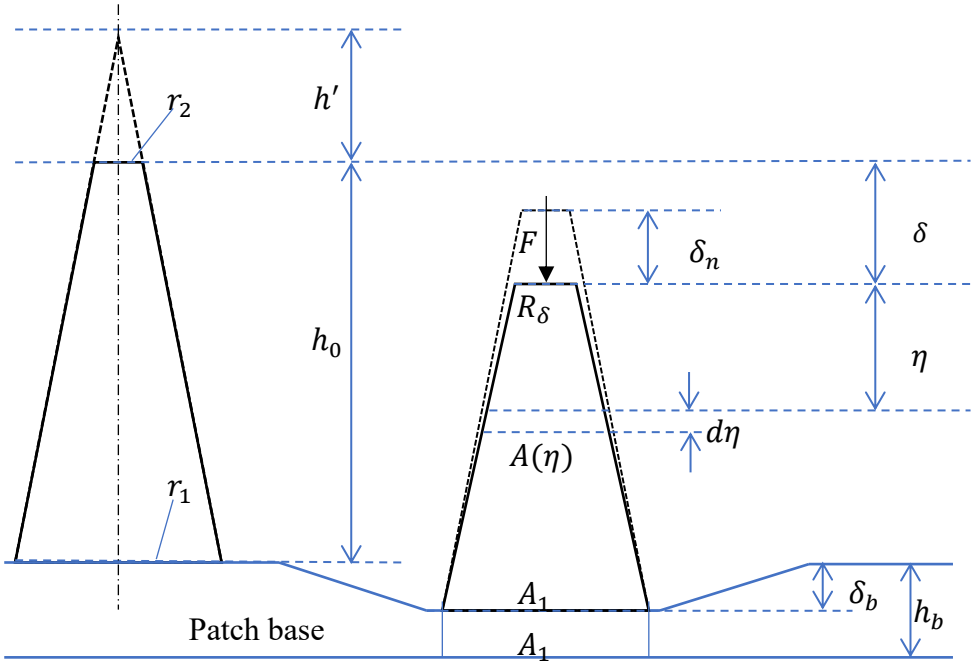

Figure 5-5 Schematic diagram of elastic deformation of a single microneedle under compression.

Assuming only normal deformation exists and the deformation is linearly elastic in small displacement (usually $\leq 2\mu m$, observed from micromanipulation experiments). Then from

similarity,

$$A(\eta) = \left(\frac{\eta + h'}{h_0 + h'}\right)^2 A_1 \tag{5-7}$$

where $A(\eta)$ is the area at η, and A_1 is the area of the microneedle bottom.

$$\delta_n = \int_0^{h_0} \frac{F}{A(\eta)E} d\eta \tag{5-8}$$

Substituting Equation (5-7) into Equation (5-8) and integrating leads to the following equation:

$$\delta_n = \frac{F}{E} \cdot \frac{(h_0 + h')h_0}{A_1 h'} \tag{5-9}$$

The displacement of the bottom is

$$\delta_b = \int_0^{h_b} \varepsilon_b \, d\eta < \int_0^{h_b} \frac{F}{EA_1} d\eta = \frac{Fh_b}{EA_1} \tag{5-10}$$

where ε_b is the strain of the microneedle base.

Combination of Equations (5-9) and (5-10) leads to

$$\frac{\delta_b}{\delta_n} < \frac{h_b h'}{(h_0 + h')h_0} = \frac{h'}{h_0 + h'} \cdot \frac{h_b}{h_0} < \frac{h'}{h_0} \cdot \frac{h_b}{h_0} \tag{5-11}$$

As the values of h_b and h_0 are in the same order, and $h' \ll h_0$, therefore

$$\delta_b \ll \delta_n \tag{5-12}$$

Thus δ_b can be neglected, i.e.,

$$\delta \approx \delta_n = \frac{F}{E} \cdot \frac{(h_0 + h')h_0}{A_1 h'} \tag{5-13}$$

where E is Young's modulus. Equation (5-13) can be written in the following form:

$$F = \frac{A_1 h' E}{(h_0 + h')h_0} \delta \tag{5-14}$$

From similarity,

$$\frac{h'}{h_0 + h'} = \frac{r_2}{r_1} \tag{5-15}$$

For the microneedles studied in this research with a shape of a truncated pyramid, the area can

be calculated using the following equation

$$A_1 = 4r_1^2 \tag{5-16}$$

Combination of Equations (5-14) to (5-16) leads to

$$F = \frac{4r_1 r_2 E}{h_0}\delta \tag{5-17}$$

Equation (5-17) can be used for elastic analysis of the experimental data of single (truncated pyramid-shaped) microneedles from using the micromanipulation technique.

5.3.3. Viscoelastic analysis of microneedles

The elastic model in Equation (5-17) can be expressed in the form of Equation (4-7) as the following equation

$$F = n_1 \cdot E \cdot \delta^{n_2} \tag{5-18}$$

where

$$\begin{aligned} n_1 &= \frac{4r_1 r_2}{h_0} \\ n_2 &= 1 \end{aligned} \tag{5-19}$$

and

$$f(\delta) = n_1 \delta^{n_2} = \frac{4r_1 r_2}{h_0}\delta \tag{5-20}$$

Following the approach in Section 4.2.3.1, for the elastic model in Equation (5-17), the viscoelastic model in Equation (4-24) can be expressed as Equation (5-21) for microneedles

$$F(t) = (1 + \psi) \cdot \frac{4r_1 r_2}{h_0}\delta_0 \cdot G(t) \tag{5-21}$$

and

$$\int_0^{\frac{t}{\tau_i}} x^{n_2-1}e^x\,dx = \int_0^{\frac{t}{\tau_i}} x^{1-1}e^x\,dx = e^{\frac{t}{\tau_i}} - 1 \tag{5-22}$$

Substituting Equations (5-19) and (5-22) into Equation (4-36) leads to

$$F(t) = (1+\psi)\frac{4r_1r_2}{h_0}v(C_0t + \sum_{i=1}^{n} C_i\tau_i(1 - e^{-\frac{t}{\tau_i}}) \tag{5-23}$$

which can be used to predict the force during the compression of single microneedles if the compliance of the force transducer is negligible.

However, **if the compliance of the force transducer is not negligible** relative to the imposed displacements, significant errors can result from using Equation (5-23). Here, two strategies can be used. One is using the **average moving speed of the force transducer tip**, which can be determined from the corresponding displacement versus time data, to substitute the moving speed of the micromanipulator v. Another is using numerical solution. The ramp function can be defined as

$$\delta(t) = vt - cF(t) \tag{5-24}$$

where c is the compliance of the transducer. Substituting Equation (5-24) into Equation (4-34) results in

$$\begin{aligned} F(t) = (1+\psi)n_1\int_0^t G(t-u)[\frac{d}{du}(vu)]du - (1 \\ +\psi)n_1c\int_0^t G(t-u)\frac{d}{du}[F(u)]du \end{aligned} \tag{5-25}$$

The second part which includes $F(t)$ (i.e., $F(u)$) itself cannot be mathematically solved. To deal with this problem, numerical solution can be used by decomposing the loading history into a sum of infinitesimal loading steps based on the Boltzmann superposition principle

(Bergström, 2015)

$$F(t) = (1+\psi)n_1 \sum_{i=1}^{\infty} G(t-\Delta t_i)\,[\delta(t) - \delta(t-\Delta t_i)] \tag{5-26}$$

where, $\Delta t_i,\ i = 1, 2, \cdots$ is infinitesimal time interval in which step loading is applied. In practice, the acquisition time (t_s) can be used as $\Delta t_i,\ i = 1, 2, \cdots$ to decompose the loading history, then Equation (5-26) can be written in the following form

$$F(jt_s) = (1+\psi)n_1 \sum_{i=1}^{j} G(it_s - t_s)\,[\delta(it_s) - \delta(it_s - t_s)] \tag{5-27}$$

where j is the sampling number. Equation (5-27) can also be written as

$$F_j = (1+\psi)n_1 \sum_{i=1}^{j} G_{i-1}(\delta_i - \delta_{i-1}) \tag{5-28}$$

and

$$F_{j-1} = (1+\psi)n_1 \sum_{i=1}^{j-1} G_{i-1}(\delta_i - \delta_{i-1}) \tag{5-29}$$

from which the following equation can be derived

$$F_j - F_{j-1} = (1+\psi)n_1 G_{j-1}(\delta_j - \delta_{j-1}) \tag{5-30}$$

The corresponding discrete form of Equation (5-24) can be written as

$$\delta_j = jvt_s - cF_j \tag{5-31}$$

and

$$\delta_{j-1} = (j-1)vt_s - cF_{j-1} \tag{5-32}$$

Thus

$$\delta_j - \delta_{j-1} = vt_s - cF_j + cF_{j-1} \tag{5-33}$$

Combination of Equation (5-30) and Equation (5-33) leads to the following recursive equation

$$F_j = \begin{cases} 0, & j = 1 \\ \dfrac{(1+\psi)n_1 v t_s G_{j-1} + (1 + n_1 c G_{j-1}) F_{j-1}}{1 + (1+\psi) n_1 c G_{j-1}}, & j = 2, 3, 4, \ldots \end{cases} \quad (5\text{-}34)$$

and

$$G_{j-1} = C_0 + \sum_{i=1}^{n} C_i e^{\frac{t_{j-1}}{\tau_i}}, \qquad j = 2, 3, 4, \ldots \quad (5\text{-}35)$$

Equations (5-34) and (5-35) can be used to predict the forces during loading in typical loading-holding experiment of microneedle tests in a numerical recursive way without the restriction of negligible transducer compliance as in Equation (5-23).

5.4 Test results and discussion

5.4.1. Results of loading tests

5.4.1.1. Mechanical strength parameters corresponding to maximum stress

Two patches of HA-300kDa microneedles from a batch were tested in the ambient temperature and humidity of 22 ± 2 ℃, 66 ± 3% Rh and 23.5 ± 2 ℃, 66 ± 3% Rh respectively. A typical curve of voltage versus sampling sequence for HA-300kDa microneedles tested is shown in Figure 5-6 and its force-displacement and stress-displacement curves are shown in Figure 5-7. The microneedle tip width $2r_1 = 13.0$ μm, the bottom width $2r_1 = 250$ μm, and the height $h_0 = 700$ μm. As described in Section 5.3.1, the force and stress both increase with the compression (displacement) at the beginning. Then the stress reaches the peak at B but the force continues increasing and reaches its peak at C after which drops significantly when the

microneedle was ruptured or bent. The rupture point is not corresponding to the maximum stress, which indicates that the main reason causing the failure of HA-300kDa microneedles may be the buckling rather than fracture (Loizidou et al., 2015; Radhika & Gnanavel, 2021). It is also noticed that a small part of the needle tip (around 10-20 μm in height) was bent before being ruptured.

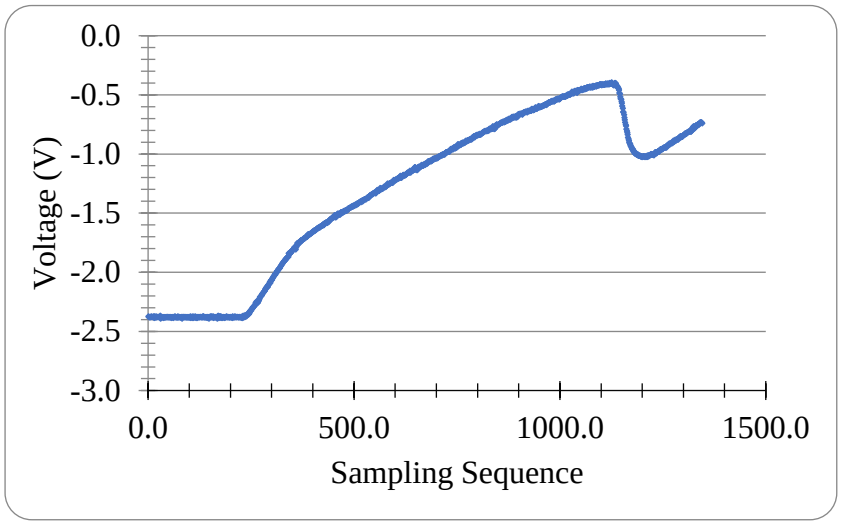

Figure 5-6 Typical voltage-sampling sequence curve generated from compression of a HA-300k microneedle

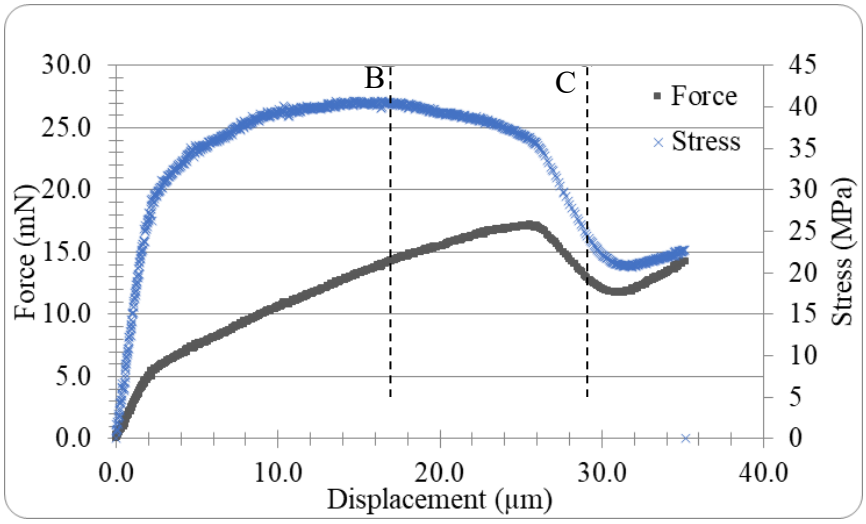

Figure 5-7 Force-displacement and stress-displacement curves from compression of the microneedle in Figure 5-6.

Figure 5-8 illustrates how the toughness is calculated using the trapezoidal numerical integration of the stress over the fractional deformation up to maximum stress with Equation (3-11). The displacement at MS, force at MS, deformation at MS, maximum stress and toughness of this microneedle were 13.6 μm, 12.7 mN, 1.94%, 40.77 MPa and 0.65 MPa respectively.

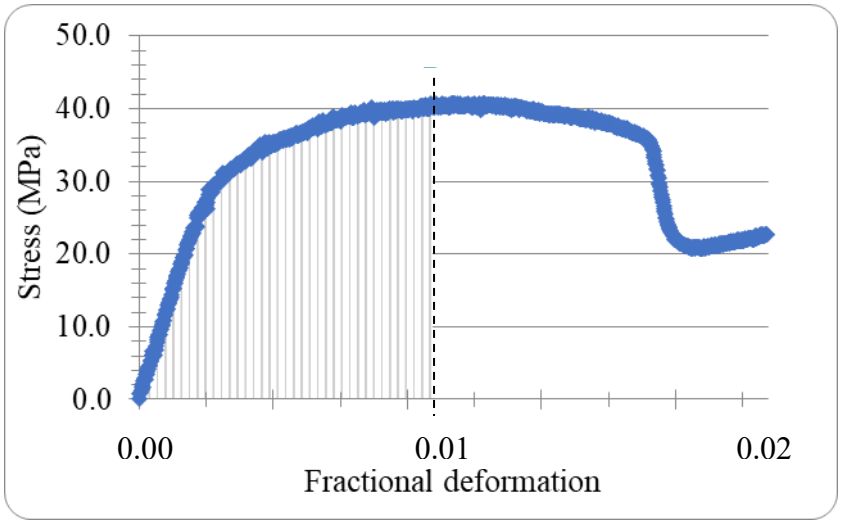

Figure 5-8 Toughness of the microneedle using integration of stress over strain up to maximum stress

Table 5-2 Results of mechanical strength at MS of two patches of HA-300kD microneedles tested (average ± SE)

Tip width ($2r_2$)(μm)	δ_{MS} (μm)	F_{MS} (mN)	ε_{MS} (%)	σ_{MS} (MPa)	T_{MS} (MPa)
13.0 ± 0.1	10.5 ± 0.5	13.8 ± 0.6	1.50 ± 0.08	49.9 ± 1.9	0.53 ± 0.04
11.6 ± 0.2	9.6 ± 0.4	12.0 ± 0.5	1.37 ± 0.05	54.5 ± 1.7	0.52 ± 0.03

The average ± standard error (SE) values of the mechanical strength parameters corresponding to MS of the two patches of HA-300kDa microneedles are summarised in Table 5-2. It can be seen that the values of the mechanical strength parameters of the two patches of HA-300kDa show no significant difference, which indicates the excellent reproducibility of the

micromanipulation technique in measuring the mechanical strength of microneedles.

5.4.1.2. Elastic analysis

For the microneedle in Sample HA-300kDa shown in Figure 5-6, the force-displacement data up to 2 μm displacement in Figure 5-7 was used to fit into the elastic model in Equation (5-17) and the experimental and the predicted force values are shown in Figure 5-9. The Young's modulus obtained is 0.56 GPa and *CoD* is 0.99, which indicates good fitting.

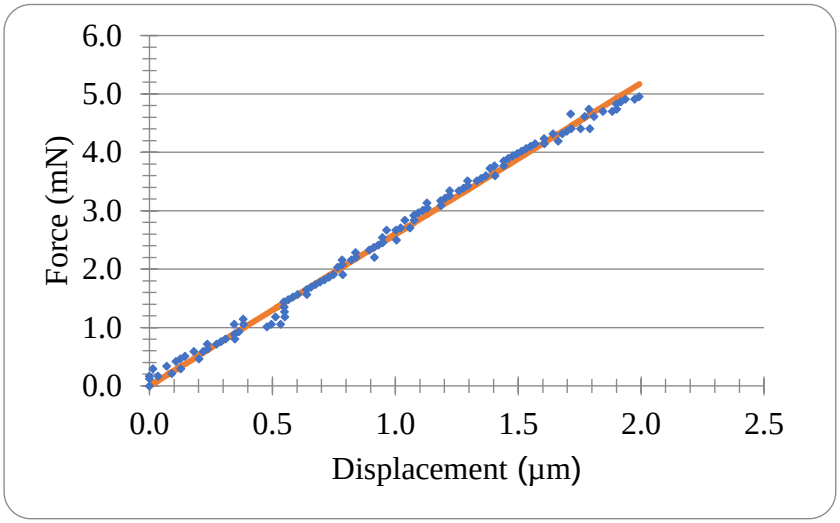

Figure 5-9 Elastic analysis of the microneedle in Figure 5-6. The line presents the fitting using Equation (5-17).

Table 5-3 Young's modulus of two patches of HA-300kDa microneedles (average ± SE)

Tip width ($2r_2$)(μm)	E (GPa)
13.0 ± 0.1	0.59 ± 0.02
11.6 ± 0.2	0.61 ± 0.02

The average ± SE values of Young's modulus of the two patches of HA-300kDa microneedles are summarised in Table 5-3. It can be seen that, similar to the results corresponding to the maximum stress, the values of the Youngs modulus of the two patches are also very consistent, which again indicates the reproducibility of the micromanipulation technique in determination

of the intrinsic mechanical properties of microneedles.

5.4.1.3. Results and discussion of melittin loaded microneedles for rheumatoid arthritis treatment

Table 5-4 lists the values of the mechanical strength parameters corresponding to MS and the Young's modulus obtained for four samples of HA-based microneedles with or without melittin (Samples 3, 4, 5, 6 in Table 5-1), tested using the micromanipulation technique (Du et al., 2021a). The ambient temperature values were all 18 ± 2℃ and the ambient humidity was 37 ± 3% Rh, 39 ± 3% Rh, 46 ± 3% Rh and 48 ± 3% Rh respectively. Totally 30 microneedles were tested for each sample patch. The listed values are average ± SE.

Table 5-4 Test results of 4 HA based microneedle samples (average ± SE)

Sample	Tip width ($2r_2$)(μm)	δ_{MS} (μm)	F_{MS} (mN)	ε_{MS} (%)	σ_{MS} (MPa)	T_{MS} (MPa)	E (GPa)
HA-10kDa	10.5 ± 0.3	13.5 ± 0.8	14.2 ± 1.2	1.9 ± 0.1	62.2 ± 1.9	0.80±0.05	0.54±0.05
Mel-HA	13.4 ± 0.6	18.3 ± 1.7	16.6 ± 2.2	2.6 ± 0.2	39.7 ± 1.9	0.70±0.08	0.34±0.04
MeHA	15.6 ± 0.9	22.1 ± 3.3	11.9 ± 1.5	3.2 ± 0.5	24.6 ± 2.2	0.41±0.05	0.21±0.04
Mel-MeHA	12.6 ± 0.9	14.8 ± 3.0	7.1 ± 1.1	2.1 ± 0.4	23.4 ± 2.0	0.28±0.04	0.22±0.04

It can be seen from the average values of the maximum stress and the Young's modulus that the HA-10kDa microneedles are strongest whilst MeHA and Mel-MeHA microneedles are weakest. The maximum stress and Young's modulus values of Mel-HA microneedles are significantly smaller than those of HA-10kDa, which indicates that the loading of melittin significantly decreased the mechanical strength of the HA-10kDa microneedles, which may

be due to the poor adhesion between melittin molecules and the HA matrix (Du et al., 2021a). However, the values of displacement and fractional deformation at MS of Mel-HA are significantly greater than those of HA-10kDa, which implies the loading of melittin made the HA-10kDa microneedles more flexible. The greater value of fractional deformation also compensated the smaller value of the maximum stress of Mel-HA, resulting in closer toughness value to HA-10kDa.

Although the maximum stress and Young's modulus values of MeHA and Mel-MeHA microneedles show no significant differences, the displacement and the fractional deformation at MS of Mel-MeHA are significantly smaller than those of MeHA, resulting in a significantly smaller value of toughness, which indicates that the loading of melittin caused the MeHA microneedles to be more brittle.

The penetration capacity of these HA-based microneedles was investigated by Trypan blue staining method by Du et al. (2021a) and it was found that the Mel-HA successfully penetrated the rat abdomen skin with the depth about 200 μm visualised with fluorescence microscopy. The loaded melittin released after piercing the skin for 3 minutes. It was also found that the Mel-MeHA successfully overcame the abdomen skin of mice but released the loaded melittin in a more sustained way. Modifying HA with crosslinked methacrylate groups decreased the release rate of the loaded melittin, which significantly improved efficacy of melittin to treat rheumatoid arthritis as well as reduced the side effects in comparison to Mel-HA microneedles (Du et al., 2021a).

It has been reported that the tensile stress of stratum corneum (SC) around the contact circumference around the microneedle tip dominates the resistance during microneedle penetration (Ranamukhaarachchi et al., 2016). Therefore, the ultimate tensile strength (UTS) of the skin provides an important criterion for prediction of microneedle penetration efficiency. The greatest UTS value of human skin reported was 27.2 ± 9.3 MPa determined by in vitro uniaxial tensile tests of human back skin dynamically at a loading speed of 1-2 m/s (Gallagher et al., 2012). The maximum stress of HA-10kDa and Mel-HA microneedles are much greater than this UTS value of human skin and can be strong enough to penetrate it successfully. It looks like that the maximum stress of MeHA and Mel-MeHA microneedles listed in Table 5-4 are not greater than the maximum UTS of human skin, which might result in insufficient penetration. However, because of the viscoelasticity, the skin failure properties depended on the loading speed applied to the skin (Joodaki & Panzer, 2018) and the UTS value of 27.2 ± 9.3 MPa was obtained at a very high tensile test speed of 1 - 2 m/s. In contrast, the UTS value of human back skin could be as small as 10.4MPa when the applied strain rate was 0.06 s^{-1} (Ottenio et al., 2015). Therefore, the MeHA and Mel-MeHA microneedles may insert into the human skin reliably with a quasi-static loading speed. Moreover, the values illustrated in Table 5-4 are obtained from quasi-static loading (the compression speed was 2μm/s) and the HA based microneedles showed notable viscoelasticity as demonstrated in Section 5.4.2, i.e., the mechanical strength of microneedles (including maximum stress) can increase with the penetration speed. If the MeHA and Mel-MeHA microneedles are administrated at a speed as

high as 1-2 m/s used to obtain the UTS value (27.2 ± 9.3 MPa) of human skin, reliable penetration may be achieved. Furthermore, the mechanical strength of skin from different parts of human body could differ significantly, e.g., the UTS of human forehead skin was 3 ± 1.5 MPa obtained by dynamic tensile tests at high strain rate of 55 s^{-1} (Jacquemoud et al., 2007) and that of human abdomen and thorax skin was 2.0-15.0MPa (Gallagher et al., 2012; Silver et al., 2001). Thus, sufficient penetration should also be achieved if the four microneedle samples characterised in this section need to be administrated into skin of other parts, such as forehead and abdomen, of human body.

On the other hand, it was reported that the value of Young's modulus of human skin also depends on the loading speed and direction as well as test methods, which was found to be 5-100kPa by indentation tests, 0.025-140MPa by tensile and torsion tests and 25-260kPa by suction tests (Kalra et al., 2016). The Young's modulus values of these four HA based microneedles are all much greater than that of human skin and therefore they could be stiff enough to pierce it reliably.

5.4.2. Results of loading-holding tests and viscoelastic analysis of microneedles

Single microneedles of Lido-HA300kDa (Sample 2 in Table 5-1) were compressed to a certain deformation and held under the transducer probe. The ambient temperature and humidity were 17 ± 2 ℃ and 38 ± 3 % Rh respectively. A typical curve of force versus displacement data is illustrated in Figure 5-10. The force dropped during the holding, which suggests some viscoelastic behaviour of the microneedle exists.

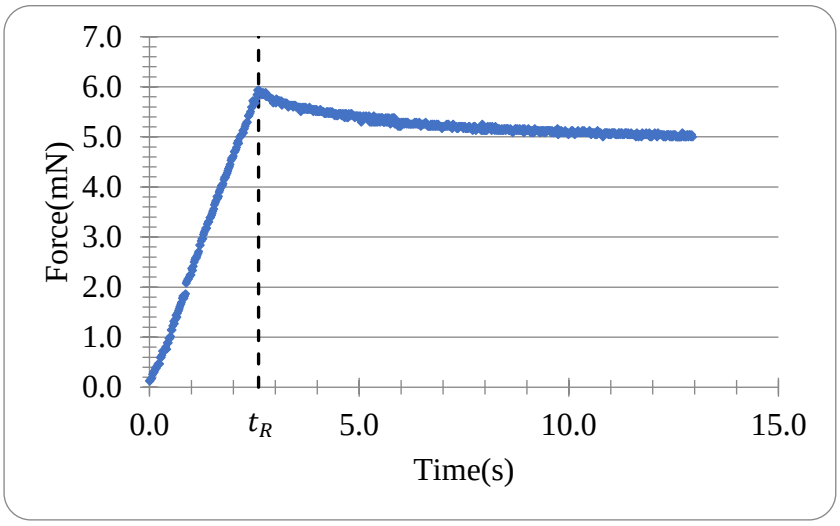

Figure 5-10 Typical force-time curve of loading-holding test of Lido-HA300kDa microneedles (tip width $2r_2 =$ 16.1 µm, bottom width $2r_1 = 250$ µm, $h_0 = 700$ µm). $t_R = 2.6s$.

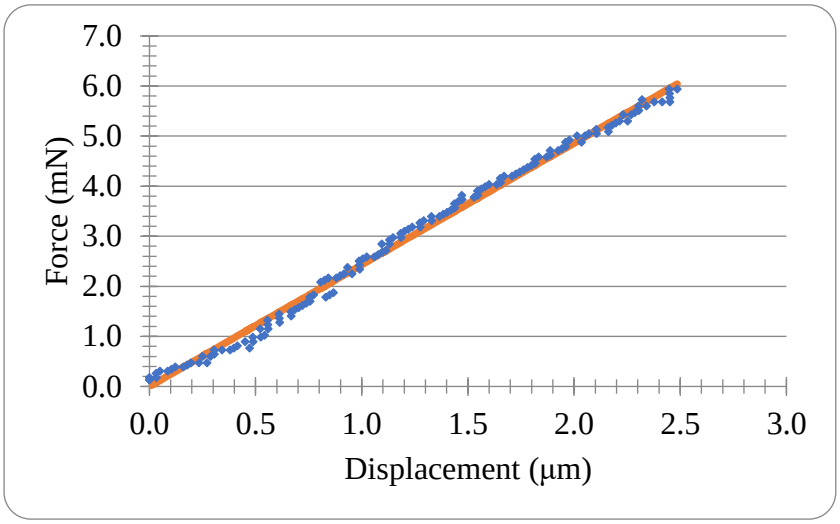

Figure 5-11 Elastic analysis of the microneedle in Figure 5-10. The line presents the fitting using Equation (5-17).

5.4.2.1. Elastic analysis

If the viscous behaviour is neglected, the force-displacement data of the Lido-HA300kDa microneedle during compression can be fitted into the elastic model in Equation (5-17) as illustrated in Figure 5-11. The Youngs modulus obtained is 422.8 MPa and the CoD is 0.99

which indicates good fitting.

5.4.2.2. Viscoelastic analysis

Letting the degree $n = 2$ and fitting the force-time data during the holding into Equation (4-28), the coefficients B_0, B_1, B_2 and the time constants τ_1 and τ_2 can be obtained as shown in Table 5-5.

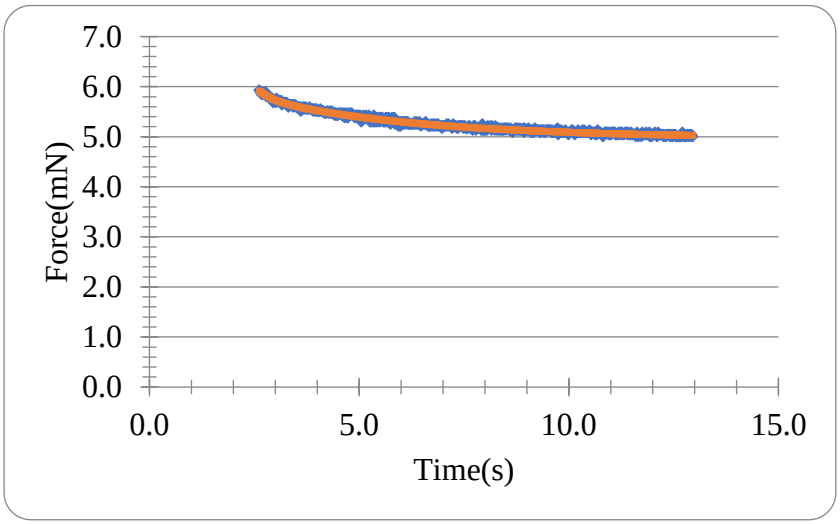

Figure 5-12 Predicted force (orange curve) and experimental force (blue points) versus time during holding

Table 5-5 Calculated values of the coefficients and relaxation times of the microneedle in Figure 5-10

Width (μm)	B_0 (mN)	B_1 (mN)	B_2 (mN)	τ_1 (s)	τ_2 (s)
16.1	4.98	1.55	534.35	3.82	0.32

Table 5-6 Values of coefficients C_0, C_1, C_2

C_0 (MPa)	C_1 (MPa)	C_2 (MPa)
228.8	49.6	63.8

It can be seen that the viscoelastic model with two relaxation times can predict the

experimental data well ($CoD = 0.98$) as illustrated in Figure 5-12. The rising time $t_R = 2.6$ s, the displacement up to the end of compression $\delta_0 = 2.52$ μm, the ramp correction factors Φ_1 and Φ_2 are 1.43 and 384.88 respectively. The coefficients C_0, C_1, C_2 are shown in Table 5-6 obtained using Equations (4-29) and (4-30).

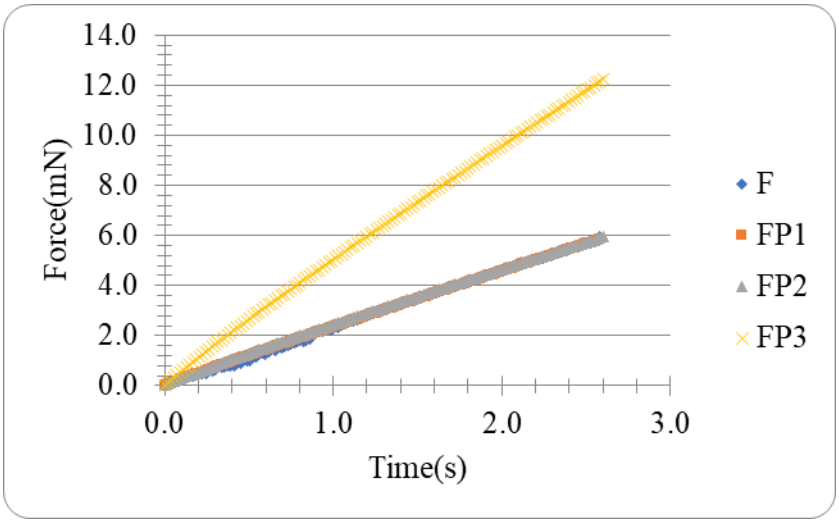

F: Experimental force

FP1: Force predicted by the numerical method using Equation (5-34)

FP2: Force predicted using Equation (5-23) with the average speed of the transducer probe

FP3: Force obtained using Equation (5-23) with the speed of the micromanipulator

Figure 5-13 Predicted force data in comparison with the experimental data corresponding to compression of the microneedle.

The force data during loading have been predicted using the parameters obtained from the holding (i.e., force relaxation) data and are shown in Figure 5-13. F is the experimental force. F-P1 is predicted by the numerical method using Equation (5-34). F-P2 is predicted using Equation (5-23) with the average compression speed of the force transducer probe, which can be determined from the corresponding displacement versus time data (δ_0/t_R). F-P3 is obtained

using Equation (5-23) with the pre-set compression speed of the fine compression micromanipulator (neglecting the compliance of the force transducer). It can be seen that the results obtained from the approach with the average compression speed and the numerical approach are both consistent with the experimental data and thus they both can be used to predict the compression force utilizing the viscoelastic parameters obtained from the data of the force relaxation corresponding to the holding. The predicted force F-P3 deviates from the experimental data significantly as the compliance of the transducer c is around 0.5 μm/mN that is not negligible with such big force in the order of mN or above.

Table 5-7 Values of shear moduli and Youngs moduli

G_0 (MPa)	G_∞ (MPa)	E_0 (MPa)	E_∞ (MPa)
171.1	114.4	513.3	343.2

The instantaneous shear modulus G_0, long-term shear modulus G_∞, instantaneous Young's modulus E_0 and long-term Young's modulus E_∞ have been obtained using Equations (4-30) to (4-33) and the values are shown in Table 5-7. The Poisson's ratio ψ of 0.5 is used. In last section, the Youngs modulus value without considering the viscous behaviour is 422.8 MPa, which lies between the values of the instantaneous Young's modulus (513.3 MPa) and long-term Young's modulus (343.2 MPa), as expected. Other tested Lido-HA300kDa microneedles showed similar results.

Totally, 26 single Lido-HA300kDa microneedles were tested in the loading-holding experiments. Their experimental data during compression were analysed using the elastic model by neglecting the viscous behaviour and the obtained Young's modulus value was 496.5

± 31.6 MPa, which lies between the obtained instantaneous and long-term Young's modulus values (619.0 ± 37.2 MPa and 390.5 ± 24.1 MPa respectively) obtained from the analysis of their holding data using the viscoelastic model. The difference between the instantaneous and long-term moduli is quite significant, which suggests that different penetration efficiency can be obtained by adjusting the insertion speed. Therefore, with a higher insertion speed, e.g., using an impact-insertion applicator (van der Maaden et al., 2014), more efficient penetration can be achieved even for microneedles that are not sufficiently strong in quasi-static penetration.

5.5 Discussion

As aforementioned in the beginning of this chapter, microneedles on a patch were usually compressed together and the average force of single microneedles was calculated by dividing the whole loading force by the number of microneedles on the patch. Then the average failure/fracture force was used to characterise the mechanical strength of microneedles in many other studies (Davis et al., 2004; Kim et al., 2018; Park et al., 2005; Park et al., 2006; Wang et al., 2018). However, the obtained failure force value was the average value and thus variations of the failure force of individual microneedles across the patch were not known. Moreover, it is not sufficient to compare the mechanical strength of microneedles simply by force as it is not an intrinsic material property that can be affected significantly by the geometry and structure of the microneedles (Du et al., 2021b). Furthermore, if the microneedles were bent first and failed later, as illustrated in Figure 5-4, the mechanical strength parameters at

the failing point may be not as relevant as those at maximum stress (before failure point) because the microneedles may slide away from the skin due to the bending, resulting in unsuccessful insertion.

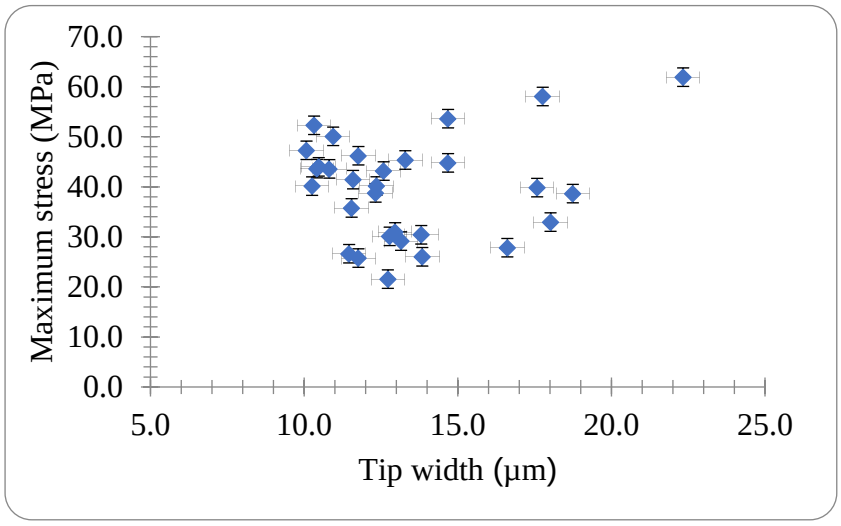

Figure 5-14 Data of maximum stress versus tip width of Mel-HA microneedles tested (Error bar represents one SE)

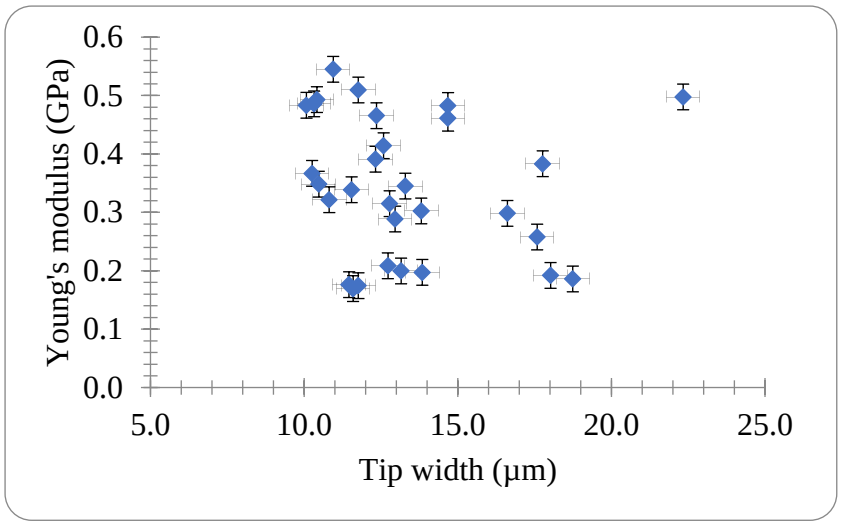

Figure 5-15 Data of Young's modulus versus tip width of Mel-HA microneedles (Error bar represents one SE)

In contrast, from using the micromanipulation, the mechanical strength parameters of single microneedles as well as their variations are determined, which can help to predict the

penetration efficiency more reliably. For example, the obtained data of maximum stress and Young's modulus of single microneedles of Mel-HA tested in Section 5.4.1.3 are illustrated in Figure 5-14 and Figure 5-15. It can be seen that all of the values of maximum stress are significantly greater than the UTS (2.0-15.0MPa) of human abdomen and thorax skin (Gallagher et al., 2012; Silver et al., 2001) and all the Young's modulus values are significantly greater than that of human skin (0.025-140MPa) (Kalra et al., 2016). Therefore, the Mel-HA microneedles can be predicted, with great confidence, to be sufficiently strong to penetrate human abdomen skin successfully. The mechanical strength parameters, including the maximum stress, Young's modulus, and the long-term and instantaneous shear and Young's moduli determined using the three developed mathematical models are independent of the geometry or structure of the microneedles, and thus can be used for comparing the mechanical strength of microneedles made of different formulations and processing conditions.

During the measurements of the microneedle samples, the ambient temperature and humidity were closely monitored and recorded as they could affect the mechanical strength of HA microneedles significantly. Wang et al. (2018) found that the mechanical strength of HA microneedles decreased significantly after storing in 25℃ temperature and 80% relative humidity for 30 minutes and their penetration efficiency decreased from 100% to 0% after storage. The decrease of the mechanical strength was found to be due to the increase of the water absorption of HA. However, when the relative humidity was under 60%, only slight decrease was found for the HA microneedles after storage for 2 hours (Wang et al., 2018). In

this work, the relative humidity values were all under 50% during the tests of the HA-10kDa, MeHA, Mel-HA and Mel-MeHA microneedle samples presented in Section 5.4.1.3 and the time spent for testing one patch was less than one hour. Therefore, the influence of the change in ambient humidity was negligible.

Furthermore, it was found that the Young's modulus of HA-300kDa microneedles was significantly greater than that of HA-10kDa and Lido-HA300kDa tested under similar ambient humidity, which suggests that lower molecular weight and loading of drug decreased the mechanical strength of polymer microneedles significantly in the co-authored paper (Du et al., 2021b). However, the obtained results of the tested HA-300kDa and HA-10kDa microneedles overlap in this project (Table 5-2 to Table 5-4). For example, the Young's modulus values of the two tested patches of HA-300kDa microneedles in Table 5-2 and the patch of HA-10kDa microneedles in Table 5-4 were 0.59 ± 0.02 GPa, 0.61 ± 0.02 GPa and 0.54 ± 0.05 GPa respectively. The Young's modulus value of the Lido-HA300kDa microneedles (in Section 5.4.2.2) obtained by fitting the compression data into the elastic model by neglecting the viscos behaviour was 0.49 ± 0.03 GPa, which also overlaps with that of the two patches of HA-300kDa microneedles. The main reason may be that the two patches of HA-300kDa microneedles were tested in 22 ± 2 ℃, 66 ± 3% Rh and 23.5 ± 2℃, 66 ± 3% Rh respectively which decreased their mechanical strength significantly, whereas the other two were tested in 18 ± 2℃, 37 ± 3% Rh and 17 ± 2℃, 38 ± 3% Rh respectively. Because the mechanical strength of HA microneedles decreased significantly when ambient humidity was greater than 60% Rh

and remained stable when relative humidity is below 40%Rh (Wang et al., 2018).

Moreover, in the analysis, single microneedles are assumed to be vertical (axis is perpendicular to the surface of the force transducer probe). Errors can be introduced when compressing tilted microneedles. Error sensitivity of the tilt angle θ_0 in the determination of the Young's modulus value from compression of single tilt microneedles was carried out. The detailed procedures are described in Appendix A. It was found that the obtained Young's modulus of tilt microneedles is smaller than its real value and the error increases with the tilt angle θ_0. Tilt angle greater than 10 degrees can cause significant error (>10%) for microneedles with big tip width (>14 μm). Therefore, microneedles that are significantly tilted should not be tested. However, for the microneedles tested in this project whose tip width was less than 20 μm, the tilt angle was within 5 degrees (which can be easily seen from the side-view camera as shown in Figure A-3), and the relative error between the obtained Young's modulus value and its real value was less than 3%.

5.6 Conclusions

The research work presented in this chapter mainly focused on development of mathematical models to determine the mechanical strength of microneedles using the micromanipulation technique and their applications in prediction of the penetration efficiency of the microneedles. Three mathematical models, i.e., the MS model, elastic model and viscoelastic model, were developed to determine the mechanical strength parameters corresponding to MS and intrinsic mechanical property parameters of single microneedles from the micromanipulation data.

Six dissolvable microneedle samples based on HA with or without loading drug were tested and their experimental data were analysed using the three mathematical models developed. The results of the mechanical strength parameters of the two patches of HA-300kDa microneedles tested under similar ambient temperature and humidity conditions were in excellent agreement, which validated the reproducibility of the micromanipulation technique in determining the mechanical strength of single microneedles.

It was found that the loading of melittin significantly decreased the mechanical strength of HA and MeHA microneedles. However, the Mel-HA and Mel-MeHA both successfully penetrated the abdomen skin of mice in the in vivo experiments undertaken by Dr Du and his colleagues (Du et al., 2021a). They have been predicted to be sufficiently strong to successfully pierce human skin after comparing their mechanical strength parameters including the maximum stress and Young's modulus with those of human skin comprehensively in this research.

The time-dependent parameters including the instantaneous and long-term shear Young's moduli of the Lido-HA300kDa microneedles obtained from the viscoelastic analysis suggests that the penetration efficiency of microneedles can depend on the insertion speed. For example, reliable piercing can be achieved by increasing the insertion speed using a machine insertion device, such as an impact-insertion applicator (van der Maaden et al., 2014) even for microneedles that cannot sufficiently penetrate the skin under a quasi-static insertion speed.

In conclusion, using the micromanipulation technique in combination with the three developed mathematical models, the intrinsic mechanical property parameters as well as their variations

of single microneedles can be precisely determined, which can be used to predict their penetration capacity comprehensively and reliably even without their geometrical or structural information. Moreover, the three developed mathematical models can also be used to analyse the experimental data of microneedle arrays tested using other techniques, including the displacement-force test station (Park et al., 2005) and the micro-mechanical test machine with a microforce sensor (Wang et al., 2018), and thus can find wide applications in academic research and development of new products based on microneedles.

CHAPTER 6: DEVELOPMENT OF AN AUTOMATIC MICROMANIPULATION SYSTEM

6.1 Introduction

As reviewed in Sections 1.1 and 2.2, the micromanipulation technique in several different versions has been widely used to test a variety of biological and non-biological micro-sized materials through a range of experiments, including compression to different deformations, compression at different speeds, compression and holding, and compression and release (Zhang et al., 2009). By analysing the experimental data with different analytical and numerical models, including the elastic, plastic, and viscoelastic models, the intrinsic mechanical properties including mechanical strength parameters of the tested single micro-sized materials can be determined, which is essential to the optimisation of their performance and functionalities from manufacturing, to further processing, storage and end-use applications. However, because the micromanipulation operation and data analysis were undertaken manually, it is time-consuming, laborious and technically demanding (Zhang et al., 2009). To make it more efficient and easier to use, a new control system needs to be devised to auto focus, auto detect and auto test single microparticles.

Among different autofocus techniques, the passive autofocus technique based on the contrast of the images is low-cost and pretty accurate so that it may be desirable to be used in the automatic micromanipulation system. In contrast-based autofocus system, focus value (FV) is used to measure the sharpness of each frame and a search algorithm is used to search for the

best in-focus position based on the FV of each frame (Zhang et al., 2018b). Although there are a range of well-developed search algorithms, e.g., mountain climbing search (MCS), for common autofocus applications such as smart digital cameras, they cannot be used directly for the autofocus system in micromanipulation based on only the sideview camera, because there may be no particles in the field of view (FOV) of the camera initially (Section 6.3.2). However, all the reviewed search algorithms are based on the assumption that the objects (e.g., particles) are already in the FOV of the camera. Therefore, new algorithms need to be developed for the autofocus system based on only the sideview camera.

A zoom module is intended to be used in the sideview camera system to see particles in a large range of sizes (Figure 6-3) by adjusting (manually) the magnification of the zoom module without changing the objective. Therefore, the magnification of the optical system may be changed and new algorithms need to be developed to determine the optical magnification automatically before autofocus, detection and micromanipulation of microparticles. Moreover, materials of some microparticle samples may be sticky so that their debris may adhere to the end of the force transducer probe after compression, which needs to be detected and cleaned before micromanipulation of other particles.

In the research presented in this chapter, a new control system has been developed to test single microparticles automatically by modifying the existing hardware system and developing new software to enable autofocusing, image processing and micromanipulation. The sample stage has been upgraded by introducing DC servo linear actuators with motion controllers to achieve

automatic motion control. A contrast-based autofocus algorithm and an object detection algorithm have been developed to focus and detect single particles automatically. Two other essential algorithms have also been developed to automatically determine the magnification of the optical system and detect possible debris adhered to the probe after compression, which can simplify the operation procedure significantly. Two samples, the MF microcapsules with lily oil as liquid core and the porous PS microspheres, were tested by both the newly developed automatic micromanipulation system and the conventional manual micromanipulation system to verify the functions of the former.

6.2 Principle of the micromanipulation system

6.2.1. Principle of the conventional micromanipulation system

The principle of the micromanipulation technique is to compress single particles between two parallel surfaces and the corresponding force and displacement data are obtained, which is reported elsewhere (Stenekes et al., 2000; Sun & Zhang, 2001; Zhang et al., 1999). The apparatus is usually based on using a bottom-view camera and a sideview camera to see the microparticles. More recently, a new version based on only one side-view camera has been developed, and the specimen can be illuminated using a light source opposite to the lens of the camera, which is highly desirable. The diagrammatic representation of this new version is shown in Figure 6-1 (Zhang et al., 2022). It mainly consists of a fine micromanipulator to hold a force transducer, a three-dimensional (3D) micromanipulator to hold the sample stage, a sideview camera, a control & data acquisition box and an industrial computer.

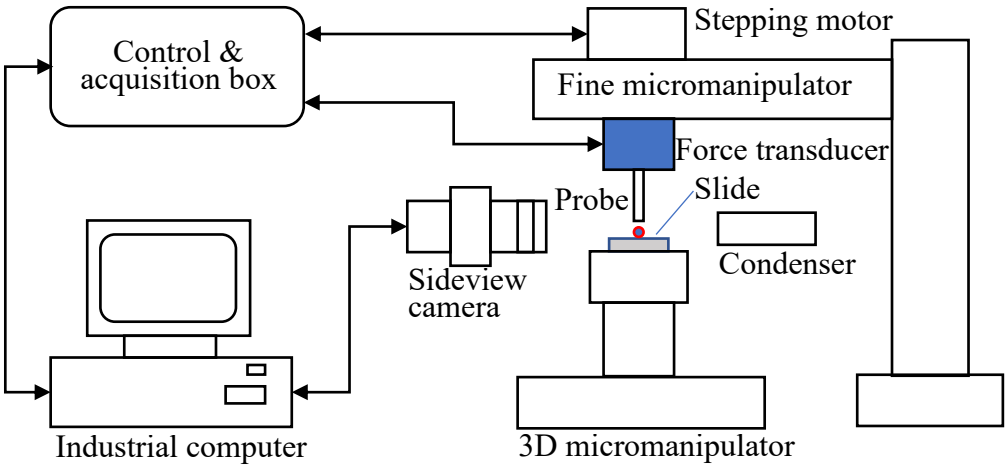

Figure 6-1 Schematic diagram of the micromanipulation system (Adapted from Zhang et al., 2022)

6.2.2. Workflow of the conventional micromanipulation system

The flowchart in Figure 6-2 illustrates how the conventional micromanipulation system is operated to test the mechanical strength of single particles. Before testing, particles are placed onto the surface of a slide fixed onto the sample stage. Initially, **the probe** of the force transducer that is mounted to the fine micromanipulator is **well focused in the sideview camera**, and can be seen from the screen of the computer. By manually moving the sample stage, particles are moved to under the probe. Single particles are manually focused, and their size is measured. If the size is in the range to test, the focused single particle will be compressed (manually started) against the end of the probe by automatically moving the force transducer down, during which the applied force (voltage) is measured by the control & data acquisition box and the data is saved in the computer. After compression, the sample stage is moved manually repetitively to focus and test single particles until required number is reached. Finally, the experimental data is analysed manually or using the developed software packages in

Chapter 3 and 4 to obtain the mechanical strength of the tested sample.

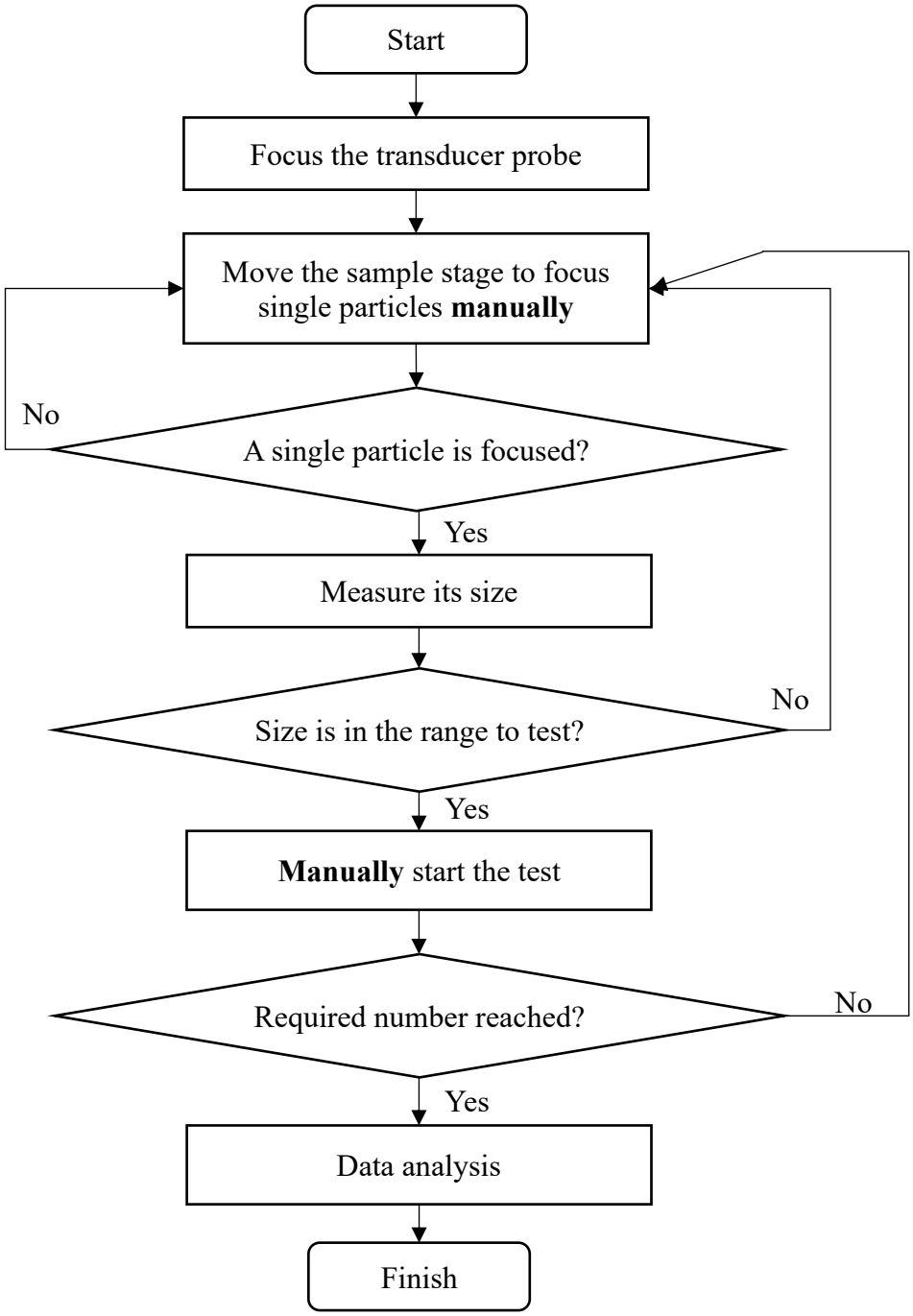

Figure 6-2 Flowchart of conventional micromanipulation system

It is worth pointing out that the force transducer probe is always in focus at the midpoint (the cylinder edges are sharp). So, any particle that is in focus and also vertically aligned

with the probe will be directly beneath it. As the depth of field of the lens is relatively very small (1.6 μm, see Table 6-1) to particle size (3~1000μm) and probe diameter (usually ≥20μm). Moreover, **the sample stage rather than the lens** is moved to search and focus single particles.

6.2.3. Hardware modification for the automatic micromanipulation system

The automatic micromanipulation system is based on the system shown in Figure 6-1. In order to achieve automatic tests, the micromanipulator holding the sample stage has been upgraded by replacing the manually operated micromanipulator with a DC servo linear actuator with a motion controller (CONEX-TRA12CC from Newport Spectra-Physics Ltd., OX, UK) to achieve automatic motion control.

6.2.4. Description of the sideview camera system

The conceptual representation of the sideview camera system is illustrated in Figure 6-3, where extension tubes or connectors are not shown. It mainly consists of an objective (20X long working distance infinity corrected objective, Edmund Optics Ltd., York, UK), a tube lens (MT-1 accessory tube lens, Edmund Optics Ltd.), a zoom module (4:1 magnification ratio donder zoom module, Edmund Optics Ltd.) and a digital camera (YW5607, ShenZhen Yangwang Technology Co., Ltd, China).

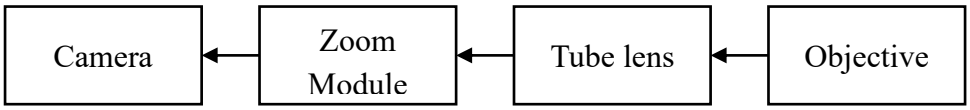

Figure 6-3 Functional blocks of the sideview optical system (Tubes not included)

6.2.5. Workflow of the automatic micromanipulation system

The flowchart of the automatic micromanipulation system is shown in Figure 6-4. After initialisation, **the probe** of the force transducer is **well focused in the sideview camera.** Then the sample stage is moved to autofocus possible microparticles. If something is focused, image processing will be carried out to detect if any requested particles exist in the focused image. If found, an automatic test will be carried out to test the single particles during which the corresponding force (voltage) versus sampling sequency/time will be recorded. Then, the system will repeat to focus and test other single particles until the required number is reached (usually 50 particles for a sample). Finally, automatic data analysis will be undertaken to obtain the mechanical strength of the tested particles. There are some similarities between the conventional and the automatic micromanipulation systems as illustrated in Figure 6-2 and Figure 6-4 respectively. Firstly, **the force transducer probe is always in focus at the midpoint (the cylinder edges are sharp)**. So, any particle that is in focus and also vertically aligned with the probe will be directly beneath it. As the depth of field of the lens is relatively very small (1.6 μm, see Table 6-1) to particle size (3~1000μm) and probe diameter (usually ≥20μm). Secondly, **the sample stage rather than the lens** is moved to search and focus single particles. Lastly, the compression is carried out automatically by the fine micromanipulator mounted with the force transducer. The main difference between the two systems lies in that **the focus, search and detection of single microparticles is undertaken manually in the conventional system but automatically** (and repetitively) in the automatic system. Therefore,

high throughput measurement can be carried out by using the newly developed automatic micromanipulation system.

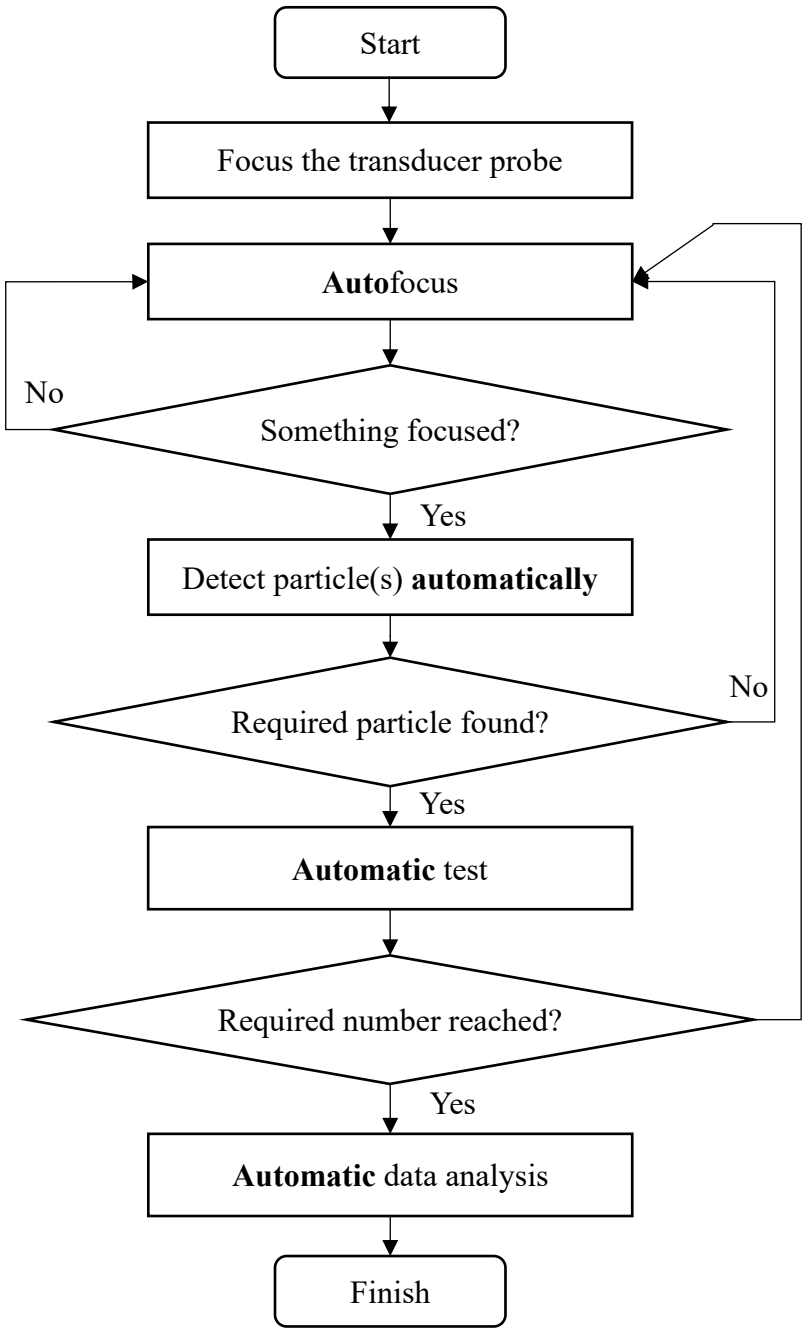

Figure 6-4 Flowchart of the automatic micromanipulation system

The whole operation involves applications of several key algorithms, including the autofocus, and automatic particle detection based on image processing, which will be presented in the

following sections.

6.3 Development of autofocus algorithm

6.3.1. Focus measure function

A focus measure function (FMF) is used to determine the focus state of an object which is essential to the autofocusing. The Brenner FMF has been used to autofocus in this work as it was found very suitable for digital images (Mir et al., 2014). Let $f(x,y)$ be the intensity (luminance or grayscale) at Pixel (x,y) in an image with size of $M \times N$ pixels and the Brenner FMF can be calculated using Equation (6-1).

$$\sum_{x=0}^{M-1}\sum_{y=0}^{N-3}[f(x,y+2)-f(x,y)]^2 \qquad (6\text{-}1)$$

6.3.2. Search algorithm

6.3.2.1. Application scenario

There are some differences between the autofocus in the automatic micromanipulation system and other applications. In common autofocus applications such as mobile phone digital camera systems (Xu et al., 2014), autofocus is the feature that aims to ensure a chosen object, e.g., a flower, is sharpened within the photo. It is assumed that the object already exists in the field of view (FOV) of the camera. But the object is not clear enough because it is not in or near the focal plane. Thus, a search algorithm is introduced to move the lens or the whole camera to let the object drop into or close enough to the focal plane. In this way, the object is well focused and sharpened in the photo. The curve of focus value (FV) versus the focus lens position (FLP)

in this scenario is illustrated in Figure 6-5. A lot of autofocus search algorithms, including mountain climbing search (MCS) algorithm and its modifications (Li et al., 2018; Ooi et al., 1990), have been developed and can work very well in such applications.

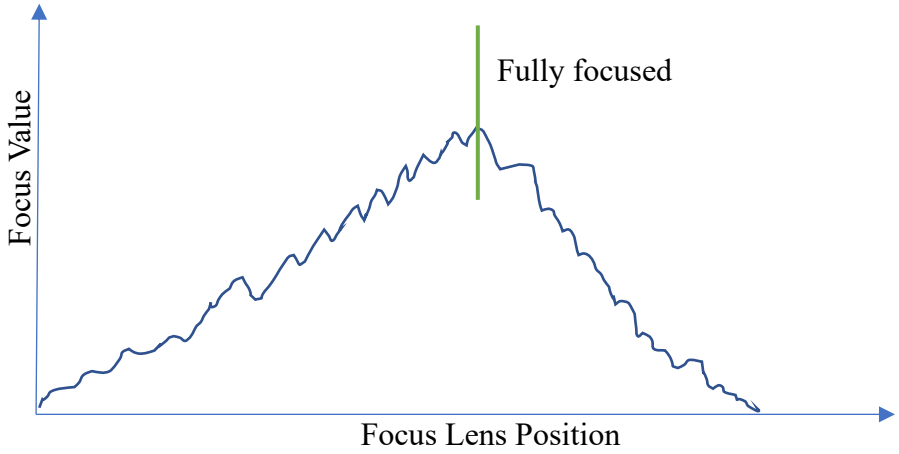

Figure 6-5 Focus value versus focus lens position in common autofocus

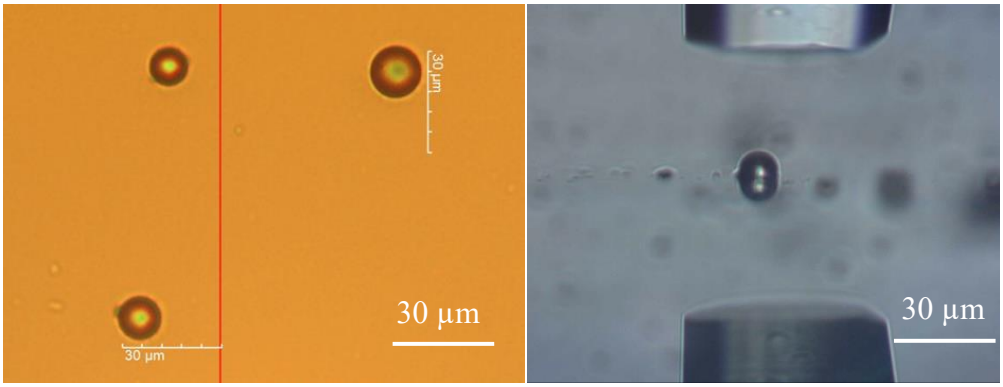

Figure 6-6 Difference between top-view (a) and side-view images (b) in autofocus

However, the circumstance to achieve the autofocus for the micromanipulation measurements is quite different. Unlike microscopy systems (Fu et al., 2015; Song et al., 2007) which usually focus specimen from the top-view (or bottom-view) images as shown in Figure 6-6a, in the automatic micromanipulation system only sideview images are obtained and used to search

and focus particles as shown in Figure 6-6b. In top-view (or bottom-view) applications, all the particles are roughly in the same plane from the camera. Therefore, if one of them is well-focused, the others will be in focus or only need to be adjusted slightly to be in focus. In contrast, from only the sideview, there are hardly multiple particles in the same plane to the camera (Figure 6-7b). Thus, almost every particle needs to be focused individually.

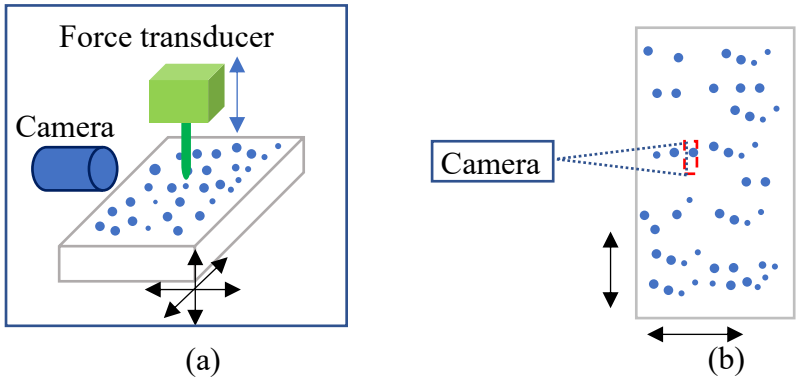

Figure 6-7 Illustration of autofocus based on only the side-view camera

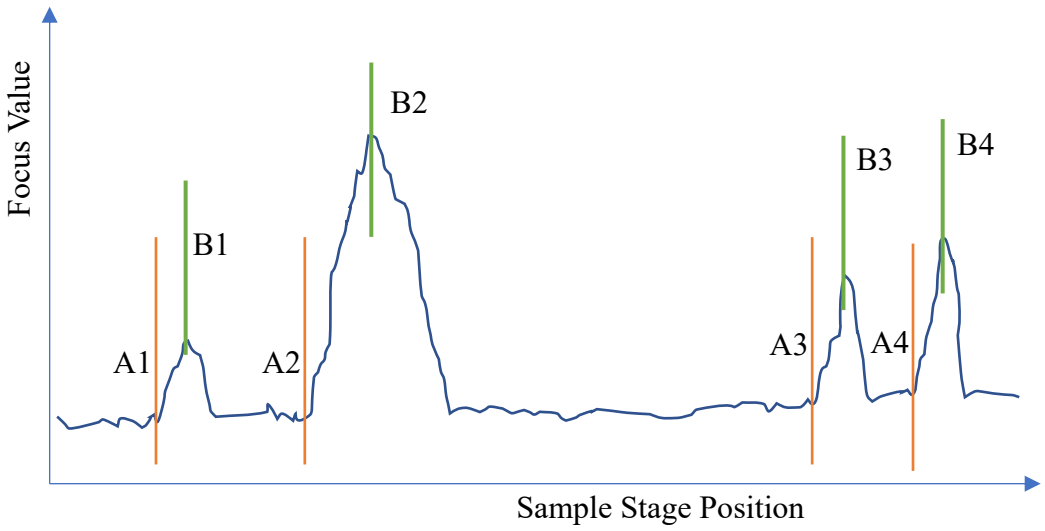

Figure 6-8 Focus value versus sample stage position in the automatic micromanipulation system

Moreover, the **sample stage** rather than the lens of the camera should be moved to let particles

on the stage be in the FOV of the sideview camera as illustrated in Figure 6-7. Initially, there may be no particle in the FOV of the camera. Therefore, firstly the sample stage needs to be moved to let the single particles go into the FOV of the camera. Then the particles can be focused using a focus search algorithm, such as MCS. The key problem here becomes how to detect the position (A1, A2, A3, A4 in Figure 6-8) where single particles first appear in the FOV of the camera.

For example, in Figure 6-8 every mountain-shaped region may correspond to a single particle. Points A1, A2, A3 and A4 correspond to the positions where the particles first appear in the FOV of the camera. Points B1, B2, B3 and B4 correspond to the position where the particles are fully focused. Points A1, A2, etc. can be called the starting points and Points B1, B2, etc. can be called the focal points. Now the challenge to find the starting point (A1, A2, etc.) is quite similar to the one to determine the starting point in the microparticle strength analysis program (Section 3.2.4). One major difference is that the baseline of FV can change with the position of the sample stage during its movement as the background images can change. To overcome this problem, the average of FV (FVW) in a time window (with a width w_t) of the sample stage movement can be used to estimate the baseline and the starting point can be determined where real-time FV starts to deviate from FVW significantly. This leads to the following criterion:

$$FL > d_1\% \tag{6-2}$$

where

$$FL = \frac{FV - FVW}{FVW} \tag{6-3}$$

d_1 is a threshold, and FVW is calculated using the following equation.

$$FVW = \frac{1}{w_t}\sum_{i=1}^{w} FV(t-i) \tag{6-4}$$

where w is the width of the moving window. The values of d_1 and w_t may depend on the kinds of particles, moving speed of the sample stage, acquisition time, etc. and need to be optimised.

Figure 6-9 shows the real data of FV, FVW and FL versus the sample stage position of a commercial PMC microcapsule with diameter around 40 μm during the process in which it appeared and then disappeared in the FOV of the sideview camera when the sample stage moved towards the sideview camera. The moving window width $w_t = 20$. It can be seen that FV and FL both increase when the particle moved towards the focal plane and decrease when the particle moved away from it. FL can be used to determine the key points (A and C).

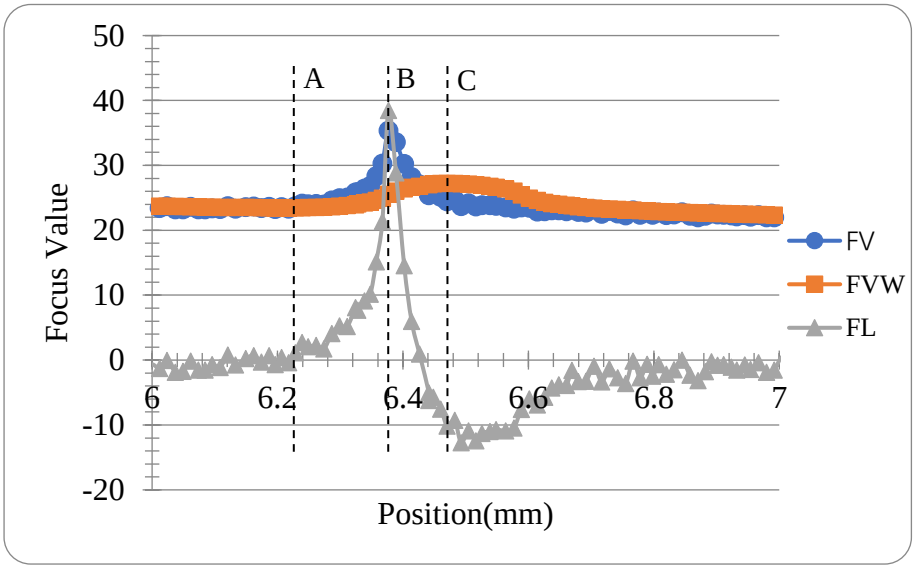

Figure 6-9 Real-time *FV*, *FVW* and *FL* data versus the sample stage position

6.3.2.2. Autofocus algorithm

The data of FV in the process of autofocus is illustrated in Figure 6-10. The FV increases from the starting point (A) where a particle starts to appear in the FOV of the camera, to the in-focus point (B), then decreases till the end point (C) after which the particle disappears from the field of view.

The autofocus algorithm can mainly be divided into three steps as follows:

Step 1 (Searching): A high speed v_1 is used to move the sample stage and a threshold d_1 is used to search the starting point A based on Inequation (6-2).

Step 2 (Focusing): A low speed v_2 is used to move the sample stage and another threshold d_2 is used to search the end point C based on Inequation (6-5) during which the series of focus value FV, motor position P and the image I (FV, P, I) are recorded.

Step 3 (Fine tuning): Find point B (corresponding to the peak value of FV in the series of (FV, P, I)) and move the sample stage back to B. Then a fine-tuning speed v_3 is used to move the sample stage around the maximum point B to tune the focus further.

$$FL < d_2\% \tag{6-5}$$

6.3.3. Estimation of autofocus parameters

In the process of autofocus shown in Figure 6-10, the moving step size in searching ΔP_1, focusing ΔP_2 and fine tuning ΔP_3 can be calculated by

$$\Delta P_1 = v_1 t_c \tag{6-6}$$

$$\Delta P_2 = v_2 t_c \tag{6-7}$$

and

$$\Delta P_3 = v_3 t_c \tag{6-8}$$

where t_c is the control loop time of the autofocus system.

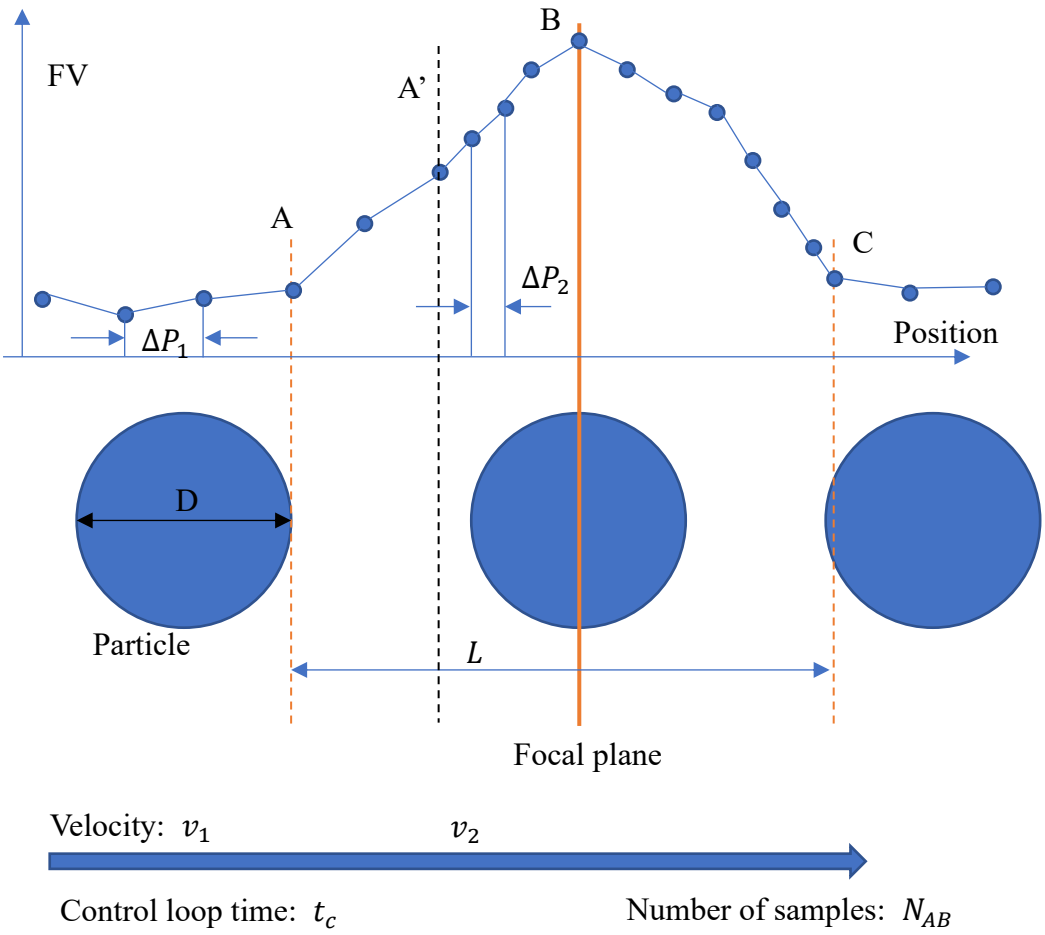

Figure 6-10 Auto focus process of a single particle

Ideally, the starting point A should be identified where it locates. However, in practice the starting point is usually identified a few points later than A (as A' in Figure 6-10) because of the moving step and threshold used. In extremely bad case, the starting point should be identified before the sample stage moving to B **at the speed of v_1**. The number of sample points from A to A' ($N_{AA'}$) can be estimated by

$$N_{AA'} \leq \frac{P_{AB}}{\Delta P_1} = \frac{L}{2 \cdot \Delta P_1} \tag{6-9}$$

where P_{AB} is the distance that the motor moved between A and B, and L is the range within which single particle appears in the field of view. To identify Point A robustly, $N_{AA'}$ should satisfy the following condition

$$N_{AA'} \geq N_0 \tag{6-10}$$

where N_0 is an integer set by the autofocus algorithm.

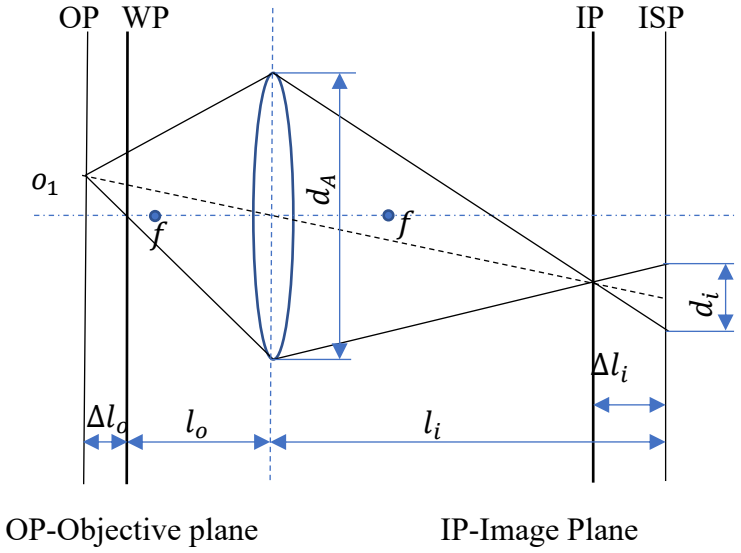

Figure 6-11 The optical imaging model

For a thin lens imaging system, if an object point is in the work plane, the well-focused image plane will overlap with the image sensor plane. Thus, a sharp image will form on the image sensor plan. However, when an object is not in the work plane but with a distance (Δl_o) to it as the object point o_1 in Figure 6-11, a circle will form in the image sensor plane.

According to similarity, the diameter of the image circle (d_i) can be calculated by

$$d_i = \frac{\Delta l_i}{l_i - \Delta l_i} d_A \tag{6-11}$$

where d_A is the diameter of the lens (aperture), l_i is the distance from the lens to the image sensor plane and Δl_i is the distance from the image plane to the image sensor plane.

The area of the image circle s_i can be calculated by the following equation

$$s_i = \frac{\pi d_i^2}{4} \tag{6-12}$$

Substituting Equation (6-11) into (6-12) leads to the following equation

$$s_i = \frac{\pi}{4}\left(\frac{\Delta l_i}{l_i - \Delta l_i}\right)^2 d_A^2 \tag{6-13}$$

Assuming the intensity of the pixels of the image circle is inversely proportional to s_i, for the same object point in two positions with a distance to the work plane of Δl_{o1} and Δl_{o2} respectively, the intensity of pixels of their image circle I_1 and I_2 are related to each other by

$$\frac{I_1}{I_2} = \frac{s_{i2}}{s_{i1}} = \left(\frac{\Delta l_{i2}}{\Delta l_{i1}}\right)^2 \left(\frac{\frac{1}{l_i - \Delta l_{i2}}}{\frac{1}{l_i - \Delta l_{i1}}}\right)^2 \tag{6-14}$$

From Gaussian lens equation (Wayne, 2019), it can be derived that

$$\frac{1}{l_i - \Delta l_{i1}} = \frac{1}{f} - \frac{1}{l_o + \Delta l_{o1}} \tag{6-15}$$

and

$$\frac{1}{l_i - \Delta l_{i2}} = \frac{1}{f} - \frac{1}{l_o + \Delta l_{o2}} \tag{6-16}$$

where f is the focal length of the lens and l_o is the work distance.

According to geometrical optics (Zhang et al., 2014b),

$$\frac{\Delta l_{i1}}{\Delta l_{o1}} = \frac{f}{l_o + \Delta l_{o1} - f} \cdot \frac{f}{l_o - f} \tag{6-17}$$

and

$$\frac{\Delta l_{i2}}{\Delta l_{o2}} = \frac{f}{l_o + \Delta l_{o2} - f} \cdot \frac{f}{l_o - f} \tag{6-18}$$

Substituting Equations (6-15) to (6-18) to Equation (6-14) results in the following equation

$$\frac{I_1}{I_2} = \frac{{\Delta l_{o2}}^2}{{\Delta l_{o1}}^2} \cdot \left(\frac{l_o + \Delta l_{o1}}{l_o + \Delta l_{o2}}\right)^2 \tag{6-19}$$

In automatic micromanipulation system, l_o is much bigger than Δl_{o1} and Δl_{o2} (e.g., for the 20X objective, $l_o = 20.0\,\text{mm}$, while Δl_{o1} and Δl_{o2} usually are in the same order of magnitude as the diameter of particles which is less than 1.0 mm). Thus,

$$l_o + \Delta l_{o1} \approx l_o + \Delta l_{o2} \tag{6-20}$$

Substituting it into Equation (6-19) results in

$$\frac{I_1}{I_2} = \frac{{\Delta l_{o2}}^2}{{\Delta l_{o1}}^2} \tag{6-21}$$

In the automatic micromanipulation system, when a single particle is within the distance of $D + \gamma$ (D is the diameter of the particle and γ is the depth of field) from the work plane, part or whole of the particle will be well focused and its corresponding pixels will have the intensity of I_H in the image captured by the camera. When the particle is out of the range of $D + \gamma$ from the work plane, their pixels in the image will have a relatively low intensity of I_F, and from Equation (6-21)

$$I_F = \left(\frac{D + \gamma}{L}\right)^2 I_H \tag{6-22}$$

If I_F is bigger than the intensity of background pixels (I_B) by a threshold I_0, the focus value will still increase so that the particle can still be detected by the auto focus algorithm.

$$I_F \geq I_B + I_0 \tag{6-23}$$

From these two equations,

$$L \leq (D+\gamma)\sqrt{\frac{I_H}{I_B+I_0}} \tag{6-24}$$

The intensity will not increase further when L is less than $D+\gamma$. Thus

$$D+\gamma \leq L \leq (D+\gamma)\sqrt{\frac{I_H}{I_B+I_0}} \tag{6-25}$$

Combination of Equation (6-9), (6-10) and (6-25) leads to the following criterion:

$$\frac{D+\gamma}{2N_0 t_c} \leq v_1 \leq \frac{D+\gamma}{2N_0 t_c}\cdot\sqrt{\frac{I_H}{I_B+I_0}} \tag{6-26}$$

During focusing and fine tuning, in order to make the particle in-focus, the step size ΔP_2 and ΔP_3 should satisfy the following two conditions:

$$\Delta P_2 < \gamma \tag{6-27}$$

and

$$\Delta P_3 < \gamma \tag{6-28}$$

The depth of field γ can be found from the specification of the objective. Then from Equations (6-7), (6-8), (6-27) and (6-28), the velocity v_2 and v_3 can be estimated by

$$v_2 < \frac{\gamma}{t_c} \tag{6-29}$$

and

$$v_3 < \frac{\gamma}{t_c} \tag{6-30}$$

From Equation (6-26), (6-29) and (6-30), the three focus searching speeds can be estimated from the parameters (γ) of the hardware system and the typical intensity values (I_B, I_H) of the pixels of background and in-focus particles.

Table 6-1 Hardware parameters of the automatic micromanipulation system

Parameter	Unit	Value	Note
γ	μm	1.6	From the specification data of the objective (20x)
N_0	-	2	From the autofocus algorithm
t_c	ms	50	Estimated from the tests on a laptop. CPU module was Intel™ i7-8750H (6 cores, 2.2 GHz base frequency). 12GB RAM. Operation system was Windows™ 10 Professional 64 bit. It mainly depends on the frame rate of the camera, performance of the computer and the work load of the computer operation system. It can be set from the UI of the software package.
I_0		5	
I_B		27	
I_H		136	

The main parameters of the hardware system are listed in Table 6-1 and the autofocus parameters can be obtained as listed in Table 6-2.

Table 6-2 Autofocus parameters for the automatic micromanipulation system

Parameter	Unit	Value	Note
v_1	μm/s	$\leq 10.5(1.6 + D)$	v_1 is determined by the Diameter (D) of the smallest particle to be focused
v_2	μm/s	< 32	
v_3	μm/s	< 32	
d_1	%	5	Empirical values from Ooi et al. (1990), which have been adopted in this work
d_2	%	5	

6.3.4. Focus on small particles

Test results show that the autofocus parameters in Table 6-2 work well for big microparticles (e.g., $D \geq 8.0$μm), the specific size limit of which depends on several factors including the

magnification of the optical system, the light source, the resolution of the camera, and colour and transparency of tested particles (see also Section 6.8). For example, for a magnification of 5.5 pixels/μm, the hardware listed in Table 6-1 and the white light source, the algorithm can focus most microparticles bigger than 8 μm including the MF microcapsules and the porous PS microspheres. For small particles, especially those smaller than 5 μm, the value of FL caused by their appearance in the images is too small to be detected by the thresholds (5%) of d_1 and d_2. Smaller threshold values can be used to detect small particles, but this will make the algorithm too sensitive to noise (Ooi et al., 1990).

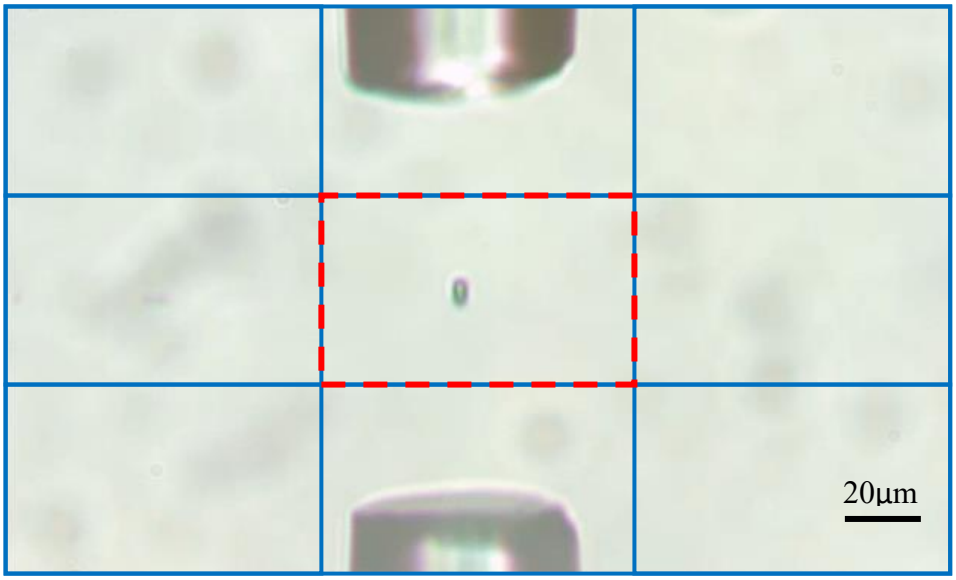

Figure 6-12 Focus on small particles in subregions

A strategy can be used by dividing the whole image into sub areas (Lin, 2018) to focus small particles as shown in Figure 6-12, in which the image is divided into 3×3 subregions and a small particle (3.5 μm) is in the Row-2-Column-2 sub image (dashed cell). The particle is relatively bigger corresponding to this sub image than to the whole image. When the sub image

is used to calculate FV, the FV will change significantly in the process to focus this particle, i.e., the thresholds (d_1 and d_2) can be set to relatively large values which will make the algorithm more robust to noise. Based on tests, dividing the image into 1 row and 3 columns is usually enough to focus particles as small as 3μm.

6.4 Development of particle detection algorithm

6.4.1. Particle detection algorithm

After autofocusing, image processing needs to be carried out to identify the **in-focus** single particle including its size and position automatically for testing. The relationship between the contours from raw image and its binary image can reflect the focus states of single particles. For example, contours of a fully in-focus particle are almost the same in both the raw greyscale image and its binary image. The particle detection algorithm is based on this phenomenon and a combination of several other algorithms of image processing (Section 6.4.2). The particle detection algorithm is divided into three steps as shown in Figure 6-13 to Figure 6-15.

Step 1: Extract edges of blobs and edges of objects. A focused source image is firstly converted to a greyscale image (101) followed by binary conversion and edge detection to convert the image into a binary image (111) and an edge image (121) respectively. Then the blobs are found and the blobs' edges are extracted by blob detection algorithm in step 112 and 113. The outer edges of objects (prone particles) are extracted in steps 122 and 123.

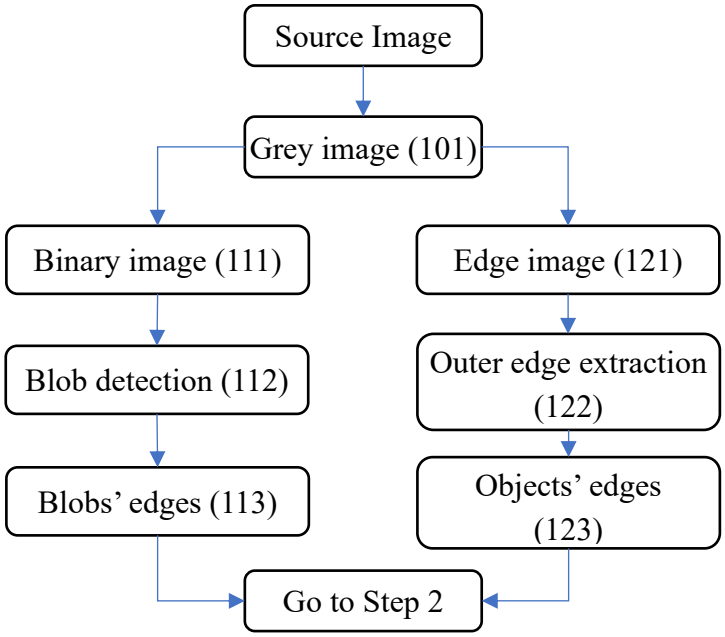

Figure 6-13 Particle detection algorithm (Step 1 of 3)

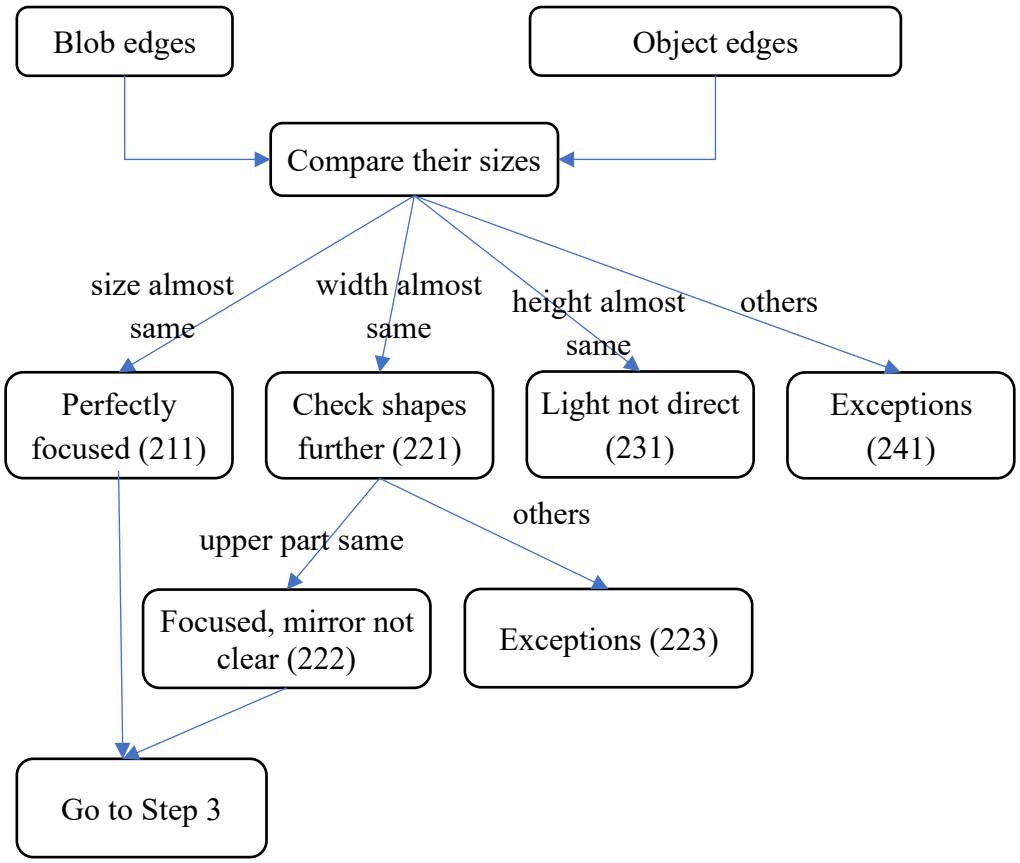

Figure 6-14 Particle detection algorithm (Step 2 of 3)

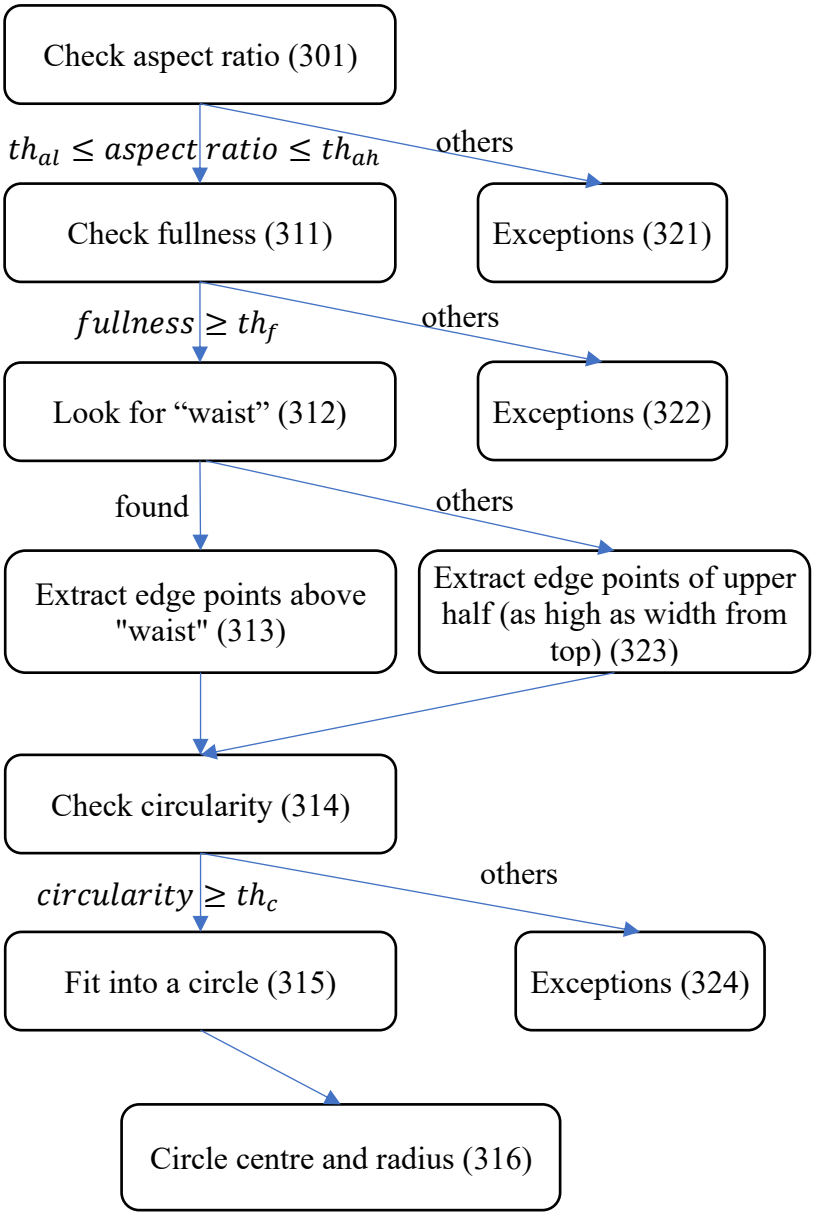

Figure 6-15 Particle detection algorithm (Step 3 of 3)

Step 2: The sizes of the blobs' edges and objects' edges obtained in Step 1 are compared one (blob) by one (object in same position as the blob). If their sizes are almost the same (the tolerance value can be set from the software UI with a default value of 3 pixels), which indicates that the object is perfectly focused (211), the algorithm will go to Step 3 directly. If their width values are almost the same (the tolerance value can be set from the software UI

with a default value of 3 pixels), the edges will be checked further to see if their upper parts are the same, which means the object is well focused but its mirror image is not sufficiently good. In this case, the algorithm will also go to Step 3. In all other cases, the algorithm will stop to restart the autofocus to focus other particles.

Step 3: Check if the focused object is a single particle using some shape features, including the aspect ratio, fullness and circularity of the edge points (Section 6.4.3 below). Firstly, the aspect ratio (301) is checked if it is in the range of the lower and upper thresholds (th_{al} and th_{ah}). If so, then the fullness (311) is checked if it is greater than the threshold (th_f). If yes, the algorithm will search the "waist" of the contour (312) where the left and right vertical contours become concave, corresponding to the glass surface. If the waist is found, the contour points upwards (Figure 6-16i) will be extracted (313). Otherwise, the contour points of upper half (as high as width from top) will be extracted (323). Then, the circularity of the extracted contour points will be calculated and checked if it is greater than the threshold (th_c). If yes, the extracted contour points will be fitted into a circle from which the diameter and location of the particle (circle centre) are determined. Otherwise, the algorithm will stop searching and focus other particles. Fitting the extracted contour into a circle is the default method to determine the particle size. Other methods include using the width of the contour or the width and height of the contour to calculate the size of the particle. For spherical particles, their results are similar. But for irregular microparticles, the default method is preferred. The method to be used can be selected from the UI of the developed software package.

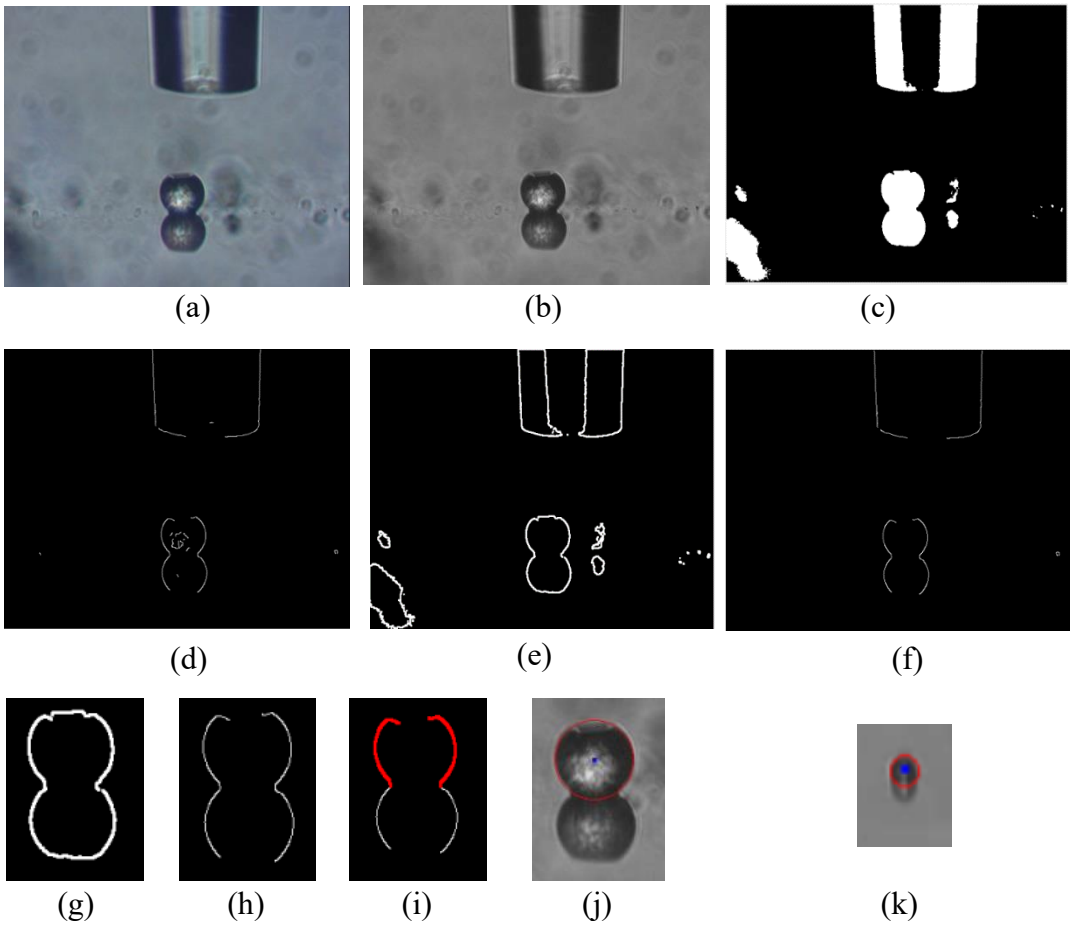

Figure 6-16 A PMC single microcapsule located by the detection algorithm

Figure 6-16 (a-j) illustrates a single microcapsule (from a commercial PMC sample) successfully identified by the particle detection algorithm, where (a) is the source image, (b) is the grey image, (c) is the binary image, (d) is the edge image, (e) is the contour image from (c), and (f) is the outer edge image extracted from (d). The sizes of the contour and outer edges in (g) and (h) of the particle are almost the same which means the particle was well focused. The "waist" was successfully found (i) and the diameter and location of the particle was determined. The diameter of the particle was 38.3μm and its centre was (155.0 μm, 160.0 μm). In contrast, the particle in (k) is very small and no “waist” was found. The contour points of

upper half (as high as width from top) were used to fit into a circle and its diameter was 7.0 μm and its centre was (274.0 μm, 128.0 μm).

6.4.2. Key image processing algorithms used

The image processing algorithms used are mainly from the open-source library Accord.NET Framework 3.8 (Accord.NET, 2017). The GrayscaleRMY class has been used to convert the raw image to greyscale image. The CannyEdgeDetector class has been used to identify edges from the greyscale image and the OtsuThreshold class and FillHoles class used to convert the greyscale images of particles to binary image. The BlobCounter class has been used to count objects and to obtain their information including bounding rectangles and edge points from the binary image and the LevenbergMarquardt class used to estimate the diameter and centre of single microparticles based on least-squares optimisation.

6.4.3. Shape features used to identify particles

Some shape features including aspect ratio, circularity and fullness have been calculated using Equations (6-31) to (6-33). Some or all of the features can be selected and used to determine if an in-focus object is a required singe particle. If values of selected features of an object are greater than their pre-set thresholds, it will be determined as a single particle. The threshold values were set empirically and a general strategy is that to detect spherical particles, the values of aspect ratio and circularity close to 1.0 and the value of fullness close to 0.79 ($\pi/4$) should be used. For irregular shaped microparticles, a smaller value of circularity should be used.

$$aspect\ ratio = \frac{height}{width} \tag{6-31}$$

$$circularity = \frac{4\pi \cdot area}{perimeter^2} \tag{6-32}$$

$$fullness = \frac{area}{width * height} \tag{6-33}$$

6.5 Other essential algorithms

6.5.1. Automatic estimation of the magnification of the video system

In the automatic micromanipulation system, the good resolution of the sideview optical system is essential to determine the size of tested particles. As the position of the probe is associated with the position of the micromanipulator to hold the force transducer, their relationship can be used to obtain the magnification of the optical system. When the micromanipulator is moving by a position increment Δp, the position of the probe in the image will be changed by Δn pixels. Thus, the magnification (M) of the optical system can be determined using the following equation

$$M = \frac{\Delta n}{\Delta p} \tag{6-34}$$

The increment of the micromanipulator position can be obtained from its motor controller automatically. To get the increment number of pixels, an algorithm needs to be introduced to automatically determine the position of the probe in the image. The motion detection algorithms in Accord.Net framework provides a solution for this, including the *CustomFrameDifferenceDetector* class, the *BlobCountingObjectsProcessing* class and the *MotionDetector* class. Using their combination can detect, highlight and obtain information of

moving objects.

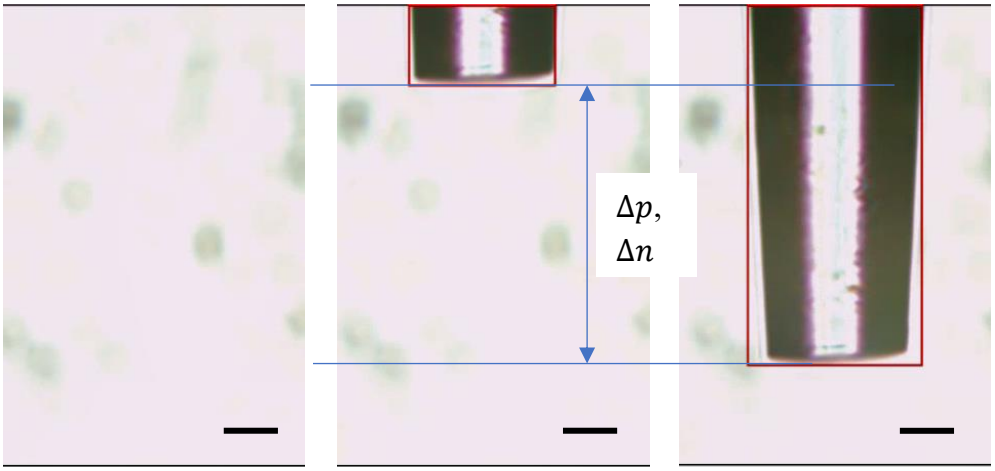

Figure 6-17 Automatic estimation of the magnification of the video system using motion detection (scale bar: 20 µm)

The procedure of using motion detection to calibrate the magnification is illustrated in Figure 6-17. At first, an image without the probe is set as the background (a) and the fine micromanipulator holding the force transducer is moving down to let the probe appear in the image and detected by motion detection and its bounding rectangle is obtained (red rectangle) (b). Finally, move the micromanipulator further down by a position increment of Δp and detect the probe again with motion detection to obtain its bounding rectangle (c). Thus, the increment of pixels Δn is obtained by the difference of the bottom of the two rectangles in (b) and (c). Finally, the magnification can be calculated using Equation (6-34).

6.5.2. Automatic detection of debris adhered to the force probe

Some particles may be sticky, and their debris is usually adhered to the force probe after compression, which needs to be removed before other particles are compressed. The motion

detection algorithms mentioned in last section has been used here to identify the debris. The procedure is illustrated in Figure 6-18. It is assumed that the probe is clean before compression (a) and the image is set as the background image. After compression, the probe returns to its initial position as shown in (b). The image in (b) is compared to the background image in (a) by the motion detection algorithms and the motion areas (different areas) and their bounding rectangle are highlighted in (c) and (d) respectively. Finally, the motion areas overlapped with the probe end and its mirror ends can be chosen as the debris adhered to the probe.

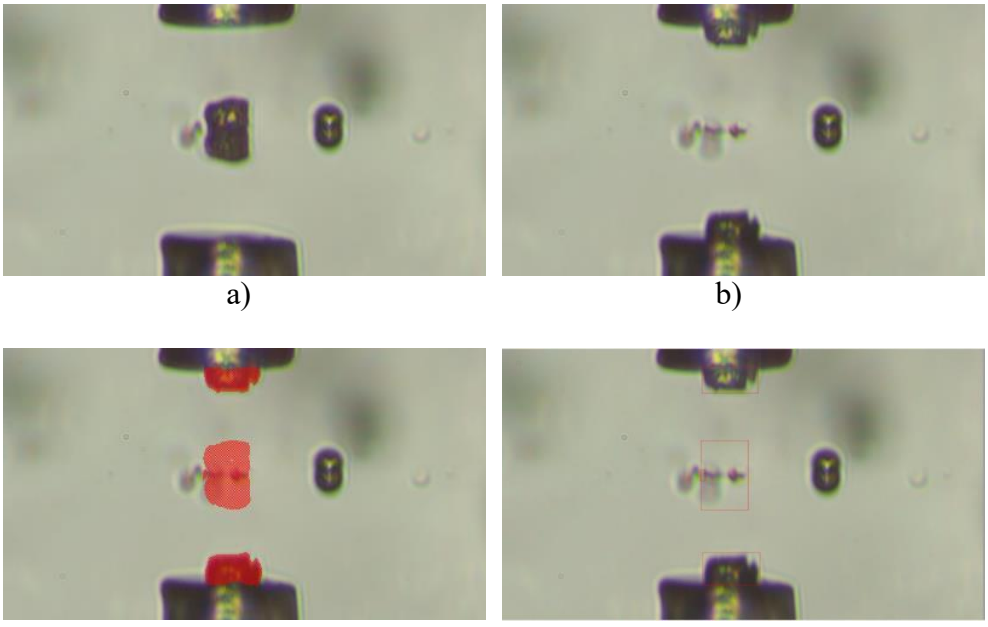

Figure 6-18 Detection of the debris adhered to the force transducer probe automatically

6.6 Operation modes of the automatic micromanipulation system

The developed automatic micromanipulation system can work in several modes, including fully-auto, semi-auto, focus-only and manual. In fully-auto mode, the system will autofocus, auto detect, auto test and auto analyse the single particles. In semi-auto mode, after a single

particle is autofocused and detected, users need to confirm if it is required and choose to test it or not. In focus-only mode, the system only automatically focuses objects without checking shape features or measuring sizes, and allows the users to measure the sizes by drawing rectangles around targeted area. The final mode is used to test micro-sized material samples with uncommon shapes, e.g., microneedles.

6.7 Verification of the developed automatic micromanipulation system

In order to verify the functions of the developed automatic micromanipulation system, two microparticle samples were tested by the automatic and the conventional micromanipulation systems respectively. The results from both systems were compared to verify the functionality of the automatic one.

6.7.1. Materials and methods

6.7.1.1. MF microcapsules with lily oil

The MF microcapsules used were synthesized via in-situ polymerisation in the same way as reported by Luo et al. (2022) and the sample was fabricated and provided by Dr Yanping He and her students, in the School of Chemical Engineering, Kunming University of Science and Technology, China. Specifically, the shell material was MF (MGF 1-1) and the core material was lily oil.

6.7.1.2. Porous PS microspheres

The porous PS microspheres used were from the same batch as those tested in Section 3.2.1.2, fabricated and provided by Dr Yanping He and her students, in the School of Chemical

Engineering, Kunming University of Science and Technology, China (Li et al., 2021b).

6.7.1.3. Test methods

Each sample was placed onto a glass slide and tested using the two systems. In every test, 50 particles were compressed to rupture and their results were analysed using the developed automatic data analysis software as presented in Chapter 3. The force transducer used was 403B-HD (Aurora Scientific Inc., Canada) with a sensitivity of 0.50 mN/V. The compression speed was 2 μm/s. The ambient temperature and humidity were 24 ± 2 ℃ and 58% ± 3% Rh when the MF microcapsules were tested (using both systems). The values were 23 ± 2 ℃ and 65% ± 3% Rh when the porous PS microspheres were tested (using both systems).

Table 6-3 Rupture strength of MF microcapsules tested by both systems

	D (μm)	δ_r (μm)	F_r (mN)	ε_r (%)	σ_r (MPa)	T_r (μN/μm)	T_c (MPa)
Auto	9.5±0.5	4.5±0.3	0.43±0.03	47.0±1.4	7.2±0.6	46.6±2.8	1.05±0.09
Conv	9.7±0.4	4.3±0.2	0.45±0.03	45.0±1.0	7.1±0.5	47.6±2.4	0.93±0.06

Table 6-4 Rupture strength of PS microspheres tested by both systems

	D (μm)	δ_r (μm)	F_r (mN)	ε_r (%)	σ_r (MPa)	T_r (μN/μm)	T_c (MPa)
Auto	10.0±0.4	1.4±0.1	1.9±0.1	14.1±0.7	24.5±0.8	184.7±7.0	1.90±0.13
Conv	9.7±0.4	1.2±0.1	1.7±0.1	12.2±0.3	23.2±0.8	169.1±5.7	1.50±0.07

6.7.2. Results and discussion

6.7.2.1. Rupture strength of the two samples obtained from the two systems

The average and standard error of rupture strength parameters of the MF microcapsules tested by the automatic micromanipulation system (auto) and the conventional system (conv) are

listed in Table 6-3, and those of the porous PS microspheres are shown in Table 6-4. It appears that for the two samples, the rupture strength results obtained from using the two micromanipulation systems have no significant difference with 95% confidence.

6.7.2.2. Performance of the automatic micromanipulation system

From auto calibration, the magnification of the video system of the automatic system was 5.5 pixels/μm. The main parameters used in the automatic micromanipulation system to detect the two samples are listed in Table 6-5. The size range was set to 4-20 μm for MF microcapsules but 4-16 μm for the PS microspheres because larger PS microspheres could not be ruptured by the 403B force transducer. It was found that among the single particles successfully focused and detected by the automatic system, 15/50 MF microcapsules and 15/54 PS microspheres were smaller than 8.0 μm, which indicates the power of the autofocus and particle detection algorithms developed in this work. The smallest MF microcapsule and PS microsphere found were 4.9 μm and 4.7 μm respectively, and the largest found were 19.6 μm and 15.3 μm respectively. Moreover, the tested 50 particles were sufficiently representative which can be seen from the average values of diameter from both the automatic and conventional micromanipulation systems (Table 6-3 and Table 6-4).

The time spent on testing 50 particles with the conventional system was usually 1-3 hours depending on the users' familiarity with the technique. In contrast, it usually only took at most 1 hour by the automatic system to test the same number of particles, including the time spent by the users to clean the debris adhered to the probe. Moreover, a lot of labour work was

needed to operate the sample stage to find single particles and to measure their size when using the conventional system, whereas no labour work was required during the test using the automatic system (in fully-auto mode) except occasionally cleaning the debris adhered to the probe.

Table 6-5 Shape feature thresholds used in the automatic micromanipulation system

Parameter	Unit	Value	Note
Size range	μm	4 - 20	Particle with diameter in the range will be tested
(th_{al}-th_{ah})		0.7 - 1.2	Aspect ratio range
th_f		0.75	Fullness threshold
th_c		0.7	Circularity threshold

6.8 Further discussion of the image quality and particle size limits

The best magnification of the optical system is 5.5 pixels/μm, corresponding to 0.176 μm per pixel in the automatic micromanipulation system. However, it does not mean that the optical system can detect particles as small as 0.176 μm, because the ability of the optical system to distinguish detail (termed as limit of resolution) depends on several factors.

The limit of resolution (or resolving power) is the smallest distance between two dots or lines that can be seen as separate entities by the optical system (Wayne, 2019). The limit of resolution (LoR) can be calculated using the following equation (Rayleigh, 1896; Wayne, 2019)

$$LoR = 1.220\frac{\lambda}{2NA} \tag{6-35}$$

where λ is the light wavelength and NA is numerical aperture of the lens. It can be seen from Equation (6-35) that the ultimate resolution ability of the microscope is determined by

the light wavelength and the NA of the objective. In the automatic micromanipulation system, the NA of the used objective is 0.42 and the light source is white with the average wavelength of 550 nm. Thus, the **theoretical** limit of resolution of the optical system is 799 nm (≈ 0.80 μm). Thus, theoretically speaking, smaller microparticles (e.g., diameter around 1μm) may be detected by the automatic micromanipulation system.

However, the quality of the image also significantly affected by the quality of the lens, as optical aberrations, including spherical and chromatic aberrations can result in blur and distortion. Thus, the resolution is also defined by how well a lens has been corrected for spherical and chromatic aberrations (Wayne, 2019). Moreover, resolution is meaningless without contrast (Wayne, 2019). Contrast can be increased by decreasing the aperture (NA) of lenses (Wayne, 2019). But Equation (6-35) indicates that the limit of resolution is increased (i.e., resolution ability decreases) by increasing the aperture of lenses. Thus, trade-off needs to be made to obtain high-quality images.

Overall, as a result of all the factors, the images obtained from the side-view camera (optical) system can capture images with sufficient quality for microparticles with diameter above around 3μm that can be successfully detected by the automatic micromanipulation system. However, theoretically speaking, if using light source with short wavelength (e.g., blue) and lenses (objectives) with large NA values and higher quality to optimise the optical hardware system, smaller microparticles may still be detected and tested by the developed automatic micromanipulation system.

6.9 Conclusions

A new micromanipulation system was developed to focus, detect, test and analyse microparticles automatically, which has significantly enhanced the power of the conventional micromanipulation technique. The principle of the automatic micromanipulation system, the autofocus and auto particle detection algorithms and two other essential algorithms for automatic determination of the magnification of the optical system and for automatic identification of particle debris adhered to the force transducer probe after compression to ensure the automatic functions were devised and implemented. Equations ((6-26), (6-29) and (6-30)) were developed to estimate the autofocus parameters from the hardware parameters of the optical system. Experiments were also carried out to characterise two microparticle samples using both the automatic and conventional micromanipulation systems to verify the former one. The results show that the newly developed automatic micromanipulation system has generated the mechanical strength data of microparticles, which are in excellent agreement with those from the conventional system. Moreover, it is much easier to use, faster and requires much less labour work to complete the same task, which is advantageous and represents a step change in improvement of the conventional micromanipulation technique.

Although the automatic micromanipulation system can only autofocus and detect microparticles not smaller than 3μm currently, even smaller microparticles (e.g., around 1 μm) can be autofocused and detected if light source with short wavelength (e.g., blue) is used and the optical hardware system is optimised.

CHAPTER 7: OVERALL CONCLUSIONS AND RECOMMENDATIONS FOR FUTURE WORK

7.1 Overall conclusions

Among all available experimental techniques to characterise the mechanical properties of micro-sized materials, the micromanipulation technique developed in the University of Birmingham UK has been demonstrated to be very powerful and been widely used to determine the mechanical properties of a variety of single biological and non-biological micro-sized materials in academic research and new product development based on these materials in collaboration with industry. However, it was largely based on manual operations and data analysis, which is quite time-consuming, laborious and technically demanding. The main aim of this project was to enhance the capability of the micromanipulation technique as well as to characterise the mechanical strength of some new micro-sized materials. The main conclusions are summarised as follows.

(1) To achieve fully automatic analysis of the rupture strength of microparticles from the raw experimental data, three algorithms (the "3σ", "3σ + window" and "3σ + window + Hertz") were developed to locate the starting point where onset of compression begins, and one algorithm ("maximum deceleration") was developed to identify the rupture point (Chapter 3). The "3σ" algorithm locates the starting point where the experimental voltage firstly deviates from the average voltage of baseline by three standard deviations of the baseline value. The "3σ + window" algorithm locates a point as the starting point from which all the following

points in a window satisfy the "3σ" algorithm. The "3σ + window + Hertz" algorithm further compensates the starting point obtained from the "3σ + window" algorithm by fitting the initial part (up to 5% fractional deformation) of force-displacement data into the Hertz model. The "maximum deceleration" algorithm identifies the rupture point where the voltage drops most significantly. The algorithms developed here work well automatically with no parameters required to be modified, which can also help researchers to deal with related problems in other applications, e.g., to find the contact point (CP) of the experimental data from using the AFM to characterise the mechanical properties of particles and particle-substrate interactions.

(2) A software package with a user-friendly UI (user interface) and incorporated with the "3σ", "3σ + window", "3σ + window + Hertz" and "maximum deceleration" algorithms was developed to automatically determine the rupture strength of single microparticles from the experimental data of micromanipulation measurements (Chapter 3). Two samples, the PU/PUF double-walled microcapsules for self-sensing and the porous PS microspheres with many potential applications, were tested using the micromanipulation technique and their experimental data were analysed automatically using the developed software package and the results were compared with those obtained manually. It was found that the results obtained from "3σ + window" or "3σ + window + Hertz" algorithms together with the "maximum deceleration" algorithm were excellently consistent with the manual results, and there is no significant difference between them. Under help of the developed software package, the rupture strength parameters can be obtained from the experimental data of single

microparticles automatically without manual interference and the time used has been shortened from 2-3 hours to within 20 minutes for a typical sample with 50 microparticles tested.

(3) Several typical elastic models and plastic models for analysing the experimental data obtained from using diametrical compression (including micromanipulation), indentation, uniaxial compression and tensile tests are summarised from which general equations of the relationship between the force and displacement were derived, including Equations (4-6), (4-7) for elastic and Equation (4-20) for plastic analysis (Chapter 4). General approaches to extend the elastic analysis to viscoelastic analysis and the plastic analysis to viscoplastic analysis were proposed following the method of Yan et al. (2009), which simplifies the procedure of deriving the viscoelastic models from elastic analysis (or viscoplastic models from plastic analysis) in other applications. For example, from the elastic model (Equation (5-17)) for microneedles (Chapter 5), the viscoelastic model was obtained easily by transforming Equation (5-17) to the general form in Equation (4-7).

Moreover, a general approach to determine the yield stress from the elastic analysis based on elastic limit was also developed, inspired by the method of Mercadé-Prieto et al. (2011a) and Zhang (2019), which can find many applications in combination with elastic models (Equations (4-6) and (4-7)).

(4) Another software package was developed and incorporated with several mathematical models, including the Hertz model (Zhang et al., 2009), the FEM simulation results for core/shell structured microcapsules (the core/shell model) (Mercadé-Prieto et al., 2011b), the

viscoelastic model (Yan et al., 2009), and the Abbott & Firestone plastic model (Paul et al., 2014), to determine the intrinsic mechanical properties of microparticles (Chapter 4). The general relationships of force versus displacement in Equations (4-6), (4-7) and (4-20) were used to facilitate the incorporation procedure. The strategies and approaches to incorporate different mathematical models into the software package were proposed and implemented, which can also be used in other related applications.

Two microparticle samples, the PLA microspheres potentially with wide applications and the MF microcapsules with lily oil as liquid core, were tested in dry condition by the micromanipulation technique and their intrinsic mechanical properties were obtained from the experimental data using the developed software package incorporated with the mathematical models. Specifically, the plastic model was used for the PLA microspheres and the core/shell model were used for the MF microcapsules. The hardness value (90.1 ± 8.2 MPa) of the PLA microspheres obtained from the software package was consistent with the reported values (80 -100 MPa) of PLA macro-materials obtained from the Shore hardness tests (Gong et al., 2017; Teymoorzadeh & Rodrigue, 2015; Vian & Denton, 2018). The MF microcapsules were found to have significant greater shell thickness (0.28 ± 0.03 μm) but much smaller Young's modulus (2.9 ± 0.3 GPa) in comparison with those MF microcapsules (shell thickness: 0.19 ± 0.01 μm, Young's modulus: 4.8 ± 0.4 GPa) tested by Mercadé-Prieto et al. (2011a), which resulted from different formulation and processing conditions used to fabricate them. For example, firstly, the molar ratio of the total formaldehyde content to melamine was 3.0 for MF microcapsules

tested in this project but 0.49 for the MF microcapsules tested by Mercadé-Prieto et al. (2011a) and it was found that higher F/M molar ratio resulted in thicker shells (Long et al., 2009). Secondly, the reaction time was only 2h for the capsules tested in this work but 4h for those tested by Mercadé-Prieto et al. (2011a) and different reaction time can affect the compactness of the MF shell depositing on the surface of the core oil which has caused MF shell with different mechanical strength.

(5) It is believed that the two software packages developed to determine the rupture strength and intrinsic mechanical properties of microparticles (Chapters 3 and 4) can also be used to automatically analyse the force-displacement (and force-time) data obtained using conventional mechanical testing machines for macro-scale materials, e.g., using texter analyser to do mechanical characterisation of biological and non-biological materials, which can have a wide range of applications.

(6) The relationship between the Hertz analysis and the core/shell model based on the FEM simulation results for core/shell structured materials was established and an equation correlating the apparent Young's modulus value of a microcapsule determined using the Hertz model by treating it as a homogeneous sphere and that of its shell material was derived (Equation (4-17)) (Chapter 4). The establishment of the relationship further validated the FEM simulation results as well as provided another method to estimate the Young's modulus of the shell material from the apparent Young's modulus obtained from the Hertz analysis that is easier to carry out, if the shell thickness is known. The results of the MF microcapsules with

lily oil as liquid core validated this relationship. From the apparent Young's modulus value (61.4 ± 7.5 MPa) obtained from the Hertz analysis, the Young's modulus of the MF shell was calculated to be 2.90 ± 0.27 GPa, which is excellently consistent with the value (2.92 ± 0.29 GPa) obtained directly from the FEM simulation results.

(7) Three mathematical models (Section 5.3), based on the MS (maximum stress) analysis, the elastic analysis, and the viscoelastic analysis, were developed to determine the intrinsic mechanical properties including the mechanical strength of single microneedles from the experimental data obtained using the micromanipulation technique (Chapter 5). From the MS analysis, the mechanical strength parameters of microneedles corresponding to MS, including the maximum stress, the displacement and deformation at MS, and the force and toughness at MS were determined from the force-displacement data and the calculated stress-fractional deformation data obtained from the micromanipulation compression tests. From the elastic analysis, the Young's modulus of the microneedles was determined from the force-displacement data. And from the viscoelastic analysis, the long-term and instantaneous shear and Young's moduli were obtained. In many other studies, the failure force of microneedles was used to predict their penetration capacity by comparing it with the insertion force required to penetrate the skin using microneedles with the same geometric parameters, especially the tip size as the required insertion force was mainly determined by interfacial area at needle tip and the applied pressure (Chi et al., 2022; Davis et al., 2004; Kim et al., 2018; Park et al., 2006), which is not sufficient since, the failure force is not an intrinsic mechanical property

parameter. In contrast, the intrinsic mechanical property parameters obtained using the three developed models in this project can be used to compare the mechanical properties of microneedle samples that can have different structures and/or different geometries comprehensively and to predict their penetration capacity more reliably. Moreover, the three developed models can also be used to analyse the experimental data of microneedles tested using other techniques, e.g., the force-travel data of microneedles obtained using the micro-mechanical test machine (Wang et al., 2018).

(8) Six samples of HA based microneedles with or without loading drug, including the HA-300kDa, Lido-HA300kDa, HA-10kDa, MeHA, Mel-HA, and Mel-MeHA (Table 5-1) were tested using the micromanipulation technique (Chapter 5). The experimental data were analysed using the three developed mathematical models (Section 5.3) from which the mechanical strength at MS, and intrinsic mechanical properties were determined. The reproducibility of micromanipulation in measuring the mechanical strength of microneedles was validated by the very consistent results of mechanical strength at MS and Young's modulus of two patches of HA-300kDa microneedles tested under similar ambient temperature and humidity conditions. It was also found that the loading of melittin significantly decreased the mechanical strength of HA and MeHA microneedles, which is consistent with the literature (Du et al., 2021b; Park et al., 2006). From the in vivo penetrating experiments undertaken on mice by Dr Du and his colleagues (Du et al., 2021a), the four microneedle samples (HA-10kDa, MeHA, Mel-HA, and Mel-MeHA) all successfully penetrated the abdomen skin of mice. In

this study, the four microneedle samples are predicted to be sufficiently strong to penetrate human skin after comparing their intrinsic material property parameters including maximum stress and Young's modulus with those of human skin. Moreover, the variations of the mechanical strength of single microneedles over a patch were obtained using the micromanipulation technique, which can be used to predict the penetration efficiency (number of successful penetrations / total number of microneedles over a patch) more precisely and reliably. Furthermore, the results of instantaneous shear and long-term Young's moduli obtained from the viscoelastic analysis of the Lido-HA300kDa microneedles suggest that more reliable penetration can be achieved by increasing the insertion speed (e.g., using an impact-insertion applicator (van der Maaden et al., 2014)) even for microneedles that may not be sufficiently strong in quasi-static penetration.

(9) A "3-step" contrast-based autofocus algorithm was developed to automatically search and focus particles by combination of the Brenner FMF (Brenner et al., 1976) and a modified mountain climbing search (MCS) algorithm (Fu et al., 2015; Ooi et al., 1990) based on only the sideview camera (Chapter 6). Unlike autofocus in other applications such as mobile phone cameras, there may be no microparticles in the field of view (FOV) of the side-view camera before focusing and unlike microscopy systems (Fu et al., 2015; Song et al., 2007) which usually focus specimen from the top-view, multiple microparticles are seldom in a same plane parallel to the sideview focal plane (Figure 6-6). Thus, the sample stage was moved side to side, end to end to let microparticles come into the FOV of the side-view camera during which

autofocus is applied. In the developed "3-step" algorithm, a high speed is used to detect the starting point where a microparticle first appears in the FOV of the side-view camera when the real-time focus value (FV) is greater than its moving average by a threshold (d_1). Then a smaller speed is used to detect the end point where the particle disappears from the FOV when the real-time FV is smaller than its moving average by another threshold (d_2), during which series of FV, image, and motor position in every control loop are saved. Finally, the sample stage is moved back to the prone in-focus point corresponding to the maximum FV and an even smaller speed was used to focus the particle further.

Equations ((6-26), (6-29) and (6-30)) were also derived to automatically estimate the autofocus parameters including the three speeds and the two thresholds from the parameters of the optical system, control cycle time and the intensity of the background and foreground pixels.

(10) An object detection algorithm was developed to detect single particles from autofocused images automatically based on Otsu thresholding, Canny edge detection, and blob detection algorithms (Accord.NET, 2017). An autofocused image is firstly converted to a grey image and then to a binary image using the Otsu thresholding algorithm. Then the edges of blobs detected from the binary image are compared with the Canny edges detected from the grey image to locate prone single particle(s). Finally, several shape features, including the aspect ratio, the circularity and fullness are used to detect real single particle(s) and their information including the position and diameter, are determined.

(11) Another two essential algorithms based on moving detection (Accord.NET, 2017) were

developed to automatically estimate the magnification of the video system and to automatically detect the debris adhered to the output probe of the force transducer. In the algorithm for automatic determination of the magnification of the video system, the fine micromanipulator is moved to let the output probe of the force transducer move a distance in the side-view videos. The pixel positions of the end of the output probe in the images before and after the movement are detected by moving detection algorithms and the magnification of the video system is determined by dividing the number of pixels the probe end moved in the video by the distance the fine manipulator moved (Equation (6-34)). This algorithm is essential for the automatic micromanipulation system in precise determination of the size and location of singe microparticles to be tested. The magnification of the video system may need changing with the size of different microparticle samples (in a large size range of 3-1000 μm) and thus recalibration should be carried out to determine the magnification before the micromanipulation tests. In the algorithm for automatic detection of debris adhered to the force probe, the adhered debris of microparticles was identified by investigating the difference between two images before and after compression using the motion detection algorithm. This is essential for the automatic micromanipulation system as the adhered debris on the probe can change the standard compression profile (between two parallel planes) and affect the measurement results.

(12) An automatic micromanipulation system was devised to search single microparticles automatically based on the conventional micromanipulation system and the developed

algorithms for autofocus, particle detection, automatic detection of the magnification of the video system and the debris adhered to the force transducer probe (Chapter 6). The micromanipulator holding the sample stage was upgraded by replacing the manually operated micromanipulator with a DC servo linear actuator with a motion controller. A software package with a user-friendly UI was developed and incorporated with the developed autofocus algorithm, the particle detection algorithm and the two essential algorithms for automatic determination of magnification of the video system and automatic detection of debris adhered to the force transducer probe. The data analysis software package was also adapted and built into the application program for automatic micromanipulation. The developed automatic micromanipulation system can work in fully auto, semi auto, focus-only and manual operation modes, which can be used in a wide range of applications.

Two samples, the MF microcapsules with lily oil as liquid core and the porous PS microspheres with many potential applications were also tested using both the developed automatic micromanipulation system and the conventional micromanipulation system. Their mechanical strength at rupture were analysed using the software package developed in Chapter 3. The test results show that the developed automatic micromanipulation system can focus, detect and test most single particles whose size is in the range of 3-1000 μm automatically. The size limited by the magnification that the optical system can provide and the limit of resolution of the optical system that is determined by the light source, numerical aperture and quality of the lenses and the optimisation of the overall optical system (Section 6.8). Theoretically speaking,

if the light source and the optical system are optimised, even smaller microparticles (e.g., around 1 μm) can still be detected by the developed automatic micromanipulation system (Section 6.8). The generated mechanical strength data from the developed automatic micromanipulation system are excellently consistent with those from the conventional micromanipulation system. The automatic micromanipulation system is much easier to use, faster, and needs much less labour work to complete the same task, which has enhanced the micromanipulation technique significantly.

7.2 Recommendations for future work

(1) The FEM simulation results for MF microcapsules with a core/shell structure and the viscoelastic model were built into the developed software package as presented in Chapter 4, which requires interacting with the Microsoft™ Excel Solver using the optimisation algorithms in Excel Solver to estimate the parameters of the models. The software package works well but needs installation of Microsoft™ Excel with the Solver add-in, which may result in extra expenditure. There are many optimisation algorithms available in open-source libraries that can be used for free, e.g., the Levenberg-Marquardt, Goldfarb-Idnani and Augmented Lagrangian algorithms in the Accord Framework library (Accord.NET, 2017). Therefore, the developed software package can be improved by incorporating proper optimisation algorithms (e.g., Levenberg-Marquardt) to work with the core/shell model and the viscoelastic model without interactions with other applications, which will be faster and easier to use as well as save money.

(2) Some microparticle samples, e.g., the porous PS microspheres, are sticky so that their debris after compression is easy to adhere to the force transducer probe, which needs removing off before compression of following single particles is carried out. An algorithm was developed in Chapter 6 to automatically detect adhered debris on the probe and a window will pop up reminding the users to clean the probe which will interrupt the work flow of the automatic micromanipulation system. Theoretically speaking, the adhesion can be tackled by coating the force transducer probe with a layer of special material that is inert to the debris. However, the adhesion can result from several mechanisms, including van-der Waals force of the debris, the electrostatic interaction between the debris and the probe surface, the capillary force between the debris and the probe surface, and microscale mechanical interlocking between the debris and the probe surface (He, 2013). Adhesion between the probe and the debris of different samples can be dominated by different mechanisms. Thus, it is essential to fully understand the mechanisms of the adhesion between different microparticle samples and the probe before proper measures are carried out to prevent the adhesion. Another possible solution is to develop an extra sub-system that can automatically clean the probe after adhered debris is identified by the automatic detection algorithm.

(3) A particle detection algorithm was developed in Chapter 6 to detect single particles in combination with several shape features, including the aspect ratio, the circularity and fullness. The threshold values of them were set empirically and worked well for the tested microparticle samples. They may need to be adjusted with samples of different feature properties. The

general adjusting strategy is that for detecting spherical particles, the values of aspect ratio and circularity close to 1.0 and the value of fullness close to 0.79 ($\pi/4$) should be used. For irregular shaped microparticles, a smaller value of circularity should be used. It may take some time for the users to master the skills for the thresholding adjusting according to different samples. Automatic adaption can be achieved by introducing the machine learning algorithms to the automatic micromanipulation system. For example, in combination with machine learning, for new kinds of samples, semi-auto mode can firstly be used which will let the user decide if the automatically detected particles are suitable for test or not and the decisions will be saved and used to train the machine learning models. After the models are sufficiently trained, the fully-auto mode can be used to test the remaining particles or other samples with the same or similar features.

References

Abbott, E. J., and Firestone, F. A. (1933). Specifying surface quality - A method based on accurate measurement and comparison. *Journal of Mechanical Engineering*, 55: 569-572.

Accord.NET. (2017). Accord.Net framework (Version 3.8) [Open-source library]. Retrieved from http://accord-framework.net/

Althaqafi, K. A., Satterthwaite, J., & Silikas, N. (2020). A review and current state of autonomic self-healing microcapsules-based dental resin composites. *Dent Mater, 36*(3): 329-342.

Aniskevich, A., Kulakov, V., Bulderberga, O., Knotek, P., Tedim, J., Maia, F., et al. (2020). Experimental characterisation and modelling of mechanical behaviour of microcapsules. *Journal of Materials Science, 55*(27): 13457-13471.

Arefin, P., Habib, M., Ahmed, N., Bhattacharjee, S., Chakraborty, D., Das, S., et al. (2021). Microspheres and microcapsules: A review of manufacturing techniques for pharmaceutical industries. *12*: 177-185.

Bakry, A. M., Abbas, S., Ali, B., Majeed, H., Abouelwafa, M. Y., Mousa, A., et al. (2016). Microencapsulation of oils: A comprehensive review of benefits, techniques, and applications. *Comprehensive Reviews in Food Science and Food Safety, 15*(1): 143-182.

Baykara, M. Z., & Schwarz, U. D. (2017). Atomic force microscopy: Methods and applications. In J. C. Lindon, G. E. Tranter, & D. W. Koppenaal (Eds.), *Encyclopedia of spectroscopy and spectrometry* (3rd ed.), Oxford: Academic Press, pp. 70-75.

BenÍtez, R., Moreno-flores, S., BolÓs, V. J., & Toca-Herrera, J. L. (2013). A new automatic contact point detection algorithm for AFM force curves. *Microscopy Research and Technique, 76*(8): 870-876.

Bennig, G. K. (1988). Atomic force microscope and method for imaging surfaces with atomic resolution. United States Patent No. 4724318. Washington, DC: P. a. T. Office.

Bergström, J. (2015). 6 - linear viscoelasticity. In J. Bergström (Ed.), *Mechanics of solid polymers*: William Andrew Publishing, pp. 309-351.

Bone, S., Vautrin, C., Barbesant, V., Truchon, S., Harrison, I., & Geffroy, C. (2011). Microencapsulated fragrances in melamine formaldehyde resins. *Chimia, 65*: 177-181.

Boyer, J., & Kramer, P. J. (1995). Measuring the water status of plants and soils. San Diego: Academic Press, Inc.

Briscoe, B. J., Sebastian, K. S., & Adams, M. J. (1994). The effect of indenter geometry on the elastic response to indentation. *Journal of Physics D: Applied Physics, 27*(6): 1156-1162.

Cai, Y., Chen, Y., Hong, X., Liu, Z., & Yuan, W. (2013). Porous microsphere and its

applications. *International journal of nanomedicine, 8*: 1111-1120.

Campos, E., Branquinho, J., Carreira, A. S., Carvalho, A., Coimbra, P., Ferreira, P., et al. (2013). Designing polymeric microparticles for biomedical and industrial applications. *European Polymer Journal, 49*(8): 2005-2021.

Chang, H., Zheng, M., Yu, X., Than, A., Seeni, R. Z., Kang, R., et al. (2017). A swellable microneedle patch to rapidly extract skin interstitial fluid for timely metabolic analysis. *Advanced Materials, 29*(37): 1702243.

Chang, Y.-R., Raghunathan, V. K., Garland, S. P., Morgan, J. T., Russell, P., & Murphy, C. J. (2014). Automated afm force curve analysis for determining elastic modulus of biomaterials and biological samples. *Journal of the Mechanical Behavior of Biomedical Materials, 37*: 209-218.

Charles, R., Saha, B., Alonso-Sarduy, L., Volterra, A., Dietler, G., & Kasas, S. (2012). Openfovea: Open-source AFM data processing software. *Nature methods, 9*: 774-775.

Chen, C. Y., Hwang, R. C., & Chen, Y. J. (2010). A passive auto-focus camera control system. *Applied Soft Computing, 10*(1): 296-303.

Chen, M. J., Zhang, Z., & Bott, T. R. (1998). Direct measurement of the adhesive strength of biofilms in pipes by micromanipulation. *Biotechnology Techniques, 12*(12): 875-880.

Chen, M. J., Zhang, Z., & Bott, T. R. (2005). Effects of operating conditions on the adhesive strength of pseudomonas fluorescens biofilms in tubes. *Colloids and Surfaces B: Biointerfaces, 43*(2): 61-71.

Chi, Y., Huang, Y., Kang, Y., Dai, G., Liu, Z., Xu, K., et al. (2022). The effects of molecular weight of hyaluronic acid on transdermal delivery efficiencies of dissolving microneedles. *European Journal of Pharmaceutical Sciences, 168*: 106075.

Choi, J.-T., Park, S.-J., & Park, J.-H. (2018). Microneedles containing cross-linked hyaluronic acid particulates for control of degradation and swelling behaviour after administration into skin. *Journal of Drug Targeting, 26*(10): 884-894.

Choudhury, N., Meghwal, M., & Das, K. (2021). Microencapsulation: An overview on concepts, methods, properties and applications in foods. *Food Frontiers, 2*(4): 426-442.

Dardano, P., Caliò, A., Di Palma, V., Bevilacqua, M. F., di Matteo, A., & de Stefano, L. (2015). A photolithographic approach to polymeric microneedles array fabrication. *Materials, 8*: 8661 - 8673.

Davies, E. R. (2017). Computer vision: Principles, algorithms, applications, learning (5th ed.). Elsevier: Academic Press.

Davis, S. P., Landis, B. J., Adams, Z. H., Allen, M. G., & Prausnitz, M. R. (2004). Insertion of microneedles into skin: Measurement and prediction of insertion force and needle fracture force. *Journal of Biomechanics, 37*(8): 1155-1163.

Deng, S., Du, G., Li, X., & Pizzi, A. (2014). Performance and reaction mechanism of zero formaldehyde-emission urea-glyoxal (UG) resin. *Journal of the Taiwan Institute of Chemical Engineers, 45*(4): 2029-2038.

Dflux, A., & Kedves, T. (2022). What is phase detection autofocus? (and why it's so important).

Retrieved from https://expertphotography.com/phase-detection-autofocus

Dinarelli, S., Girasole, M., & Longo, G. (2018). FC_analysis: A tool for investigating atomic force microscopy maps of force curves. *BMC Bioinformatics, 19*(1): 258.

Du, G., He, P., Zhao, J., He, C., Jiang, M., Zhang, Z., et al. (2021a). Polymeric microneedle-mediated transdermal delivery of melittin for rheumatoid arthritis treatment. *J Control Release*, *336*: 537-548.

Du, G., Zhang, Z., He, P., Zhang, Z., & Sun, X. (2021b). Determination of the mechanical properties of polymeric microneedles by micromanipulation. *J Mech Behav Biomed Mater, 117*: 104384.

Duan, H., Qiu, T., Guo, L., Ye, J., & Li, X. (2015). The microcapsule-type formaldehyde scavenger: The preparation and the application in urea-formaldehyde adhesives. *Journal of Hazardous Materials, 293*: 46-53.

Fambri, L., Pegoretti, A., Fenner, R., Incardona, S. D., & Migliaresi, C. (1997). Biodegradable fibres of poly(l-lactic acid) produced by melt spinning. *Polymer, 38*(1): 79-85.

Farah, S., Anderson, D. G., & Langer, R. (2016). Physical and mechanical properties of PLA, and their functions in widespread applications - A comprehensive review. *Adv Drug Deliv Rev, 107*: 367-392.

Faraji Rad, Z., Prewett, P. D., & Davies, G. J. (2021). An overview of microneedle applications, materials, and fabrication methods. *Beilstein Journal of Nanotechnology, 12*: 1034 - 1046.

Fernandez-Gonzalez, A. (2011). Stabilization of functional ingredients by microencapsulation: Interfacial polymerisation (Ph.D. thesis), University of Birmingham, Retrieved from http://etheses.bham.ac.uk/id/eprint/3577.

Fonseca, D. F. S., Vilela, C., Pinto, R. J. B., Bastos, V., Oliveira, H., Catarino, J., et al. (2021). Bacterial nanocellulose-hyaluronic acid microneedle patches for skin applications: In vitro and in vivo evaluation. *Mater Sci Eng C Mater Biol Appl, 118*: 111350.

Frank, G. (Mannheim, DE), Biastoch, Ralf (Speyer, DE), Kummer, Matthias (Weisenheim, DE). (2001). Microcapsules of low-formaldehyde melamine/formaldehyde resins. United States Patent No. US-6261483-B1. Washington, DC: P. a. T. Office. Retrived from: https://www.freepatentsonline.com/6261483.html

Fu, G., Cao, Y., & Lu, M. (2015). A fast auto-focusing method of microscopic imaging based on an improved MCS algorithm. *Journal of Innovative Optical Health Sciences, 08*(05): 1550020.

Gallagher, A. J., Anniadh, A. N., Bruyère, K., Ottenio, M., Xie, H., & Gilchrist, M. D. (2012). Dynamic tensile properties of human skin. *IRCOBI Conference* (Dublin (Ireland), 2012 September 12-14) Dublin: International Research Council on the Biomechanics of Injury.

Garcia-Diego, C., & Cuellar, J. (2005). Synthesis of macroporous poly(styrene-co-divinylbenzene) microparticles using n-Heptane as the porogen: Quantitative effects of the DVB concentration and the monomeric fraction on their structural characteristics.

Industrial & Engineering Chemistry Research, 44(22): 8237-8247.

García, J., Rios, I., & Fonthal, F. (2016, 19-21 Oct. 2016). Design and analysis of microneedles structures for transdermal drug delivery. 2016 IEEE ANDESCON, 2016, pp. 1-4, DOI: 10.1109/ANDESCON.2016.7836202.

Garlotta, D. (2001). A literature review of poly(lactic acid). *Journal of Polymers and the Environment, 9*: 63-84.

Garrett, T. R., Bhakoo, M., & Zhang, Z. (2008). Bacterial adhesion and biofilms on surfaces. *Progress in Natural Science, 18*(9): 1049-1056.

Gergely, C., Senger, B., Voegel, J. C., Hörber, J. K. H., Schaaf, P., & Hemmerlé, J. (2001). Semi-automatized processing of AFM force-spectroscopy data. *Ultramicroscopy, 87*(1): 67-78.

Ghosh Dastidar, D., Saha, S., & Chowdhury, M. (2018). Porous microspheres: Synthesis, characterisation and applications in pharmaceutical & medical fields. *International Journal of Pharmaceutics, 548*(1): 34-48.

Gittard, S. D., Chen, B., Xu, H., Ovsianikov, A., Chichkov, B. N., Monteiro-Riviere, N. A., et al. (2013). The effects of geometry on skin penetration and failure of polymer microneedles. *Journal of Adhesion Science and Technology, 27*(3): 227-243.

Gokmen, M. T., & Du Prez, F. E. (2012). Porous polymer particles—A comprehensive guide to synthesis, characterization, functionalization and applications. *Progress in Polymer Science, 37*(3): 365-405.

Gong, M., Zhao, Q., Dai, L., Li, Y., & Jiang, T. (2017). Fabrication of polylactic acid/hydroxyapatite/graphene oxide composite and their thermal stability, hydrophobic and mechanical properties. *Journal of Asian Ceramic Societies, 5*: 160-168.

Gray, A., Egan, S., Bakalis, S., & Zhang, Z. (2016). Determination of microcapsule physicochemical, structural, and mechanical properties. *Particuology, 24*(C): 32-43.

Gurusamy, V., Kannan, S., & G.Nalini. (2014). Review on image segmentation techniques. In *2014 National Conference on Recent Trends and Research Issues in Computer Science (RTRICS)* (Podi: 2014 September 10). Podi: Retrived from https://www.researchgate.net/publication/273127438_REVIEW_ON_IMAGE_SEGMENTATION_TECHNIQUES

Ha, S. (2005, November). Above the curve: Six sigma learning begins at home. *Industrial Engineer, 37*(11): 36-41.

Han, K. T. M., & Uyyanonvara, B. (2016, 20-22 March 2016). A survey of blob detection algorithms for biomedical images. In *7th International Conference of Information and Communication Technology for Embedded Systems (IC-ICTES)*, pp. 57-60, DOI: 10.1109/ICTEmSys.2016.7467122

He, J. Y., Zhang, Z. L., & Kristiansen, H. (2009). Nanomechanical characterization of single micron-sized polymer particles. *Journal of Applied Polymer Science, 113*(3): 1398-1405.

He, J. Y., Zhang, Z. L., Midttun, M., Fonnum, G., Modahl, G. I., Kristiansen, H., et al. (2008).

Size effect on mechanical properties of micron-sized PS-DVB polymer particles. *Polymer, 49*(18): 3993-3999.

He, L., Ren, X., Gao, Q., Zhao, X., Yao, B., & Chao, Y. (2017). The connected-component labeling problem: A review of state-of-the-art algorithms. *Pattern Recognition, 70*: 25-43.

He, Y. (2013). Understanding the interactions between microcapsules and fabric surfaces. (Ph.D thesis), University of Birmingham, Retrieved from http://etheses.bham.ac.uk/id/eprint/9233

He, Y., Bowen, J., Andrews, J. W., Liu, M., Smets, J., & Zhang, Z. (2014). Adhesion of perfume-filled microcapsules to model fabric surfaces. *J Microencapsul, 31*(5): 430-439.

Heinrich, V., & Rawicz, W. (2005). Automated, high-resolution micropipet aspiration reveals new insight into the physical properties of fluid membranes. *Langmuir : the ACS journal of surfaces and colloids, 21*(5): 1962-1971.

Hsu, W.-Y., Lee, C.-S., Chen, P.-J., Chen, N.-T., Chen, F.-Z., Yu, Z.-R., et al. (2009). Development of the fast astigmatic auto-focus microscope system. *Measurement Science and Technology, 20*(4): 045902.

Hu, J., Chen, H.-Q., & Zhang, Z. (2009). Mechanical properties of melamine formaldehyde microcapsules for self-healing materials. *Materials Chemistry and Physics, 118*(1): 63-70.

Huang, Y., Yu, H., Wang, L., Shen, D., Ni, Z., Ren, S., et al. (2022). Research progress on cosmetic microneedle systems: Preparation, property and application. *European Polymer Journal, 163*: 110942.

Hüsken, D., Steudle, E., & Zimmermann, U. (1978). Pressure probe technique for measuring water relations of cells in higher plants. *Plant Physiology, 61*(2): 158-163.

Israni, D., Patel, S., & Shah, A. (2016). Comparison of different techniques of camera autofocusing 2016.

Jacquemoud, C., Bruyere-Garnier, K., & Coret, M. (2007). Methodology to determine failure characteristics of planar soft tissues using a dynamic tensile test. *Journal of Biomechanics, 40*(2): 468-475.

Joodaki, H., & Panzer, M. B. (2018). Skin mechanical properties and modeling: A review. *Proceedings of the Institution of Mechanical Engineers, Part H: Journal of Engineering in Medicine, 232*: 323 - 343.

Jung-Hwan, P., Allen, M. G., & Prausnitz, M. R. (2004). Biodegradable polymer microneedles: Fabrication, mechanics and transdermal drug delivery. In *The 26th Annual International Conference of the IEEE Engineering in Medicine and Biology Society* (San Francisco, CA, USA, 2004 September 1-5): 2654-2657

Jyothi, N. V., Prasanna, P. M., Sakarkar, S. N., Prabha, K. S., Ramaiah, P. S., & Srawan, G. Y. (2010). Microencapsulation techniques, factors influencing encapsulation efficiency. *J Microencapsul, 27*(3): 187-197.

Kalra, A., Lowe, A., & Al-Jumaily, A. M. (2016). Mechanical behaviour of skin: A review. *Journal of Material Sciences & Engineering, 5*: 1-7.

Kehtarnavaz, N., & Oh, H. J. (2003). Development and real-time implementation of a rule-based auto-focus algorithm. *Real-Time Imaging, 9*(3): 197-203.

Kelly, P. (2013). Mechanics lecture notes: An introduction to solid mechanics. Retrieved from http://homepages.engineering.auckland.ac.nz/~pkel015/SolidMechanicsBooks/index.html

Kim, H. K., Lee, S. H., Lee, B. Y., Kim, S. J., Sung, C. Y., Jang, N. K., et al. (2018). A comparative study of dissolving hyaluronic acid microneedles with trehalose and poly(vinyl pyrrolidone) for efficient peptide drug delivery. *Biomater Sci, 6*(10): 2566-2570.

Kim, K., Sung, J., Lee, J., Song, J., & Chin, I.-J. (2006). Microencapsulation of electrophoretic tio2 nanoparticles for electronic ink. *Molecular Crystals and Liquid Crystals, 445*(1): 43/[333]-348/[338].

Kim, Y.-C., Park, J.-H., & Prausnitz, M. R. (2012). Microneedles for drug and vaccine delivery. *Advanced Drug Delivery Reviews, 64*(14): 1547-1568.

Kulpa, Z. (1977). Area and perimeter measurement of blobs in discrete binary pictures. *Computer Graphics and Image Processing, 6*(5): 434-451.

Lasdon, L. S., Waren, A. D., Jain, A., & Ratner, M. (1978). Design and testing of a generalized reduced gradient code for nonlinear programming. *ACM Trans. Math. Softw., 4*(1): 34–50.

Lee, H. Y., Lee, S. J., Cheong, I. W., & Kim, J. H. (2002). Microencapsulation of fragrant oil via in situ polymerization: Effects of ph and melamine-formaldehyde molar ratio. *Journal of Microencapsulation, 19*(5): 559-569.

Lee, K. Y., Peters, M. C., & Mooney, D. J. (2001). Controlled drug delivery from polymers by mechanical signals. *Advanced Materials, 13*(11): 837-839.

Li, G., He, Y., Han, W., Yu, Y., Zhu, L., Si, T., et al. (2021a). An improved solvent evaporation method to produce poly (lactic acid) microspheres via foam-transfer. *Int J Biol Macromol, 172*: 114-123.

Li, G., Yu, Y., Han, W., Zhu, L., Si, T., Wang, H., et al. (2021b). Solvent evaporation self-motivated continual synthesis of versatile porous polymer microspheres via foaming-transfer. *Colloids and Surfaces A: Physicochemical and Engineering Aspects, 615*.

Li, J., Chen, J., Wang, P., & Loffeld, O. (2018). A coarse-to-fine autofocus approach for very high-resolution airborne stripmap sar imagery. *IEEE Transactions on Geoscience and Remote Sensing, 56*(7): 3814-3829.

Li, Y., Zhang, J., Zhang, W., Tian, H., & Chen, X. (2015). Novel microcapsules for drug and gene delivery. *Journal of Controlled Release, 213*: e130-e131.

Lin, Y. (2018). Auto-focusing methods and apparatus. China Patent No. WOCN17098301, Retrived from https://www.freepatentsonline.com/y2012/0327195.html

Liu, K. K., Williams, D. R., & Briscoe, B. J. (1998). The large deformation of a single micro-

elastomeric sphere. *Journal of Physics D: Applied Physics, 31*(3): 294-303.

Liu, M. (2010). Understanding the mechanical strength of microcapsules and their adhesion on fabric surfaces. (Ph.D thesis), University of Birmingham, Retrieved from http://etheses.bham.ac.uk/id/eprint/673.

Liu, R., Ma, G., Meng, F.-T., & Su, Z.-G. (2005). Preparation of uniform-sized PLA microcapsules by combining shirasu porous glass membrane emulsification technique and multiple emulsion-solvent evaporation method. *Journal of Controlled Release, 103*(1): 31-43.

Liu, S., Wu, G., Zhang, X., Yu, J., Liu, M., Zhang, Y., et al. (2019). Preparation and properties of poly (lactic acid) (PLA) suture loaded with PLA microspheres enclosed drugs (PM-Ds). *The Journal of The Textile Institute, 110*(11): 1596-1605.

Liu, T., & Zhang, Z. (2004). Mechanical properties of desiccated ragweed pollen grains determined by micromanipulation and theoretical modelling. *Biotechnol Bioeng, 85*(7): 770-775.

Liu, W., Christian, G. K., Zhang, Z., & Fryer, P. J. (2002). Development and use of a micromanipulation technique for measuring the force required to disrupt and remove fouling deposits. *Food and Bioproducts Processing, 80*(4): 286-291.

Liu, W., Christian, G. K., Zhang, Z., & Fryer, P. J. (2006a). Direct measurement of the force required to disrupt and remove fouling deposits of whey protein concentrate. *International Dairy Journal, 16*(2): 164-172.

Liu, W., Fryer, P. J., Zhang, Z., Zhao, Q., & Liu, Y. (2006b). Identification of cohesive and adhesive effects in the cleaning of food fouling deposits. *Innovative Food Science & Emerging Technologies, 7*(4): 263-269.

Liu, W., Zhang, Z., & Fryer, P. J. (2006c). Identification and modelling of different removal modes in the cleaning of a model food deposit. *Chemical Engineering Science, 61*(22): 7528-7534.

Loizidou, E. Z., Williams, N. A., Barrow, D. A., Eaton, M. J., McCrory, J., Evans, S. L., et al. (2015). Structural characterisation and transdermal delivery studies on sugar microneedles: Experimental and finite element modelling analyses. *European Journal of Pharmaceutics and Biopharmaceutics, 89*: 224-231.

Long, Y., York, D., Zhang, Z., & Preece, J. (2009). Microcapsules with low content of formaldehyde: Preparation and characterization. *Journal of Materials Chemistry - J MATER CHEM, 19*.

Lulevich, V. V., Andrienko, D., & Vinogradova, O. I. (2004). Elasticity of polyelectrolyte multilayer microcapsules. *J Chem Phys, 120*(8): 3822-3826.

Luo, S., Gao, M., Pan, X., Wang, Y., He, Y., Zhu, L., et al. (2022). Fragrance oil microcapsules with low content of formaldehyde: Preparation and characterization. *Colloids and Surfaces A: Physicochemical and Engineering Aspects*: 129019.

Ma, G. (2014). Microencapsulation of protein drugs for drug delivery: Strategy, preparation, and applications. *Journal of Controlled Release, 193*: 324-340.

Maia, F., Tedim, J., Bastos, A. C., Ferreira, M. G. S., & Zheludkevich, M. L. (2014). Active sensing coating for early detection of corrosion processes. *RSC Advances, 4*(34): 17780-17786.

Marrugo, A., Millán, M., & Abril, H. (2014). Implementation of an image based focusing algorithm for non-mydriatic retinal imaging. In *2014 III International Congress of Engineering Mechatronics and Automation (CIIMA)*, 1-3.

Mashmoushy, H., Zhang, Z., & Thomas, C. R. (1998). Micromanipulation measurement of the mechanical properties of baker's yeast cells. *Biotechnology Techniques, 12*(12): 925-929.

Mattice, J. M., Lau, A. G., Oyen, M. L., & Kent, R. W. (2006). Spherical indentation load-relaxation of soft biological tissues. *Journal of Materials Research, 21*(8): 2003-2010.

McCrudden, M. T., McAlister, E., Courtenay, A. J., González-Vázquez, P., Singh, T. R., & Donnelly, R. F. (2015). Microneedle applications in improving skin appearance. *Exp Dermatol, 24*(8): 561-566.

Mendanha, D. V., Molina Ortiz, S. E., Favaro-Trindade, C. S., Mauri, A., Monterrey-Quintero, E. S., & Thomazini, M. (2009). Microencapsulation of casein hydrolysate by complex coacervation with spi/pectin. *Food Research International, 42*(8): 1099-1104.

Meng, Y., Zhang, Z., Yin, H., & Ma, T. (2018). Automatic detection of particle size distribution by image analysis based on local adaptive canny edge detection and modified circular hough transform. *Micron, 106*: 34-41.

Mercadé-Prieto, R., Allen, R., York, D., Preece, J. A., Goodwin, T. E., & Zhang, Z. (2011a). Compression of elastic–perfectly plastic microcapsules using micromanipulation and finite element modelling: Determination of the yield stress. *Chemical Engineering Science, 66*(9): 1835-1843.

Mercadé-Prieto, R., Allen, R., York, D., Preece, J. A., Goodwin, T. E., & Zhang, Z. (2012). Determination of the failure stresses for fluid-filled microcapsules that rupture near the elastic regime. *Experimental Mechanics, 52*: 1435-1445.

Mercadé-Prieto, R., Nguyen, B., Allen, R., York, D., Preece, J. A., Goodwin, T. E., et al. (2011b). Determination of the elastic properties of single microcapsules using micromanipulation and finite element modeling. *Chemical Engineering Science, 66*(10): 2042-2049.

Mercadé-Prieto, R., & Zhang, Z. (2012). Mechanical characterization of microspheres - capsules, cells and beads: A review. *Journal of Microencapsulation, 29*(3): 277-285.

Mercadé-Prieto, R., Allen, R., Zhang, Z., York, D., Preece, J. A., & Goodwin, T. E. (2012). Failure of elastic-plastic core–shell microcapsules under compression. *AIChE Journal, 58*(9): 2674-2681.

Microspheres-Online. (2022). Retrieved from https://www.microspheres.us/

Mir, H., Xu, P., & Beek, P. (2014). An extensive empirical evaluation of focus measures for digital photography. In *Proc. SPIE 9023*, Digital Photog. X, 2014.

Mir, H., Xu, P., Chen, R., & Beek, P. (2015). An autofocus heuristic for digital cameras based

on supervised machine learning. *Journal of Heuristics, 21*(5): 599-616.

Mirzaei, M., & Rafsanjani, H. K. (2017). An automatic algorithm for determination of the nanoparticles from tem images using circular hough transform. *Micron, 96*: 86-95.

Mishra, D. K., Yu, J., & Leung, C. K. Y. (2018). Self-sensing and self-healing 'smart' cement-based materials – A review of the state of the art. In *Sixth International Conference on Durability of Concrete Structur* (University of Leeds, 2018 July 18-20). Leeds: University of Leeds.

Mohanta, R., & Sethi, B. (2012). A review of genetic algorithm application for image segmentation. *International Journal of Computer Applications in Technology, 3*(2): 720-723.

Monclus, M. A., Young, T. J., & Di Maio, D. (2010). AFM indentation method used for elastic modulus characterization of interfaces and thin layers. *Journal of Materials Science, 45*(12): 3190-3197.

Montgomery, D. C., Peck, E. A., & Vining, G. G. (2012). Introduction to linear regression analysis (5th ed.). Hoboken: Wiley-Blackwell.

Mordehai, D., Lee, S.-W., Backes, B., Srolovitz, D. J., Nix, W. D., & Rabkin, E. (2011). Size effect in compression of single-crystal gold microparticles. *Acta Materialia, 59*(13): 5202-5215.

Müller, E., Chung, J. T., Zhang, Z., & Sprauer, A. (2005). Characterization of the mechanical properties of polymeric chromatographic particles by micromanipulation. *Journal of Chromatography A, 1097*(1): 116-123.

Neuman, K. C., & Nagy, A. (2008). Single-molecule force spectroscopy: Optical tweezers, magnetic tweezers and atomic force microscopy. *Nature methods, 5*(6): 491-505.

Nguyen, B. V., Wang, Q. G., Kuiper, N. J., El Haj, A. J., Thomas, C. R., & Zhang, Z. (2010). Biomechanical properties of single chondrocytes and chondrons determined by micromanipulation and finite-element modelling. *Journal of the Royal Society Interface, 7*(53): 1723-1733.

Nguyen, T. B., & Chung, S. T. (2009). An improved real-time blob detection for visual surveillance. In *2nd International Congress on Image and Signal Processing* (Tianjin, China, 2009 October 17-19), 1-5.

Nguyen, V. B., Wang, C. X., Thomas, C. R., & Zhang, Z. (2009). Mechanical properties of single alginate microspheres determined by microcompression and finite element modelling. *Chemical Engineering Science, 64*(5): 821-829.

O'Sullivan, M., Zhang, Z., & Vincent, B. (2009). Silica-shell/oil-core microcapsules with controlled shell thickness and their breakage stress. *Langmuir, 25*(14): 7962-7966.

Olderøy, M., Xie, M., Andreassen, J.-P., Strand, B., Zhang, Z., & Sikorski, P. (2012). Viscoelastic properties of mineralized alginate hydrogel beads. *Official Journal of the European Society for Biomaterials, 23*(7): 1619-1627.

Ooi, K., Izumi, K., Nozaki, M., & Takeda, I. (1990). An advanced autofocus system for video camera using quasi condition reasoning. *IEEE Transactions on Consumer Electronics,*

36(3): 526-530.

Otsu, N. (1979). A threshold selection method from gray-level histograms. *IEEE Transactions on Systems, Man, and Cybernetics, 9*(1): 62-66.

Ottenio, M., Tran, D., Ní Annaidh, A., Gilchrist, M. D., & Bruyère, K. (2015). Strain rate and anisotropy effects on the tensile failure characteristics of human skin. *Journal of the Mechanical Behavior of Biomedical Materials, 41*: 241-250.

Pan, X., York, D., Preece, J. A., & Zhang, Z. (2012). Size and strength distributions of melamine-formaldehyde microcapsules prepared by membrane emulsification. *Powder Technology, 227*: 43-50.

Park, J.-H., Allen, M. G., & Prausnitz, M. R. (2005). Biodegradable polymer microneedles: Fabrication, mechanics and transdermal drug delivery. *Journal of Controlled Release, 104*(1): 51-66.

Park, J.-H., Allen, M. G., & Prausnitz, M. R. (2006). Polymer microneedles for controlled-release drug delivery. *Pharmaceutical Research, 23*(5): 1008-1019.

Paul, J., Romeis, S., Tomas, J., & Peukert, W. (2014). A review of models for single particle compression and their application to silica microspheres. *Advanced Powder Technology, 25*(1): 136-153.

Pinkard, H., Phillips, Z., Babakhani, A., Fletcher, D., & Waller, L. (2019). Deep learning for single-shot autofocus microscopy. *Optica, 6*: 794.

Prausnitz, M. R. (2004). Microneedles for transdermal drug delivery. *Advanced Drug Delivery Reviews, 56*(5): 581-587.

Pukelsheim, F. (1994). The three sigma rule. *The American Statistician, 48*(2): 88-91.

Qi, F., Wu, J., Li, H., & Ma, G. (2019). Recent research and development of PLGA/PLA microspheres/nanoparticles: A review in scientific and industrial aspects. *Frontiers of Chemical Science and Engineering, 13*(1): 14-27.

Qi, F., Wu, J., Yang, T., Ma, G., & Su, Z. (2014). Mechanistic studies for monodisperse exenatide-loaded PLGA microspheres prepared by different methods based on SPG membrane emulsification. *Acta Biomaterialia, 10*(10): 4247-4256.

Radhika, C., & Gnanavel, B. K. (2021). Buckling analysis of polymer microneedle for transdermal drug delivery. *Materials Today: Proceedings, 46*: 3538-3541.

Rana, S., Pichandi, S., Fangueiro, R., & Correia, A. (2016). A review on smart self-sensing composite materials for civil engineering applications. *AIMS Material Science, 3*: 357-379.

Ranamukhaarachchi, S. A., Lehnert, S., Ranamukhaarachchi, S. L., Sprenger, L., Schneider, T., Mansoor, I., et al. (2016). A micromechanical comparison of human and porcine skin before and after preservation by freezing for medical device development. *Scientific Reports, 6*(1): 32074.

Rayleigh, L. (1896). Xv. On the theory of optical images, with special reference to the microscope. *The London, Edinburgh, and Dublin Philosophical Magazine and Journal of Science, 42*(255): 167-195.

Reszko, A. E., Sadick, N. S., Magro, C. M., & Farber, J. (2009). Late-onset subcutaneous nodules after poly-l-lactic acid injection. *Dermatol Surg, 35*(2): 380-384.

Roche, S., Ibarz, G., Crespo, C., Chiminelli, A., Araujo, A., Santos, R., et al. (2022). Self-sensing polymeric materials based on fluorescent microcapsules for the detection of microcracks. *Journal of Materials Research and Technology, 16*: 505-515.

Sasakura, T. (1999). Automatic focusing device using phase difference detection. United States Patent No. 5995144. Washington, DC: P. a. T. Office.

Shojaei-Baghini, E., Zheng, Y., & Sun, Y. (2013). Automated micropipette aspiration of single cells. *Annals of Biomedical Engineering, 41*(6): 1208-1216.

Silver, F. H., Freeman, J. W., & DeVore, D. (2001). Viscoelastic properties of human skin and processed dermis. *Skin Res Technol, 7*(1): 18-23.

Smith, A. E., Zhang, Z., & Thomas, C. R. (2000). Wall material properties of yeast cells: Part 1. Cell measurements and compression experiments. *Chemical Engineering Science, 55*(11): 2031-2041.

Smith, S. W. (1997). The scientist and engineer's guide to digital signal processing. California: California Technical Publishing.

Song, Y., Chen, K.-F., Wang, J.-J., Liu, Y., Qi, T., & Li, G. L. (2019). Synthesis of polyurethane/poly(urea-formaldehyde) double-shelled microcapsules for self-healing anticorrosion coatings. *Chinese Journal of Polymer Science, 38*(1): 45-52.

Song, Y., Li, M., & Sun, L. (2007). A new auto-focusing algorithm for optical microscope based automated system.

Stenekes, R. J. H., De Smedt, S. C., Demeester, J., Sun, G., Zhang, Z., & Hennink, W. E. (2000). Pore sizes in hydrated dextran microspheres. *Biomacromolecules, 1*(4): 696-703.

Šumiga, B., Knez, E., Vrtačnik, M., Ferk Savec, V., Staresinic, M., & Boh Podgornik, B. (2011). Production of melamine-formaldehyde PCM microcapsules with ammonia scavenger used for residual formaldehyde reduction. *Acta chimica Slovenica, 58*: 14-25.

Sun, G., & Zhang, Z. (2001). Mechanical properties of melamine-formaldehyde microcapsules. *Journal of microencapsulation, 18*: 593-602.

Sun, G., & Zhang, Z. (2002). Mechanical strength of microcapsules made of different wall materials. *International Journal of Pharmaceutics, 242*(1): 307-311.

Tekin, R., Bac, N., & Erdogmus, H. (2013). Microencapsulation of fragrance and natural volatile oils for application in cosmetics, and household cleaning products. *Macromolecular Symposia, 333*.

Teymoorzadeh, H., & Rodrigue, D. (2015). Biocomposites of wood flour and polylactic acid: Processing and properties. *Journal of Biobased Materials and Bioenergy, 9*: 1-6.

van der Maaden, K., Sekerdag, E., Jiskoot, W., & Bouwstra, J. (2014). Impact-insertion applicator improves reliability of skin penetration by solid microneedle arrays. *The AAPS Journal, 16*(4): 681-684.

Vian, W. D., & Denton, N. L. (2018). Hardness comparison of polymer specimens produced

with different processes. In *ASEE IL-IN Section Conference*, 3.

Wang, C., Pritchard, J., & Thomas, C. R. (2006a). Investigation of the mechanics of single tomato fruit cells. *Journal of Texture Studies, 37*: 597-606.

Wang, C. X., Cowen, C., Zhang, Z., & Thomas, C. R. (2005). High-speed compression of single alginate microspheres. *Chemical Engineering Science, 60*(23): 6649-6657.

Wang, L., Hukin, D., Pritchard, J., & Thomas, C. (2006b). Comparison of plant cell turgor pressure measurement by pressure probe and micromanipulation. *Biotechnology Letters, 28*(15): 1147-1150.

Wang, Q. G., Magnay, J. L., Nguyen, B., Thomas, C. R., Zhang, Z., El Haj, A. J., et al. (2009). Gene expression profiles of dynamically compressed single chondrocytes and chondrons. *Biochemical and Biophysical Research Communications, 379*(3): 738-742.

Wang, Q. L., Ren, J. W., Chen, B. Z., Jin, X., Zhang, C. Y., & Guo, X. D. (2018). Effect of humidity on mechanical properties of dissolving microneedles for transdermal drug delivery. *Journal of Industrial and Engineering Chemistry, 59*: 251-258.

Wang, X., Wu, X., Xing, H., Zhang, G., Shi, Q., E, L., et al. (2017). Porous nanohydroxyapatite/collagen scaffolds loading insulin PLGA particles for restoration of critical size bone defect. *ACS Applied Materials & Interfaces, 9*(13): 11380-11391.

Wayne, R. (2019). Light and video microscopy (3rd ed.): Academic Press.

Wei, Y., Chen, H., Wang, H., Wei, D., Wu, Y., & Fan, K. (2019). Detection of nano-particles based on machine vision. In *2019 IEEE International Conference on Manipulation, Manufacturing and Measurement on the Nanoscale (3M-NANO)* (Zhenjiang: 2019, August 4-8): 189-192.

Whelehan, M., & Marison, I. (2011). Microencapsulation using vibrating technology. *Journal of microencapsulation, 28*: 669-688.

Xiong, Y., & Shafer, S. A. (1993). Depth from focusing and defocusing. In *Proceedings of IEEE Conference on Computer Vision and Pattern Recognition* (New York, USA: 1993 June 15-17): 68-73.

Xu, X., Zhang, X., Fu, H., Chen, L., Zhang, H., & Fu, X. (2014). Robust passive autofocus system for mobile phone camera applications. *Computers & Electrical Engineering, 40*(4): 1353-1362.

Xu, Y., Gao, F., Wu, T., Bennett, K. M., Charlton, J. R., & Sarkar, S. (2019). U-Net with optimal thresholding for small blob detection in medical images. *2019 IEEE 15th International Conference on Automation Science and Engineering (CASE)*: 1761-1767.

Xue, J., & Zhang, Z. (2009). Physical, structural, and mechanical characterization of calcium-shellac microspheres as a carrier of carbamide peroxide. *Journal of Applied Polymer Science, 113*(3): 1619-1625.

Yan, Y., Zhang, Z., Stokes, J. R., Zhou, Q.-Z., Ma, G.-H., & Adams, M. J. (2009). Mechanical characterization of agarose micro-particles with a narrow size distribution. *Powder Technology, 192*(1): 122-130.

Yang, J., Liu, X., Fu, Y., & Song, Y. (2019). Recent advances of microneedles for biomedical

applications: Drug delivery and beyond. *Acta Pharm Sin B, 9*(3): 469-483.

Yang, Y., Bajaj, N., Xu, P., Ohn, K., Tsifansky, M. D., & Yeo, Y. (2009). Development of highly porous large PLGA microparticles for pulmonary drug delivery. *Biomaterials, 30*(10): 1947-1953.

Yap, S. F., Adams, M., Seville, J., & Zhang, Z. (2006). Understanding the mechanical properties of single micro-particles and their compaction behaviour. *China Particuology, 4*(1): 35-40.

Yap, S. F., Adams, M. J., Seville, J. P. K., & Zhang, Z. (2008). Single and bulk compression of pharmaceutical excipients: Evaluation of mechanical properties. *Powder Technology, 185*(1): 1-10.

Yuan, H., Li, G., Yang, L., Yan, X., & Yang, D. (2015). Development of melamine-formaldehyde resin microcapsules with low formaldehyde emission suited for seed treatment. *Colloids and Surfaces B: Biointerfaces, 128*: 149-154.

Yuheng, S., & Hao, Y. (2017). Image segmentation algorithms overview. In *2017 Asia Modelling Symposium (AMS)*, Kota Kinabalu: 2017. Retrieved from https://doi.org/10.48550/arXiv.1707.02051

Zeleniakienė, D., Leišis, V., Griškevičius, P., Bulderberga, O., & Aniskevich, A. (2016). A numerical simulation of mechanical properties of smart polymer composite with microcapsules for damage sensing applications.

Zhang, H., Xiang, S., Luan, Q., Bao, Y., Deng, Q., Zheng, M., et al. (2018a). Development of poly (lactic acid) microspheres and their potential application in pickering emulsions stabilization. *International Journal of Biological Macromolecules, 108*: 105-111.

Zhang, T., Zhang, Q., Chen, J., Fang, K., Dou, J., & Gu, N. (2014a). The controllable preparation of porous PLGA microspheres by the oil/water emulsion method and its application in 3d culture of ovarian cancer cells. *Colloids and Surfaces A: Physicochemical and Engineering Aspects, 452*: 115-124.

Zhang, X., Fan, F., Gheisari, M., & Srivastava, G. (2019). A novel auto-focus method for image processing using laser triangulation. *IEEE Access, 7*: 64837-64843.

Zhang, X., Liu, Z., Jiang, M., & Chang, M. (2014b). Fast and accurate auto-focusing algorithm based on the combination of depth from focus and improved depth from defocus. *Optics Express, 22*(25): 31237-31247.

Zhang, Y., Baiocco, D., Mustapha, A. N., Zhang, X., Yu, Q., Wellio, G., et al. (2020). Hydrocolloids: Nova materials assisting encapsulation of volatile phase change materials for cryogenic energy transport and storage. *Chemical Engineering Journal, 382*.

Zhang, Y., Liu, L., Gong, W., Yu, H., Wang, W., Zhao, C., et al. (2018b). Autofocus system and evaluation methodologies: A literature review. *Sensors and Materials, 30*: 1165-1174.

Zhang, Z. (2016). Novel micromanipulation studies of biological and non-biological materials. (D.Sc. thesis), University of Birmingham, Retrieved from

http://etheses.bham.ac.uk/id/eprint/6512.

Zhang, Z. (2019). Determination of the viscoelastic and plastic properties of capsules based on micromanipulation measurement and finite element analysis. *Unpublished*. School of Chemical Engineering, University of Birmingham.

Zhang, Z., al-Rubeai, M., & Thomas, C. R. (1992a). Effect of Pluronic F-68 on the mechanical properties of mammalian cells. *Enzyme Microb Technol, 14*(12): 980-983.

Zhang, Z., Ferenczi, M. A., Lush, A. C., & Thomas, C. R. (1991). A novel micromanipulation technique for measuring the bursting strength of single mammalian cells. *Applied Microbiology and Biotechnology, 36*(2): 208-210.

Zhang, Z., Ferenczi, M. A., & Thomas, C. R. (1992b). A micromanipulation technique with a theoretical cell model for determining mechanical properties of single mammalian cells. *Chemical Engineering Science, 47*(6): 1347-1354.

Zhang, Z., He, Y., & Zhang, Z. (2022). Micromanipulation and automatic data analysis to determine the mechanical strength of microparticles. *Micromachines, 13*(5): 751.

Zhang, Z., Saunders, R., & Thomas, C. R. (1999). Mechanical strength of single microcapsules determined by a novel micromanipulation technique. *J Microencapsul, 16*(1): 117-124.

Zhang, Z., Stenson, J. D., & Thomas, C. R. (2009). Chapter 2 micromanipulation in mechanical characterisation of single particles. In J. Li (Ed.), *Advances in chemical engineering*: Academic Press, pp. 29-85.

Zhao, L., & Zhang, Z. (2004). Mechanical characterization of biocompatible microspheres and microcapsules by direct compression. *Artif Cells Blood Substit Immobil Biotechnol, 32*(1): 25-40.

Zheng, X., Lei, Q., Yao, R., Gong, Y., & Yin, Q. (2018). Image segmentation based on adaptive k-means algorithm. *EURASIP Journal on Image and Video Processing, 2018*(1): 68.

Zheng, X., Wang, Q., Li, Y., Xu, S., & Li, Y. (2020). Fabrication of self-reactive microcapsules as color visual sensing for damage reporting. *Journal of Materials Science, 55*(21): 8861-8867.

Appendix A. Errors caused by compressing tilt microneedles

It was found that some microneedles were not vertical among a same patch and the obtained results can differ with the real values. When a tilt (the initial tilt angle is θ_0) microneedle is under compressing, the load F can be divided into the compression part F_C which is along the axis of the microneedle and bending part F_B which is perpendicular to F_C as illustrated in Figure A-1a.

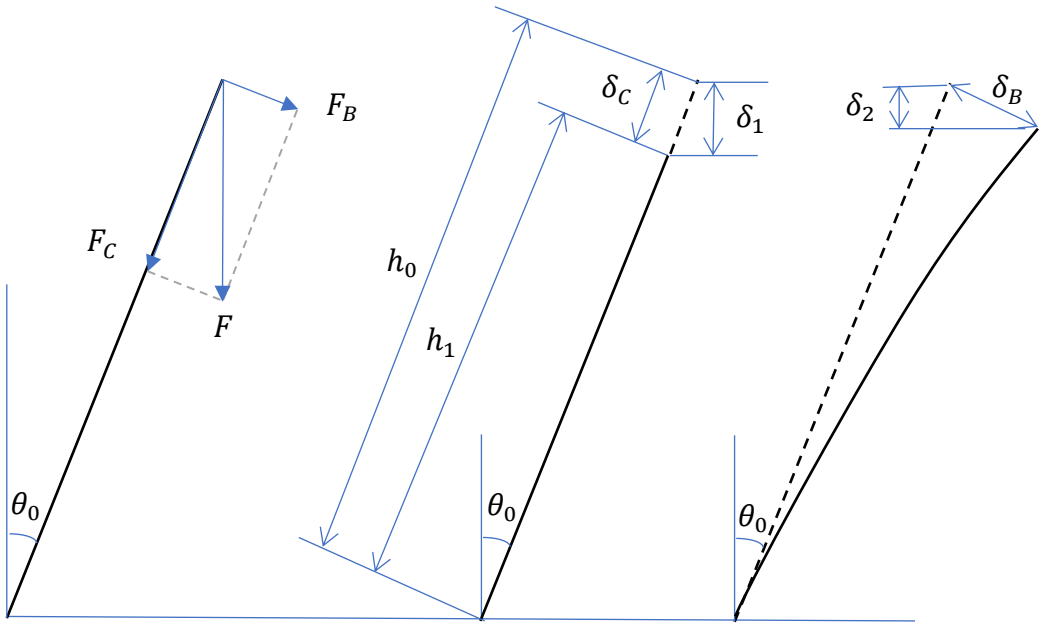

(a) Loading decomposition

(b) Displacement from compression

(c) Displacement from bending

Figure A-1 Schematic diagram of a tilt microneedle under loading (force probe not shown)

The two loads are related to the overall force as the following two equations.

$$F_C = F \cdot \cos\theta_0 \tag{A-1}$$

and

$$F_B = F \cdot \sin\theta_0 \tag{A-2}$$

The corresponding vertical displacement δ_1 and the compression displacement along the axis of the microneedle caused by the compression load F_C are related with the following equation (Figure A-1b)

$$\delta_1 = \delta_C \cdot \cos\theta_0 \tag{A-3}$$

The corresponding vertical displacement δ_2 caused by bending is illustrated in Figure A-1c. For simplicity, assuming the microneedle is a cantilever beam (the maximum bending stress is constant in all cross-sections along the axis) and the deflection δ_B caused by the bending load F_B (at the tip) can be evaluated using the following equation (Saracoglu et al., 2022)

$$\delta_B = \frac{8F_B h_0^3}{E \cdot 2r_1 \cdot (2r_1)^3} = \frac{1}{2}\frac{h_0^3}{r_1^4}\frac{F_B}{E} \tag{A-4}$$

Combination of Equations (5-17), (A-2) and (A-4) leads to

$$\delta_B = \frac{2r_2 h_0^2}{r_1^3}\delta \sin\theta_0 \tag{A-5}$$

For simplicity, assuming the deflection δ_B is along the direction of F_B, thus the resulted vertical displacement δ_2 from bending can be estimated as

$$\delta_2 = \delta_B \sin\theta_0 \tag{A-6}$$

The overall vertical displacement

$$\delta = \delta_1 + \delta_2 \tag{A-7}$$

Combination of Equations (A-5) to (A-7) leads to

$$\delta_C = (1 - \frac{2r_2 h_0^2}{r_1^3}\sin^2\theta_0)\frac{\delta}{\cos\theta_0} \tag{A-8}$$

The **true** Young's modulus of tilt microneedles (E_T) can be determined using the loading and displacement along the microneedle long axis,

$$F_C = \frac{4r_1 r_2 E_T}{h_0}\delta_C \tag{A-9}$$

The determined Young's modulus $\hat{E}$ is estimated from the following equation

$$F = \frac{4r_1 r_2 \hat{E}}{h_0}\delta \tag{A-10}$$

Thus, from Equations (A-9) and (A-10) the following equation can be obtained

$$\frac{F}{F_C} = \frac{\hat{E}}{E_C}\frac{\delta}{\delta_C} \tag{A-11}$$

Combination it with Equations (A-1) and (A-8) leads to

$$\frac{\hat{E}}{E_C} = \frac{1 - \frac{2r_2 h_0^2}{r_1^3}\sin^2\theta_0}{\cos^2\theta_0} = \frac{1 - \frac{2r_2 h_0^2}{r_1^3}\sin^2\theta_0}{1 - \sin^2\theta_0} \tag{A-12}$$

Thus, the relative error $e_r(\hat{E})$

$$e_r(\hat{E}) = (\frac{2r_2 h_0^2}{r_1^3} - 1)\frac{\sin^2\theta_0}{1 - \sin^2\theta_0} \times 100\% \tag{A-13}$$

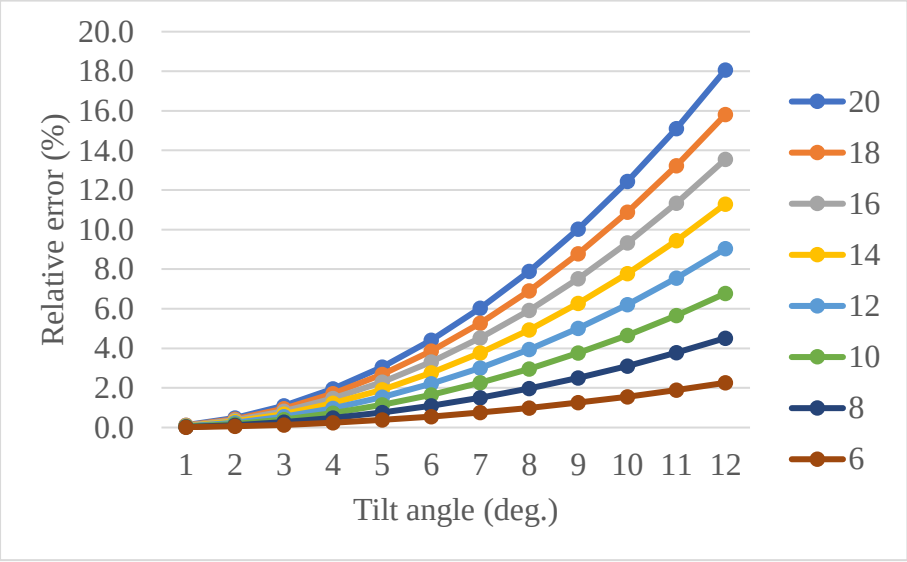

Figure A-2 Curves of the relative error versus tilt angle of microneedle with different tip width ($2r_2$)

Specifically, for the microneedle samples characterised in this research, $h_0 = 700\ \mu m$, $r_1 = 125$ μm, the curves of the relative error versus tilt angle of a microneedle with different tip

width ($2r_2$) are shown in Figure A-2. It can be seen that the relative error increases with the tilt angle for a certain tip width, and a tilt angle greater than 10 degrees can result in big relative error (>10%) for microneedles with big tips (>14μm). Therefore, microneedles that are significantly tilt should not be tested. However, if the tilt angle θ_0 is less than 5 degrees (Figure A-3), which can be easily seen from the side-view camera during the tests, the relative error should be less than 3%.

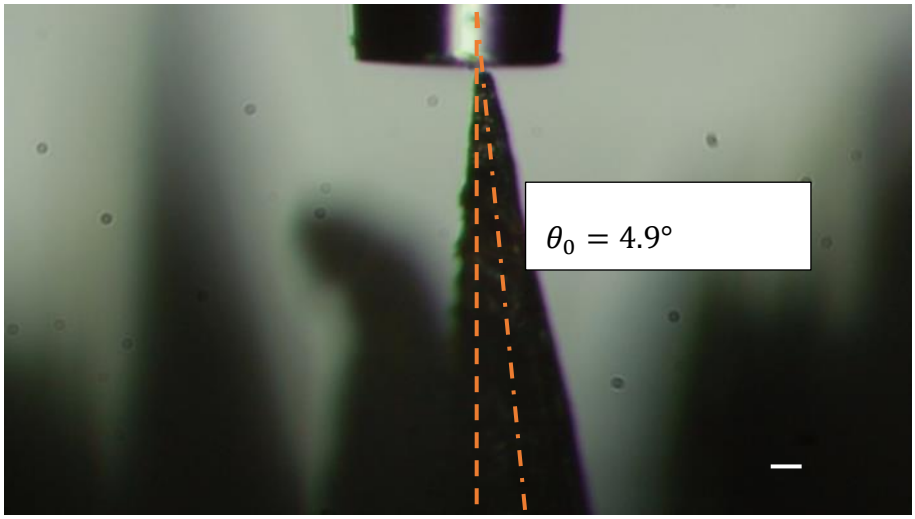

Figure A-3 Tilt angle with value of around 5° can be seen by eyes (tip width: 11.2 μm, scale bar: 20 μm)

Appendix B. Conferences and seminar attendance

12th Global Chinese Chemical Engineers Symposium (GCCES-10), Nanjing, China, 2020, oral presentation (online).

8th UK–China International Particle Technology Forum (PTF8), Dali, China, 2021, oral presentation.